
Integrated Description of Heavy Ion Collisions at RHIC and The LHC

Sangwook Ryu

Department of Physics
McGill University
Montréal, Québec H3A 2T8
Canada

Submitted in July 2016

A Thesis submitted to the
Faculty of Postdoctoral and Graduate Studies
in partial fulfillment of the requirements for the degree of
Doctor of Philosophy

© Sangwook Ryu, 2016

CONTENTS

Abstract	xiii
Résumé	xiv
Acknowledgments	xvii
Statement of Originality	xviii
1 Introduction	1
1.1 Hot QCD Matter in Heavy Ion Collisions	1
1.2 Quantum Chromodynamics	10
1.3 Evolution of Parton Distribution Functions and the Saturation Scale	13
1.4 Many-body QCD Near Thermal Equilibrium	19
2 Bulk Dynamics of QCD Medium	21
2.1 IP-Glasma Pre-thermalization Dynamics	22
2.1.1 The Impact Parameter Dependent Saturation (IP-Sat) Model	22
2.1.2 Classical Yang-Mills (CYM) Dynamics	25
2.1.3 Initial Energy Density and Flow Velocity Profiles	30
2.2 Second-Order Viscous Hydrodynamics	33
2.2.1 Kinetic Theory	33
2.2.2 Equations of Motion for Viscous Corrections	35
2.2.3 14-Moment Approximation	37
2.2.4 Temperature-dependent Bulk Viscosity	39
2.2.5 Equation of State	40
3 Post-particlization Dynamics	47
3.1 Transition from Hydrodynamics to Particle Dynamics	48
3.1.1 Cooper-Frye Formalism	48
3.1.2 Sampling Procedure	52
3.1.3 Verification of Sampling	56
3.1.4 Necessity of Microscopic Transport	58
3.2 Hadronic Cascade	66
3.3 Jet Energy Loss	74
3.3.1 AMY Formalism for Radiative Energy Loss	74
3.3.2 Collisional Energy Loss	75
3.3.3 Monte-Carlo Implementation of Energy Loss	75
4 Observables and Results	77
4.1 Definitions of Observables	78
4.2 Global Observables	84
4.3 p_T -differential Observables	97
4.4 Extension to Higher p_T with Jets	110

5	Conclusion	117
6	Appendices	120
6.1	Coordinate Systems and Kinematic Variables	120
6.2	Derivation of CYM for the IP-Glasma	122
6.3	Necessity of Second-Order Viscous Hydrodynamics	125
6.4	Derivation of Viscous Hydrodynamics	128
6.5	Linearized Boltzmann Transport Equation	134
6.5.1	General Formulation	134
6.5.2	Two-component System of Meson and Baryon	135
6.6	String Excitation and Fragmentation in UrQMD	138
	References	142

LIST OF FIGURES

1.1	This figure shows colliding nuclei, pre-equilibrium dynamics, thermalization, sQGP evolution, phase transition from QGP to hadrons and hadronic re-scattering.	2
1.2	Flow chart of the event generator for heavy ion collisions. Figure from [23].	3
1.3	QCD Feynman rules. Conventions and notations of [42] are followed.	12
1.4	Deep inelastic scattering in the parton model. An electron exchanges momentum with a parton inside proton (top). The leading order contributions in the case of quark or antiquark (bottom left) and gluon (bottom right) are shown.	14
1.5	Squared matrix elements, averaged over initial states and summed over final states, of collinear emission of quarks and gluons.	15
1.6	Partons inside a nucleon with different momentum scale Q and light-cone momentum fraction x . Figure taken from [45].	17
2.1	Leading-order diagrams that contribute to the dipole cross section. .	23
2.2	Color rotation of $q\bar{q}$ dipole scattered off a hadron target. If the size of dipole y_\perp is smaller than the saturation length scale r_S (left), the colors of quark and antiquark rotate in the same way. However, if the dipole is larger than r_S , quark and antiquark rotate differently in the color space.	24
2.3	(left) Due to the uncertainty principle, a parton carrying the light-cone momentum fraction x and transverse momentum p_T has the finite extend Δx^\pm . $P^+ = (E + p^z)/\sqrt{2}$ is the light-cone momentum of a hadron. (right) The wee partons see the hard partons fluctuating slowly and bumpy in the x^+ and x^- -directions, respectively.	26
2.4	The lightcone configuration of the ultrarelativistic heavy ion collisions. The worldlines of the colliding nuclei moving in $\pm z$ directions are $x^\mp = 0$, respectively.	27
2.5	The temperature dependence of the bulk viscosity over entropy density used in this study (left) and bulk relaxation time τ_Π as a function of temperature (right). The QGP side of the ζ/s is taken from Ref.[71] and the hadronic side is taken from Ref.[73]. The peak temperature is set to be $T_{\text{peak}} = 180 \text{ MeV}$ in this work. This parametrization was used in [24].	41
2.6	The energy density (left) and entropy density (right) as functions of temperature. The equation of state is obtained from hadronic resonance gas and lattice QCD calculation with vanishing baryonic chemical potential [76, 81].	44

2.7	The trace anomaly (left) and speed of sound (right) as functions of temperature. The equation of state is obtained from hadronic resonance gas and lattice QCD calculation with vanishing baryonic chemical potential [76, 81].	45
3.1	Temperature is decreasing at \mathbf{x}_1 where $u^\mu \Delta \Sigma_\mu > 0$ while it remains unchanged at \mathbf{x}_2 where $u^\mu \Delta \Sigma_\mu = 0$ (left). In the case of $u^\mu \Delta \Sigma_\mu < 0$ at \mathbf{x}_3 , temperature is increasing and there is no particlization (right).	53
3.2	p_T spectra and p_T -differential $v_2\{2\}$ of pions, Kaons, and protons from sampling and integration of Cooper-Frye formula. This calculation is performed for a single hydro event for 10-20% centrality of Pb+Pb collision with 2.76 TeV. “Int. w/o Neg.” and “Int. w/ Neg.” correspond to equations (3.52) and (3.1), respectively. 20000 events are sampled to obtain the results shown as “sampling”.	60
3.3	p_T -differential $v_3\{2\}$ and $v_4\{2\}$ of pions, Kaons, and protons from sampling and integration of Cooper-Frye formula. This calculation is performed for a single hydro event for 10-20% centrality of Pb+Pb collision with 2.76 TeV. “Int. w/o Neg.” and “Int. w/ Neg.” correspond to equations (3.52) and (3.1), respectively. 20000 events are sampled to obtain the results shown as “sampling”.	61
3.4	p_T spectra and p_T -differential $v_2\{2\}$ of pions, Kaons, and protons from different cases of δf in the Cooper-Frye formula. This calculation is performed for a single hydro event for 10-20% centrality of Pb+Pb collision with 2.76 TeV.	62
3.5	p_T -differential $v_3\{2\}$ and $v_4\{2\}$ of pions, Kaons, and protons from different cases of δf in the Cooper-Frye formula. This calculation is performed for a single hydro event for 10-20% centrality of Pb+Pb collision with 2.76 TeV.	63
3.6	Total volume (sum of $u^\mu \Delta \Sigma_\mu$) of surface elements with specific transverse distance and proper time τ (left top), transverse flow speed u_T (right top), shear viscosity (left bottom), and bulk viscosity (right bottom). These are obtained from single event of IP-Glasma and hydrodynamics for 10-20% centrality of Pb+Pb collision with 2.76 TeV. The shear viscosity to entropy density ratio η/s is set to be 0.095 and temperature-dependent bulk viscosity is taken from 2.5. Temperature of the isothermal hypersurface is $T_{\text{sw}} = 145$ MeV.	64
3.7	Total volume (sum of $u^\mu \Delta \Sigma_\mu$) of surface elements with specific transverse distance and proper time τ (left top), transverse flow speed u_T (right top), shear viscosity (left bottom), and bulk viscosity (right bottom). These are obtained from single event of IP-Glasma and hydrodynamics for 10-20% centrality of Au+Au collision with 200 GeV. The shear viscosity to entropy density ratio η/s is set to be 0.06 and temperature-dependent bulk viscosity is taken from 2.5. Temperature of the isothermal hypersurface is $T_{\text{sw}} = 165$ MeV.	65
3.8	Two particles in the center-of-mass frame approaching each other with impact parameter d_\perp	67

4.1	The anisotropic energy density profiles with ellipticity (left) and triangularity (right) lead to the elliptic flow v_2 and triangular flow v_3 , respectively.	78
4.2	Integrated $v_2\{2\}$, $v_2\{4\}$, $v_3\{2\}$ and $v_4\{2\}$ as functions of centrality. The shear viscosity is set to $\eta/s = 0.16$ with vanishing bulk viscosity to fit the ALICE data [1]. The bands show the range of v_n with varying switching temperature between 135 MeV and 165 MeV. The upper and lower limits of bands correspond to 135 MeV and 165 MeV, respectively. The statistical error of the model calculation is approximately 5%.	84
4.3	Integrated $v_2\{2\}$, $v_2\{4\}$, $v_3\{2\}$ and $v_4\{2\}$ as functions of centrality. The shear viscosity is set to be $\eta/s = 0.095$ with the finite bulk viscosity and the switching temperature is set to be $T_{sw} = 145$ MeV which is favoured by the proton multiplicity and mean p_T . The solid line and the dashed line correspond to the full UrQMD and the UrQMD without collisions, respectively. The statistical error of the model calculation is approximately 5%.	86
4.4	Switching temperature scan of mid-rapidity multiplicity of identified particles for centrality classes 0–5%, 10–20%, 20–30% and 30–40%. The shear viscosity is set to be $\eta/s = 0.16$ with vanishing bulk viscosity. The dashed lines and bands are the ALICE data [111] and statistical errors. The statistical error of the model calculation is approximately 1%.	89
4.5	Switching temperature scan of mean p_T of identified particles for centrality classes 0–5%, 10–20%, 20–30% and 30–40%. The shear viscosity is set to be $\eta/s = 0.16$ with vanishing bulk viscosity. The dashed lines and bands are the ALICE data [111] and statistical errors. The statistical error of the model calculation is less than 1%.	90
4.6	Switching temperature scan of mid-rapidity multiplicity of identified particles for centrality classes 0–5%, 10–20%, 20–30% and 30–40%. The shear viscosity is set to be $\eta/s = 0.095$ with finite bulk viscosity. The dashed lines and bands are the ALICE data [111] and statistical errors. The statistical error of the model calculation is approximately 1%.	91
4.7	Switching temperature scan of mean p_T of identified particles for centrality classes 0–5%, 10–20%, 20–30% and 30–40%. The shear viscosity is set to be $\eta/s = 0.095$ with finite bulk viscosity. The dashed lines and bands are the ALICE data [111] and statistical errors. The statistical error of the model calculation is less than 1%.	92
4.8	Total volume (sum of $u^\mu \Delta \Sigma_\mu$) of surface elements which yield specific transverse speed. Pions move outward faster than heavier particles due to their lower mass. The radial velocity is dimensionless given that the natural unit $c = 1$ is chosen.	93

4.9	Pions have more radial speed than kaons and protons although they originate with the same flow velocity (left). Resonance scattering push protons outward while pions are decelerated. It also makes the spectra isotropic (right).	93
4.10	Mid-rapidity multiplicity (left panels) and mean p_T (right panels) of identified particles as functions of centrality.	94
4.11	Switching temperature scan of mid-rapidity multiplicity of multi-strange baryons for centrality classes 0 – 5%, 10 – 20%, 20 – 30% and 30 – 40%. The shear viscosity is set to be $\eta/s = 0.095$ with finite bulk viscosity. The statistical error of the model calculation is approximately 2%.	95
4.12	Switching temperature scan of mean p_T of multi-strange baryons for centrality classes 0 – 5%, 10 – 20%, 20 – 30% and 30 – 40%. The shear viscosity is set to be $\eta/s = 0.095$ with finite bulk viscosity. The statistical error of the model calculation is approximately 1%.	96
4.13	p_T spectra of identified hadrons for centrality classes 0 – 5%, 10 – 20%, 20 – 30%, and 30 – 40% of Pb + Pb collisions with $\sqrt{s_{NN}} = 2.76$ TeV. The solid curves and the dashed curves correspond to the full UrQMD and the UrQMD without collisions, respectively. The ALICE data are from [111]. The statistical errors in the calculation are shown as the bands around the curves.	100
4.14	p_T differential $v_n\{2\}$ ($n = 2, 3$ and 4) of charged hadrons for centrality classes 0 – 5%, 10 – 20%, 20 – 30% and 30 – 40% of Pb + Pb collisions with $\sqrt{s_{NN}} = 2.76$ TeV. The statistical errors in the calculation are shown as the bands around the curves. The ALICE data [1] and CMS [2, 3] data were also shown for comparison.	101
4.15	p_T -differential $v_2\{2\}$ of identified hadrons for centrality classes 0 – 5%, 10 – 20%, 20 – 30%, and 30 – 40% of Pb + Pb collisions with $\sqrt{s_{NN}} = 2.76$ TeV. The solid curves and the dashed curves correspond to the full UrQMD and the UrQMD without collisions, respectively. The ALICE data are from [4]. The statistical errors in the calculation are shown as the bands around the curves.	102
4.16	$v_3\{2\}$ of identified hadrons for centrality classes 0 – 5%, 10 – 20%, 20 – 30%, and 30 – 40% of Pb + Pb collisions with $\sqrt{s_{NN}} = 2.76$ TeV. The solid curves and the dashed curves correspond to the full UrQMD and the UrQMD without collisions, respectively. The statistical errors in the calculation are shown as the bands around the curves.	103
4.17	$v_4\{2\}$ of identified hadrons for centrality classes 0 – 5%, 10 – 20%, 20 – 30%, and 30 – 40% of Pb + Pb collisions with $\sqrt{s_{NN}} = 2.76$ TeV. The solid curves and the dashed curves correspond to the full UrQMD and the UrQMD without collisions, respectively. The statistical errors in the calculation are shown as the bands around the curves.	104

4.18	p_T spectra (upper) and differential $v_2\{2\}$ (lower) of strange baryons of Pb + Pb collisions with $\sqrt{s_{NN}} = 2.76$ TeV. The solid curves and the dashed curves correspond to the full UrQMD and the UrQMD without collisions, respectively. The ALICE data [116, 117] are also shown. The statistical errors in the calculation are shown as the bands around the curves.	105
4.19	p_T spectra of identified hadrons for centrality classes 0 – 5%, 10 – 20%, 20 – 30%, and 30 – 40% of Au + Au collisions with $\sqrt{s_{NN}} = 200$ GeV. The solid curves and the dashed curves correspond to the full UrQMD and the UrQMD without collisions, respectively. The PHENIX data are from [121]. The statistical errors in the calculation are shown as the bands around the curves.	106
4.20	p_T -differential $v_2\{2\}$ of identified hadrons for centrality classes 0 – 5%, 10 – 20%, 20 – 30%, and 30 – 40% of Au + Au collisions with $\sqrt{s_{NN}} = 200$ GeV. The solid curves and the dashed curves correspond to the full UrQMD and the UrQMD without collisions, respectively. The STAR data are from [122]. The statistical errors in the calculation are shown as the bands around the curves.	107
4.21	p_T -differential $v_2\{4\}$, $v_3\{2\}$, and $v_4\{2\}$ of charged hadrons for centrality classes 0 – 5%, 10 – 20%, 20 – 30%, and 30 – 40% of Au + Au collisions with $\sqrt{s_{NN}} = 200$ GeV. The PHENIX [5] and STAR [122] data are also shown. The statistical errors in the calculation are shown as the bands around the curves.	108
4.22	Eccentricity $\epsilon_2(\Sigma)$ of isothermal hypersurface with switching temperature T_{sw} of Pb + Pb collisions at the LHC and Au + Au collisions at RHIC. “FD” indicates <i>feeddown</i> where one has the resonance decays only while “w/ Coll.” stands for the full UrQMD calculations with scatterings.	109
4.23	p_T spectra of identified hadrons and R_{AA} of charged hadrons of Pb+Pb collisions with $\sqrt{s_{NN}} = 2.76$ TeV. The calculations do not include the MARTINI jets. The ALICE data of p_T spectra and R_{AA} are from [124] and [7], respectively.	110
4.24	p_T spectra of identified hadrons and R_{AA} of charged hadrons of Pb+Pb collisions with $\sqrt{s_{NN}} = 2.76$ TeV. The calculations include the MARTINI jets. The ALICE data of p_T spectra and R_{AA} are from [124] and [7], respectively. Figures shown in [23].	113
4.25	p_T -differential $v_2\{2\}$ of identified hadrons for centrality class 20 – 30% of Pb + Pb collisions with $\sqrt{s_{NN}} = 2.76$ TeV. The ALICE data are from [4]. Figures shown in [23].	114
4.26	Higher harmonics $v_3(p_T)$ (upper) and $v_4(p_T)$ (lower) of charged hadrons for centrality class 20–30% of Pb+Pb collisions with $\sqrt{s_{NN}} = 2.76$ TeV. The CMS data are from [3]. Figures shown in [23].	115
6.1	Production of hadrons in string fragmentation of UrQMD shown in configuration space. The “yo-yo” formation time [130] is used.	141

LIST OF TABLES

1.1	Quark flavors and their electric charges	10
3.1	The r - u^r correlation $C(r, u^r; \Sigma)$ on the hypersurfaces.	58
3.2	Baryon species included in UrQMD	66
3.3	Meson species included in UrQMD. The notation J^{PC} for the particle state is explained in [91].	67
3.4	The matrix elements of resonance excitation processes of nucleon-nucleon collisions. The parameters are determined to fit the pp scattering data [96].	69
3.5	Parameters for the the total and elastic $p\bar{p}$ cross sections with $p_{\text{lab}} > 5 \text{ GeV}$	71

Abstract

In this dissertation, the IP-Glasma pre-thermalization dynamics, viscous hydrodynamics, high-energy jets, and hadronic re-scattering are consistently combined to build a hybrid model for heavy ion collisions. The pre-thermalization dynamics of mid-rapidity gluons is described by the classical Yang-Mills equation with the color charges obtained from the saturation scale. The viscous hydrodynamics, which governs evolution of the QGP medium, is derived from the kinetic theory. The shear and bulk viscosities and second-order transport coefficients are considered in this work. To take the intermediate and high-energy particles into account, production of jets and their energy loss must be properly included. Given that the mean-free-path becomes comparable to macroscopic length scales, the microscopic transport for hadronic re-scattering becomes necessary. Au-Au collisions at RHIC and Pb-Pb collisions at the LHC are considered as the applications of this hybrid model. The model calculations are compared with the experimental data putting emphasis on the effects of the bulk viscosity and hadronic re-scattering. The bulk viscosity, which has the negative contribution to the pressure, turns out to be essential for simultaneous description of the multiplicity, radial flow, and anisotropic flow. The hadronic re-scattering is shown to be important to reproduce the baryon distribution. Its effects on pions becomes also significant if one has lower collision energy. In addition, the hadronic re-scattering enables one to describe the energy loss of jets in the hadronic stage. It is shown that the hadronic processes, as well as the partonic ones, have significant effects on jets and must be included to study the jet-medium interactions.

Résumé

Dans cette thèse, un modèle hybride des collisions d'ions lourds est construit. Ce dernier contient une étape précédant l'équilibre thermique (l'étape de pré-équilibre) dont la dynamique est décrite par le model IP-Glasma. L'étape suivante de l'évolution est dirigée par l'hydrodynamique visqueuse, ainsi que par l'interaction de jets de grande impulsion transverse avec ce milieu hydrodynamique. En fin, toutes les particules, autant du jet que celles du milieu hydrodynamique, sont hadronisées et leur interaction antérieure est gouvernée par un modèle de transport hadronique. La dynamique pré-équilibre (IP-Glasma) est formulée via l'équation Yang-Mills classique décrivant l'évolution de la distribution des gluons, qui sont produits par la charge des couleurs obtenue via l'échelle de saturation. L'hydrodynamique visqueuse, régissant l'évolution du plasma quark-gluon, est retrouvée à partir de la théorie cinétique. La viscosité de cisaillement, la viscosité de volume ainsi que les autres coefficients de transport de second ordre sont considérés dans la présente étude. De plus, afin d'inclure les particules dont l'impulsion transverse peut atteindre des valeurs significatives, la perte d'énergie des jets, due à leur interaction avec le milieu, est également considérée. Lorsque le libre parcours moyen atteint l'échelle macroscopique, un modèle de transport hadronique est utilisé. Ce modèle hybride est appliqué tant aux collisions Au-Au produites au RHIC, qu'aux collisions Pb-Pb générées au sein du LHC. Les calculs de ce modèle hybride sont comparés aux données expérimentales accumulées par ces deux accélérateurs, déterminant ainsi les effets que la viscosité de volume ainsi que la diffusion des particules, décrites par le transport hadronique, ont sur les observables examinées. Cet étude montre que la viscosité de volume, contribuant négativement à la pression hydrodynamique, est indispensable afin de décrire à la fois la multiplicité de particules, leur flux radial ainsi que leur flux anisotrope. Le transport hadronique, quant à lui, est nécessaire pour obtenir une juste reproduction de la distribution des baryons. Son rôle dans la description des pions augmente au fur et à mesure que l'énergie de collision diminue. Finalement, pour bien reproduire l'influence des jets sur les hadrons observés, il est crucial d'avoir une bonne modélisation de l'interaction de ces derniers autant avec le milieu hydrodynamique, que le milieu décrit par le transport hadronique. En effet, l'interaction entre le jet et le milieu hydrodynamique est une source de perte d'énergie au niveau partonique pour le jet, alors que la perte d'énergie hadronique est régie par l'interactions des

hadrons provenant du jet avec ceux présents suite à l'hadronisation du milieu hydrodynamique. Donc, cette thèse constitue l'une des premières études complètes de l'interaction entre le jet et le milieu.

Acknowledgments

I would like to begin with my most sincere thanks to my supervisor Prof. Sangyong Jeon. His guidance and patience cannot be overemphasized when it comes to my study at McGill. He provided worthwhile opportunities for me to present and improve my work by participating in many conferences. He also managed to provide the McGill nuclear theory group with the large amount of computational resources.

I also thank to another mentor Prof. Charles Gale who gave valuable advices. He helped me keep my research well-oriented toward the results shown in this thesis.

I thank to Jean-François Paquet, Gabriel Denicol, Chun Shen, and Björn Schenke for the collaboration which lead to the important results shown in this thesis. Their willingness to spend time explaining and discussing enabled me to develop understanding of pre-thermalization dynamics, viscous hydrodynamics and microscopic transport.

I would also like to express my gratitude to Gojko Vujanovic for helping translate the abstract into French and Scott McDonald for proofreading my manuscript from cover to cover. I thank to Clint Young, Matthew Luzum, Igor Kozlov and Chanwook Park for helpful discussions to expand knowledge of physics involved in heavy ion collisions. I also thank to Pasi Huovinen for making a new version of equation of state used in this work.

In addition, I would like to mention that this work would not have been possible without CPU resources of the supercomputer Guillimin. The operation of Guillimin is funded by the Canada Foundation for Innovation (CFI), the National Science and Engineering Research Council (NSERC), NanoQuebec, and the Fonds Quebecois de Recherche sur la Nature et les Technologies (FQRNT).

I would like to take this opportunity to express my thank to the Natural Sciences and Engineering Research Council of Canada (NSERC) for the financial support.

Lastly, I deeply thank to my parents, family and friends. Their encouragement, together with the interest in physics, made my study at McGill one of the most fascinating moments in my life.

Statement of Originality

The following list specifies my contributions to the results presented in this thesis.

- Chapter 2 is a literature review about the pre-thermalization dynamics and the viscous hydrodynamics.
- Chapter 3 includes my original work to devise a sampling procedure for the particlization as described in Section 3.1. Coupling **MARTINI** jets and particlization with **UrQMD** cascade is also my original contribution.
- In Chapter 4, generation and analysis of events to compute the hadronic observables are my contributions. The pre-thermalization dynamics and hydrodynamic calculation were performed by Jean-François Paquet, Gabriel Denicol, Chun Shen, Björn Schenke, Sangyong Jeon and Charles Gale. I am the primary author of [23, 24]. The following results were published in [24] with the co-authors
 - Integrated flow coefficients v_n 's of charged hadrons (Figures 4.2 and 4.3)
 - Mid-rapidity multiplicity of identified hadrons (Figures 4.4 and 4.6)
 - mean- p_T of identified hadrons (Figures 4.5 and 4.7)
 - p_T -spectra of identified hadrons (Figure 4.13)
 - p_T -differential v_n 's of charged hadrons (Figure 4.14)

and the following results were presented in [23] with the co-authors.

- p_T -spectra of identified hadrons for higher p_T (Figure 4.24)
- R_{AA} of charged hadrons for higher p_T (Figure 4.24)
- Elliptic flow v_2 of identified hadrons for higher p_T (Figure 4.25)
- Higher flow harmonics of charged hadrons for higher p_T (Figure 4.26)

Integrated Description of Heavy Ion Collisions at RHIC and The LHC

Introduction

1.1 *Hot QCD Matter in Heavy Ion Collisions*

For a few decades, the QCD (Quantum Chromodynamics) matter in high temperature has drawn much attention from the nuclear physics community. It is also of interest in cosmology as the temperature of the early universe was high enough to have deconfined matter of quarks and gluons, or *quark-gluon plasma* (QGP). Several experiments have been carried out to probe the properties of QGP. The most important ones are collisions of heavy nuclei with a variety of energies at Relativistic Heavy Ion Collider (RHIC) and the Large Hadron Collider (LHC). As anticipated from the composite nature of the nucleus, those experiments show many phenomena which are not observed in collisions of elementary particles and have clear characteristics originating from strongly interacting plasma of quarks and gluons. The QGP matter is strongly interacting in the sense that the mean-free-path of the constituent quarks and gluons is very small and the system behaves like a fluid. This is partially due to the large occupation number of the low momentum gluons in the initial state whose coupling is not so small or perturbative. Observation of the anisotropic flow coefficients [1, 2, 3, 4, 5, 6] in the momentum distribution strongly support the collectivity of the QGP matter. While bulk dynamics of the QGP and hadronic medium dominates the non-perturbative low- p_T regime, it also has relevant effects on the high- p_T regime through the jet-medium interactions. The measurements of the nuclear modification factor R_{AA} [7, 8, 9, 10, 11] in heavy ion collisions indicate that there is large suppression of jets due to energy loss in the medium.

For a theoretical study of QGP and hadronic matter created in heavy ion collisions, it is necessary to develop a realistic event generator with different physics involved. One needs to take relevant physical processes at each stage into account. Heavy ion collisions begin with the fluctuating initial conditions. Then the system thermalizes to form QGP which is well described by viscous hydrodynamics. As the system expands due to the pressure gradient, it becomes dilute and the mean free path becomes comparable to the system size. At this time the system can no longer maintain local equilibrium. The non-equilibrium dynamics, described with the transport theory, dominates until we have the final state particles. Figure 1.1 shows a

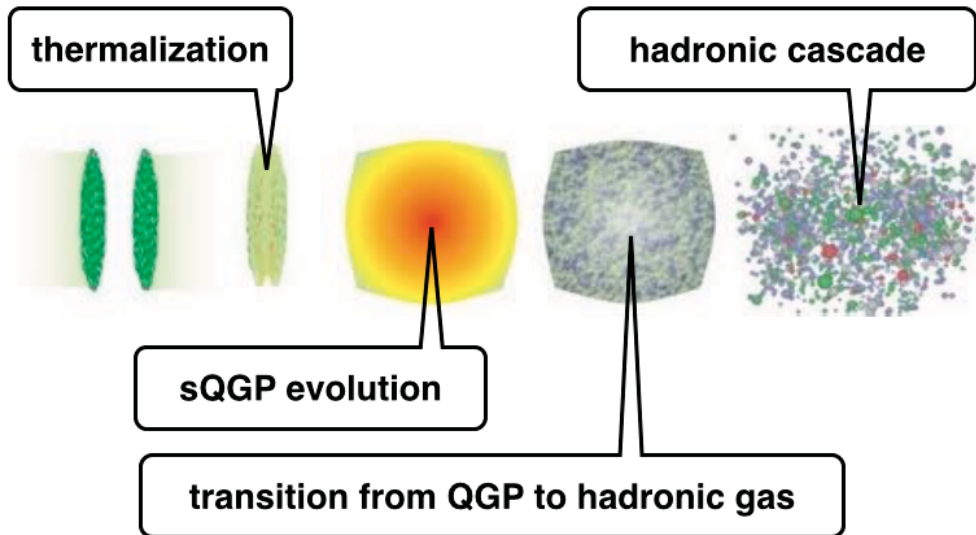


Figure 1.1: This figure shows colliding nuclei, pre-equilibrium dynamics, thermalization, sQGP evolution, phase transition from QGP to hadrons and hadronic re-scattering.

picture of heavy ion collisions described above. There have been many studies on each stage of collisions and integrated description. To incorporate physical aspects governing different stages of heavy ion collisions, hybrid approaches were adopted by many works [12, 13, 14, 15, 16, 17, 18, 19, 20]. The previous hybrid models combined the hydrodynamics, which evolution of strongly interacting fireball, and the hadronic re-scattering after particlization. The significance and uniqueness of this work are that it demonstrates the necessity of the bulk viscosity and extends the applicability

of hybrid approach to the higher p_T range by including jets.

Even though there has been much progress on the physics of each stage of heavy ion collisions, it is also necessary to have an integrated model which combines all of those stages for a better understanding of QCD matter. This work focuses on building an event generator combining the IP-Glasma [21] initial conditions, second-order viscous hydrodynamics, quenching of the high- p_T jets, Cooper-Frye particlization [22] and hadronic re-scattering to describe heavy ion collisions at RHIC and the LHC. The structure of the event generator is shown in Figure 1.2. The pre-thermalization

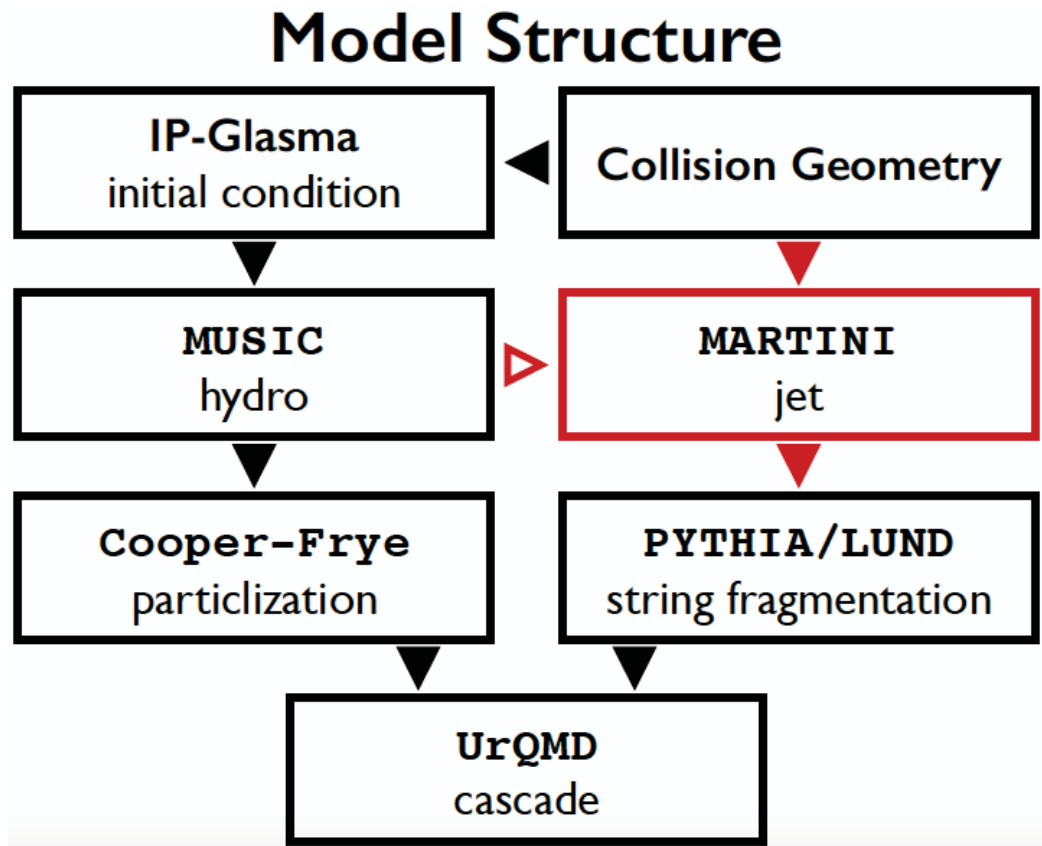


Figure 1.2: Flow chart of the event generator for heavy ion collisions. Figure from [23].

dynamics and viscous hydrodynamics, which govern the low-momentum partons and hadrons, are reviewed in Chapter 2. Transition from the hydrodynamics to microscopic transport and post-particlization dynamics are described in Chapter 3. Chapter 4 is mainly about the observables measured in heavy ion collisions and the cal-

ulation will be compared with the experimental data. It will be demonstrated that the bulk viscosity is crucial in describing particle spectra [24]. Effects of the hadronic re-scattering and high- p_T jets also will be shown [23]. In Chapter 5, this work and its implication in heavy ion phenomenology will be summarized. In addition, future works and improvements will be discussed.

We wrap up this section by briefly summarizing the models often used in each stage of heavy ion collisions.

• Pre-thermalization Dynamics

One of the simplest approaches for the pre-equilibrium dynamics is the MC-Glauber model [25], which describes the position of nucleons in each nucleus based on Wood-Saxon distribution. Participant is defined as a nucleon that experiences at least one NN binary collision. Each participant is assumed to contribute a Gaussian energy or entropy distribution. The energy density at $\tau = \tau_0$ is given by the sum of Gaussians

$$\epsilon_{\text{MC-Glb.}}(\mathbf{x}_T, \eta_s) = \left(\frac{1}{\tau_0} \frac{dE}{d\eta_s} \right) \sum_{i=1}^{N_{\text{part}}} \frac{1}{2\pi\sigma_0^2} \exp \left[-\frac{1}{2\sigma_0^2} (\mathbf{x}_T - \mathbf{x}_{T,i})^2 \right] \quad (1.1)$$

where $dE/d\eta_s$ is energy per unit space-time rapidity per participant and $\mathbf{x}_{T,i}$ is position of the i -th participant in the transverse plane. The coordinate system and kinematic variables for heavy ion collisions, including the proper time τ and the space-time rapidity η_s , are defined in Section 6.1.

Even though the MC-Glauber initial condition has fluctuations in positions of nucleons inside a nucleus, it does not have sub-nucleonic degrees of freedom. By considering kinematics of the gluon production, one obtains $x_{1,2}\sqrt{s} = p_T e^{\pm y}$ and reaches to the point that the low- x contributions dominate evolution of the system at mid-rapidity i.e., the kinematic region around $y = 0$. x , \sqrt{s} , p_T and y are the energy fraction, collision energy, transverse momentum and rapidity, respectively. Definitions of the kinematic variables are summarized in Section 6.1. The MC-KLN model [26], named after Kharzeev, Levin, and Nardi, takes partonic degrees of freedom through unintegrated gluon distribution function

(uGDF)

$$\phi_{\text{KLN}}(x, \mathbf{k}_\perp) \sim \frac{1}{Q_{S,A}^2(x)} \frac{Q_{S,A}^2(x)}{\max[Q_{S,A}^2(x), k_\perp^2]} \quad (1.2)$$

where $Q_{S,A}$ is the saturation scale which specifies the spatial extent of gluons in the transverse plane. Based on the k_T -factorization approach [27], the initial entropy density is proportional to the gluon distribution given by [28]

$$\begin{aligned} \frac{dN_g}{d^2\mathbf{x}_T dy} &= \frac{4\pi^2 N_c}{N_c^2 - 1} \int \frac{d^2\mathbf{p}_T}{p_T^2} \int d^2\mathbf{k}_T \alpha_S \phi_A \left(x_1 = \frac{p_T e^y}{\sqrt{s_{NN}}}, \mathbf{k}_T; \mathbf{x}_T \right) \\ &\times \phi_B \left(x_2 = \frac{p_T e^{-y}}{\sqrt{s_{NN}}}, \mathbf{p}_T - \mathbf{k}_T; \mathbf{x}_T \right) \end{aligned} \quad (1.3)$$

where the gluon distribution functions ϕ_A and ϕ_B implicitly depend on the position \mathbf{x}_T in the transverse plane by having the saturation scale $Q_S(x, \mathbf{x}_T)$ as a function of \mathbf{x}_T .

In the IP-Glasma model [21], which is used in this work and will be explained in detail in Section 2.1, the pre-equilibrium dynamics of the gluon fields is governed by the classical Yang-Mills (CYM) dynamics

$$\partial_\mu F^{\mu\nu} - ig[A_\mu, F^{\mu\nu}] = -gJ^\nu \quad (1.4)$$

with color charge current consisting of the high- x partons in the colliding nuclei. Due to the sub-nucleonic fluctuations, the IP-Glasma initial conditions have been quite successful in describing the anisotropic flow coefficients v_n 's and their distributions [29].

• Viscous Hydrodynamics

This governs the QGP phase and there have been many implementations of ideal [30, 31] and viscous [32] hydrodynamics to describe the evolution of QGP matter. **MUSIC** [33] is one of the most sophisticated hydrodynamic models since it has the shear and bulk viscosities and the second-order transport coefficients derived from the Boltzmann transport equation in the 14-moments approximation [34] and it is the one used in this work. The 3 + 1D hydrodynamics of the QGP is described by the conservation equations of following energy-momentum

tensor

$$T^{\mu\nu} = \epsilon u^\mu u^\nu - (P + \Pi) \Delta^{\mu\nu} + \pi^{\mu\nu} \quad (1.5)$$

where $\Delta^{\mu\nu} = g^{\mu\nu} - u^\mu u^\nu$. The shear viscous tensor $\pi^{\mu\nu}$ and the bulk pressure Π are governed by the equations

$$\tau_\Pi \dot{\Pi} + \Pi = -\zeta \theta - \delta_{\Pi\Pi} \Pi \theta + \lambda_{\Pi\pi} \pi^{\mu\nu} \sigma_{\mu\nu} \quad (1.6)$$

$$\begin{aligned} \tau_\pi \dot{\pi}^{\langle\mu\nu\rangle} + \pi^{\mu\nu} &= 2\eta \sigma^{\mu\nu} - \delta_{\pi\pi} \pi^{\mu\nu} \theta + \varphi_7 \pi_\alpha^{\langle\mu} \pi^{\nu\rangle\alpha} \\ &\quad - \tau_{\pi\pi} \pi_\alpha^{\langle\mu} \sigma^{\nu\rangle\alpha} + \lambda_{\pi\Pi} \Pi \sigma^{\mu\nu} \end{aligned} \quad (1.7)$$

where ζ and η are the shear and bulk viscosities, respectively. Unlike the Navier-Stokes formalism, causality is guaranteed by the bulk and shear relaxation times τ_Π and τ_π . Other coefficients — $\delta_{\Pi\Pi}$, $\lambda_{\Pi\pi}$, $\delta_{\pi\pi}$, φ_7 , $\tau_{\pi\pi}$ and $\lambda_{\pi\Pi}$ — are called the second-order transport coefficients since they are coefficients of terms which are at least second-order in the spatial derivatives. The QGP evolution also has been found to be sensitive to the equation of state as it determines the pressure and its gradient as functions of energy density.

• Jet Quenching

The jet quenching is a consequence of energy loss of jets in the thermal plasma. There are two processes of energy loss considered in this work — radiative and collisional processes. In the radiative process, jet partons lose energy by emitting photons or gluons. The photon emission rate, in terms of the current-current correlator and polarization vectors, is given by

$$|\mathbf{p}| \frac{d\Gamma_\gamma}{d^3\mathbf{p}} = \frac{1}{2(2\pi)^3} \sum_\lambda \epsilon_{(\lambda)}^{*\mu}(\mathbf{p}) \epsilon_{(\lambda)}^\nu(\mathbf{p}) W_{\mu\nu}(p) \quad (1.8)$$

$$W^{\mu\nu}(p) = e^2 \int d^4x e^{ip \cdot x} \text{Tr} [\rho J^\mu(x) J^\nu(0)] \quad (1.9)$$

$$\rho = \sum_i |i\rangle \mathcal{P}_i \langle i| \quad (1.10)$$

where J^μ is the electromagnetic charge current operator. The density operator ρ is sum of all projection operators weighted by the probability \mathcal{P}_i to find the quantum state $|i\rangle$. In the case of the thermal medium, one has

$\rho_{\text{eq}} = \frac{1}{Z} \exp \left[-\frac{1}{T} (H - \sum_C \mu_C N_C) \right]$ where H , N_C , and Z are the Hamiltonian, conserved charge, and partition function, respectively. The AMY formalism [35, 36] allows one to evaluate $W^{\mu\nu}$ by solving an integral equation. The collisional energy loss is due to the $2 \rightarrow 2$ scattering between jet and thermal partons. The rate of collisional energy loss is given by

$$\begin{aligned} \frac{d\Gamma_{\text{coll}}}{d\omega}(E_{\mathbf{p}}, \omega, T) &= \frac{2\pi d_k}{2E_{\mathbf{p}} \cdot 2E_{\mathbf{p}'}} \int \frac{d^3\mathbf{k}}{(2\pi)^3 2E_{\mathbf{k}}} \int \frac{d^3\mathbf{k}'}{(2\pi)^3 2E_{\mathbf{k}'}} \\ &\times \delta(E_{\mathbf{p}} - E_{\mathbf{p}'} - \omega) \delta(E_{\mathbf{k}'} - E_{\mathbf{k}} - \omega) \\ &\times |\mathcal{M}(p, k \rightarrow p', k')|^2 f(k, T) (1 \pm f(k', T)) \end{aligned} \quad (1.11)$$

where $\omega = E_{\mathbf{p}} - E_{\mathbf{p}'}$ is the amount of energy loss and $f(k, T)$ is the distribution function of thermal partons. The \pm signs are for bosons and fermions, respectively. The matrix element \mathcal{M} from the effective thermal propagator was considered in [37] to obtain Γ_{coll} . The jet quenching can be quantified in terms of the nuclear modification factor R_{AA} which is defined as

$$R_{AA}(p_T) = \frac{1}{N_{\text{BC}}} \cdot \frac{dN/d^2\mathbf{p}_T dy|_{AA}}{dN/d^2\mathbf{p}_T dy|_{pp}} \quad (1.12)$$

where N_{BC} is the number of nucleon-nucleon binary collisions. If there is no jet-medium interaction, the p_T spectra of nuclear-nuclear collisions would be that of proton-proton collisions scaled by N_{BC} . Monte-Carlo implementation of the energy loss is summarized in Section 3.3 and slightly modified by shadowing and anti-shadowing in the nuclear parton distribution functions.

• Particlization and Re-scattering

After evolving the QGP and hadronic matter down to some temperature, it is necessary to transform the hydrodynamics into particles such that energy and momentum are conserved. The Cooper-Frye formalism [22] provides a relation between 3-dimensional hypersurface Σ and spectra of particles emerging out of Σ

$$\frac{dN}{d^3\mathbf{p}} = \frac{d}{(2\pi)^3} \int_{\Sigma} f(x, \mathbf{p}) \frac{p^\mu d^3\Sigma_\mu}{E_{\mathbf{p}}} \quad (1.13)$$

where d is the degeneracy factor. The normal vector $d^3\Sigma_\mu$ is an exterior product of three displacement vectors tangential to Σ . Since the system hydrodynamically evolves before this particlization, it is assumed that the distribution function is still close to that of thermal equilibrium

$$f(x, \mathbf{p}) = f_0(x, \mathbf{p}) + \delta f_{\text{shear}}(x, \mathbf{p}) + \delta f_{\text{bulk}}(x, \mathbf{p}) \quad (1.14)$$

where f_{shear} and f_{bulk} are the corrections to the distribution function from the shear and bulk viscosity, respectively. Their functional forms and details of the sampling procedure are the subjects of Section 3.1.

The last stage of heavy ion collisions is the hadronic re-scattering which is governed by non-equilibrium dynamics. The **UrQMD** model [38, 39] is one of the most realistic models to describe a dilute system of hadrons with masses up to 2.25 GeV. In the event average, **UrQMD** evolves the system according to the Boltzmann's transport equation

$$p^\mu \partial_\mu f_n(t, \mathbf{x}, \mathbf{p}) = \mathcal{C}_n[f] \quad (1.15)$$

where $\mathcal{C}_n[f]$ is the collision term and the cross sections are based on the experimental data. The hadronic contents and their scattering processes involved in **UrQMD** are reviewed in Section 3.2.

• Comparison with Experimental Data

Heavy ion collision programs in the LHC and RHIC have put emphasis on the particle distribution function in the momentum space. The particle spectra in the midrapidity are expressed in terms of the p_T spectra and anisotropic flow coefficients, which characterize the radial and angular dependences, respectively

$$E_{\mathbf{p}} \frac{dN}{d^3\mathbf{p}} = \frac{1}{2\pi p_T} \frac{dN}{dp_T dy} \left[1 + 2 \sum_{n=1}^{\infty} v_n(p_T, y) \cos(n(\phi - \Phi_n)) \right] \quad (1.16)$$

where $(2\pi p_T)^{-1} dN/dp_T$, $v_n(p_T)$ and Φ_n are the p_T spectra, p_T -differential flow coefficient and event plane angle, respectively. Many experiments have been carried out to measure those observables and their correlations. It is possible to

compute the observables in accordance with experimental measurements since an event generator, which realizes a hybrid model for description of heavy ion collisions, was employed in this work. Their definitions and comparisons are shown in Chapter 4.

1.2 Quantum Chromodynamics

Since this work is concerning the QGP and hadronic matters created in heavy ion collisions, a brief description of the quantum chromodynamics which governs quarks and gluons is in order. Understanding elementary particles and their interactions is one of the most important objectives of physics. The identification of constituent fermions of protons and other hadrons was the beginning of our current understanding of the strong interaction. Quarks and antiquarks were first hypothesized by Gell-Mann and Zweig to explain quantum numbers of light mesons and baryons. Spin, parity and electric charge could be reproduced with assumption that mesons are quark-antiquark bound states and baryons are bound states of three quarks. It was also proposed that there must be 6 different flavours of quarks to take all discovered hadrons into account. For example, π^+ is a $u\bar{d}$ bound state with vanishing spin and

flavor	electric charge (e)
up (u)	+ 2/3
down (d)	- 1/3
strange (s)	- 1/3
charm (c)	+ 2/3
bottom (b)	- 1/3
top (t)	+ 2/3

Table 1.1: Quark flavors and their electric charges

relative orbital angular momentum. In addition, it can be shown that baryons have integral electric charge.

However, it turned out to be impossible to construct some of the observed baryons if spin and electric charge are the only quantum numbers of quarks. For example, Δ^{++} baryon, which is interpreted as a uuu bound state with zero orbital angular momentum, has spin 3/2 and electric charge +2. Since all three spins need to be aligned parallel, the wavefunction of Δ^{++} is symmetric in the spin space and spatial space and it contradicts Fermi-Dirac statistics, which states that exchange of any two

identical fermions yields an overall minus sign. Greenberg, Han and Nambu resolved this by introducing another quantum number, which is called color, carried by quarks [40, 41]. Hence, if a baryon wavefunction is antisymmetric in the color space while it is symmetric in the spin space and spatial space, it is totally antisymmetric overall and obeys the spin-statistics theorem.

Quantum Chromodynamics takes quarks in fundamental representation of the non-Abelian SU(3) gauge group with gauge bosons, known as gluons, mediating interactions among quarks. Dynamics of quarks and gluons in QCD is characterized by the following Lagrangian

$$\mathcal{L}_{\text{QCD}} = -\frac{1}{2} \text{Tr} (F^{\mu\nu} F_{\mu\nu}) + \bar{q}_i (i\gamma^\mu \partial_\mu - m_i) q_i + g \bar{q}_i \gamma^\mu A_\mu q_i \quad (1.17)$$

$$F^{\mu\nu} = \partial^\mu A^\nu - \partial^\nu A^\mu - ig[A^\mu, A^\nu] \quad (1.18)$$

where A^μ and q_i are gluon and quark fields, respectively. The interaction between quarks and gluons is characterized by the coupling constant g . One important feature of non-Abelian gauge theory is that gauge bosons interact with themselves and this can be seen in the equation (1.17) which has terms with more than two gauge fields. This non-linearity makes systems of QCD matter difficult to understand. Nevertheless, one can do perturbative calculation as a series expansion in the coupling constant g if $g \ll 1$. This can be done with diagrammatic method in which set of rules are assigned to computation of any diagram with particle propagations and interaction vertices. Feynman rules of QCD are described in Figure 1.3. In addition to physical observables such as cross sections, dependence of strong coupling on momentum scale can be obtained. This running coupling is determined from the anomalous dimension γ and beta function β according to the Callan-Symanzik equation

$$\left[M \frac{\partial}{\partial M} + \beta(g) \frac{\partial}{\partial g} + n\gamma(g) \right] G^{(n)}(x_1, \dots, x_n; M, g) = 0 \quad (1.19)$$

where $G^{(n)}$ is n -point Green function. To determine how β and γ depend on the renormalization scale M , one has to compute loop corrections to the Green functions. After some algebra, one obtains the leading order contribution to the β -function of

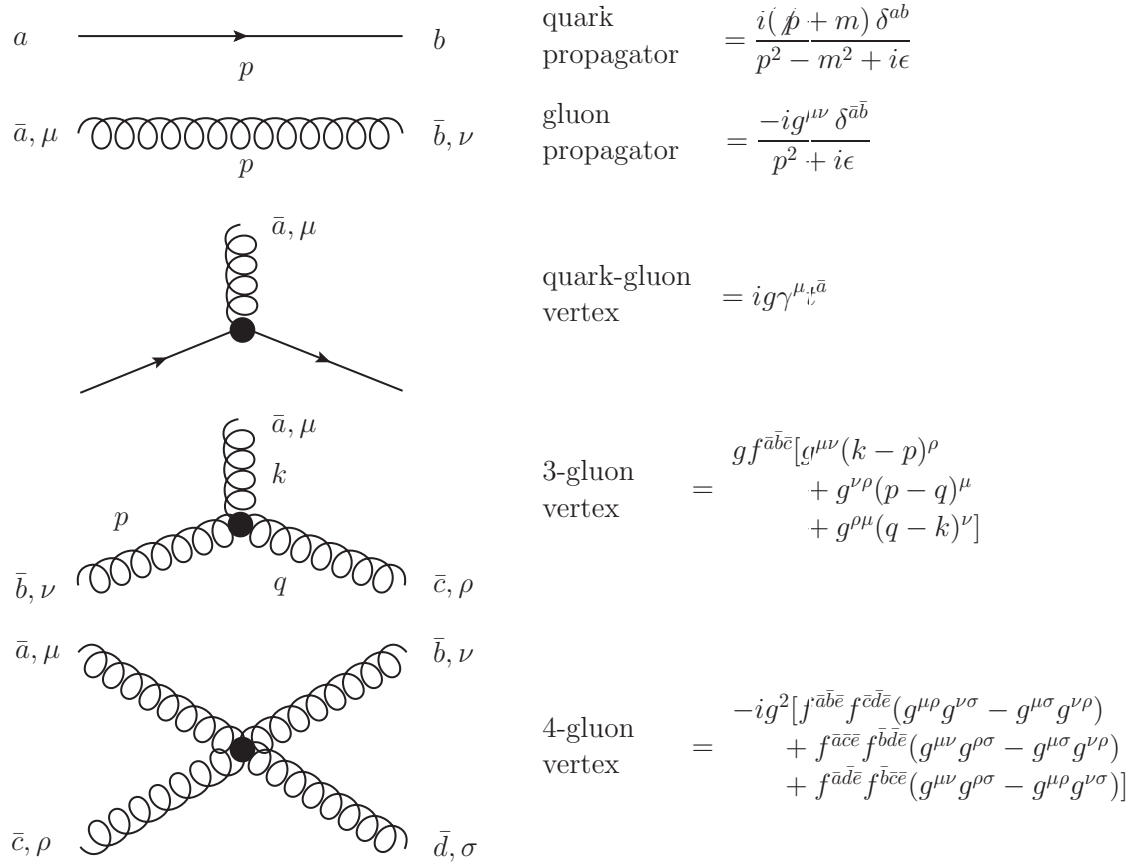


Figure 1.3: QCD Feynman rules. Conventions and notations of [42] are followed.

QCD with N_f quark flavors

$$\beta(g) = M \frac{\partial}{\partial M} g + o(g^4) \quad (1.20)$$

$$= -\frac{g^3}{(4\pi)^2} \left[\frac{11}{3} C_2(G) - \frac{4}{3} N_f C(N_c) \right] + o(g^4) \quad (1.21)$$

It must be noted that behavior of the running coupling depends on the nature of gauge group which is reflected in the constant $C(r)$ and Casimir operator $C_2(r)$. Those quantities for a given representation r of a Lie group are defined as

$$\text{tr} (t_r^a t_r^b) = C(r) \delta^{ab} \quad (1.22)$$

$$\sum_a t_r^a t_r^a = C_2(r) \mathbf{1} \quad (1.23)$$

where t_r^a is a generator matrix satisfying commutation relation $[t_r^a, t_r^b] = if^{abc} t_r^c$. There are $N_c^2 - 1$ generators of the $SU(N_c)$ group. In addition to the fundamental representa-

tion $r = N_c$, another representation of interest is called adjoint representation $r = G$ where $(t_G^a)_{bc} = -if^{abc}$. In the QCD β -function in equation (1.21), $C_2(r = G) = N_c$ and $C(r = N_c) = 1/2$. Therefore, with three colors $N_c = 3$, one obtains the negative delta functions and running coupling which decreases with the renormalization scale

$$\begin{aligned}\alpha_s(M) &= \frac{g^2(M)}{4\pi} \\ &= \alpha_s(M_0) \left[1 + \frac{\alpha_s(M_0)}{2\pi} \left(11 - \frac{2}{3}N_f \right) \ln \frac{M}{M_0} \right]^{-1}\end{aligned}\quad (1.24)$$

which connects the couplings at different momentum scales. Since the choice of renormalization scale is arbitrary, it can be set to be momentum scale Q of the experiment. Then it is possible to rewrite the running coupling in terms of Q as

$$\alpha_s(Q) = \frac{2\pi}{(11 - 2N_f/3) \ln(Q/\Lambda_{\text{QCD}})} \quad (1.25)$$

where $\Lambda_{\text{QCD}} \sim 200 \text{ MeV}$ is a scale at which the coupling becomes strong and therefore the perturbation approach is invalid. The equation (1.25) also implies that the strong interaction becomes weak as the momentum of the probe increases, a property known as asymptotic freedom.

1.3 Evolution of Parton Distribution Functions and the Saturation Scale

The initial state of heavy ion collisions is dominated by low energy gluons abundantly present in an ultra-relativistic nucleus. Within perturbative QCD, the behavior of the partons is described by the parton distribution functions. In this section, we briefly describe how the parton distribution function behaves as the energy scale changes. In particular the phenomena of gluon saturation which becomes important at high energies is discussed. Due to asymptotic freedom, it is not possible to describe the hadronic structure as a composite system of quarks and gluons based on perturbation theory. This can be effectively dealt with in the parton model, which was initially proposed by Bjorken and Feynman to explain large rate of $e^- + p$ deep inelastic scattering. According to the parton model, deep inelastic scattering is a process in

which large momentum transfer from electron to proton knocks out a parton belonging to the proton as depicted in Figure 1.4. The parton model describes structure of any

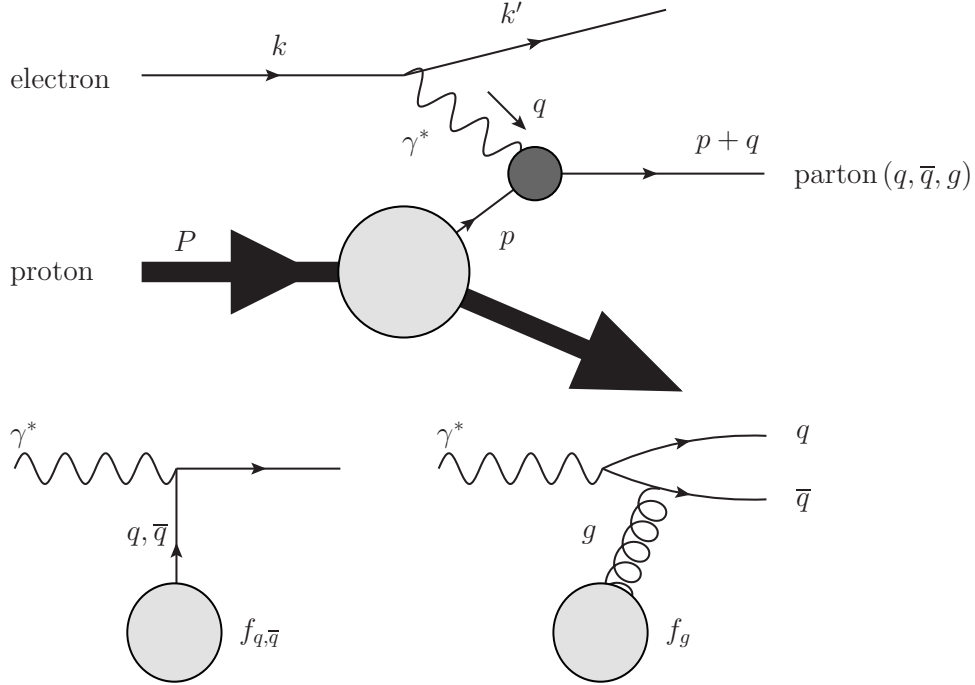


Figure 1.4: Deep inelastic scattering in the parton model. An electron exchanges momentum with a parton inside proton (top). The leading order contributions in the case of quark or antiquark (bottom left) and gluon (bottom right) are shown.

hadron with ultrarelativistic speed in terms of parton distribution function (PDF) $f_i(x, Q^2)$ which determines probability distribution of finding a parton of species i with light-cone momentum fraction x

$$f_i(x, Q^2) dx = \left(\begin{array}{l} \text{number of partons of species } i \\ \text{satisfying } x < p^+/P^+ < x + dx \end{array} \right) \quad (1.26)$$

where the light-cone momentum is defined as $p^\pm = (p^t \pm p^z)/\sqrt{2}$ with the z -axis is direction in which the hadron is moving. Another argument Q is the momentum scale of probe and can be identified with the momentum transfer in the experiment as $Q^2 = -q^2$. PDF's must satisfy the following momentum conservation equation

$$\sum_i \int_0^1 dx x f_i(x, Q^2) = 1 \quad (1.27)$$

where i runs over all quark and antiquark flavours and gluon. Equation (1.27) states that the momenta of all constituent partons must sum to that of the hadron.

There are other constraints regarding the number of valence quarks. A proton, for example, has two u and one d as its valence quarks. Therefore, the proton PDF must satisfy the following sum rules

$$\int_0^1 dx [f_u(x, Q^2) - f_{\bar{u}}(x, Q^2)] = 2 \quad (1.28)$$

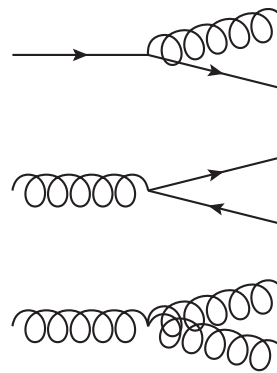
$$\int_0^1 dx [f_d(x, Q^2) - f_{\bar{d}}(x, Q^2)] = 1 \quad (1.29)$$

$$\int_0^1 dx [f_q(x, Q^2) - f_{\bar{q}}(x, Q^2)] = 0 \quad \text{for } s, c, b, \text{ and } t \quad (1.30)$$

It is possible to factorize the deep inelastic cross section into perturbative $e^- + \text{parton}$ process and non-perturbative PDF

$$\begin{aligned} & \sigma(e^-(k) + p(P) \rightarrow e^-(k') + X) \\ &= \sum_i \int_0^1 dx f_i(x, Q^2) \sigma(e^-(k) + i(xP) \rightarrow e^-(k') + i(xP + q)) \end{aligned} \quad (1.31)$$

It must be also noted that, since the collinear emission of a parton carries a factor of $\alpha_s(Q^2) \ln(Q^2/\Lambda_{\text{QCD}}^2)$ which is order of 1, contributions of multiple parton splitting are comparable to the leading order diagram. The DGLAP equations [43], named



$$\begin{aligned} \sum_{\text{fin.}} \langle |\mathcal{M}|^2 \rangle_{\text{init.}} &= 8\pi C_2(N_c) \frac{\alpha_s p_\perp^2}{z(1-z)} \left[\frac{1 + (1-z)^2}{z} \right] \\ \sum_{\text{fin.}} \langle |\mathcal{M}|^2 \rangle_{\text{init.}} &= \frac{8\pi N_c C_2(N_c)}{N_c^2 - 1} \frac{\alpha_s p_\perp^2}{z(1-z)} [z^2 + (1-z)^2] \\ \sum_{\text{fin.}} \langle |\mathcal{M}|^2 \rangle_{\text{init.}} &= 16\pi C_2(G) \alpha_s p_\perp^2 \left[\frac{1}{z(1-z)} - 1 \right]^2 \end{aligned}$$

Figure 1.5: Squared matrix elements, averaged over initial states and summed over final states, of collinear emission of quarks and gluons.

after Dokshitzer, Gribov, Lipatov, Altarelli, and Parisi, governs dependence of PDF

on the momentum scale Q^2 by taking parton evolution with collinear emissions into account

$$\begin{aligned}
Q^2 \frac{\partial}{\partial Q^2} f_q(x, Q^2) &= \frac{\alpha_s(Q^2)}{2\pi} \int_x^1 \frac{dz}{z} \{P_{q \leftarrow q}(z) f_q(x/z, Q^2) + P_{q \leftarrow g}(z) f_g(x/z, Q^2)\} \\
Q^2 \frac{\partial}{\partial Q^2} f_{\bar{q}}(x, Q^2) &= \frac{\alpha_s(Q^2)}{2\pi} \int_x^1 \frac{dz}{z} \{P_{q \leftarrow q}(z) f_{\bar{q}}(x/z, Q^2) + P_{q \leftarrow g}(z) f_g(x/z, Q^2)\} \\
Q^2 \frac{\partial}{\partial Q^2} f_g(x, Q^2) &= \frac{\alpha_s(Q^2)}{2\pi} \int_x^1 \frac{dz}{z} \{P_{g \leftarrow q}(z) \sum_q [f_q(x/z, Q^2) + f_{\bar{q}}(x/z, Q^2)] \\
&\quad + P_{g \leftarrow g}(z) f_g(x/z, Q^2)\} \tag{1.32}
\end{aligned}$$

where the splitting functions $P_{j \leftarrow i}$, which is obtained from amplitude of collinear emission of parton j from i as in Figure 1.5, are

$$\begin{aligned}
P_{q \leftarrow q}(z) &= \frac{N_c^2 - 1}{2N_c} \left[\frac{1+z^2}{(1-z)_+} + \frac{3}{2} \delta(1-z) \right] \\
P_{g \leftarrow q}(z) &= \frac{N_c^2 - 1}{2N_c} \left[\frac{1+(1-z)^2}{z} \right] \\
P_{q \leftarrow g}(z) &= \frac{1}{2} [z^2 + (1-z)^2] \\
P_{g \leftarrow g}(z) &= 2N_c \left[\frac{1-z}{z} + \frac{z}{(1-z)_+} + z(1-z) + \left(\frac{11}{12} - \frac{N_{q,1}}{18} \right) \delta(1-z) \right] \tag{1.33}
\end{aligned}$$

where $N_{q,1} = 3$ is number of light quark flavors (u , d , and s) and $1/(1-x)_+$ is defined as

$$\int_0^1 dx \frac{f(x)}{(1-x)_+} \equiv \int_0^1 dx \frac{f(x) - f(1)}{(1-x)}. \tag{1.34}$$

One can find from the splitting functions that gluons dominate the low- x dynamics since the splitting functions $P_{g \leftarrow q}$ and $P_{g \leftarrow g}$ behave as $1/x$. In the case of pure glue without quarks, the only relevant splitting function is $P_{g \leftarrow g}(x) \simeq 2N_c/x$ for low x and DGLAP equation becomes

$$xf_g(x, Q^2) - xf_g(x, Q_0^2) = \frac{N_c \alpha_s}{\pi} \int_{Q_0^2}^{Q^2} \frac{dQ'^2}{Q'^2} \int_x^1 \frac{dz}{z} z f_g(z, Q'^2) \tag{1.35}$$

One can solve this integral equation with an initial condition $xf_g(x, Q_0^2) = \mathcal{N}_g$ to obtain the following solution

$$xf_g(x, Q^2) = \mathcal{N}_g \sum_{n=0}^{\infty} \left(\frac{1}{n!} \right)^2 \left(\frac{N_c \alpha_s}{\pi} \right)^n \left(\ln \frac{Q^2}{Q_0^2} \right)^n \left(\ln \frac{1}{x} \right)^n \tag{1.36}$$

$$\sim \mathcal{N}_g \exp \left[2 \sqrt{\frac{N_c \alpha_s}{\pi}} \ln \left(\frac{Q^2}{Q_0^2} \right) \ln \left(\frac{1}{x} \right) \right] \quad (1.37)$$

which is known as double leading log (DLL) approximation. (Derivation and conventions are following Ref. [44].) One can find that the gluon distribution rises as $xf_g(x) \sim x^{-\lambda_g}$ as $x \rightarrow 0$ leading to violation of unitarity.

To resolve this contradiction, it was proposed that a phenomenon called saturation occurs below some small x and the non-linear effects somehow compensate the growth of gluon distribution. Saturation is characterized by a momentum scale $Q_s(x)$ which is called the saturation scale and at $Q \leq Q_s(x)$ for given x , or at $x \leq x_0$ for given $Q = Q_s(x_0)$, distance among emitters is comparable to $1/Q$ and non-linear effects, such as gluon fusions, become relevant. This is shown in Figure 1.6. Plenty of studies

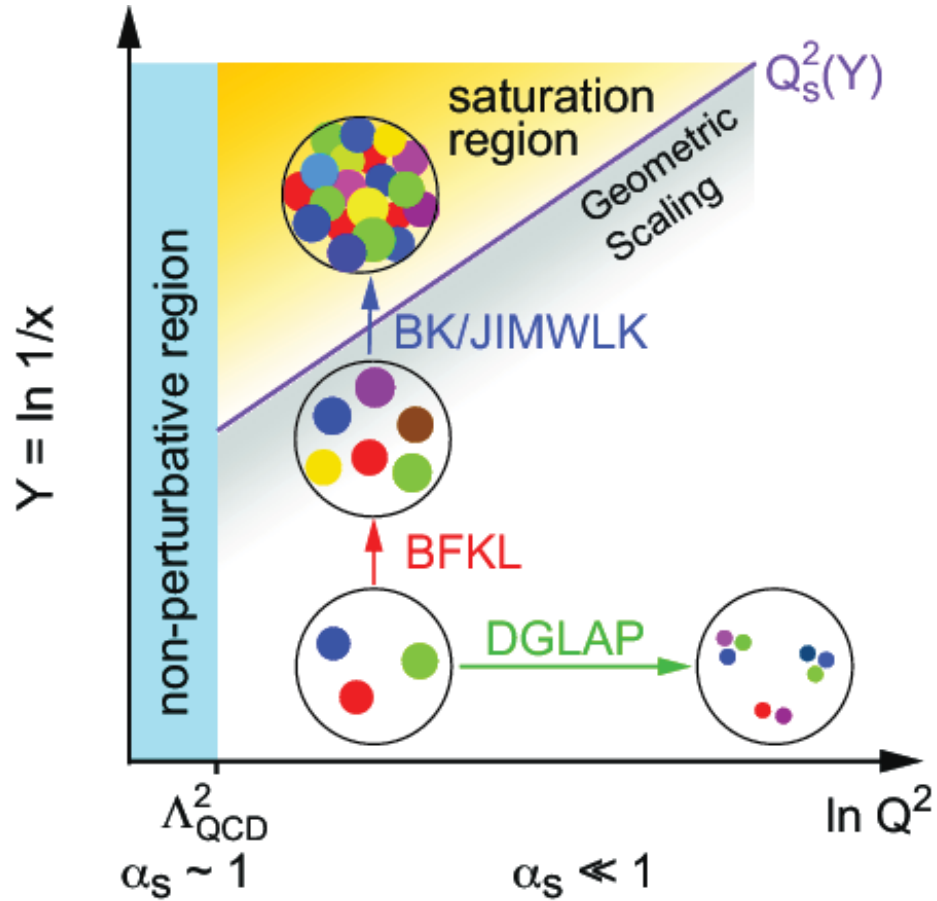


Figure 1.6: Partons inside a nucleon with different momentum scale Q and light-cone momentum fraction x . Figure taken from [45].

on saturation have been performed based on $e^- + p$ deep inelastic scattering data. As shown in Figure 1.4, the leading contribution from gluons must be scattering of $q\bar{q}$ dipole and proton. In general, the scattering cross section of a virtual photon γ^* and any hadron h can be written as

$$\sigma_{\lambda}^{\gamma^*+h}(x, Q^2) = \sum_q \int_0^1 dz \int d^2\mathbf{y}_{\perp} |\Psi_{\lambda}^q(e_q, m_q, z, Q^2, \mathbf{y}_{\perp})|^2 \sigma^{q\bar{q}+h}(\mathbf{y}_{\perp}, x) \quad (1.38)$$

$$\sigma^{q\bar{q}+h}(\mathbf{y}_{\perp}, x) = 2 \int d^2\mathbf{b}_{\perp} \mathcal{N}(x, \mathbf{y}_{\perp}, \mathbf{b}_{\perp}) \quad (1.39)$$

where $\Psi_{\lambda}^q(e_q, m_q, z, Q^2, \mathbf{y}_{\perp})$ is the amplitude that a virtual photon with polarization λ fluctuates into $q\bar{q}$ pair with size y_{\perp} and z the is ratio of light-cone momentum carried by the quark to that of the virtual photon. The first description of deep inelastic scattering based on the saturation is GBW model [46], named after Golec-Biernat and Wüsthoff. In the GBW model, the dipole cross section $\sigma^{q\bar{q}+p}$ is expressed in terms of the saturation scale as

$$\sigma_{\text{GBW}}^{q\bar{q}+p}(\mathbf{y}_{\perp}, x) = \sigma_0 \left[1 - \exp \left(-\frac{1}{4} y_{\perp}^2 Q_{S,p}^2(x) \right) \right] \quad (1.40)$$

$$Q_{S,p}^2(x) = Q_0^2 \left(\frac{x_0}{x} \right)^{\lambda} \quad (1.41)$$

It can be seen from equation (1.40) that the cross section is increasing with dipole size for $y_{\perp} Q_{S,p} < 1$ and converges to a constant value as y_{\perp} becomes larger than $Q_{S,p}^{-1}$. It was possible to reasonably describe $e + p$ deep inelastic scattering carried in HERA [47, 48] with the GBW model. The saturation length scale $R_{S,p} = Q_{S,p}^{-1}$ can be interpreted as the spatial extend of gluons in transverse plane. The GBW model, however, does not address the spatial distribution of gluons in a proton. An impact parameter dependent saturation (IP-Sat) model was proposed by Kowalski and Teaney [49]. In the IP-Sat model, dependence on impact parameter comes into the dipole scattering through the thickness function $T(\mathbf{b}_{\perp})$

$$\mathcal{N}_{\text{IP-Sat}}(x, \mathbf{y}_{\perp}, \mathbf{b}_{\perp}) = 1 - \exp \left(-\frac{\pi^2}{2N_c} \alpha_s(\mu^2) y_{\perp}^2 x f_g(x, \mu^2) T(\mathbf{b}_{\perp}) \right) \quad (1.42)$$

Saturation plays important roles in describing the pre-thermalization dynamics of heavy ion collisions. See Section 2.1. One can see [50] for a detailed review of saturation.

1.4 Many-body QCD Near Thermal Equilibrium

If the many-body system of QCD is near thermal equilibrium, one can rely on the thermodynamics and linear response of the finite-temperature QCD [51]. The thermodynamics of the QCD matter begins with computation of the partition function Z as

$$Z = \text{Tr} \exp \left[-\frac{1}{T} (H - \sum_C \mu_C N_C) \right] \quad (1.43)$$

$$= \sum_n d_n \exp \left[-\frac{1}{T} (E_n - \sum_C \mu_C N_{C,n}) \right] \quad (1.44)$$

where H and N_C are the Hamiltonian and conserved charge operators derived from the QCD Lagrangian (1.17), respectively. The trace can be written as a sum over all eigenvalues of energy and conserved charges to get the second equality. Given that several eigenstates can have the same eigenvalue, one has the degeneracy factor d_n . The transport coefficients describe how the system reacts to the small deviation from equilibrium. In this work, the shear (η) and bulk (ζ) viscosities are of interest and they can be computed from the Kubo formulae

$$\eta = \frac{1}{10} \lim_{\omega \rightarrow 0} \frac{1}{\omega} \int d^4x e^{i\omega t} \langle [\mathcal{S}^{\mu\nu}(x), \mathcal{S}_{\mu\nu}(0)] \rangle \theta(t) \quad (1.45)$$

$$\zeta = \frac{1}{9} \lim_{\omega \rightarrow 0} \frac{1}{\omega} \int d^4x e^{i\omega t} \langle [\Theta(x), \Theta(0)] \rangle \theta(t) \quad (1.46)$$

$$\mathcal{S}^{\mu\nu} = \Delta^\mu_\alpha \Delta^\nu_\beta T^{\alpha\beta} - \frac{1}{3} \Delta^{\mu\nu} (\Delta_{\alpha\beta} T^{\alpha\beta}) \quad \text{and} \quad \Theta = T^\mu_\mu$$

where $\Delta^{\mu\nu} = u^\mu u^\nu - g^{\mu\nu}$ is the projection operator transverse to the flow velocity. $\langle \dots \rangle$ denotes the ensemble average over the thermal distribution.

2

Bulk Dynamics of QCD Medium

In this chapter, the bulk dynamics of the low-momentum partons and hadrons are described. Section 2.1 is devoted to the IP-Glasma pre-thermalization dynamics from the collision to $\tau_0 \sim 1$ fm at which the system is assumed to reach local thermal equilibrium. Hydrodynamics with shear and bulk viscosities along with equation of states is described in Section 2.2.

2.1 IP-Glasma Pre-thermalization Dynamics

It is important to have a good model of pre-thermalization dynamics of partons since the non-trivial initial conditions as characterized by the energy density distribution and flow velocity affect the determination of properties of the QCD medium. The initial state fluctuations also must be taken into account properly to describe a variety of observables which depend on geometry and fluctuation in different ways. In the IP-Glasma model, the initial states of two approaching nuclei are characterized by the small x gluons, which will eventually interact and form QGP. As the occupation number of these small x gluons is large, the dynamics of the colliding system in the pre-thermalization stage is modelled by classical Yang-Mills dynamics.

2.1.1 The Impact Parameter Dependent Saturation (IP-Sat) Model

To calculate the gluon distributions in the initial state using classical Yang-Mills theory, one first needs to know the distribution of the color currents which source the classical gluon field. In this work, the charge currents are obtained in terms of the gluon distribution function f_g and the saturation scale Q_s . Determination of the saturation scale is based on the IP-Sat model [49, 52], which emerged as a description of $\gamma^* + p$ scattering within the dipole picture.

It was shown in [53] that, by summing all diagrams in Figure 2.1, the cross section $\sigma^{q\bar{q}}$ of small size $q\bar{q}$ dipole scattered off a hadronic target is related to the gluon distribution as

$$\sigma^{q\bar{q}}(x, \mathbf{y}_\perp) = \frac{\pi^2}{N_c} \alpha_s(\mu^2) y_\perp^2 x f_g(x, \mu^2) \quad (2.1)$$

where y_\perp is the size of $q\bar{q}$ dipole. The momentum scale is given as $\mu^2 = \mu_0^2 + C/y_\perp^2$ with C set to be 4. If a $q\bar{q}$ dipole goes through gluon cloud whose spatial distribution is characterized by $\rho(\mathbf{b}_\perp, z)$ with normalization $\int dz \int d^2\mathbf{b}_\perp \rho(\mathbf{b}_\perp, z) = 1$, probability that the dipole does not experience any scattering is given as [49, 52]

$$|S(x, \mathbf{y}_\perp, \mathbf{b}_\perp)|^2 = \exp \left(-\sigma^{q\bar{q}}(x, \mathbf{y}_\perp) \int_{-\infty}^{\infty} dz \rho(\mathbf{b}_\perp, z) \right) \quad (2.2)$$

$$= \exp \left(-\frac{\pi^2}{N_c} \alpha_s(\mu^2) y_\perp^2 x f_g(x, \mu^2) T(\mathbf{b}_\perp) \right) \quad (2.3)$$

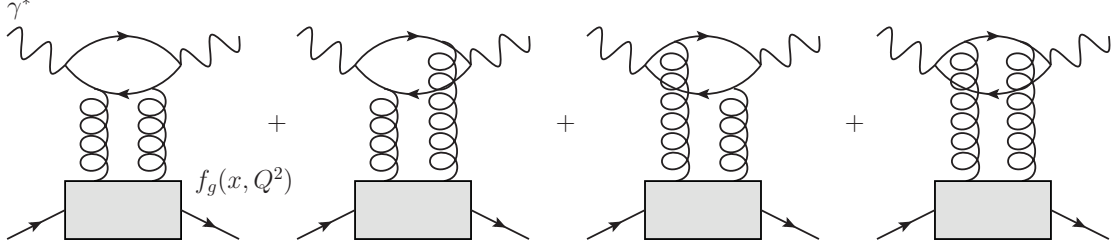


Figure 2.1: Leading-order diagrams that contribute to the dipole cross section.

where the thickness function $T(\mathbf{b}_\perp)$ is defined as

$$T(\mathbf{b}_\perp) = \int_{-\infty}^{\infty} dz \rho(\mathbf{b}_\perp, z). \quad (2.4)$$

This probability is connected to the saturation scale $Q_{S,p}$ as

$$|S(x, \mathbf{y}_\perp, \mathbf{b}_\perp)|^2 = \exp\left(-\frac{1}{2} y_\perp^2 Q_{S,p}^2(x, \mathbf{b}_\perp)\right). \quad (2.5)$$

It can be also identified with the square of the S -matrix element and the differential cross section can be obtained as

$$\frac{d\sigma^{q\bar{q}+h}}{d^2\mathbf{b}_\perp} = 2[1 - \text{Re } S(\mathbf{b}_\perp)] \quad (2.6)$$

$$= 2 \left[1 - \exp\left(-\frac{\pi^2}{2N_c} \alpha_s(\mu^2) y_\perp^2 x f_g(x, \mu^2) T(\mathbf{b}_\perp)\right) \right]. \quad (2.7)$$

This result can be used to compute $\sigma_\lambda^{\gamma^*+h}$ according to the equation (1.39) with $\mathcal{N}_{\text{IP-Sat}}$ given by

$$\mathcal{N}_{\text{IP-Sat}}(x, \mathbf{y}_\perp, \mathbf{b}_\perp) = 1 - \exp\left(-\frac{\pi^2}{2N_c} \alpha_s(\mu^2) y_\perp^2 x f_g(x, \mu^2) T(\mathbf{b}_\perp)\right) \quad (2.8)$$

In the case that proton is the target, the thickness function is assumed to be Gaussian

$$T(\mathbf{b}_\perp) = \frac{1}{2\pi B_G} \exp\left(-\frac{b_\perp^2}{2B_G}\right) \quad (2.9)$$

The gluon distribution function at a reference scale μ_0 is given as [52]

$$x f_g(x, \mu_0^2) = A_g x^{-\lambda_g} (1-x)^{5.6} \quad (2.10)$$

where measurements of the proton structure function F_2 [54, 55] yield $A_g = 2.55$, $\lambda_g = 0.02$, and $\mu_0^2 = 1.17 \text{ GeV}^2$ for $m_{u,d,s} = 0.14 \text{ GeV}$ and $m_c = 1.4 \text{ GeV}$. The large- x behavior of the gluon distribution function f_g in equation (2.10) is based on the

Martin-Roberts-Stirling-Thorne (MRST) parametrization [56]. Note that the quark masses come in evaluation of the amplitude that a virtual photon fluctuates into a $q\bar{q}$ pair in equation (1.38). Then the distribution function at an arbitrary momentum scale is given by evolving with leading-order DGLAP equation without quarks

$$\mu^2 \frac{\partial}{\partial \mu^2} f_g(x, \mu^2) = \frac{\alpha_s(\mu^2)}{2\pi} \int_x^1 \frac{dz}{z} P_{g \leftarrow g}(z) f_g(x/z, \mu^2) \quad (2.11)$$

The model calculations were compared with the HERA data to obtain values of the parameters in [57, 58]. The equation (2.3) implies that there is a length scale r_S at

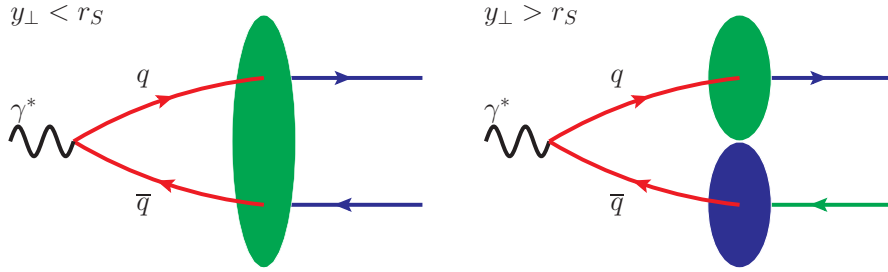


Figure 2.2: Color rotation of $q\bar{q}$ dipole scattered off a hadron target. If the size of dipole y_\perp is smaller than the saturation length scale r_S (left), the colors of quark and antiquark rotate in the same way. However, if the dipole is larger than r_S , quark and antiquark rotate differently in the color space.

which $|S(y_\perp)|^2$ significantly deviates from 1. A possible interpretation is shown in Figure 2.2. If the $q\bar{q}$ dipole is smaller than r_S , color rotations of quark and antiquark occur in the same way and one has $|S(y_\perp)|^2 \sim 1$. In the case of $y_\perp > r_S$, quark and antiquark are scattered off by gluons with different colors and color rotations are different resulting in $|S(y_\perp)|^2 < 1$. The saturation momentum scale of a proton $Q_{S,p}(x, \mathbf{b}_\perp)$ is defined as

$$Q_{S,p}^2(x, \mathbf{b}_\perp) = \frac{2}{r_{S,p}^2} \quad (2.12)$$

$$= \frac{2\pi^2}{N_c} \alpha_s(\mu^2(r_{S,p}^2)) x f_g(x, \mu^2(r_{S,p}^2)) T(\mathbf{b}_\perp) \quad (2.13)$$

$$\mu^2 = \mu_0^2 + \frac{C}{r_{S,p}^2} \quad (2.14)$$

from which one finds that $|S(|\mathbf{y}_\perp| = r_{S,p})|^2 = e^{-1}$. In the case of heavy ion collisions where the target is a nucleus with A nucleons, the thickness function and saturation

scale can be generalized as

$$T(\mathbf{b}_\perp) \rightarrow \sum_{i=1}^A T(\mathbf{b}_\perp - \mathbf{b}_{\perp,i}) \quad (2.15)$$

$$Q_{S,A}^2(x, \mathbf{b}_\perp) = \frac{2\pi^2}{N_c} \alpha_s(\mu^2(r_{S,A}^2)) x f_g(x, \mu^2(r_{S,A}^2)) \sum_{i=1}^A T(\mathbf{b}_\perp - \mathbf{b}_{\perp,i}) \quad (2.16)$$

where $\mathbf{b}_{\perp,i}$ is position of i -th nucleon in the transverse plane. The spatial distribution of nucleons is determined by a Woods-Saxon probability distribution function $\rho_A(\mathbf{x})$

$$\rho_A(|\mathbf{x}| = r) = \frac{\rho_0}{1 + \exp[(r - R_A)/\delta]} \quad (2.17)$$

$$\int d^3\mathbf{x} \rho_A(\mathbf{x}) = A \quad (2.18)$$

where R_A and δ characterize the size of the nucleus and how slowly the number density of nucleons decreases from the center to edge, respectively. Once the positions of nucleons in three-dimensional space are determined based on equation (2.17), they are projected onto the transverse plane to obtain $\mathbf{b}_{\perp,i}$. Since the coupling term becomes comparable to the kinetic term at the saturation scale i.e. $Q_s \sim gA$, one can obtain a relation between color charge squared per unit area in transverse plane $g^2\Lambda_S^2$ and saturation scale as

$$g^2\Lambda_S^2 \sim Q_s^2 \quad (2.19)$$

based on the fact that the occupation number $N \sim \int \frac{dk^+}{k^+} \int d^2\mathbf{k}_\perp a_k^\dagger a_k$ is proportional to A^2 .

2.1.2 Classical Yang-Mills (CYM) Dynamics

With the color currents determined as above, one can now calculate the initial gluons fields of the projectile and the target nuclei before the collision based on the McLerran-Venugopalan (MV) model [59, 60, 61]. Figure 2.3 shows the extend of partonic fluctuation in the x^\pm directions. The small- x parton sees the hard parton almost *frozen* i.e. changing very slowly in the x^+ direction due to time dilation. In addition, the hard parton is localized in a small region around the x^+ axis. Therefore,

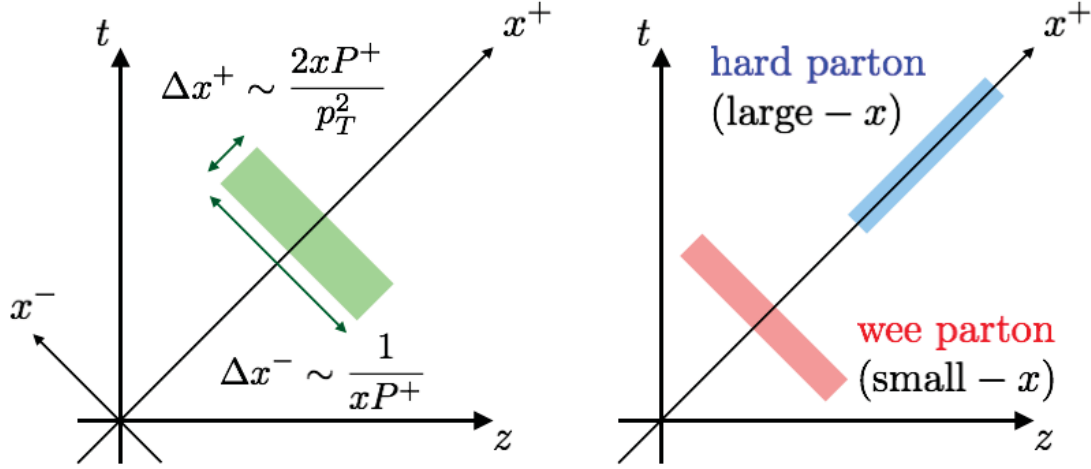


Figure 2.3: (left) Due to the uncertainty principle, a parton carrying the light-cone momentum fraction x and transverse momentum p_T has the finite extend Δx^\pm . $P^+ = (E + p^z)/\sqrt{2}$ is the light-cone momentum of a hadron. (right) The wee partons see the hard partons fluctuating slowly and bumpy in the x^+ and x^- -directions, respectively.

the color charge current J^μ carried by the hard partons moving in the $+z$ direction has the following form

$$J^\mu = \delta^{+\mu} \delta(x^-) \Sigma(\mathbf{x}_T) \quad (2.20)$$

$$= \delta^{+\mu} \delta(x^-) \Sigma^a(\mathbf{x}_T) t^a \quad (2.21)$$

where $\Sigma(\mathbf{x}_T)$ is the color charge per unit transverse area and t^a are the generator matrices of $SU(N_c)$ gauge group. The \pm indices of the light-cone coordinates are defined as

$$K^\pm \equiv \frac{1}{\sqrt{2}}(K^0 \pm K^3) \quad \text{and} \quad K_\pm \equiv \frac{1}{\sqrt{2}}(K^0 \mp K^3). \quad (2.22)$$

Fluctuation of the color charge density is assumed to be Gaussian with the following weighting functional

$$\mathcal{W}_{\text{MV}}[\Sigma] = \frac{1}{\mathcal{Z}_{\text{MV}}} \exp \left[- \int d^2 \mathbf{x}_T \frac{\Sigma^a(\mathbf{x}_T) \Sigma^a(\mathbf{x}_T)}{2 g^2 \Lambda_S^2} \right] \quad (2.23)$$

$$\mathcal{Z}_{\text{MV}} = \int \mathcal{D}\Sigma \exp \left[- \int d^2 \mathbf{x}_T \frac{\Sigma^a(\mathbf{x}_T) \Sigma^a(\mathbf{x}_T)}{2 g^2 \Lambda_S^2} \right] \quad (2.24)$$

where $\int \mathcal{D}\Sigma$ denotes the integration over all possible configurations of Σ . The correlation function is given by

$$\langle \Sigma^a(\mathbf{x}'_T) \Sigma^b(\mathbf{x}''_T) \rangle = \int \mathcal{D}\Sigma \mathcal{W}_{\text{MV}}[\Sigma] \Sigma^a(\mathbf{x}'_T) \Sigma^b(\mathbf{x}''_T) \quad (2.25)$$

$$= g^2 \Lambda_S^2 \delta^{ab} \delta^2(\mathbf{x}'_T - \mathbf{x}''_T). \quad (2.26)$$

Given that the large- x hard partons serve as the color sources, the gauge field dominated by the small- x gluons is governed by the classical Yang-Mills (CYM) equations

$$\partial_\mu F^{\mu\nu} - ig[A_\mu, F^{\mu\nu}] = -gJ^\nu \quad \text{where} \quad (2.27)$$

$$F^{\mu\nu} = \partial^\mu A^\nu - \partial^\nu A^\mu - ig[A^\mu, A^\nu]. \quad (2.28)$$

Determination of the initial conditions for the gluon field is based on the formulation in [62, 63]. Let us consider a highly energetic nucleus moving in the $+z$ direction.

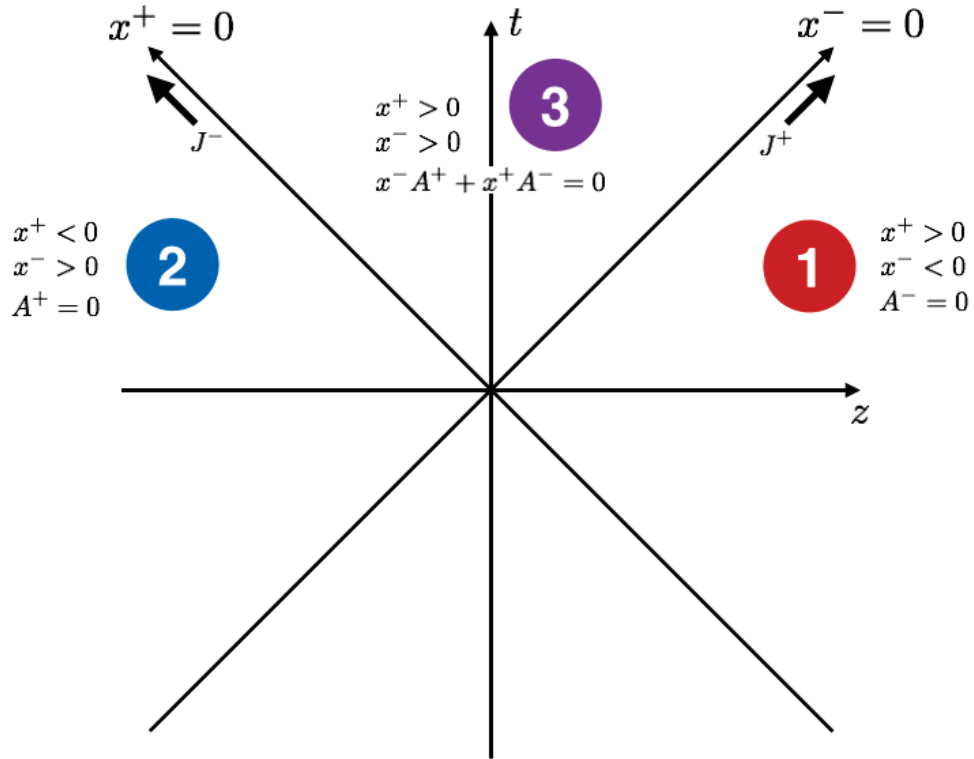


Figure 2.4: The lightcone configuration of the ultrarelativistic heavy ion collisions. The worldlines of the colliding nuclei moving in $\pm z$ directions are $x^\mp = 0$, respectively.

Then speed of the nucleus is very close to that of light and we can approximate the color charge as

$$gJ^\mu = \delta^{+\mu} \rho_{(2)}(x^-, \mathbf{x}_T) \quad (2.29)$$

In this case, one has the non-trivial gluon field in the spacetime region 2 of the figure 2.4. It can be also seen that, since there is no overlap between the past light-cone of the region 2 and the worldline $x^+ = 0$, the gluon field in the region 2 is not affected by the nucleus moving in the $-z$ direction. First, one can find the gluon field of region 2 in the covariant gauge $\partial_\mu A_C^\mu = 0$ with A_C^i and $A_C^- = 0$ and gauge transform into the light-cone gauge where $A^+ = 0$. The only non-zero component of the field strength is

$$F^{i+} = \partial^i A_C^+ - \partial^+ A_C^i - ig[A_C^i, A_C^+] = \partial^i A_C^+ \quad (2.30)$$

and the CYM becomes

$$\partial_i F^{i+} - ig[A_{C,i}, F^{i+}] = \partial_i \partial^i A_C^+ \quad (2.31)$$

$$= -gJ^+ = -\rho_{(2)}(x^-, \mathbf{x}_T). \quad (2.32)$$

Therefore, A_C^+ is

$$A_C^+ = \frac{1}{\nabla_T^2} \rho_{(2)}(x^-, \mathbf{x}_T). \quad (2.33)$$

The gluon field in the light-cone gauge can be found by identifying the gauge transformation which satisfies the equation

$$\begin{aligned} A^+ &= U A_C^+ U^\dagger + \frac{i}{g} U \partial^+ U^\dagger \\ &= U A_C^+ U^\dagger + \frac{i}{g} U \partial_- U^\dagger \end{aligned} \quad (2.34)$$

$$= 0. \quad (2.35)$$

Therefore, the gauge transformation matrix U satisfies

$$\partial_- U^\dagger = ig A_C^+ U^\dagger \quad (2.36)$$

and it can be written in terms of the color source

$$U^\dagger = \mathcal{P} \exp \left[ig \int_{-\infty}^{x^-} dz^- \frac{1}{\nabla_T^2} \rho_{(2)}(z^-, \mathbf{x}_T) \right] \quad (2.37)$$

The other components of the gluon field are

$$\begin{aligned} A^- &= U A_C^- U^\dagger + \frac{i}{g} U \partial^- U^\dagger \\ &= \frac{i}{g} U \partial_+ U^\dagger = 0 \end{aligned} \quad (2.38)$$

and

$$\begin{aligned} A^i &= U A_C^i U^\dagger + \frac{i}{g} U \partial^i U^\dagger \\ &= -\frac{i}{g} U \partial_i U^\dagger \end{aligned} \quad (2.39)$$

where one has an extra minus sign by lowering the index i . For a nucleus moving in the $-z$ direction, the color charge current is

$$gJ^\mu = \delta^{-\mu} \rho_{(1)}(x^+, \mathbf{x}_T) \quad (2.40)$$

As shown in Figure 2.4, the region 1 is causally affected by the nucleus moving backward and the light-cone gauge is $A^- = 0$. One can compute the gluon field A_C^μ in the covariant gauge with $A_C^i = 0$ and $A_C^+ = 0$ and gauge transform into the light-cone gauge as in the case of nucleus moving forward. The only non-zero component of $F^{\mu\nu}$ is

$$F^{i-} = \partial^i A_C^-. \quad (2.41)$$

The CYM becomes

$$\partial_i F^{i-} - ig[A_{C,i}, F^{i-}] = \partial_i \partial^i A_C^- \quad (2.42)$$

$$= -gJ^- = -\rho_{(1)}(x^+, \mathbf{x}_T). \quad (2.43)$$

Therefore, A_C^- is

$$A_C^- = \frac{1}{\nabla_T^2} \rho_{(1)}(x^+, \mathbf{x}_T). \quad (2.44)$$

The gauge transform into the light-cone gauge and the gluon field can be found in the similar manner

$$U^\dagger = \mathcal{P} \exp \left[ig \int_{-\infty}^{x^+} dz^+ \frac{1}{\nabla_T^2} \rho_{(1)}(z^+, \mathbf{x}_T) \right] \quad (2.45)$$

In the region 1, one has $A^+ = 0$. As a result, the gluon fields in the region 1 and 2 are written as

$$A_{(1,2)}^i = -\frac{i}{g} U_{(1,2)} \partial_i U_{(1,2)}^\dagger \quad (2.46)$$

$$U_{(1,2)}^\dagger(x^\pm, \mathbf{x}_T) = \mathcal{P} \exp \left[ig \int_{-\infty}^{x^\pm} dz^\pm \frac{1}{\nabla_T^2} \rho_{(1,2)}(z^\pm, \mathbf{x}_T) \right] \quad (2.47)$$

Once the gluon field before the collision is found, The gluon field after the collision can be obtained by making the following ansatz for the gluon field in region 3

$$A^\pm = \pm x^\pm \alpha(\tau, \mathbf{x}_T) \theta(x^+) \theta(x^-) \quad (2.48)$$

$$A^i = \alpha_3^i(\tau, \mathbf{x}_T) \theta(x^+) \theta(x^-) \\ + \alpha_1^i(x^+, \mathbf{x}_T) \theta(x^+) \theta(-x^-) + \alpha_2^i(x^-, \mathbf{x}_T) \theta(-x^+) \theta(x^-) \quad (2.49)$$

where the gauge is chosen to be the Fock-Schwinger gauge $A^\tau = x^+ A_+ + x^- A_- = 0$ in region 3 and $\theta(x)$ is the step function. The proper time τ is defined as $\tau = \sqrt{t^2 - z^2} = \sqrt{2x^+ x^-}$. One deduces the following initial conditions for the gauge field

$$\Sigma_{(1,2)} = \partial_i \alpha_{1,2}^i(x^\pm = 0) \quad (2.50)$$

$$\alpha_3^i(\tau = +0) = \alpha_1^i(x^+ = 0) + \alpha_2^i(x^- = 0) \quad (2.51)$$

$$\alpha(\tau = +0) = -\frac{ig}{2} [\alpha_{1i}(x^+ = 0), \alpha_2^i(x^- = 0)] \quad (2.52)$$

where the surface color charge density $\Sigma_{(1,2)}$ is defined as

$$\Sigma_{(1,2)}(\mathbf{x}_T) \equiv \int_{-\epsilon}^{+\epsilon} dx^\pm \rho_{(1,2)}(x^\pm, \mathbf{x}_T) \quad (2.53)$$

Derivation of equations (2.51) and (2.52) is shown in Section 6.2. The classical gluon field evolves until $\tau = \tau_0$ and the thermalization is presumed to occur during that time. The thermalization time τ_0 is bounded by a lower limit since there must be enough collisions to make the gluon distribution isotropic. In addition, there is also an upper limit to guarantee that the system is dense enough to be described in terms of the classical fields. In this work τ_0 is considered to be a model parameter and set to be 0.4 fm. This part of the model is usually referred to as the Glasma model [64]. The name IP-Glasma thus is a combination of the IP-Sat and the Glasma.

2.1.3 Initial Energy Density and Flow Velocity Profiles

It is assumed that, after a certain period of evolution with classical Yang-Mills dynamics, the system reaches local thermal equilibrium and hydrodynamics becomes applicable. To set up the initial condition of hydrodynamic evolution, one has to find

the energy-momentum tensor $T^{\mu\nu}$ and solve the equation

$$T^\mu_\nu u^\nu = \epsilon u^\mu \quad (2.54)$$

for the energy density ϵ and flow velocity u^μ . The Noether's theorem allows one to compute the energy momentum tensor in terms of the classical fields based on translation symmetry. Since the low- x gluons dominate the midrapidity dynamics, it is reasonable to assume that the energy-momentum tensor is that of the gluon fields. Hence, for a translation $x^\mu \rightarrow x^\mu + \delta x^\mu$, one has

$$\mathcal{L}_g = -\frac{1}{2} \text{Tr} (F^{\mu\nu} F_{\mu\nu}) \quad (2.55)$$

$$\delta x^\lambda \partial_\lambda \mathcal{L}_g = \mathcal{L}_g(A + \delta A) - \mathcal{L}_g(A) \quad (2.56)$$

$$= \partial_\mu \left[\frac{\partial \mathcal{L}_g}{\partial (\partial_\mu A^{a,\nu})} \cdot \delta A^{a,\nu} \right] \quad (2.57)$$

$$= -2 \partial_\mu \text{Tr} (F^\mu_\nu \delta A^\nu) \quad (2.58)$$

where the infinitesimal change in the gauge field must be specified in terms of δx . The gauge symmetry of the Lagrangian must be properly taken into account. For any quantity \mathcal{Q} which transforms as $\mathcal{Q} \rightarrow V \mathcal{Q} V^\dagger$ under gauge transformation $V \in \text{SU}(N_c)$, it is possible to show $[D_\mu, \mathcal{Q}] \rightarrow V [D_\mu, \mathcal{Q}] V^\dagger$. Therefore, one has $\delta F_{\mu\nu} = \delta x^\lambda [D_\lambda, F_{\mu\nu}]$ to ensure that $\delta \mathcal{L}_g = \mathcal{L}_g(A + \delta A) - \mathcal{L}_g(A)$ is gauge-invariant. The relation between the field strength and gauge field $[D_\mu, D_\nu] = -ig F_{\mu\nu}$, in conjunction with the Bianchi identity, leads to the expression for δA

$$\delta F_{\mu\nu} = \delta x^\lambda [D_\lambda, F_{\mu\nu}] \quad (2.59)$$

$$\begin{aligned} &= -\delta x^\lambda [D_\mu, F_{\nu\lambda}] - \delta x^\lambda [D_\nu, F_{\lambda\mu}] \\ &= \delta x^\lambda [D_\mu, F_{\lambda\nu}] - \delta x^\lambda [D_\nu, F_{\lambda\mu}] \end{aligned} \quad (2.60)$$

$$= [D_\mu, \delta A_\nu] - [D_\nu, \delta A_\mu] \quad (2.61)$$

where one finds $\delta A_\mu = \delta x^\lambda F_{\lambda\mu}$. Substitution into equation (2.58) yields

$$0 = -2 \delta x^\lambda \partial_\mu \text{Tr} (F^\mu_\nu F_{\lambda}{}^\nu) - \delta x^\lambda \partial_\lambda \mathcal{L}_g \quad (2.62)$$

$$= \delta x^\nu \partial_\mu \left[-2 \text{Tr} (F^{\mu\lambda} F_{\nu\lambda}) + \frac{1}{2} g^{\mu\nu} \text{Tr} (F^{\alpha\beta} F_{\alpha\beta}) \right] \quad (2.63)$$

$$= \delta x_\nu \partial_\mu T^{\mu\nu} \quad (2.64)$$

$$T^{\mu\nu} = -2 \operatorname{Tr} (F^{\mu\lambda} F^\nu{}_\lambda) + \frac{1}{2} g^{\mu\nu} \operatorname{Tr} (F^{\alpha\beta} F_{\alpha\beta}) . \quad (2.65)$$

Hydrodynamics begins to apply with ϵ and w^μ obtained from equation (2.54).

2.2 Second-Order Viscous Hydrodynamics

Once the system reaches local thermal equilibrium, its time evolution can be described by viscous hydrodynamics. Properties of the hot QCD medium such as transport coefficients characterize how it responds to the initial anisotropy or inhomogeneity and have significant effects on the final state observables. This section is concerned with the second-order viscous hydrodynamics. The causality issue in the first-order Navier-Stokes hydrodynamics is discussed in Section 6.3.

2.2.1 Kinetic Theory

In this section, we briefly discuss the kinetic theory derivation of the hydrodynamic equations that are solved in **MUSIC** [33]. The transport theory describes time evolution of a system out of equilibrium. The Boltzmann distribution function $f(t, \mathbf{x}, \mathbf{p})$ is the number density in the phase space and the Boltzmann transport equation governs the time evolution of $f(t, \mathbf{x}, \mathbf{p})$

$$p^\mu \partial_\mu f_n = \mathcal{C}_n[f] \quad (2.66)$$

where $\mathcal{C}_n[f]$ is the collision kernel which is a functional of f . The subscript n denotes the particle species involved in the system. In the case of $2 \rightarrow 2$ scattering process, whose matrix element is \mathcal{M} , one has

$$\begin{aligned} \mathcal{C}_n[f] = & \frac{1}{2} \sum_{n', l, l'} d_{n'} d_l d_{l'} \frac{1}{16} \int_{\mathbf{p}'} \int_{\mathbf{k}} \int_{\mathbf{k}'} (2\pi)^4 \delta^{(4)}(p + p' - k - k') \\ & \times |\mathcal{M}((l, \mathbf{k}), (l', \mathbf{k}') \rightarrow (n, \mathbf{p}), (n', \mathbf{p}'))|^2 \\ & \times \left[f_l(\mathbf{k}) f_{l'}(\mathbf{k}') \tilde{f}_n(\mathbf{p}) \tilde{f}_{n'}(\mathbf{p}') - f_n(\mathbf{p}) f_{n'}(\mathbf{p}') \tilde{f}_l(\mathbf{k}) \tilde{f}_{l'}(\mathbf{k}') \right] \end{aligned} \quad (2.67)$$

$$\tilde{f}_n(\mathbf{p}) = 1 + a_n f_n(\mathbf{p}) \quad \text{where} \quad a_n = \begin{cases} +1 & \text{for Bose-Einstein} \\ -1 & \text{for Fermi-Dirac} \\ 0 & \text{for Boltzmann} \end{cases} \quad (2.68)$$

where $\int_{\mathbf{k}} = \frac{d^3 \mathbf{k}}{(2\pi)^3 E_{\mathbf{k}}}$ and d_n is the degeneracy factor of particle species n . The summation goes over all relevant species involved in the system. One gets the following

relation between the Boltzmann distribution function and the energy-momentum tensor

$$T^{\mu\nu}(t, \mathbf{x}, \mathbf{p}) = \sum_n d_n \int \frac{d^3\mathbf{p}}{(2\pi)^3 E_{\mathbf{p}}} p^\mu p^\nu f_n(t, \mathbf{x}, \mathbf{p}) \quad (2.69)$$

Let us consider a small deviation from local thermal equilibrium where the distribution function can be written as $f = f_0 + \delta f$

$$f_0 = \frac{1}{\exp[(p \cdot u - \mu)/T] \mp 1} \quad (2.70)$$

If there is no particle diffusion, the energy momentum tensor can be decomposed as a sum of ideal part and viscous correction

$$T^{\mu\nu} = \epsilon_0 u^\mu u^\nu - (P_0 + \Pi) \Delta^{\mu\nu} + \pi^{\mu\nu} \quad (2.71)$$

where ϵ_0 , P_0 are the energy density and pressure in the thermal equilibrium, respectively and they are related by the equation of state. Time evolutions of the shear ($\pi^{\mu\nu}$) and bulk (Π) viscous corrections are derived by the shear effect and expansion of the system as shown below. Then one obtains the following equation for δf

$$D_u \delta f = -D_u f_0 - \frac{1}{p \cdot u} p^\mu \nabla_\mu f + \frac{1}{p \cdot u} \mathcal{C}[f] \quad (2.72)$$

where the following notations are used

$$D_u Q \equiv u^\nu \partial_\nu Q$$

$$\Delta_{\mu\nu} = g_{\mu\nu} - u_\mu u_\nu$$

$$\nabla_\mu Q = \Delta_{\mu\nu} \partial^\nu Q$$

Integration of the previous transport equation (2.72) over momentum space and summation over species lead to

$$D_u (\pi^{\mu\nu} - \Pi \Delta^{\mu\nu}) = -D_u (\epsilon_0 u^\mu u^\nu - P_0 \Delta^{\mu\nu}) - \sum_n d_n \int_{\mathbf{p}} \frac{p^\mu p^\nu}{p \cdot u} p^\alpha \nabla_\alpha f_n + \sum_n d_n \int_{\mathbf{p}} \frac{p^\mu p^\nu}{p \cdot u} \mathcal{C}_n[f]. \quad (2.73)$$

The left hand side and right hand side become

$$\text{LHS} = D_u \pi^{\mu\nu} - (D_u \Pi) \Delta^{\mu\nu} + \Pi (u^\nu D_u u^\mu + u^\mu D_u u^\nu) \quad \text{and} \quad (2.74)$$

$$\begin{aligned}
\text{RHS} = & -(D_u \epsilon_0) u^\mu u^\nu + (D_u P_0) \Delta^{\mu\nu} - (\epsilon_0 + P_0) (u^\nu D_u u^\mu + u^\mu D_u u^\nu) \\
& - \nabla_\alpha \left[\sum_n d_n \int_{\mathbf{p}} \frac{p^\mu p^\nu}{p \cdot u} p^\alpha f_n \right] - (\nabla_\alpha u_\beta) \left[\sum_n d_n \int_{\mathbf{p}} \frac{p^\mu p^\nu}{(p \cdot u)^2} p^\alpha p^\beta f_n \right] \\
& + \sum_n d_n \int_{\mathbf{p}} \frac{p^\mu p^\nu}{p \cdot u} \mathcal{C}_n[f], \tag{2.75}
\end{aligned}$$

respectively. Therefore, one writes the equations of motion for Π and $\pi^{\mu\nu}$ as

$$\begin{aligned}
D_u \pi^{\mu\nu} - (D_u \Pi) \Delta^{\mu\nu} = & -(D_u \epsilon_0) (u^\mu u^\nu - c_s^2 \Delta^{\mu\nu}) - (\epsilon_0 + P_0 + \Pi) (u^\nu D_u u^\mu + u^\mu D_u u^\nu) \\
& - (H_3)^{\mu\nu} - (H_4)^{\mu\nu} + \sum_n d_n \int_{\mathbf{p}} \frac{p^\mu p^\nu}{p \cdot u} \mathcal{C}_n[f] \tag{2.76}
\end{aligned}$$

where

$$c_s^2 \equiv \frac{\partial P_0}{\partial \epsilon_0} \quad (\text{speed of sound})^2 \tag{2.77}$$

$$(H_3)^{\mu\nu} \equiv \nabla_\alpha \left[\sum_n d_n \int_{\mathbf{p}} \frac{p^\mu p^\nu}{p \cdot u} p^\alpha f_n \right] \quad \text{and} \tag{2.78}$$

$$(H_4)^{\mu\nu} \equiv (\nabla_\alpha u_\beta) \left[\sum_n d_n \int_{\mathbf{p}} \frac{p^\mu p^\nu}{(p \cdot u)^2} p^\alpha p^\beta f_n \right]. \tag{2.79}$$

2.2.2 Equations of Motion for Viscous Corrections

The energy-momentum conservation equation is

$$\partial_\mu T^{\mu\nu} = 0 \tag{2.80}$$

The conservation equation can be expressed in terms of ϵ_0 , P_0 , Π and $\pi^{\mu\nu}$

$$\partial_\mu T^{\mu\nu} = u_\mu D_u T^{\mu\nu} + \nabla_\mu T^{\mu\nu} \tag{2.81}$$

$$\begin{aligned}
& = u^\nu D_u \epsilon_0 + (\epsilon_0 + P_0 + \Pi) D_u u^\nu + (\epsilon_0 + P_0 + \Pi) \theta u^\nu \\
& \quad + u_\mu D_u \pi^{\mu\nu} - \nabla^\nu (P_0 + \Pi) + \nabla_\mu \pi^{\mu\nu} \\
& = 0 \tag{2.82}
\end{aligned}$$

where $\theta \equiv \nabla_\alpha u^\alpha$ quantifies the expansion rate of the system. Contraction of the previous equation with u_ν yields

$$D_u \epsilon_0 = -(\epsilon_0 + P_0 + \Pi) \theta - u_\mu u_\nu D_u \pi^{\mu\nu} - u_\nu \nabla_\mu \pi^{\mu\nu} \tag{2.83}$$

$$= -(\epsilon_0 + P_0 + \Pi) \theta + \pi^{\mu\nu} D_u (u_\mu u_\nu) + \pi^{\mu\nu} \nabla_\mu u_\nu \tag{2.84}$$

$$= -(\epsilon_0 + P_0 + \Pi) \theta + \pi^{\mu\nu} \sigma_{\mu\nu} \tag{2.85}$$

where the shear tensor $\sigma_{\mu\nu}$ is defined as

$$\sigma_{\mu\nu} \equiv \frac{1}{2} \left(\nabla_\mu u_\nu + \nabla_\nu u_\mu - \frac{2}{3} \theta \Delta_{\mu\nu} \right). \quad (2.86)$$

By substituting equation (2.85) into (2.82), one can rewrite the conservation equation as

$$\nabla^\mu (P_0 + \Pi) = (\epsilon_0 + P_0 + \Pi) D_u u^\mu - \pi^{\mu\nu} D_u u_\nu + \nabla_\nu \pi^{\mu\nu} + (\pi^{\alpha\beta} \sigma_{\alpha\beta}) u^\mu. \quad (2.87)$$

Equation (2.76), in conjunction with the conservation equation (2.87), leads to the following equations of motion for the shear viscous tensor $\pi^{\mu\nu}$ and bulk pressure Π [34]

$$\begin{aligned} D_u \Pi + C = & - \left[\left(\frac{1}{3} - c_s^2 \right) (\epsilon_0 + P_0) - \frac{2}{9} (\epsilon_0 - 3P_0) - \frac{1}{9} \sum_n d_n m_n^4 I_{n|-2,0} \right] \theta \\ & - (1 - c_s^2) \Pi \theta + \frac{1}{9} \left(\sum_n d_n m_n^4 \rho_{n|-2} \right) \theta \\ & + \left(\frac{1}{3} - c_s^2 \right) \pi^{\alpha\beta} \sigma_{\alpha\beta} + \frac{1}{3} \sum_n d_n m_n^2 (\rho_{n|-2})^{\alpha\beta} \sigma_{\alpha\beta} \\ D_u \pi^{\langle\mu\nu\rangle} + C^{\mu\nu} = & 2 \left[\frac{4}{5} P_0 + \frac{1}{15} (\epsilon_0 - 3P_0) - \frac{1}{15} \sum_n d_n m_n^4 I_{n|-2,0} \right] \sigma^{\mu\nu} \\ & - \left(\frac{4}{3} \pi^{\mu\nu} + \frac{1}{3} \sum_n d_n m_n^2 (\rho_{n|-2})^{\mu\nu} \right) \theta \\ & + \left(\frac{6}{5} \Pi - \frac{2}{15} \sum_n d_n m_n^4 \rho_{n|-2} \right) \sigma^{\mu\nu} \\ & - \frac{10}{7} \pi^{\alpha\langle\mu} \sigma^{\nu\rangle}_\alpha - \frac{4}{7} \sum_n d_n m_n^2 (\rho_{n|-2})^{\alpha\langle\mu} \sigma^{\nu\rangle}_\alpha + 2 \pi^{\alpha\langle\mu} \omega^{\nu\rangle}_\alpha \\ & - (X_{4,0})^{\mu\nu\alpha\beta} \sigma_{\alpha\beta} \end{aligned} \quad (2.88)$$

where the following definitions were used

$$\omega_{\mu\nu} \equiv \frac{1}{2} (\nabla_\mu u_\nu - \nabla_\nu u_\mu) \quad (\text{vorticity}) \quad (2.90)$$

$$I_{n|l,q} \equiv \frac{1}{(2q+1)!!} \int_{\mathbf{p}} (p \cdot u)^{l-2q} (-\Delta_{\mu\nu} p^\mu p^\nu)^q f_{n,0} \quad (2.91)$$

$$\rho_{n|l} \equiv \int_{\mathbf{p}} (p \cdot u)^l \delta f_n \quad (2.92)$$

$$(\rho_{n|l})^{\mu\nu} \equiv \int_{\mathbf{p}} (p \cdot u)^l p^{\langle\mu} p^{\nu\rangle} \delta f_n \quad (2.93)$$

$$C = \frac{1}{3} \sum_n d_n \int_{\mathbf{p}} \frac{m_n^2}{p \cdot u} \mathcal{C}_n[f] \quad (2.94)$$

$$C^{\mu\nu} = - \sum_n d_n \int_{\mathbf{p}} \frac{p^{\langle\mu} p^{\nu\rangle}}{p \cdot u} \mathcal{C}_n[f] \quad (2.95)$$

in which $A^{\langle\mu\nu\rangle}$ is defined as

$$A^{\langle\mu\nu\rangle} \equiv \frac{1}{2} \left[\Delta_\alpha^\mu \Delta_\beta^\nu A^{\alpha\beta} - \frac{2}{3} \Delta^{\mu\nu} (A^{\alpha\beta} \Delta_{\alpha\beta}) \right] \quad (2.96)$$

A more detailed derivation of the previous equations is available in Section 6.4. In principle, the collision kernel \mathcal{C}_n is a complicated functional of distribution function and transition amplitude. Hence, computations in the equations (2.94) and (2.95) from first principles are challenging. In this work, the 14-moment approximation, which postulates the functional form of δf , is adopted to obtain the equations of motion for Π and $\pi^{\mu\nu}$ in a closed form.

2.2.3 14-Moment Approximation

To get equations (2.88) and (2.89) in closed forms, one has to obtain the moments $\rho_{n|l}$ and $(\rho_{n|l})^{\mu\nu}$ in terms of Π and $\pi^{\mu\nu}$. The 14-moment approximation, which was first introduced in [65], is employed in this work to have the functional form of δf_n . For a single-component gas with Boltzmann statistics, the viscous correction δf is assumed to be

$$\frac{\delta f(\mathbf{p})}{f_0(\mathbf{p})} = [E_0 + B_0 m^2 + D_0 (p \cdot u) - 4B_0 (p \cdot u)^2] \Pi + \lambda_n p \cdot \delta n + B_2 \pi_{\mu\nu} p^\mu p^\nu \quad (2.97)$$

where δn^μ is diffusion in the number current n^μ . In this work, vanishing diffusion is assumed and $\lambda_n = 0$. One can solve for the remaining coefficients B_0 , D_0 , E_0 and B_2 from the following conditions

$$0 = \int \frac{d^3 \mathbf{p}}{(2\pi)^3 E_{\mathbf{p}}} (p \cdot u) \delta f(\mathbf{p}) \quad (2.98)$$

$$0 = \int \frac{d^3 \mathbf{p}}{(2\pi)^3 E_{\mathbf{p}}} (p \cdot u)^2 \delta f(\mathbf{p}) \quad (2.99)$$

$$\Pi = \int \frac{d^3 \mathbf{p}}{(2\pi)^3 E_{\mathbf{p}}} \frac{1}{3} (-\Delta_{\mu\nu} p^\mu p^\nu) \delta f(\mathbf{p}) \quad (2.100)$$

The equations of motion for Π and $\pi^{\mu\nu}$ become

$$D_u \Pi + C = - \left[\left(\frac{1}{3} - c_s^2 \right) (\epsilon_0 + P_0) - \frac{2}{9} (\epsilon_0 - 3P_0) - \frac{1}{9} m^4 I_{-2,0} \right] \theta - \left[1 - c_s^2 - \frac{m^4}{9} \gamma_2^{(0)} \right] \Pi \theta + \left[\frac{1}{3} - c_s^2 + \frac{m^2}{3} \gamma_2^{(2)} \right] \pi^{\mu\nu} \sigma_{\mu\nu} \quad (2.101)$$

$$D_u \pi^{\langle\mu\nu\rangle} + C^{\mu\nu} = 2 \left[\frac{4}{5} P_0 + \frac{1}{15} (\epsilon_0 - 3P_0) - \frac{1}{15} m^4 I_{-2,0} \right] \sigma^{\mu\nu} - \left[\frac{10}{7} + \frac{4}{7} m^2 \gamma_2^{(2)} \right] \pi^{\alpha\langle\mu} \sigma^{\nu\rangle}_{\alpha} - \left[\frac{4}{3} + \frac{1}{3} m^2 \gamma_2^{(2)} \right] \pi^{\mu\nu} \theta + \left[\frac{6}{5} - \frac{2}{15} m^4 \gamma_2^{(0)} \right] \Pi \sigma^{\mu\nu} \quad (2.102)$$

where $\gamma_l^{(0)}$ and $\gamma_l^{(2)}$ are defined as

$$\gamma_l^{(0)} \Pi = \int \frac{d^3 \mathbf{p}}{(2\pi)^3 E_{\mathbf{p}}} \frac{1}{(p \cdot u)^l} \delta f(\mathbf{p}) \quad (2.103)$$

$$\gamma_l^{(0)} = (E_0 + B_0 m^2) I_{-l,0} + D_0 I_{1-l,0} - 4B_0 I_{2-l,0} \quad (2.104)$$

$$\gamma_l^{(2)} \pi^{\mu\nu} = \int \frac{d^3 \mathbf{p}}{(2\pi)^3 E_{\mathbf{p}}} \frac{p^{\langle\mu} p^{\nu\rangle}}{(p \cdot u)^l} \delta f(\mathbf{p}) \quad (2.105)$$

$$\gamma_l^{(2)} = \frac{I_{4-l,2}}{I_{4,2}}. \quad (2.106)$$

It is also necessary to specify the functional forms of C and $C^{\mu\nu}$ to have the equations of motion for Π and $\pi^{\mu\nu}$ in a closed form. The collision term of the linearized Boltzmann transport equation in Section 6.5 implies that the leading-order contributions to C and $C^{\mu\nu}$ is linear in Π and $\pi^{\mu\nu}$. By considering the tensor structures, one has

$$C = \frac{\Pi}{\tau_{\Pi}} + (\text{higher orders in } \Pi \text{ and } \pi^{\mu\nu}) \quad (2.107)$$

$$C^{\mu\nu} = \frac{\pi^{\mu\nu}}{\tau_{\pi}} + (\text{higher orders in } \Pi \text{ and } \pi^{\mu\nu}) \quad (2.108)$$

where τ_{Π} and τ_{π} are the bulk and shear relaxation times, respectively. If one considers the non-linear terms of Π and $\pi^{\mu\nu}$ in the collision terms C and $C^{\mu\nu}$, the equations of motion can be written as [66, 67]

$$\tau_{\Pi} D_u \Pi + \Pi = -\zeta \theta - \delta_{\Pi\Pi} \Pi \theta + \lambda_{\Pi\pi} \pi^{\mu\nu} \sigma_{\mu\nu} \quad (2.109)$$

$$\tau_{\pi} D_u \pi^{\langle\mu\nu\rangle} + \pi^{\mu\nu} = 2\eta \sigma^{\mu\nu} - \delta_{\pi\pi} \pi^{\mu\nu} \theta + \frac{9}{70 P_0} \pi_{\alpha}^{\langle\mu} \pi^{\nu\rangle\alpha} - \tau_{\pi\pi} \pi_{\alpha}^{\langle\mu} \sigma^{\nu\rangle\alpha} + \lambda_{\pi\Pi} \Pi \sigma^{\mu\nu} \quad (2.110)$$

In the limit of small mass [34], the shear and bulk viscosities are given as

$$\frac{\zeta}{\tau_{\Pi}(\epsilon_0 + P_0)} = \left(\frac{1}{3} - c_s^2 \right) - \frac{2}{9} \left(\frac{\epsilon_0 - 3P_0}{\epsilon_0 + P_0} \right) - \frac{1}{9} \frac{m^4 I_{-2,0}}{\epsilon_0 + P_0} \quad (2.111)$$

$$= 15 \left(\frac{1}{3} - c_s^2 \right)^2 + o(m^5/T^5) \quad (2.112)$$

$$\frac{\eta}{\tau_{\pi}(\epsilon_0 + P_0)} = \frac{4}{5} \left(\frac{P_0}{\epsilon_0 + P_0} \right) + \frac{1}{15} \left(\frac{\epsilon_0 - 3P_0}{\epsilon_0 + P_0} \right) - \frac{1}{15} \frac{m^4 I_{-2,0}}{\epsilon_0 + P_0} \quad (2.113)$$

$$= \frac{1}{5} + o(m^2/T^2) \quad (2.114)$$

and the second-order transport coefficients are

$$\frac{\delta_{\pi\pi}}{\tau_{\pi}} = \frac{4}{3} + o(m^2/T^2) \quad (2.115)$$

$$\frac{\tau_{\pi\pi}}{\tau_{\pi}} = \frac{10}{7} + o(m^2/T^2) \quad (2.116)$$

$$\frac{\lambda_{\pi\Pi}}{\tau_{\pi}} = \frac{6}{5} + o(m^2/T^2) \quad (2.117)$$

$$\frac{\delta_{\Pi\Pi}}{\tau_{\Pi}} = 1 - c_s^2 + o(m^4/T^4) \quad (2.118)$$

$$\frac{\lambda_{\Pi\pi}}{\tau_{\Pi}} = \frac{8}{5} \left(\frac{1}{3} - c_s^2 \right) + o(m^4/T^4) \quad (2.119)$$

where c_s is the speed of sound. In this work, ζ/s as a function of temperature is specified and η/s is assumed to be constant. The bulk and shear relaxation times τ_{Π} and τ_{π} are computed from equations (2.112) and (2.114), respectively

$$\tau_{\Pi} = \frac{s}{15 (1/3 - c_s^2)^2 (\epsilon_0 + P_0)} \frac{\zeta}{s} \quad (2.120)$$

$$\tau_{\pi} = \frac{5 s}{\epsilon_0 + P_0} \frac{\eta}{s} \quad (2.121)$$

Other second-order transport coefficients are computed from equations (2.115)-(2.119). Therefore, once the equation of state, the shear viscosity and the bulk viscosity are known, all other transport coefficients can be determined. In **MUSIC** which performs the hydrodynamic evolution in this study, all the transport coefficients (2.115)-(2.121) are included.

2.2.4 Temperature-dependent Bulk Viscosity

Transport coefficients, such as shear and bulk viscosities, of hot QCD matter are required to quantify how the medium responds to the initial inhomogeneity and

anisotropy. In this study, the shear viscosity of QGP is taken as a constant multiple of the entropy density. The temperature dependence of the bulk viscosity, however, turned out to be not as simple.

The bulk viscosity can be computed with the Kubo-type linear response theory at finite-temperature QCD. The Kubo formula for bulk viscosity is

$$\zeta = \frac{1}{9} \lim_{\omega \rightarrow 0} \frac{1}{\omega} \int d^4x e^{i\omega t} \langle [\Theta(x), \Theta(0)] \rangle \theta(t) \quad (2.122)$$

where Θ is the trace T^μ_μ . It was shown in [68] that, for a pure gluon system, the Green function of trace anomaly in finite temperature satisfies

$$\left(T \frac{\partial}{\partial T} - 4 \right) \langle \Theta \rangle = \int_0^{1/T} d\tau \int d^3\mathbf{x} \langle \Theta(\tau, \mathbf{x}) \Theta(0, \mathbf{0}) \rangle \quad (2.123)$$

where the angled bracket denotes thermal average. This was done, based on dimensional analysis, by writing the free energy in terms of temperature and momentum scale Λ which is independent of renormalization scale. The bulk viscosity of SU(3) gluon system was computed [69], from equation (2.123) in conjunction with the lattice calculation [70]. This was extended to incorporate the light quarks [71]. Even though the bulk viscosity is small for high temperature [72], it becomes comparable to the shear viscosity at the cross-over region.

The bulk viscosity of the hadronic matter was computed in [73] from the mass spectrum $\rho(m) = \rho_{\text{HG}}(m) + \rho_{\text{HS}}(m)$ of hadronic system

$$\rho_{\text{HG}}(m) = \theta(M_0 - m) \sum_i d_i \delta(m - m_i) \quad (2.124)$$

$$\rho_{\text{HS}}(m) = \theta(m - M_0) \frac{A}{(m^2 + m_0^2)^{5/4}} \exp(m/T_H) \quad (2.125)$$

where $m_0 = 0.5 \text{ GeV}$ and $A = 0.5 \text{ GeV}^{3/2}$. The summation for ρ_{HG} is over all known hadrons [74] lighter than $M_0 = 2 \text{ GeV}$. It is assumed that the mass spectrum above M_0 follows the Hagedorn state [75]. Figure 2.5 shows the parameterization of the ratio of the bulk viscosity to entropy density.

2.2.5 Equation of State

So far, there are 11 unknowns (ϵ_0 , P_0 , u^μ , Π and $\pi^{\mu\nu}$) while there are 10 equations (conservation equation and equation of motion for Π and $\pi^{\mu\nu}$). The equation of

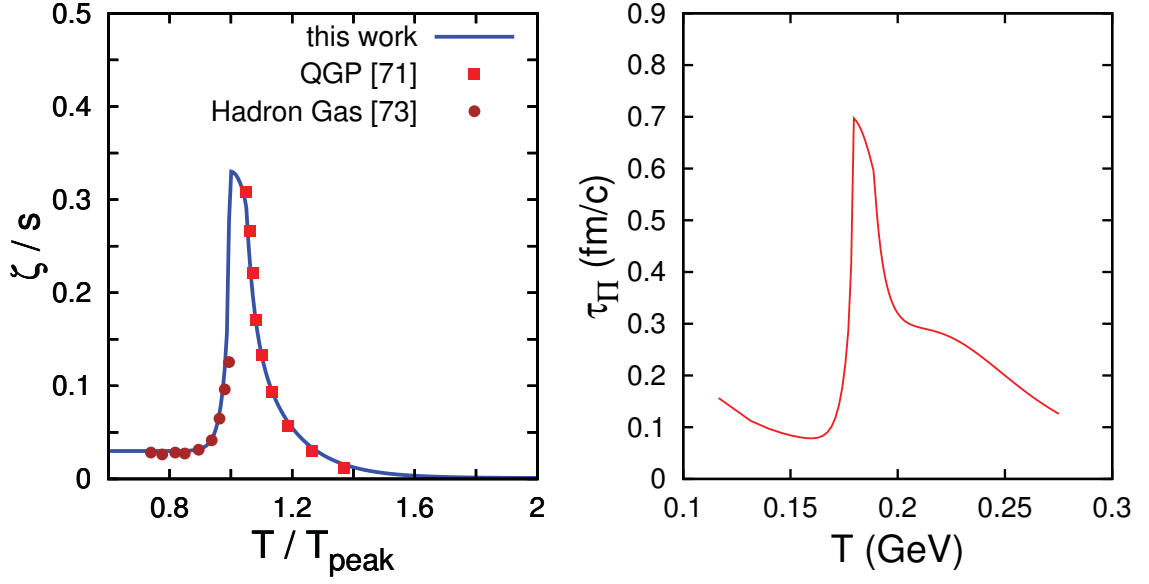


Figure 2.5: The temperature dependence of the bulk viscosity over entropy density used in this study (left) and bulk relaxation time τ_Π as a function of temperature (right). The QGP side of the ζ/s is taken from Ref.[71] and the hadronic side is taken from Ref.[73]. The peak temperature is set to be $T_{\text{peak}} = 180 \text{ MeV}$ in this work. This parametrization was used in [24].

state (EoS) provides pressure as a function of energy density. Therefore there are as many equation as unknowns. EoS is sensitive to the particle contents, such as mass spectrum and interaction, of the system. In this work, **s95p** parametrization [76], constructed from non-interacting hadronic resonance gas and quark-gluon plasma with vanishing chemical potentials, was used. For the high-temperature QGP sector, the trace $\Theta \equiv \epsilon - 3P$ is assumed to have a form

$$\frac{\Theta_{\text{QGP}}(T)}{T^4} = \frac{d_2}{T^2} + \frac{d_4}{T^4} + \frac{c_1}{T^{n_1}} + \frac{c_2}{T^{n_2}} \quad \text{for } T > T_0. \quad (2.126)$$

Then the QGP equation of state is matched with that of hadronic resonance gas such that the trace and its first and second derivative are continuous at $T = T_0$. Once the pressure for $T > T_0$ is specified, other thermodynamic quantities can be obtained from the trace using the following identity

$$\frac{\partial}{\partial T} \left(\frac{P}{T^4} \right) = \frac{1}{T^5} \left[T \left(\frac{\partial P}{\partial T} \right)_{\{\mu_C\}} - 4P \right] \quad (2.127)$$

$$= \frac{1}{T^5} (Ts - 4P) \quad (2.128)$$

$$= \frac{1}{T^5} \left(\Theta - \sum_C \mu_C n_C \right) \quad (2.129)$$

where $Ts = \epsilon + P - \sum_C \mu_C n_C$ is the thermodynamic relation. For non-zero chemical potentials and charge densities, the expression for the entropy density s becomes

$$\frac{s}{T^3} = \frac{1}{T^4} \left(\epsilon + P - \sum_C \mu_C n_C \right) \quad (2.130)$$

$$= \frac{\Theta}{T^4} + 4 \frac{P}{T^4} - \frac{1}{T^4} \sum_C \mu_C n_C \quad (2.131)$$

$$= \frac{\Theta(T, \mu)}{T^4} + 4 \frac{P(T_0, \mu)}{T_0^4} - \frac{1}{T^4} \sum_C \mu_C \left(\frac{\partial P}{\partial \mu_C} \right)_T (T, \mu) \\ + 4 \int_{T_0}^T \frac{dT'}{T'^5} \left[\Theta(T', \mu) - \sum_C \mu_C \left(\frac{\partial P}{\partial \mu_C} \right)_T (T', \mu) \right] \quad (2.132)$$

While the equation of state used in this work assumes zero chemical potentials, this is a good approximation in the mid-rapidity region of heavy ion collisions where low- x gluons dominate the dynamics. Even though the approximation of the zero chemical potential does not hold in the intermediate and high- x region, production of the mid-rapidity hadrons is dominated by the low- x gluons mentioned above. Continuity of derivatives of Θ_{QGP} and Θ_{HRG} at $T = T_0$ provides expressions for c_1 and c_2 as

$$c_1 = \frac{n_2 + 1}{n_1(n_1 - n_2)} T_0^{n_1+1} \Theta'_{\text{HRG}}(T_0) + \frac{1}{n_1(n_1 - n_2)} T_0^{n_1+2} \Theta''_{\text{HRG}}(T_0) \\ + \frac{2(n_2 - 2)}{n_1(n_1 - n_2)} d_2 T_0^{n_1-2} + \frac{4(n_2 - 4)}{n_1(n_1 - n_2)} d_4 T_0^{n_1-4} \quad (2.133)$$

$$c_2 = \frac{n_1 + 1}{n_2(n_2 - n_1)} T_0^{n_2+1} \Theta'_{\text{HRG}}(T_0) + \frac{1}{n_2(n_2 - n_1)} T_0^{n_2+2} \Theta''_{\text{HRG}}(T_0) \\ + \frac{2(n_1 - 2)}{n_2(n_2 - n_1)} d_2 T_0^{n_2-2} + \frac{4(n_1 - 4)}{n_2(n_2 - n_1)} d_4 T_0^{n_2-4} \quad (2.134)$$

The entropy density s_{QGP} obtained from Θ_{QGP} becomes

$$\frac{s_{\text{QGP}}}{T^3} = 4 \frac{P(T_0)}{T_0^4} + d_2 \left(\frac{2}{T_0^2} - \frac{1}{T^2} \right) + \frac{d_4}{T_0^4} \\ + \frac{c_1}{n_1} \left(\frac{4}{T_0^{n_1}} - \frac{n_1 - 4}{T^{n_1}} \right) + \frac{c_2}{n_2} \left(\frac{4}{T_0^{n_2}} - \frac{n_2 - 4}{T^{n_2}} \right) \quad (2.135)$$

It was shown in [77] that the energy density obtained from lattice calculation reaches 90% of the ideal gas value ϵ_{SB} at $T \simeq 500$ MeV. Based on this, an additional condition,

requiring that the entropy density at $T = 800$ MeV must be 95% of the ideal gas value s_{SB} , was imposed to determine the equation of state. A different value of the entropy density $s = 0.9 s_{\text{SB}}$ at $T = 800$ MeV was also considered in [76] and it was shown that the difference in the observables is negligible. The parameters — d_2 , d_4 , c_1 , c_2 , n_1 , n_2 , and T_0 — are determined such that Θ_{QGP} fits the lattice calculation shown in [78] for $T > 250$ MeV. The entropy density in the ideal gas limit is given as

$$\frac{s_{\text{SB}}}{T^3} = [8(N_c^2 - 1) + 14N_{f,l}N_c] \frac{\zeta(4)}{\pi^2} \quad (2.136)$$

where $N_{f,l}$ is the number of light quark flavors in consideration and $\zeta(s) = \sum_{n=1}^{\infty} 1/n^s$ is the Riemann-zeta function. Since u , d , and s quarks (and antiquarks) were considered and there are three colors, $N_{f,l} = 3$ and $N_c = 3$. To complete the equation of state, one has to have the equation of state for the hadronic sector.

For construction of the hadronic EoS, interactions among hadrons must be taken into account. However, for the interacting gas of π , K and N , it was demonstrated in [79] that those interactions can be handled by including resonances. Therefore, treating the hadronic system as a non-interacting resonance gas can be a good approximation. Then, the pressure is given as

$$P_{\text{HRG}} = \sum_{i \in \text{mesons}} d_i \int \frac{d^3\mathbf{k}}{(2\pi)^3} \frac{|\mathbf{k}|^2}{3E_{\mathbf{k},i}} \frac{1}{z_i^{-1} \exp(E_{\mathbf{k},i}/T) - 1} + \sum_{i \in \text{baryons}} d_i \int \frac{d^3\mathbf{k}}{(2\pi)^3} \frac{|\mathbf{k}|^2}{3E_{\mathbf{k},i}} \frac{1}{z_i^{-1} \exp(E_{\mathbf{k},i}/T) + 1} \quad (2.137)$$

$$z_i = \exp\left(\frac{1}{T} \sum_C \mu_C C_i\right) \quad (2.138)$$

where $E_{\mathbf{k},i} = (m_i^2 + |\mathbf{k}|^2)^{1/2}$ and C_i is a conserved charge C carried by i -th species. It is possible to obtain the trace anomaly Θ_{HRG} from the pressure and its derivative according to equation (2.129)

$$\Theta = T^5 \frac{\partial}{\partial T} \left(\frac{P}{T^4} \right) + \sum_C \mu_C \left(\frac{\partial P}{\partial \mu_C} \right)_T \quad (2.139)$$

Then, for temperatures between 70 MeV and 190 MeV and a vanishing chemical potential, Θ_{HRG} is fitted with the following function

$$\frac{\Theta_{\text{HRG}}}{T^4} = a_1 T^{l_1} + a_2 T^{l_2} + a_3 T^{l_3} + a_4 T^{l_4} \quad (2.140)$$

where the exponents are integers satisfying $0 \leq l_1 < l_2 < l_3 < l_4 \leq 10$. In addition to the continuity conditions and $s_{\text{QGP}}(T = 800 \text{ MeV}) = 0.95 \times s_{\text{SB}}$, lattice calculations for trace anomaly were used to determine the parameters. The energy density and

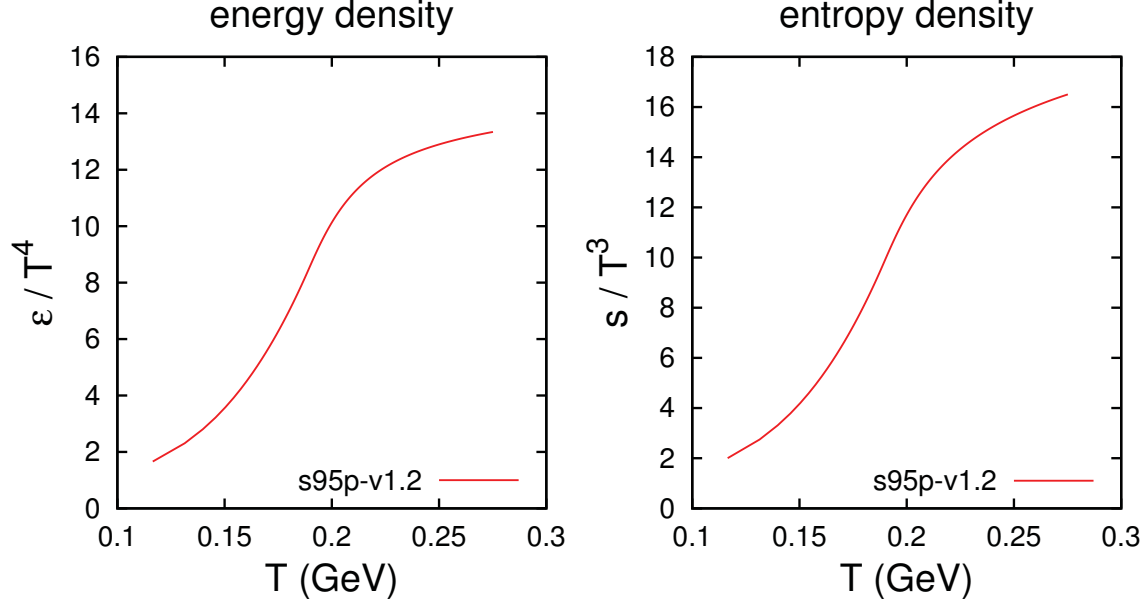


Figure 2.6: The energy density (left) and entropy density (right) as functions of temperature. The equation of state is obtained from hadronic resonance gas and lattice QCD calculation with vanishing baryonic chemical potential [76, 81].

entropy density as functions of temperature are shown in Figure 2.6 and the trace anomaly and speed of sound are shown in Figure 2.7. It must be also noted that a variant (**s95p-v1.2** in Figures 2.6 and 2.7) of the **s95p-v1** parametrization was used in this work. While the original **s95p-v1** involves hadronic resonances up to 2 GeV mass available in the Review of Particle Physics 2004 [80], the **s95p-v1.2** parametrization was constructed based on the hadronic contents in UrQMD [81] to couple hydrodynamic inputs to the UrQMD hadronic cascade without loss of the energy-momentum conservation.

While it was assumed in this work that the system is in chemical equilibrium, it is also possible to deal with a system getting out of the chemical equilibrium during hydrodynamic evolution. This can be done with partial chemical equilibrium (PCE) [82]. The idea of PCE states that inelastic scattering processes, which change the

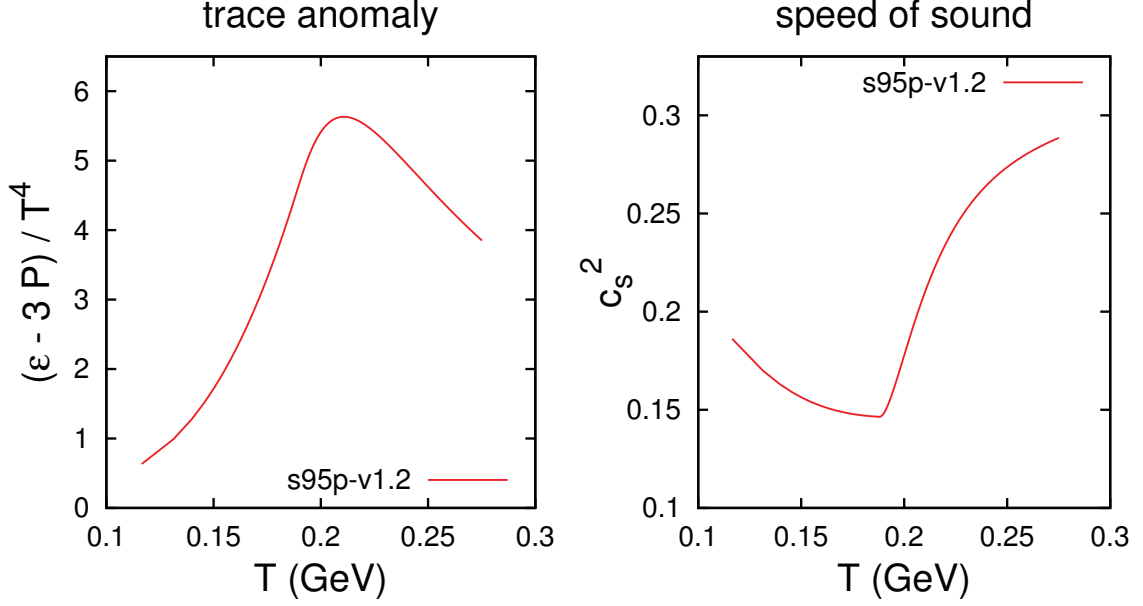


Figure 2.7: The trace anomaly (left) and speed of sound (right) as functions of temperature. The equation of state is obtained from hadronic resonance gas and lattice QCD calculation with vanishing baryonic chemical potential [76, 81].

number of hadrons, are suppressed once the system is cooled down below a temperature T_{ch} . Therefore, effective numbers of stable particles, taking decay processes of unstable resonances into account, are conserved for $T < T_{\text{ch}}$. The effective number \bar{N}_j can be written as

$$\bar{N}_j = N_j + \sum_{r \in \text{unst.}} d_{r \rightarrow j} N_r \quad (2.141)$$

where the summation is over unstable resonances and $d_{r \rightarrow j}$ is the average number of species j resulting from decay of resonance r . The thermodynamic relations become

$$TdS = dU + PdV - \sum_C \mu_C dN_C - \sum_{j \in \text{st.}} \bar{\mu}_j d\bar{N}_j \quad (2.142)$$

$$Ts = \epsilon + P - \sum_C \mu_C n_C - \sum_{j \in \text{st.}} \bar{\mu}_j \bar{n}_j \quad (2.143)$$

where $\bar{\mu}_j$ is the chemical potential associated with the conserved effective number \bar{N}_j . The condition for determination of $\{\bar{\mu}(T)\}$ is a constant ratio of \bar{n}_j to the entropy density for $T < T_{\text{ch}}$

$$\frac{\bar{n}_j(T, \{\bar{\mu}(T)\})}{s(T, \{\bar{\mu}(T)\})} = \frac{\bar{n}_j(T_{\text{ch}}, \{\bar{\mu} = 0\})}{s(T_{\text{ch}}, \{\bar{\mu} = 0\})} \quad (2.144)$$

The entropy density s can be computed from the thermodynamic relation $s = (\partial P / \partial T)_{\{\mu_C\}, \{\bar{\mu}\}}$ where the pressure P is given as

$$P_{\text{HRG(PCE)}} = \sum_{i \in \text{mesons}} d_i \int \frac{d^3 \mathbf{k}}{(2\pi)^3} \frac{|\mathbf{k}|^2}{3E_{\mathbf{k},i}} \frac{1}{z_i^{-1} \exp[(E_{\mathbf{k},i} - \bar{\mu}_i(T))/T] - 1} \\ + \sum_{i \in \text{baryons}} d_i \int \frac{d^3 \mathbf{k}}{(2\pi)^3} \frac{|\mathbf{k}|^2}{3E_{\mathbf{k},i}} \frac{1}{z_i^{-1} \exp[(E_{\mathbf{k},i} - \bar{\mu}_i(T))/T] + 1} \quad (2.145)$$

The summation is over both stable and unstable hadrons and the effective chemical potential $\bar{\mu}_r$ of unstable hadron is given as

$$\bar{\mu}_r = \sum_{j \in \text{st.}} d_{r \rightarrow j} \bar{\mu}_j. \quad (2.146)$$

This procedure enables one to put non-equilibrium dynamics in hydrodynamic description of the late stage of heavy ion collisions. The chemical freezeout temperature T_{ch} in Au+Au collisions at RHIC was estimated based on PCE in [83]. The equations of state from the more recent lattice QCD calculations with PCE were constructed in [84]. However, in this work and other hybrid models, microscopic transport in the hadronic stage handles the evolution of the system after it gets out of chemical equilibrium. The chemical freeze-out generally occurs in the hadronic re-scattering.

It is worth mentioning the difference between the PCE and the hybrid approach used in this work. In PCE, the chemical freeze-out is characterized by a single freeze-out temperature T_{ch} below which all inelastic processes cease. In the hybrid model used in this work, however, the inelastic collisions are still allowed in the microscopic transport and the chemical freeze-out occurs later than the switching into re-scattering. Hence, if one switches into the microscopic transport at the isothermal hypersurface with temperature T_{sw} , then $T_{\text{ch},i} < T_{\text{sw}}$ for the hadronic species i . In principle, one can find $T_{\text{ch},i}$ by considering time evolution of the particle distribution in the re-scattering phase. However, determination of $T_{\text{ch},i}$ in the hybrid model is computationally demanding and left as a future study.

3

Post-particlization Dynamics

In this chapter, the transition or *particlization* from hydrodynamics into microscopic transport and the post-particlization dynamics are described. In Section 3.1, the transition from hydrodynamics to particles, based on the Cooper-Frye formalism with details of sampling procedure, is explained. The **UrQMD** model, which is the microscopic transport for hadronic re-scattering, is reviewed in Section 3.2. Lastly, the formalism of the radiative and collisional jet energy losses and its Monte-Carlo implementation is explained in Section 3.3.

3.1 Transition from Hydrodynamics to Particle Dynamics

As the QGP evolves hydrodynamically, it expands and cools. At some point, the temperature of the system will become low enough that the dominant degrees of freedom become hadronic. As long as the mean free path of the hadronic system is still smaller than the system size, viscous hydrodynamics still applies. However, as the system continues to expand and cools, the mean free path will eventually become comparable to macroscopic scales of the system and a microscopic transport model is necessary to properly describe the time evolution. Since the microscopic transport **UrQMD** describes hadronic re-scattering by means of N -body simulation, it is necessary to statistically transform the macroscopic information from hydrodynamics into particles.

3.1.1 Cooper-Frye Formalism

The Cooper-Frye formalism [22] provides a relation between the particle spectrum with degeneracy factor d in momentum space and distribution function

$$\frac{dN}{d^3\mathbf{p}} = \frac{d}{(2\pi)^3} \int_{\Sigma} [f_0(x, \mathbf{p}) + \delta f_{\text{shear}}(x, \mathbf{p}) + \delta f_{\text{bulk}}(x, \mathbf{p})] \frac{p^\mu d^3\Sigma_\mu}{E_{\mathbf{p}}}. \quad (3.1)$$

where $d^3\Sigma_\mu$ is a normal vector and given as an exterior product of three displacement vectors tangential to the hypersurface Σ . The distribution function $f = f_0 + \delta f_{\text{shear}} + \delta f_{\text{bulk}}$ depends on the macroscopic information obtained from hydrodynamics. It can be shown that the Cooper-Frye formalism transforms hydrodynamics into particles such that energy and momentum are conserved. For a single-component gas, one obtains the total four-momentum

$$\mathcal{P}^\mu = \int p^\mu \frac{dN}{d^3\mathbf{p}} d^3\mathbf{p} \quad (3.2)$$

$$= \int_{\Sigma} T^{\mu\nu}(x) d^3\Sigma_\nu \quad (3.3)$$

where

$$T^{\mu\nu}(x) = \frac{d}{(2\pi)^3} \int \frac{p^\mu p^\nu}{E_{\mathbf{p}}} f(x, \mathbf{p}) d^3\mathbf{p} \quad (3.4)$$

is the kinetic theory stress-energy tensor. Momentum flowing out of a given hypersurface element is given as contraction of the energy-momentum tensor and the

3D hypersurface element. In addition, one can compute the number of particles \mathcal{N} flowing out of the hypersurface as

$$\mathcal{N} = \int \frac{dN}{d^3\mathbf{p}} d^3\mathbf{p} \quad (3.5)$$

$$= \int_{\Sigma} n^{\mu}(x) d^3\Sigma_{\mu} \quad (3.6)$$

where

$$n^{\mu}(x) = \frac{d}{(2\pi)^3} \int \frac{p^{\mu}}{E_{\mathbf{p}}} f(x, \mathbf{p}) d^3\mathbf{p} \quad (3.7)$$

is the number current. The current vector can be decomposed as $n^{\mu} = n u^{\mu} + \delta n^{\mu}$ where n and δn^{μ} are number density and diffusion current, respectively.

Since the system deviates from local thermal equilibrium, there are viscous correction δf to the distribution function. There are two formalisms commonly used to find the derivation of the viscous corrections. In Chapman-Enskog approximation, given that the local thermal equilibrium holds in the case of vanishing mean-free-path, the viscous correction can be expanded in powers of Knudsen number Kn . Kn is defined as ratio of mean-free-path to a macroscopic scale given by the system size or the expansion rate

$$f = f_0 + \sum_{k=1} \delta f_{(k)} (\text{Kn})^k \quad (3.8)$$

Alternatively, one can expand the viscous correction in momentum with corresponding moments and this is Grad's moment method. In particular, the 14-moment approximation yields

$$\delta f = f_0 (1 \pm f_0) (\Xi_{\mu} p^{\mu} + \Xi_{\mu\nu} p^{\mu} p^{\nu}) \quad (3.9)$$

where Ξ_{μ} and $\Xi_{\mu\nu}$ are a four-vector and a symmetric tensor, respectively, and there are $4 + 10$ unknowns. For a single-component gas, it is possible to add a scalar term Ξ and the constraint that $\Xi_{\mu\nu}$ is traceless. However, for a multi-component gas, this equivalence does not hold since each species has different mass and one has

$$\Xi_{\mu\nu} p^{\mu} p^{\nu} = \frac{\Xi^{\mu}}{4} m^2 + \tilde{\Xi}_{\mu\nu} p^{\mu} p^{\nu} \quad \text{with} \quad \tilde{\Xi}^{\mu}_{\mu} = 0 \quad (3.10)$$

and the first term in the RHS cannot be replaced with a species-independent scalar term [85]. The tensor structure of the viscous correction to energy-momentum tensor

implies that the scalar part of the moment expansion is associated with the bulk viscosity. The shear stress tensor $\pi^{\mu\nu}$, on the other hand, can be related to the traceless part of $\Xi^{\mu\nu}$ regardless of whether the system is single or multi-component. To avoid the ambiguity described above, the bulk viscous correction δf_{bulk} , obtained from the leading-order Chapman-Enskog approximation with relaxation time approximation [86], was adopted in this work. The Boltzmann equation with the relaxation time approximation reads

$$p^\mu \partial_\mu f_n = -\frac{p \cdot u}{\tau_{\text{HG}}} (f_n - f_{0,n}) \quad (3.11)$$

where τ_{HG} is the relaxation time of hadronic gas. The leading-order viscous correction $\delta f_{(1)}$ is given by the LHS of equation (3.11) with equilibrium distribution function $f_{(0)}$. It can be seen that τ_{HG} is on the order of the mean-free-path and the spatial gradient introduces a factor of $1/L_{\text{macro}}$ so one has

$$\tau_{\text{HG}} \frac{p^\mu}{p \cdot u} \partial_\mu f_{(0)} = -\delta f_{(1)} \sim \frac{l_{\text{mfp}}}{L_{\text{macro}}} f_{(0)} \quad (3.12)$$

and, in the case of vanishing chemical potentials,

$$\delta f_{(1)} = \frac{\tau_{\text{HG}}}{p \cdot u} f_0 (1 \pm f_0) p^\mu \partial_\mu \left(\frac{p \cdot u}{T} \right) \quad (3.13)$$

$$\begin{aligned} &= \frac{\tau_{\text{HG}}}{T p \cdot u} f_0 (1 \pm f_0) p^\mu p^\nu \left(\partial_\mu u_\nu - \frac{u_\nu \partial_\mu T}{T} \right) \\ &= \frac{\tau_{\text{HG}}}{T p \cdot u} f_0 (1 \pm f_0) p^\mu p^\nu \left(\partial_\mu u_\nu - \frac{u_\nu \partial_\mu P_0}{Ts} \right) \end{aligned} \quad (3.14)$$

$$\begin{aligned} &= \frac{\tau_{\text{HG}}}{T p \cdot u} f_0 (1 \pm f_0) p^\mu p^\nu \\ &\quad \times \left[u_\mu D_u u_\nu + \nabla_\mu u_\nu - u_\mu u_\nu \frac{D_u P_0}{\epsilon_0 + P_0} - u_\nu \frac{\nabla_\mu P_0}{\epsilon_0 + P_0} \right] \end{aligned} \quad (3.15)$$

$$= \frac{\tau_{\text{HG}}}{T p \cdot u} f_0 (1 \pm f_0) p^\mu p^\nu \left[\sigma_{\mu\nu} + \frac{1}{3} \Delta_{\mu\nu} \theta + \left(\frac{\partial P_0}{\partial \epsilon_0} \right) u_\mu u_\nu \theta \right] \quad (3.16)$$

where $\sigma_{\mu\nu}$ and θ are the shear tensor and expansion rate, respectively. To obtain the last two equalities, the thermodynamic relation $Ts = \epsilon_0 + P_0$ and energy-momentum conservation are used

$$D_u \epsilon_0 = -(\epsilon_0 + P_0) \theta - u_\mu \partial_\nu (\pi^{\mu\nu} - \Delta^{\mu\nu} \Pi) \quad (3.17)$$

$$\nabla^\mu P_0 = (\epsilon_0 + P_0) D_u u^\mu + \Delta^{\mu\alpha} \partial^\nu (\pi_{\nu\alpha} - \Delta_{\nu\alpha} \Pi) \quad (3.18)$$

where the terms from derivatives of viscous corrections are neglected since they are second order in the Knudsen number. Since the equation of motion for Π implies that $\Pi \simeq -\zeta\theta$ and the leading-order δf_{bulk} must be linear in Π , the bulk viscous correction in this work is assumed to be in the following form

$$\delta f_{\text{bulk}} = -f_0(1 \pm f_0) \frac{C_{\text{bulk}}\Pi}{T p \cdot u} p^\mu p^\nu \left(\frac{1}{3} \Delta_{\mu\nu} + c_s^2 u_\mu u_\nu \right) \quad (3.19)$$

where c_s is the speed of sound which is determined from equation (2.77). The normalization constant C_{bulk} is determined such that the contribution of δf_{bulk} to the energy-momentum tensor is the same as $-\Delta^{\mu\nu}\Pi$

$$-\Delta^{\mu\nu}\Pi = \sum_n d_n \int \frac{d^3\mathbf{p}}{(2\pi)^3 E_{\mathbf{p}}} p^\mu p^\nu \delta f_{\text{bulk},n} \quad (3.20)$$

By contracting with $-g_{\mu\nu}$, one obtains

$$3\Pi = -\sum_n d_n m_n^2 \int \frac{d^3\mathbf{p}}{(2\pi)^3 E_{\mathbf{p}}} \delta f_{\text{bulk},n} \quad (3.21)$$

$$\begin{aligned} &= \frac{C_{\text{bulk}}\Pi}{T} \sum_n d_n m_n^2 \int \frac{d^3\mathbf{p}}{(2\pi)^3 E_{\mathbf{p}}} f_{0,n}(1 \pm f_{0,n}) \frac{p^\mu p^\nu}{p \cdot u} \left(\frac{1}{3} \Delta_{\mu\nu} + c_s^2 u_\mu u_\nu \right) \\ &= \frac{C_{\text{bulk}}\Pi}{T} \sum_n d_n m_n^2 \int \frac{d^3\mathbf{k}}{(2\pi)^3 E_{\mathbf{k}}} f_{0,n}(1 \pm f_{0,n}) \left[\frac{m_n^2}{3E_{\mathbf{k}}} - \left(\frac{1}{3} - c_s^2 \right) E_{\mathbf{k}} \right] \end{aligned} \quad (3.22)$$

and

$$\frac{T}{C_{\text{bulk}}} = \frac{1}{3} \sum_n d_n m_n^2 \int \frac{d^3\mathbf{k}}{(2\pi)^3 E_{\mathbf{k}}} f_{n,0} (1 \pm f_{n,0}) \left[\frac{m_n^2}{3E_{\mathbf{k}}} - \left(\frac{1}{3} - c_s^2 \right) E_{\mathbf{k}} \right]. \quad (3.23)$$

The general form of δf_{shear} can be written as

$$\begin{aligned} \delta f_{\text{shear}} &= f_0 \tilde{f}_0 \chi_{\text{shear}}(\mathbf{p}) \\ \tilde{f}_0 &= 1 + a f_0 \end{aligned} \quad (3.24)$$

where a is defined in equation (2.68) and χ_{shear} characterizes the dependences on momentum and other thermodynamic quantities. To obtain the leading-order contribution to χ_{shear} , one has to find a scalar quantity which is linear in $\pi^{\mu\nu}$. Since $\pi^{\mu\nu}$ is orthogonal to the flow velocity u^μ , the only possibility is $\pi_{\mu\nu} p^\mu p^\nu \mathcal{I}_{\text{shear}}(\mathbf{p})$ where $\mathcal{I}_{\text{shear}}$ is a scalar function of \mathbf{p} . In general, $\mathcal{I}_{\text{shear}}$ contains several powers in \mathbf{p} . However, in

this work, $\mathcal{I}_{\text{shear}}$ is assumed to be independent of \mathbf{p} and therefore χ_{shear} has quadratic dependence on $|\mathbf{p}|$. It was shown in [87] that this *quadratic ansatz* or one-function ansatz, together with the Boltzmann statistics, yields the QGP shear viscosity reasonably close to that from the variation approach. For a massless Boltzmann gas, one has

$$\chi_{\text{shear}}(\mathbf{p}) = \frac{\pi_{\mu\nu} p^\mu p^\nu}{2(\epsilon_0 + P_0)T^2} \quad (3.25)$$

and it was demonstrated in [88, 89] that χ_{shear} of the pion gas with Bose-Einstein statistics only differs from (3.25) by a few percent. In this work, it is assumed that equation (3.25) holds for all hadronic species.

3.1.2 Sampling Procedure

The particlization procedure begins with determination of multiplicity. For each discretized hypersurface element, the average number of particles is computed as

$$\langle N \rangle_{1\text{-cell}} = \begin{cases} [n_0(x) + \delta n_{\text{bulk}}(x)] u^\mu \Delta \Sigma_\mu & \text{if } u^\mu \Delta \Sigma_\mu \geq 0 \\ 0 & \text{otherwise} \end{cases} \quad (3.26)$$

where the number density in equilibrium n_0 and bulk viscous correction δn_{bulk} are

$$n_0(x) = d \int \frac{d^3 \mathbf{k}}{(2\pi)^3} f_0(\mathbf{k}) \quad (3.27)$$

$$= \frac{dm^2 T}{2\pi^2} \sum_{l=1}^{\infty} \frac{a^{l-1}}{l} e^{l\mu/T} K_2 \left(\frac{lm}{T} \right) \quad (3.28)$$

$$\delta n_{\text{bulk}}(x) = d \int \frac{d^3 \mathbf{k}}{(2\pi)^3} \delta f_{\text{bulk}}(\mathbf{k}) \quad (3.29)$$

$$= \frac{dm^2 T}{2\pi^2} \sum_{l=1}^{\infty} a^{l-1} e^{l\mu/T} C_{\text{bulk}} \Pi \times \left[\left(\frac{1 - 3c_s^2}{l} \right) K_2 \left(\frac{lm}{T} \right) - c_s^2 \frac{m}{T} K_1 \left(\frac{lm}{T} \right) \right] \quad (3.30)$$

and a depends on the spin-statistics and its value is defined in equation (2.68). It must be noted that $\Delta \Sigma_\mu$ is determined such that it is oriented toward the region with $T < T_{\text{sw}}$. Given that the particlization occurs as the temperature and the number density decreases, particles are sampled only if $u^\mu \Delta \Sigma_\mu$ is positive since negative $u^\mu \Delta \Sigma_\mu$ corresponds to increasing temperature at given hypersurface element

as shown in Figure 3.1. Then, the number of particles are sampled according to a

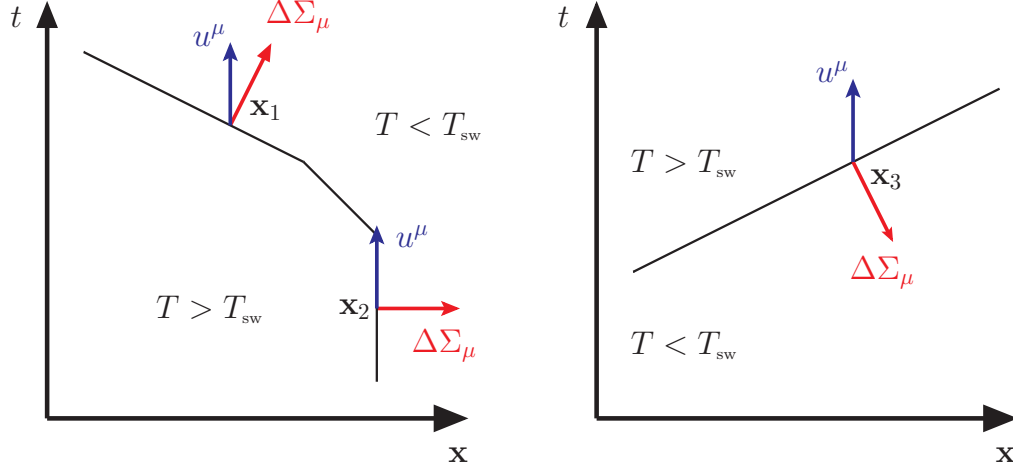


Figure 3.1: Temperature is decreasing at \mathbf{x}_1 where $u^\mu \Delta \Sigma_\mu > 0$ while it remains unchanged at \mathbf{x}_2 where $u^\mu \Delta \Sigma_\mu = 0$ (left). In the case of $u^\mu \Delta \Sigma_\mu < 0$ at \mathbf{x}_3 , temperature is increasing and there is no particlization (right).

Poisson distribution whose average is $\langle N \rangle_{1\text{-cell}}$

$$P_{1\text{-cell}}(N) = \frac{1}{N!} \langle N \rangle^N e^{-\langle N \rangle} \quad (3.31)$$

It must be noted that variance $\langle N^2 \rangle - \langle N \rangle^2$ is not same as the average $\langle N \rangle$ in the case of Bose-Einstein or Fermi-Dirac distribution

$$\langle N^2 \rangle - \langle N \rangle^2 = dV \int \frac{d^3 \mathbf{k}}{(2\pi)^3} f_0(\mathbf{k}) (1 \pm f_0(\mathbf{k})) \quad (3.32)$$

$$\neq \langle N \rangle \quad (3.33)$$

while $\langle N^2 \rangle - \langle N \rangle^2 = \langle N \rangle$ for the Poisson distribution. Nevertheless, in the temperature range between 135 MeV and 165 MeV, the difference is less than 10% for pions and smaller for heavier hadrons. Therefore, one can still rely on the Poisson distribution as a good approximation.

After the number of particles is determined, the momentum of each particle is

sampled according to the following distribution function

$$\left. \frac{dN}{d^3\mathbf{p}} \right|_{1\text{-cell}} = \begin{cases} \frac{d}{(2\pi)^3} [f_0(x, \mathbf{p}) + \delta f_{\text{shear}}(x, \mathbf{p}) + \delta f_{\text{bulk}}(x, \mathbf{p})] \frac{p^\mu \Delta \Sigma_\mu}{E_{\mathbf{p}}} & \text{if } f_0 + \delta f_{\text{shear}} + \delta f_{\text{bulk}} > 0 \text{ and } p^\mu \Delta \Sigma_\mu > 0 \\ 0 & \text{otherwise} \end{cases} \quad (3.34)$$

The sampled momentum is accepted only if $p^\mu \Delta \Sigma_\mu$ is positive and this condition is based on the fact that p^μ giving negative $p^\mu \Delta \Sigma_\mu$ represents a particle going back into the fluid. The equilibrium distribution function f_0 and viscous correction δf are

$$f_0 = \frac{1}{\exp(p \cdot u/T) \mp 1} \quad (3.35)$$

$$\delta f_{\text{shear}} = f_0(1 + af_0) \frac{\pi_{\mu\nu} p^\mu p^\nu}{2(\epsilon_0 + P_0)T^2} \quad (3.36)$$

$$\delta f_{\text{bulk}} = -f_0(1 + af_0) \frac{C_{\text{bulk}}}{T} \left[\frac{m^2}{3(p \cdot u)} - \left(\frac{1}{3} - c_s^2 \right) (p \cdot u) \right] \Pi \quad (3.37)$$

where a and C_{bulk} are defined in equations (2.68) and (3.23), respectively. Since only the leading-order correction of δf is considered, $f_0 + \delta f$ can be negative for high p_T . Sampling momenta of particles according to the equation (3.34) is not straightforward since its dependence on the momentum is complicated. Therefore, in the actual sampling, a rejection method with an isotropic envelop function (also known as the hat function) was used. Since $d^3\mathbf{p}/E_{\mathbf{p}}$ is Lorentz-invariant, it is possible to sample a momentum in the rest frame of fluid and then boost it into the lab frame

$$N(\mathbb{R}) = d \int_{\Sigma} \int_{\mathbb{R}(\mathbf{p})} \frac{d^3\mathbf{p}}{(2\pi)^3 E_{\mathbf{p}}} f(\mathbf{x}, \mathbf{p}) p^\mu d\Sigma_\mu \quad (3.38)$$

$$= d \int_{\Sigma} \int_{\mathbb{R}(\mathbf{q})} \frac{d^3\mathbf{q}}{(2\pi)^3 E_{\mathbf{q}}} f(\mathbf{x}, \mathbf{q}) q^\mu \overline{d\Sigma}_\mu \quad (3.39)$$

where $\overline{d\Sigma}_\mu$ is the normal vector in the rest frame of the fluid. The momenta p^μ and q^μ , in the lab and fluid rest frames, are related by a Lorentz transformation $\Lambda(u)$

$$p^\mu = \Lambda^\mu{}_\nu q^\nu \quad \text{where} \quad \Lambda(u) = \begin{pmatrix} u^0 & u^j \\ u^i & \delta^{ij} + \frac{u^i u^j}{u^0 + 1} \end{pmatrix} \quad (3.40)$$

All tensors such as flow velocity and shear stress tensor are boosted into the rest frame of fluid and momentum q^μ sampled in that frame is boosted back into the lab

frame. The rejection method of sampling requires an envelop function which is always larger than the probability distribution function

$$\mathcal{F}_{\text{env}}(q) = \left\{ f_0(q) + \frac{1}{2} f_0(q) (1 \pm f_0(q)) \mathcal{W}_{\text{shear}} \frac{q^2}{T^2} + f_0(q) (1 \pm f_0(q)) \mathcal{W}_{\text{bulk}} \left[\frac{m^2}{3E_{\mathbf{q}}T} + \left(\frac{1}{3} - c_s^2 \right) \frac{E_{\mathbf{q}}}{T} \right] \right\} \mathcal{V} \quad (3.41)$$

$$\mathcal{W}_{\text{shear}} = \frac{1}{(\epsilon_0 + P_0)} \sum_{i,j=1}^3 |\bar{\pi}^{ij}| \quad (3.42)$$

$$\mathcal{W}_{\text{bulk}} = |C_{\text{bulk}} \Pi| \quad (3.43)$$

$$\mathcal{V} = \frac{d}{(2\pi)^3} \left(|u^\mu \Delta \Sigma_\mu| + \sum_{i=1}^3 |\Delta \Sigma_i| \right) \quad (3.44)$$

where $\bar{\pi}^{\mu\nu}$ is the shear stress tensor in the rest frame of the fluid. To construct a stepwise envelop function, lattice points in $0 \leq q \leq Q_{\text{max}}$ with even spacing were set up. The probability that momentum of sampled particle is between q_i and q_{i+1} is given as

$$\mathcal{P}_{\text{env}}(q_i < |\mathbf{q}| < q_{i+1}) = 4\pi \mathcal{N}_{\text{env}} (q_{i+1}^3 - q_i^3) \times \begin{cases} \mathcal{F}_{\text{env}}|_i & \text{if } d_q \mathcal{F}_{\text{env}}|_i < 0 \text{ and } d_q \mathcal{F}_{\text{env}}|_{i+1} < 0 \\ \mathcal{F}_{\text{env}}|_{i+1} & \text{if } d_q \mathcal{F}_{\text{env}}|_i > 0 \text{ and } d_q \mathcal{F}_{\text{env}}|_{i+1} > 0 \\ \max(\mathcal{F}_{\text{env}}|_i, \mathcal{F}_{\text{env}}|_{i+1}) & \text{if } d_q \mathcal{F}_{\text{env}}|_i < 0 \text{ and } d_q \mathcal{F}_{\text{env}}|_{i+1} > 0 \\ \mathcal{F}_{\text{env}}|_i + [\mathcal{F}_{\text{env}}|_{i+1} - \mathcal{F}_{\text{env}}|_i - d_q \mathcal{F}_{\text{env}}|_{i+1}(q_{i+1} - q_i)] \left(\frac{d_q \mathcal{F}_{\text{env}}|_i}{d_q \mathcal{F}_{\text{env}}|_i - d_q \mathcal{F}_{\text{env}}|_{i+1}} \right) & \text{if } d_q \mathcal{F}_{\text{env}}|_i > 0 \text{ and } d_q \mathcal{F}_{\text{env}}|_{i+1} < 0 \end{cases} \quad (3.45)$$

where $d_q \mathcal{F}$ is $d\mathcal{F}/dq$ and $|_i$ means evaluated at q_i . The normalization constant \mathcal{N}_{env} was determined from the condition that $\sum_i \mathcal{P}_{\text{env}}(q_i < |\mathbf{q}| < q_{i+1}) = 1$. The maximum magnitude of momentum Q_{max} was set to be $40 \times T$ and number of lattice points was 300 for calculations shown in this thesis. It must be noted that, since the envelop function \mathcal{P}_{env} is stepwise and constant in each momentum bin, the probability distribution $d\mathcal{P}_{[q_i, q_{i+1}]} / dq$ of the magnitude $q = |\mathbf{q}|$ of momentum inside each bin becomes

$$\frac{d}{dq} \mathcal{P}_{[q_i, q_{i+1}]} = \frac{3q^2}{q_{i+1}^3 - q_i^3} \quad \text{and} \quad \int_{q_i}^{q_{i+1}} dq \cdot \frac{d}{dq} \mathcal{P}_{[q_i, q_{i+1}]} = 1. \quad (3.46)$$

Hence, provided that the momentum bin is determined based on \mathcal{P}_{env} , the magnitude can be sampled according to

$$|\mathbf{q}| = [q_i^3 + (q_{i+1}^3 - q_i^3)\mathcal{X}_q]^{1/3} \quad (3.47)$$

where \mathcal{X}_q is a random variable with uniform distribution between 0 and 1. Orientation of the momentum is determined as

$$\theta_q = \arccos(1 - 2\mathcal{X}_\theta) \quad (3.48)$$

$$\phi_q = 2\pi\mathcal{X}_\phi \quad (3.49)$$

where \mathcal{X}_θ and \mathcal{X}_ϕ are random variables with uniform distribution between 0 and 1. Therefore, the three-momentum \mathbf{q} sampled according to the stepwise envelop function (3.45) is

$$\mathbf{q} = |\mathbf{q}| (\sin \theta_q \cos \phi_q, \sin \theta_q \sin \phi_q, \cos \theta_q) \quad (3.50)$$

Then one has to decide if \mathbf{q} is accepted or not based on the real distribution function (3.34). This can be done by accepting the momentum if the following condition is satisfied

$$\frac{\mathcal{X}_{\text{rej}} \mathcal{P}_{\text{env}}(q_i < |\mathbf{q}| < q_{i+1})}{4\pi \mathcal{N}_{\text{env}}(q_{i+1}^3 - q_i^3)} < \frac{dN}{d^3\mathbf{q}} \Big|_{1\text{-cell}} \quad (3.51)$$

where \mathcal{X}_{rej} is sampled between 0 and 1 according to the uniform distribution function.

3.1.3 Verification of Sampling

By comparing the momentum spectra obtained from the sampling routine with that from the Riemann integration of Cooper-Frye formula, one can demonstrate the validity of the sampling procedure. It must be noted that particles and their momenta are sampled according to

$$\begin{aligned} \frac{dN}{d^3\mathbf{p}} \Big|_{\text{sample}} &= \frac{d}{(2\pi)^3} \int_{\Sigma} \mathcal{P}_{(+)} \left(\frac{p^\mu d^3\Sigma_\mu}{E_{\mathbf{p}}} \right) \\ &\times \mathcal{P}_{(+)} [f_0(x, \mathbf{p}) + \delta f_{\text{shear}}(x, \mathbf{p}) + \delta f_{\text{bulk}}(x, \mathbf{p})] \end{aligned} \quad (3.52)$$

which is different from equation (3.1) due to the presence of

$$\mathcal{P}_{(+)}(x) = \begin{cases} x & \text{if } x > 0 \\ 0 & \text{if } x < 0 \end{cases}. \quad (3.53)$$

Figure 3.2 and 3.3 show the p_T spectra and p_T -differential $v_n\{2\}$ of pions, Kaons, and protons at the point of particlization. The original momentum distribution functions of identified hadrons are well reproduced by the sampling process. It is also shown that the negative contribution to the distribution function is not relevant for $p_T < 2.5$ GeV. The effects of the negative contributions were also discussed in Ref. [90].

It is also notable to address the effect of viscous corrections δf_{shear} and δf_{bulk} to the distribution function. Figures 3.4 and 3.5 show the uncertainties in momentum space distributions of identified hadrons associated with δf . One can see that the effect of δf is less than 10 % in p_T range around $\langle p_T \rangle$ where the particles are most abundant. In addition, the effect of δf_{shear} is negligible while δf_{bulk} makes significant distortions of the p_T spectra and $v_2(p_T)$. The higher harmonics v_3 and v_4 are significantly affected by both of δf_{shear} and δf_{bulk} . Therefore, in addition to the viscous corrections to the energy-momentum tensor, the viscous corrections to the Boltzmann distribution function must be taken into account for the particle spectra at the intermediate and higher p_T .

In the sampling procedure described above, there is no guarantee that a particlized hadron does not re-enter a region with temperature higher than T_{sw} . However, it is possible to estimate how likely this is by looking at the correlation between the radial distance r and velocity u^r . The correlation between r and u^r can be defined as

$$C(r, u^r; \Sigma) = \frac{1}{\sigma_r \sigma_{u^r}} (\langle r u^r \rangle_\Sigma - \langle r \rangle_\Sigma \langle u^r \rangle_\Sigma) \quad (3.54)$$

$$\langle \mathcal{Q} \rangle_\Sigma \equiv \frac{1}{\mathcal{V}_\Sigma} \int_\Sigma \mathcal{Q} u^\mu d\Sigma_\mu \quad \text{where} \quad \mathcal{V}_\Sigma = \int_\Sigma u^\mu d\Sigma_\mu \quad (3.55)$$

$$\sigma_{\mathcal{Q}} \equiv (\langle \mathcal{Q}^2 \rangle_\Sigma - \langle \mathcal{Q} \rangle_\Sigma^2)^{1/2} \quad (3.56)$$

where u^μ is flow velocity and $\langle \mathcal{Q} \rangle_\Sigma$ is volume-weighted average of a quantity \mathcal{Q} over hypersurface Σ . Note that, since the number of particles emerging from a hypersurface element is proportional to $u^\mu d\Sigma_\mu$, $\langle \cdots \rangle_\Sigma$ is also the multiplicity-weighted average. Table 3.1 shows the correlation $C(r, u^r; \Sigma)$ for different collision energies and switching temperatures. The radial distance and velocity are strongly correlated. Therefore, a

	Pb + Pb, 2.76 TeV	Pb + Pb, 2.76 TeV	Au + Au, 200 GeV
	$\eta/s = 0.095$	$\eta/s = 0.095$	$\eta/s = 0.06$
	$T_{\text{sw}} = 145 \text{ MeV}$	$T_{\text{sw}} = 165 \text{ MeV}$	$T_{\text{sw}} = 165 \text{ MeV}$
0 – 5%	0.903	0.929	0.868
10 – 20%	0.874	0.87	0.774
20 – 30%	0.855	0.827	0.69
30 – 40%	0.809	0.743	0.604

Table 3.1: The r - u^r correlation $C(r, u^r; \Sigma)$ on the hypersurfaces.

particle sampled far from the center of collision moves faster away from the fireball and it is unlikely to go to a region with higher temperature, since temperature decreases as distance from the center of fireball increases. This also can be seen at Figures 3.6 and 3.7 which show distributions of volume $u^\mu d\Sigma_\mu$ over proper time τ , radial flow velocity u^r , and viscosities. The distributions over r and u^r indicate that the radial flow velocity is correlated with radial distance in the transverse plane. Comparison between Figures 3.6 and 3.7 also reveals that the fireball lives longer for the higher collision energy. This is due to the higher temperature is reached in more energetic collisions and it takes longer to cool down.

3.1.4 Necessity of Microscopic Transport

The validity of hydrodynamics depends on the microscopic and macroscopic length scales. Provided that the cross sections and number density are known, one can estimate the mean-free-path l_{mfp} which is microscopic

$$l_{\text{mfp},i} \simeq \left[\sum_j \sigma_{(i,j)} n_j \right]^{-1} \quad (3.57)$$

where $\sigma_{(i,j)}$ is the cross section of incoming particles i and j . For a multi-component system, collisions with different species and corresponding number densities must be taken into account. Therefore, one has the summation over all particle species. In the case of heavy ion collisions, the expansion rate $\theta = \nabla_\mu u^\mu$ can be a macroscopic scale.

From the Navier-Stokes relation, it is possible to estimate the Knudsen number as

$$\text{Kn}_i \simeq \left[\sum_j \sigma_{(i,j)} n_j \right]^{-1} \frac{|\Pi|}{\zeta} \quad (3.58)$$

$$= \left[\sum_j \sigma_{(i,j)} n_j \right]^{-1} \left(\frac{T}{\zeta/s} \right) \frac{|\Pi|}{\epsilon + P}. \quad (3.59)$$

One can obtain $\Pi/(\epsilon + P) \simeq 0.015$ based on Figures 3.6 and 3.7. Using the cross section $\sigma_{\pi^+\pi^-} \simeq 40 \text{ mb}$ employed in UrQMD [38], along with the assumption that the number density n_i is given by the thermal distribution, one has $l_{\text{mfp},\pi^-} \simeq 4 \text{ fm}$ for pions at $T_{\text{sw}} = 145 \text{ MeV}$. This mean-free-path is comparable to the inverse of the expansion rate $\theta^{-1} \simeq 3 \text{ fm}$ and the system size $L_{\text{size}} \simeq 8 \text{ fm}$. Therefore one obtains

$$l_{\text{mfp},\pi^-} \sim \theta^{-1} \sim L_{\text{size}} \quad (3.60)$$

which leads to the conclusion that hydrodynamics becomes no longer adequate and it is necessary to switch to the microscopic transport.

Pb + Pb with $\sqrt{s_{\text{NN}}} = 2.76 \text{ TeV}$ (10 – 20%)
 shear+bulk, $\eta/s = 0.095$, and $T_{\text{sw}} = 145 \text{ MeV}$

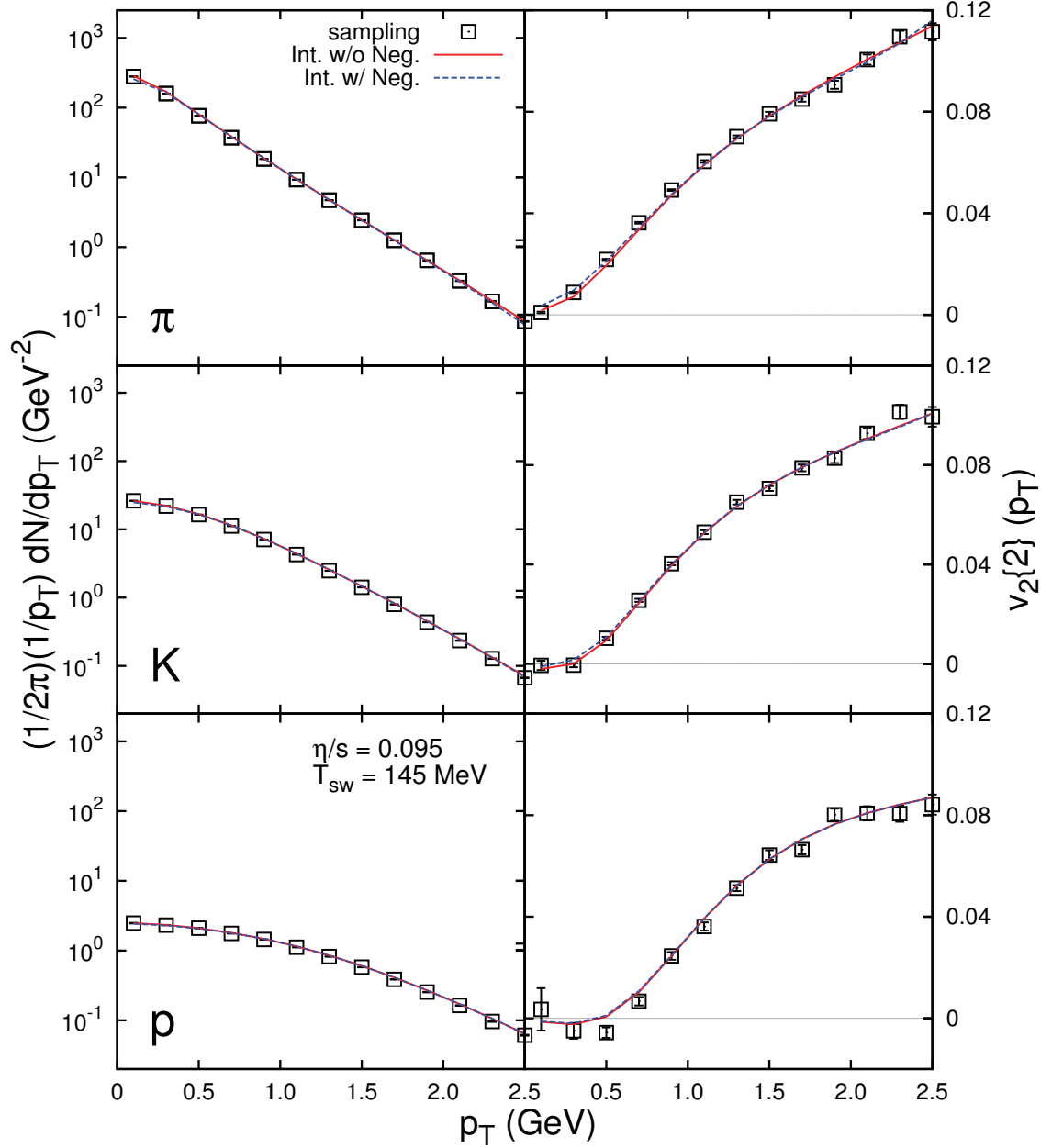


Figure 3.2: p_T spectra and p_T -differential $v_2\{2\}$ of pions, Kaons, and protons from sampling and integration of Cooper-Frye formula. This calculation is performed for a single hydro event for 10-20% centrality of Pb+Pb collision with 2.76 TeV. “Int. w/o Neg.” and “Int. w/ Neg.” correspond to equations (3.52) and (3.1), respectively. 20000 events are sampled to obtain the results shown as “sampling”.

Pb + Pb with $\sqrt{s_{\text{NN}}} = 2.76 \text{ TeV}$ (10 – 20%)
 shear+bulk, $\eta/s = 0.095$, and $T_{\text{sw}} = 145 \text{ MeV}$

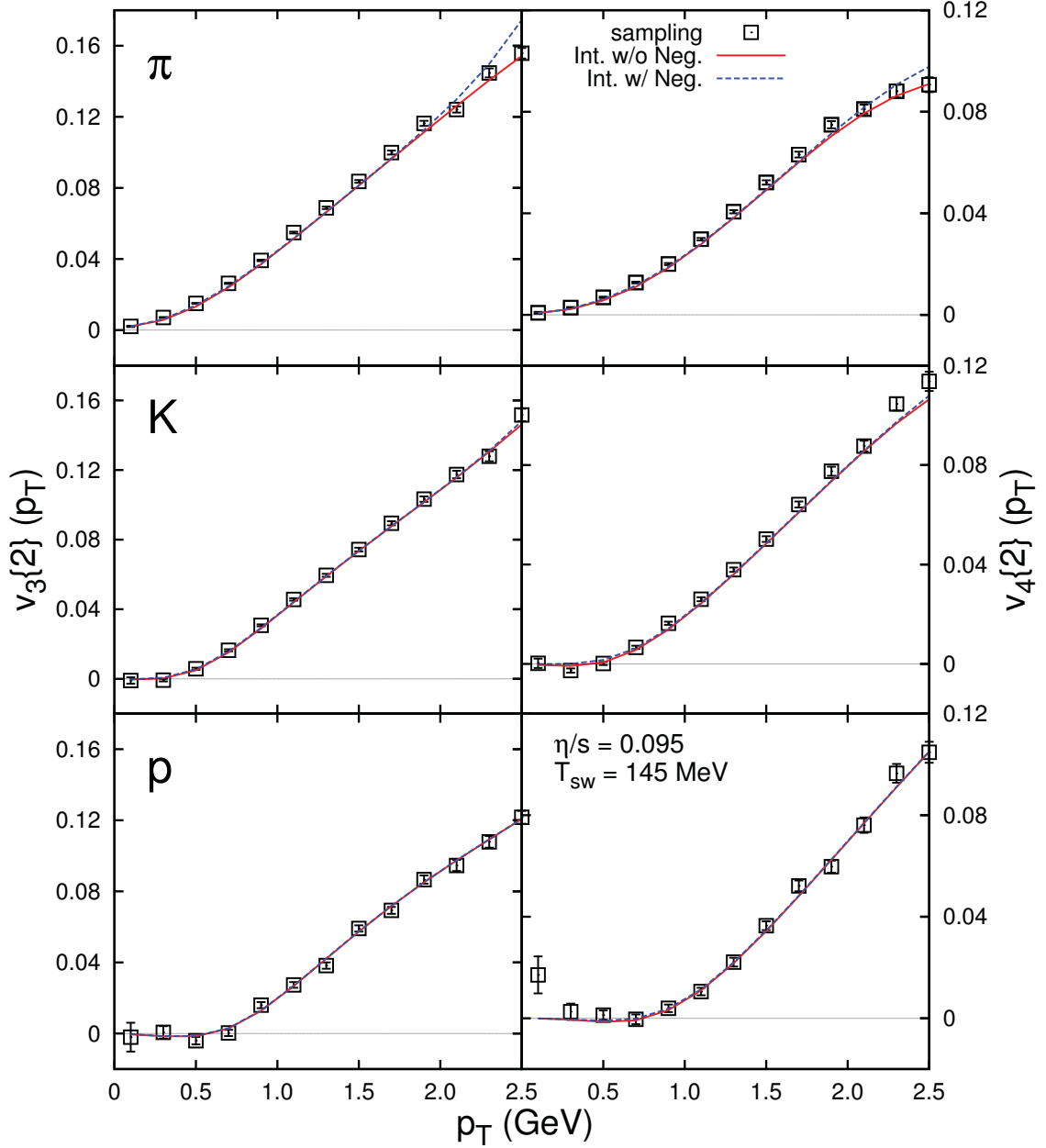


Figure 3.3: p_T -differential $v_3\{2\}$ and $v_4\{2\}$ of pions, Kaons, and protons from sampling and integration of Cooper-Frye formula. This calculation is performed for a single hydro event for 10-20% centrality of Pb+Pb collision with 2.76 TeV. “Int. w/o Neg.” and “Int. w/ Neg.” correspond to equations (3.52) and (3.1), respectively. 20000 events are sampled to obtain the results shown as “sampling”.

Pb + Pb with $\sqrt{s_{\text{NN}}} = 2.76$ TeV (10 – 20%)
 shear+bulk, $\eta/s = 0.095$, and $T_{\text{sw}} = 145$ MeV

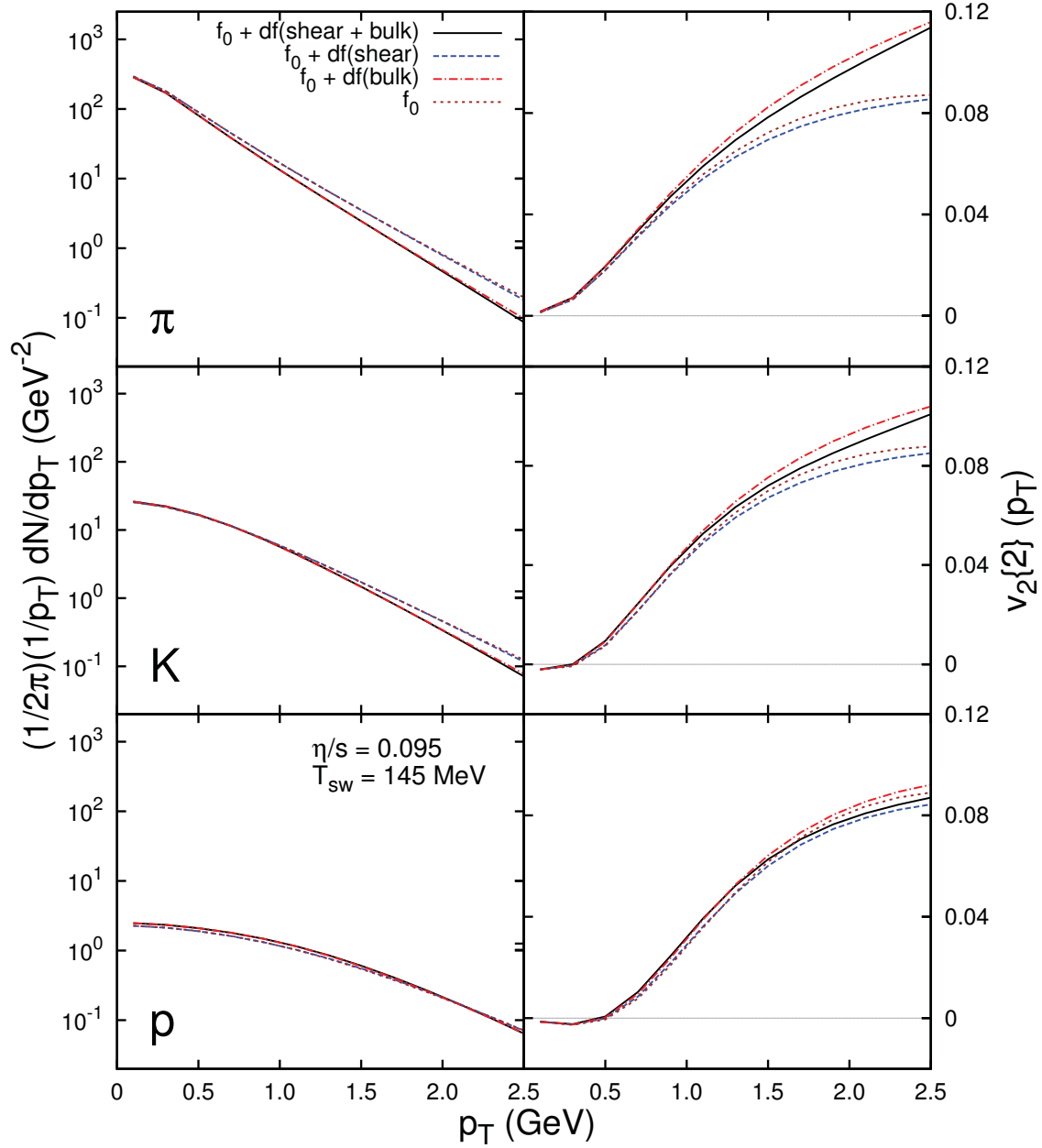


Figure 3.4: p_T spectra and p_T -differential $v_2\{2\}$ of pions, Kaons, and protons from different cases of δf in the Cooper-Frye formula. This calculation is performed for a single hydro event for 10-20% centrality of Pb+Pb collision with 2.76 TeV.

Pb + Pb with $\sqrt{s_{\text{NN}}} = 2.76 \text{ TeV}$ (10 – 20%)
 shear+bulk, $\eta/s = 0.095$, and $T_{\text{sw}} = 145 \text{ MeV}$

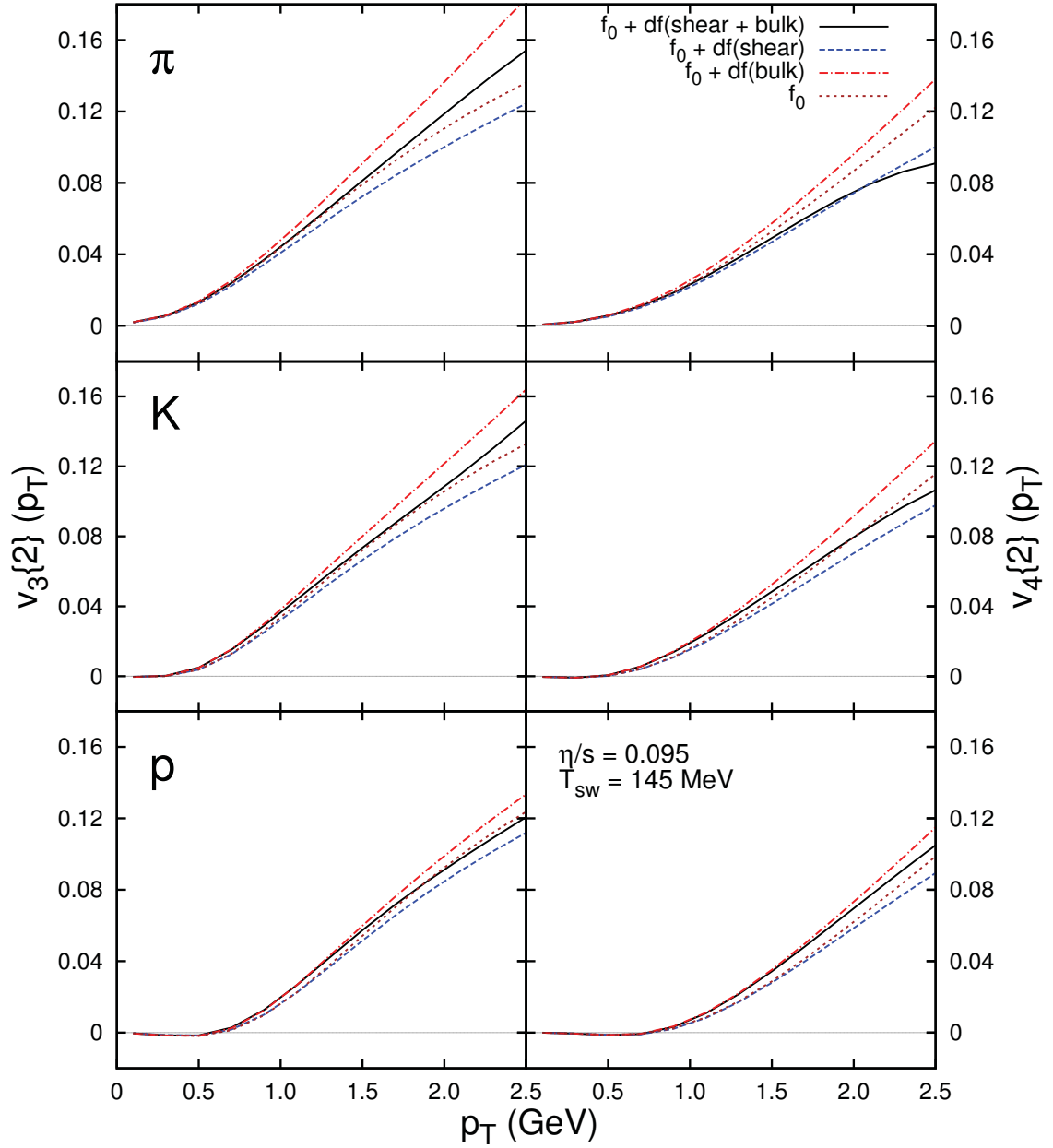


Figure 3.5: p_T -differential $v_3\{2\}$ and $v_4\{2\}$ of pions, Kaons, and protons from different cases of δf in the Cooper-Frye formula. This calculation is performed for a single hydro event for 10-20% centrality of Pb+Pb collision with 2.76 TeV.

Pb + Pb with $\sqrt{s_{\text{NN}}} = 2.76 \text{ TeV}$ (10 – 20%)
 shear+bulk, $\eta/s = 0.095$, and $T_{\text{sw}} = 145 \text{ MeV}$

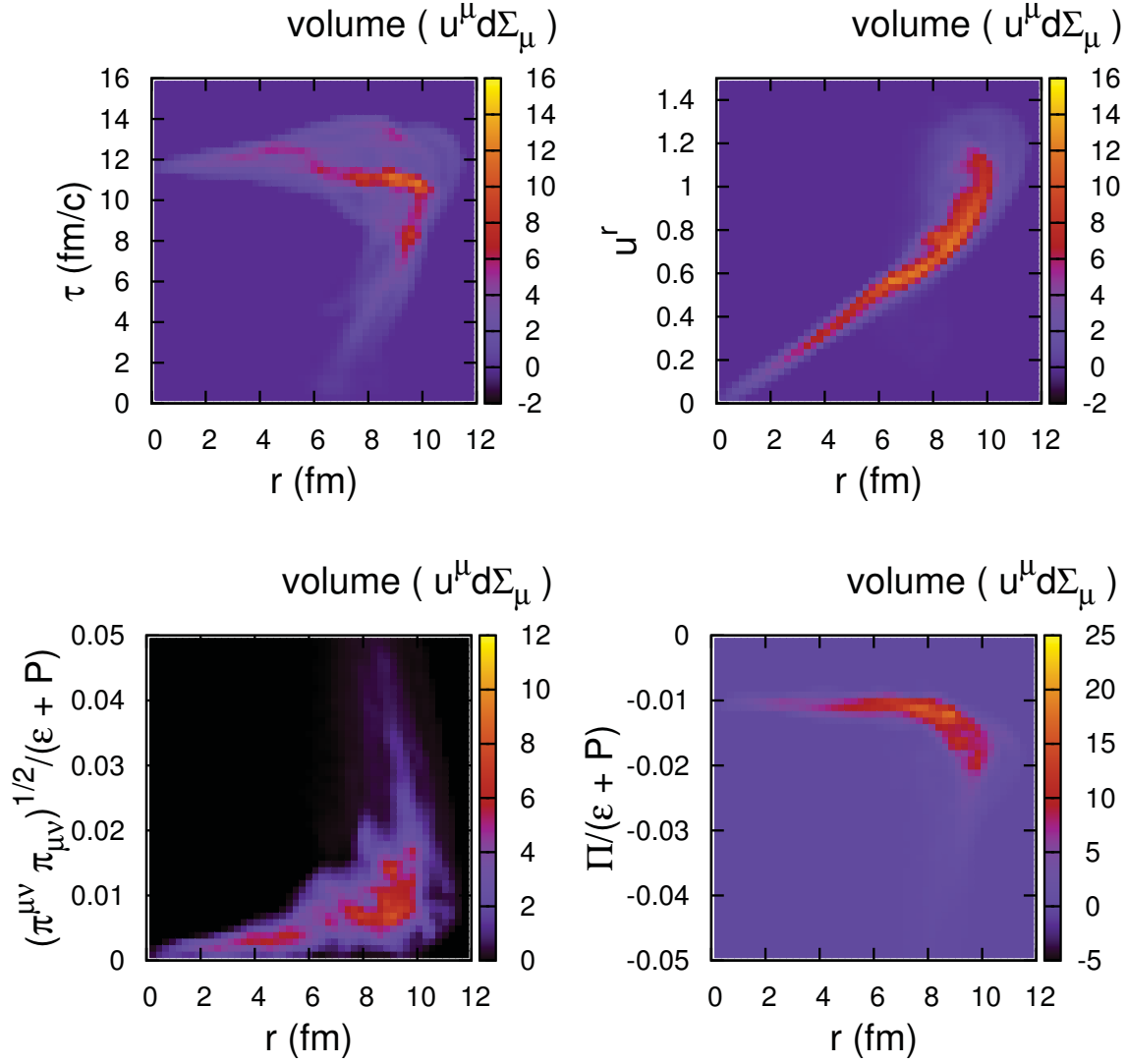


Figure 3.6: Total volume (sum of $u^\mu \Delta \Sigma_\mu$) of surface elements with specific transverse distance and proper time τ (left top), transverse flow speed u_T (right top), shear viscosity (left bottom), and bulk viscosity (right bottom). These are obtained from single event of IP-Glasma and hydrodynamics for 10-20% centrality of Pb+Pb collision with 2.76 TeV. The shear viscosity to entropy density ratio η/s is set to be 0.095 and temperature-dependent bulk viscosity is taken from 2.5. Temperature of the isothermal hypersurface is $T_{\text{sw}} = 145 \text{ MeV}$.

Au + Au with $\sqrt{s_{\text{NN}}} = 200 \text{ GeV}$ (10 – 20%)
 shear+bulk, $\eta/s = 0.06$, and $T_{\text{sw}} = 165 \text{ MeV}$

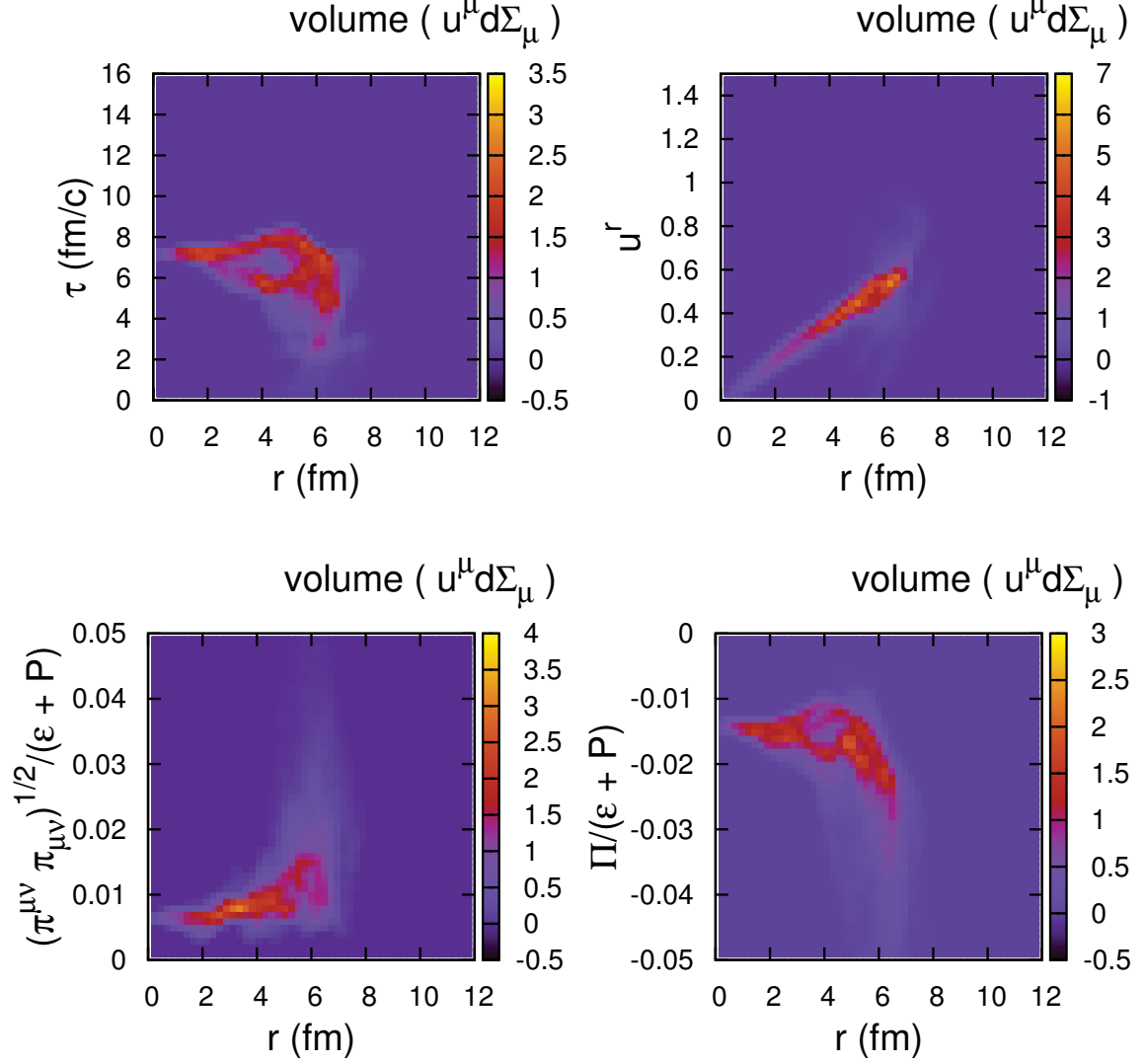


Figure 3.7: Total volume (sum of $u^\mu \Delta \Sigma_\mu$) of surface elements with specific transverse distance and proper time τ (left top), transverse flow speed u_T (right top), shear viscosity (left bottom), and bulk viscosity (right bottom). These are obtained from single event of IP-Glasma and hydrodynamics for 10-20% centrality of Au+Au collision with 200 GeV. The shear viscosity to entropy density ratio η/s is set to be 0.06 and temperature-dependent bulk viscosity is taken from 2.5. Temperature of the isothermal hypersurface is $T_{\text{sw}} = 165 \text{ MeV}$.

3.2 Hadronic Cascade

After particlization, the hadrons now enter the hadronic re-scattering stage. In this study, this part of the heavy ion collisions is described by UrQMD [38, 39] which is microscopic transport for hadrons. This section contains a brief review of Ref. [38]. Baryons and mesons included in UrQMD model are listed in Tables 3.2 and 3.3, respectively. Since the collision term of Boltzmann transport equation involves two-

Nucleon	Delta	Lambda	Sigma	Xi	Omega
N_{938}	Δ_{1232}	Λ_{1116}	Σ_{1192}	Ξ_{1317}	Ω_{1672}
N_{1440}	Δ_{1600}	Λ_{1405}	Σ_{1385}	Ξ_{1530}	
N_{1520}	Δ_{1620}	Λ_{1520}	Σ_{1660}	Ξ_{1690}	
N_{1535}	Δ_{1700}	Λ_{1600}	Σ_{1670}	Ξ_{1820}	
N_{1650}	Δ_{1900}	Λ_{1670}	Σ_{1775}	Ξ_{1950}	
N_{1675}	Δ_{1905}	Λ_{1690}	Σ_{1790}	Ξ_{2025}	
N_{1680}	Δ_{1910}	Λ_{1800}	Σ_{1915}		
N_{1700}	Δ_{1920}	Λ_{1810}	Σ_{1940}		
N_{1710}	Δ_{1930}	Λ_{1820}	Σ_{2030}		
N_{1720}	Δ_{1950}	Λ_{1830}			
N_{1900}		Λ_{1890}			
N_{1990}		Λ_{2100}			
N_{2080}		Λ_{2110}			
N_{2190}					
N_{2200}					
N_{2250}					

Table 3.2: Baryon species included in UrQMD

particle distribution function, which is not necessarily the same as the product of single-particle distribution functions, obtaining the evolution of multi-particle correlations is complicated with the transport equation. Even though the only source of correlation is hydrodynamic flow at the point of particlization, the system develops

J^{PC}	0^{-+}	1^{--}	0^{++}	1^{++}	1^{+-}	2^{++}	$(1^{--})^*$	$(1^{--})^{**}$
	π	ρ	a_0	a_1	b_1	a_2	ρ_{1450}	ρ_{1700}
	K	K^*	K_0^*	K_1^*	K_1	K_2^*	K_{1410}^*	K_{1680}^*
	η	ω	f_0	f_1	h_1	f_2	ω_{1420}	ω_{1662}
	η'	ϕ	f_0^*	f_1'	h_1'	f_2'	ϕ_{1680}	ϕ_{1900}

Table 3.3: Meson species included in UrQMD. The notation J^{PC} for the particle state is explained in [91].

additional *non-flow* correlations during hadronic re-scattering. Therefore, the UrQMD model keeps track of all particles to maintain information on multi-particle correlations. Determination of when and which particles collide is based on the collision criterion with cross sections of several processes. Given that two particles with mo-

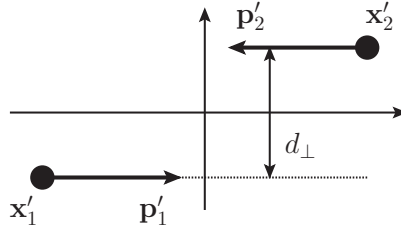


Figure 3.8: Two particles in the center-of-mass frame approaching each other with impact parameter d_{\perp} .

menta \mathbf{p}_1 and \mathbf{p}_2 are on the spatial positions \mathbf{x}_1 and \mathbf{x}_2 , respectively at initial time t_0 in the lab frame, the impact parameter d_{\perp} between two particles in the center-of-mass frame is described in Figure 3.8 and given as

$$d_{\perp}^2 = d^2 - d_{\parallel}^2 \quad (3.61)$$

$$= |\mathbf{x}'_1 - \mathbf{x}'_2|^2 - \frac{[(\mathbf{x}'_1 - \mathbf{x}'_2) \cdot (\mathbf{p}'_1 - \mathbf{p}'_2)]^2}{|\mathbf{p}'_1 - \mathbf{p}'_2|^2} \quad (3.62)$$

Prime denotes that it is evaluated in the center-of-mass frame and \mathbf{x}' and \mathbf{p}' are connected with \mathbf{x} and \mathbf{p} via Lorentz transformation $\Lambda(U_{\text{CM}})$. The four-velocity U_{CM}^{μ} of the center of mass in lab frame is given as

$$U_{\text{CM}}^{\mu} = \frac{p_1^{\mu} + p_2^{\mu}}{\sqrt{(p_1 + p_2)^2}} \quad (3.63)$$

and the Lorentz transformation is given in (3.40). A geometrical interpretation of scattering cross section is used to set a collision criterion

$$d_{\perp}^2 \leq \sqrt{\frac{\sigma_{\text{tot}}}{\pi}} \quad (3.64)$$

where σ_{tot} is the total cross section of incoming particles and depends on the collision energy and types of particles. It is also necessary to determine when the collision occurs which is done by obtaining the time t_{coll} of closest approach in the lab frame according to

$$[\mathbf{x}_1 - \mathbf{x}_2 + (\mathbf{v}_1 - \mathbf{v}_2)(t_{\text{coll}} - t_0)] \cdot (\mathbf{v}_1 - \mathbf{v}_2) = 0 \quad (3.65)$$

where \mathbf{v} is the velocity. In terms of the lab frame energy and momentum, t_{coll} can be written as

$$t_{\text{coll}} - t_0 = -\frac{(\mathbf{x}_1 - \mathbf{x}_2) \cdot (\mathbf{p}_1/E_1 - \mathbf{p}_2/E_2)}{|\mathbf{p}_1/E_1 - \mathbf{p}_2/E_2|^2}. \quad (3.66)$$

Description of the collision processes also requires information on the cross sections. In the **UrQMD** model, the total cross sections of different processes are assumed to have the following forms [38].

- **Nucleon-Nucleon Scatterings**

There are three types of nucleon-nucleon scattering processes — elastic, resonance excitation and string excitation. The total and elastic cross sections are based on the CERN/HERA parametrization of proton-proton and proton-neutron scatterings [92]. The cross sections of resonance excitation processes have the following form

$$\sigma_{(1,2 \rightarrow 3,4),\text{res}}(\sqrt{s}) \sim (2S_3 + 1)(2S_4 + 1) \cdot \frac{1}{s} \frac{\langle p_{3,4} \rangle}{\langle p_{1,2} \rangle} |\mathcal{M}_{\text{res}}(\sqrt{s}, m_3, m_4)|^2 \quad (3.67)$$

where the momentum in the center-of-mass frame $\langle p_{i,j} \rangle$ is expressed as

$$\langle p_{i,j}(\sqrt{s}) \rangle = \int dm' \int dm'' p_{\text{CM}}(\sqrt{s}, m', m'') A_i(m') A_j(m'') \quad (3.68)$$

$$p_{\text{CM}}(\sqrt{s}, m_i, m_j) = \frac{1}{2\sqrt{s}} [(s - (m_i + m_j)^2)(s - (m_i - m_j)^2)]^{1/2} \quad (3.69)$$

and A_i and S_i are the mass distribution and spin of the particle i , respectively. Unstable resonances are taken into account by having Breit-Wigner mass distribution with pole mass m_i and finite width

$$A_i(m) = \mathcal{N}_A \frac{\Gamma(m)}{(m - m_i)^2 + \Gamma^2(m)/4} \quad (3.70)$$

where \mathcal{N}_A is the normalization constant. In the case of a stable particle with vanishing width, one has $A_i(m) = \delta(m - m_i)$. The matrix elements of different resonance excitation processes are listed in Table 3.4. The string excitation

process	matrix element	parameter
$N, N \rightarrow N, \Delta_{1232}$	$ \mathcal{M}_{\text{res}} ^2 = A \frac{m_\Delta^2 \Gamma_\Delta^2}{(s - m_\Delta^2)^2 + m_\Delta^2 \Gamma_\Delta^2}$	$m_\Delta = 1.232 \text{ GeV}$ $\Gamma_\Delta = 0.115 \text{ GeV}$ $A = 40000$
$N, N \rightarrow N, N^*$ $N, N \rightarrow N, \Delta^*$ $N, N \rightarrow N^*, \Delta_{1232}$ $N, N \rightarrow \Delta_{1232}, \Delta^*$	$ \mathcal{M}_{\text{res}} ^2 = A \frac{1}{(m_3 - m_4)^2 (m_3 + m_4)^2}$	$A = \begin{cases} 6.3 \\ 12 \\ 3.5 \\ 3.5 \end{cases}$
$N, N \rightarrow \Delta_{1232}, \Delta_{1232}$	$ \mathcal{M}_{\text{res}} ^2 = A$	$A = 2.8$

Table 3.4: The matrix elements of resonance excitation processes of nucleon-nucleon collisions. The parameters are determined to fit the pp scattering data [96].

process $(N, N) \rightarrow (N, \text{string})$ is also taken into account and its cross section is given as

$$\sigma_{\text{string}} = \sigma_{\text{tot}} - \sigma_{\text{el}} - \sum \sigma_{\text{res}} \quad (3.71)$$

where the summation is over all relevant final states. The string excitation and fragmentation processes in **UrQMD** are described in Appendix 6.6.

• Resonance Decays

The decay process of a resonance is implemented via the mass-dependent decay width. The total decay width $\Gamma_{\text{tot}}(m)$ of a resonance with mass m is the sum

of the partial decay widths with relevant exit channels

$$\Gamma_{\text{tot}}(m) = \sum_{(i,j)} \Gamma_{(i,j)}(m) \quad (3.72)$$

The partial decay width $\Gamma_{R \rightarrow (i,j)}$ for the decay of a resonance with mass m into particles i and j with orbital angular momentum l is

$$\Gamma_{(i,j)}(m) = \Gamma_{R,(i,j)} \frac{m_R}{m} \left(\frac{\langle p_{i,j}(m) \rangle}{\langle p_{i,j}(m_R) \rangle} \right)^{2l+1} \left[\frac{5}{6} + \frac{1}{6} \left(\frac{\langle p_{i,j}(m) \rangle}{\langle p_{i,j}(m_R) \rangle} \right)^{2l} \right]^{-1} \quad (3.73)$$

where m_R and $\Gamma_{R,(i,j)}$ are the pole mass and decay width at the pole, respectively. How long a resonance lasts is determined by a Monte-Carlo sampling of the exponential decay law with the lifetime $\tau_R = 1/\Gamma_R$ and the final state is determined based on the branching ratio.

• Baryon-Antibaryon Processes

The total and elastic proton-antiproton scattering cross sections for the lab frame momentum p_{lab} , which is in the fixed-target experiment, less than 5 GeV are parametrized as

$$\sigma_{(p,\bar{p}),\text{tot}}(\text{mb}) = \begin{cases} 75 + 43.1 p^{-1} + 2.6 p^{-2} - 3.9 p & : 0.3 < p < 5 \\ 271.6 \exp(-1.1 p^2) & : p < 0.3 \end{cases} \quad (3.74)$$

$$\sigma_{(p,\bar{p}),\text{el}}(\text{mb}) = \begin{cases} 31.6 + 18.3 p^{-1} + 1.1 p^{-2} - 3.8 p & : 0.3 < p < 5 \\ 78.6 & : p < 0.3 \end{cases} \quad (3.75)$$

where p is p_{lab} in GeV. In the case of $p\bar{p}$ collisions with $p_{\text{lab}} > 5$ GeV, the cross sections have the following form

$$\sigma_{(p,\bar{p}),\text{tot/el}}(p_{\text{lab}} > 5 \text{ GeV}) = A + B p^n + C \ln^2 p + D \ln p \quad (3.76)$$

The values of parameters are shown in Table 3.5. The $p\bar{p}$ annihilation cross section is parameterized as

$$\sigma_{(p,\bar{p}),\text{ann}}(\sqrt{s}) = \sigma_{\text{ann},0} \frac{s_0}{s} \left[\frac{A^2 s_0}{(s - s_0)^2 + A^2 s_0} + B \right] \quad (3.77)$$

where $\sigma_{\text{ann},0} = 120 \text{ mb}$, $s_0 = 4m_{\text{N}}^2$, $A = 0.05 \text{ GeV}$ and $B = 0.6$ [93]. The neutron-antiproton cross section is assumed to be identical to the proton-antiproton

	A (mb)	B (mb)	n	C (mb)	D (mb)
σ_{tot}	38.4	77.6	-0.64	0.26	-1.2
σ_{el}	10.2	52.7	-1.16	0.125	-1.28

Table 3.5: Parameters for the the total and elastic $p\bar{p}$ cross sections with $p_{\text{lab}} > 5 \text{ GeV}$.

cross section based on the observation that they are very similar [94]. The cross sections of other baryon-antibaryon scatterings are evaluated by scaling $\sigma_{(p,\bar{p})}$ with the ratio of corresponding cross sections in the additive quark model (AQM)

$$\sigma_{(B,\bar{B})} = \frac{\sigma_{BB(\text{AQM})}}{\sigma_{NN(\text{AQM})}} \cdot \sigma_{(p,\bar{p})} \quad (3.78)$$

In UrQMD, the baryon-antibaryon annihilation is implemented by annihilating a single quark-antiquark pair and rearranging the remaining constituents to form two mesonic strings. Therefore, one has $(B, \bar{B}) \rightarrow (\text{string}, \text{string})$. All other processes are called diffractive and the cross section is

$$\sigma_{\text{diff}} = \sigma_{\text{tot}} - \sigma_{\text{el}} - \sigma_{\text{ann}}. \quad (3.79)$$

The diffractive scattering leads to excitation of resonances or strings.

• Additive Quark Model

Due to the fact that experimental data are not available for some processes involved in UrQMD, one has to extrapolate from the processes with data. In the UrQMD model, this is done with the additive quark model (AQM) [95]. In the AQM, cross section of any hadronic collision is given as

$$\sigma_{hh(\text{AQM}),\text{tot}} = \sigma_{NN,\text{tot}} \left(\frac{n_1}{3} \right) \left(\frac{n_2}{3} \right) \left(1 - 0.4 \frac{n_{s,1}}{n_1} \right) \left(1 - 0.4 \frac{n_{s,2}}{n_2} \right) \quad (3.80)$$

$$\sigma_{hh(\text{AQM}),\text{el}} = \sigma_{NN,\text{el}} \left(\frac{\sigma_{hh(\text{AQM}),\text{tot}}}{\sigma_{NN,\text{tot}}} \right)^{2/3} \quad (3.81)$$

where n_i is the number of quark and antiquark constituents and $n_{s,i}$ is the number of strange quarks and antiquarks.

- **Detailed Balance**

The detailed balance, which is based on the time-reversal symmetry, is employed in UrQMD to simulate processes where experimental data are not available. It states that the matrix element of certain process is the same as the reverse process

$$|\mathcal{M}_{(3,4) \rightarrow (1,2)}|^2 = |\mathcal{M}_{(1,2) \rightarrow (3,4)}|^2 \quad (3.82)$$

In UrQMD, the detailed balance is applied for the resonant meson-meson, meson-baryon scatterings and resonance-nucleon/resonance-resonance scatterings such as $(\Delta_{1232}, \Delta_{1232}) \rightarrow (N, N)$ process. When one computes the cross section of the reverse process, the kinematics and degeneracies must be taken into account

$$\begin{aligned} \frac{d\sigma}{d\Omega} \Big|_{(3,4) \rightarrow (1,2)} &= \frac{\langle p_{1,2}^2 \rangle (2S_1 + 1)(2S_2 + 1)}{\langle p_{3,4}^2 \rangle (2S_3 + 1)(2S_4 + 1)} \\ &\times \sum_{J=J_-}^{J_+} \langle j_1, m_1, j_2, m_2 || J, M \rangle \frac{d\sigma}{d\Omega} \Big|_{(1,2) \rightarrow (3,4)} \end{aligned} \quad (3.83)$$

$$\langle p_{i,j}^2(\sqrt{s}) \rangle = \int dm' \int dm'' p_{\text{CM}}^2(\sqrt{s}, m', m'') A_i(m') A_j(m'') \quad (3.84)$$

where p_{CM} and A_i are defined in the equations (3.69) and (3.70), respectively. In addition, $|j, m\rangle$ denotes the eigenstate of isospin and its third component with the eigenvalues j and m , respectively. The summation limits of the Clebsch-Gordan coefficients are

$$J_- = \max(|j_1 - j_2|, |j_3 - j_4|) \quad (3.85)$$

$$J_+ = \min(j_1 + j_2, j_3 + j_4). \quad (3.86)$$

- **Meson-Baryon and Meson-Meson Scatterings**

The low-energy meson-baryon and meson-meson interactions are dominated by the resonance scatterings, where incoming particles excite a resonance as an intermediate state. The cross section of resonance scattering is

$$\begin{aligned} \sigma_{(1,2),\text{res}} &= \sum_R \langle j_1, m_1, j_2, m_2 || J_R, M_R \rangle \\ &\times \frac{2S_R + 1}{(2S_1 + 1)(2S_2 + 1)} \frac{\pi}{p_{\text{CM}}^2} \frac{\Gamma_{R \rightarrow (1,2)} \Gamma_{R,\text{tot}}}{(\sqrt{s} - M_R)^2 + \Gamma_{R,\text{tot}}^2/4} \end{aligned} \quad (3.87)$$

where the summation goes over all resonances that can decay into the incoming particles 1 and 2. The cross section with particular exit channel with particles 3 and 4, $\sigma_{(1,2 \rightarrow 3,4),\text{res}}$ can be obtained by replacing $\Gamma_{R,\text{tot}}$ with $\Gamma_{R \rightarrow (3,4)}$ and the summation is over all resonances that can decay into 3 and 4 as well. In addition, for the meson-meson scattering, a constant elastic cross section $\sigma_{(M,M),\text{el}} = 5 \text{ mb}$ is added to fit the data [96].

For the angular distribution of outgoing particles, the elastic NN cross section from the collision term of relativistic Boltzmann-Uehling-Uhlenbeck (RBUU) equation [97] is used in **UrQMD**. The angular dependence in the center-of-mass frame comes from the t and u channels.

3.3 Jet Energy Loss

For an integrated description of heavy ion collisions, one needs to have the high- p_T particles resulting from jets, as well as the low- p_T bulk dynamics of the medium. It must be also noted that, due to the jet-medium interactions, the high- p_T spectra are not same as the superposition of nucleon-nucleon binary collisions. In this section, production of the high- p_T partons, their energy loss due to the radiative and collisional processes, and the Monte-Carlo implementation in MARTINI [98] are briefly described.

3.3.1 AMY Formalism for Radiative Energy Loss

If an incident particle emits a photon or gluon as a consequence of scattering with particles in the medium, the formation time τ_{form} is determined by how much the intermediate state deviates from the on-shell state. In the case of a thermal medium with strong coupling constant g , one has $\tau_{\text{form}} \sim (g^2 T)^{-1}$ and this is on the order of the mean-free-time of the incident particle. Therefore, contributions to the transition rate from multiple scatterings are not independent of each other, a phenomenon known as the LPM effect [99]. In the AMY formalism [35, 36], infinite number of diagrams which contribute to the current-current correlator are summed by solving an integral equation. The rate of radiative energy loss is given as [100, 101]

$$\begin{aligned} \frac{d\Gamma_{\text{rad}}}{dk}(p, k) &= \frac{C_s g^2}{16\pi p^7} \cdot \frac{e^{k/T}}{e^{k/T} \pm 1} \cdot \frac{e^{(p-k)/T}}{e^{(p-k)/T} \pm 1} \\ &\times \left\{ \begin{array}{ll} \frac{1+(1-x)^2}{x^3(1-x)^2} & \text{if } q \rightarrow qg \\ N_f \frac{x^2+(1-x)^2}{x^2(1-x)^2} & \text{if } g \rightarrow q\bar{q} \\ \frac{1+x^4+(1-x)^4}{x^3(1-x)^3} & \text{if } g \rightarrow gg \end{array} \right\} \cdot \int \frac{d^2\mathbf{h}}{(2\pi)^2} 2\mathbf{h} \cdot \text{Re } \mathbf{F}(\mathbf{h}, p, k) \quad (3.88) \end{aligned}$$

where p is the initial energy of the jet parton and k is amount of the energy loss. The momentum fraction x of the radiated particle is given as $x = k/p$. The quadratic Casimir is $C_s = C_F = 4/3$ for quark/antiquark and $C_s = C_A = 3$ for gluon. $\mathbf{F}(\mathbf{h}, p, k)$ in the integrand of equation (3.88) is obtained by solving the following integral equation

$$2\mathbf{h} = i \delta E(\mathbf{h}, p, k) \mathbf{F}(\mathbf{h}, p, k) + g^2 \int \frac{d^2\mathbf{q}_\perp}{(2\pi)^2} \frac{m_D^2}{q_\perp^2 (q_\perp^2 + m_D^2)}$$

$$\begin{aligned} & \times \{ (C_s - C_A/2) [\mathbf{F}(\mathbf{h}) - \mathbf{F}(\mathbf{h} - k \mathbf{q}_\perp)] + (C_A/2) [\mathbf{F}(\mathbf{h}) - \mathbf{F}(\mathbf{h} + p \mathbf{q}_\perp)] \\ & + (C_A/2) [\mathbf{F}(\mathbf{h}) - \mathbf{F}(\mathbf{h} - (p - k) \mathbf{q}_\perp)] \} \end{aligned} \quad (3.89)$$

$$m_D^2 = \frac{1}{6} (2N_c + N_f) g^2 T^2 \quad (3.90)$$

$$\delta E(\mathbf{h}, p, k) = \frac{|\mathbf{h}|^2}{2pk(p-k)} + \frac{m_k^2}{2k} + \frac{m_{p-k}^2}{2(p-k)} - \frac{m_p^2}{2p} \quad (3.91)$$

where m_p , m_{p-k} , and m_k denote the medium induced thermal masses of the initial state parton, final state parton, and radiated one, respectively. Explicitly,

$$m^2 = \begin{cases} \frac{g^2 T^2}{12} (2N_c + N_f) & \text{for gluon} \\ \frac{g^2 T^2}{3} & \text{for quark/antiquark} \end{cases} \quad (3.92)$$

3.3.2 Collisional Energy Loss

The jet parton can lose energy by $2 \rightarrow 2$ scattering processes with other partons belonging to the medium. The rate of collisional energy loss with amount ω is computed in [37] from

$$\begin{aligned} \frac{d\Gamma_{\text{coll}}}{d\omega}(E_{\mathbf{p}}, \omega) &= \frac{2\pi d_k}{2E_{\mathbf{p}} \cdot 2E_{\mathbf{p}'}} \int \frac{d^3 \mathbf{k}}{(2\pi)^3 2E_{\mathbf{k}}} \int \frac{d^3 \mathbf{k}'}{(2\pi)^3 2E_{\mathbf{k}'}} \\ &\quad \times \delta(E_{\mathbf{p}} - E_{\mathbf{p}'} - \omega) \delta(E_{\mathbf{k}'} - E_{\mathbf{k}} - \omega) \\ &\quad \times |\mathcal{M}(p, k \rightarrow p', k')|^2 f(k, T) (1 \pm f(k', T)) \end{aligned} \quad (3.93)$$

where $E_{\mathbf{p}} = |\mathbf{p}|$ for a massless parton and d_k is the degeneracy factor. The transition amplitude $|\mathcal{M}(p, k \rightarrow p', k')|^2$ is obtained by mean of effective thermal propagator [102]. In addition, it was also shown in [37] that the separation between hard ($|\mathbf{p} - \mathbf{p}'| \sim \sqrt{E_{\mathbf{p}} T}$) and soft ($|\mathbf{p} - \mathbf{p}'| \sim gT$) scales does not make relevant difference.

3.3.3 Monte-Carlo Implementation of Energy Loss

The Monte-Carlo simulation of jet energy loss is done with **MARTINI** [98]. The initial production of jet partons can be handled with perturbative QCD due to large momentum transfer. Once the collision geometry, in terms of the locations of binary collisions, is specified, the probability P_{jet} of having a hard collision at each binary

collision is given as

$$P_{\text{jet}}(\hat{p}_{T,\text{min}}) = \frac{\sigma_{(N,N),\text{jet}}(\hat{p}_{T,\text{min}})}{\sigma_{(N,N),\text{inel}}} \quad (3.94)$$

$$\sigma_{(N,N),\text{jet}}(\hat{p}_{T,\text{min}}) = \sum_{i,j} \int_0^1 dx_1 f_i(x_1) \int_0^1 dx_2 f_j(x_2) \sigma_{(i,j)}(x_1, x_2; \hat{p}_{T,\text{min}}) \quad (3.95)$$

where $\sigma_{(N,N),\text{inel}}$ is the total inelastic cross section of nucleon-nucleon interaction. The summations are over partonic species and f_i is the parton distribution function of i in a nucleon. $\sigma_{(i,j)}(x_1, x_2; \hat{p}_{T,\text{min}})$ is the cross section of $2 \rightarrow 2$ partonic process of i and j with the light-cone momentum fractions x_1 and x_2 , respectively. The scattered partons are considered to acquire the transverse momenta larger than $\hat{p}_{T,\text{min}}$.

If a hard process is determined to happen, the jet partons are generated by PYTHIA 8.1 [103, 104] in conjunction with LHAPDF [105]. In this work, CTEQ5L parton distribution function [106] were used and the nuclear shadowing effects were taken into account the EKS98 parametrization [107]. The probability that a jet parton experiences the energy loss in each time step is given as $P = \Gamma \Delta t$. Then the functional form of $d\Gamma/d\omega$ is used to determine the amount of energy lost in the medium. Once the jet parton gets out of QGP phase, it is assumed to fragment into hadrons. This is done by making color-neutral strings out of the jet partons and sampled thermal partons and fragmenting them with PYTHIA.

Observables and Results

The hybrid approach shown in the previous chapter allows one to study the hot QCD matter by comparing with experimental measurements. In this work, the switching temperature T_{sw} and the shear viscosity η are considered as the parameters to be determined from the experimental data. The thermalization time τ_0 , the bulk viscosity ζ and the strong coupling α_S of the energy loss are fixed throughout this work. In Section 4.1, observables measured in heavy ion collisions are defined in terms of final state information. The hybrid model simulations were performed for comparison with the Au+Au collisions with $\sqrt{s_{NN}} = 200 \text{ GeV}$ at RHIC and Pb+Pb collisions with $\sqrt{s_{NN}} = 2.76 \text{ TeV}$ at the LHC. Sections 4.2 and 4.3 show the global and p_T -differential observables, respectively. It is demonstrated that bulk viscosity is crucial in comprehensively describing both of p_T spectra and azimuthal anisotropy. It is also shown that the hadronic re-scattering, or *afterburner*, in the late stage of collision is necessary in getting baryonic observables. The results of high- p_T jets are shown in Section 4.4 focusing on the energy loss due to the hadronic re-scattering.

4.1 Definitions of Observables

One of the most important observables is the momentum-space distribution of identified or charged hadrons. It can be decomposed as

$$E_{\mathbf{p}} \frac{dN}{d^3\mathbf{p}} = \frac{1}{2\pi p_T} \frac{dN}{dp_T dy} \left[1 + 2 \sum_{n=1}^{\infty} v_n(p_T) \cos[n(\phi_p - \Phi_n)] \right] \quad (4.1)$$

where y and Φ_n are the rapidity and reference angle, respectively. This work is focused on the mid-rapidity observables around $y = 0$ and hydrodynamic evolution was performed in 2 + 1D spacetime assuming boost invariance. The coefficients v_n 's measure how efficiently the coordinate space anisotropy is translated into the momentum space anisotropy by the system evolution. The anisotropic energy density profile results in the anisotropic pressure gradient as shown in Figure 4.1. The p_T spectra of identified

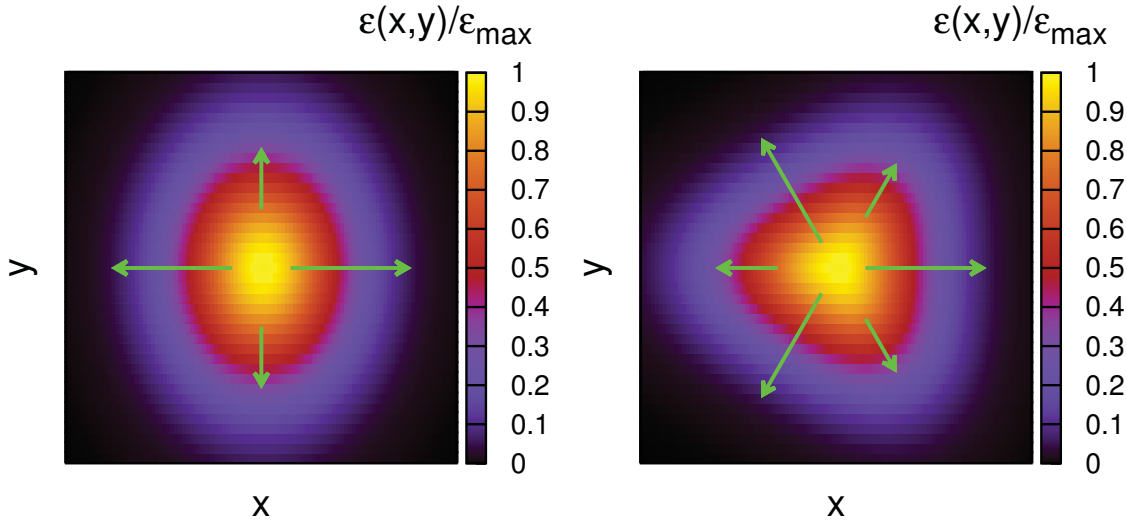


Figure 4.1: The anisotropic energy density profiles with ellipticity (left) and triangularity (right) lead to the elliptic flow v_2 and triangular flow v_3 , respectively.

hadrons are determined by counting the number of particles inside corresponding p_T bin

$$\left. \frac{1}{2\pi p_T} \frac{dN}{dp_T} \right|_{|y| < 0.5} (p_i < p_T < p_{i+1}) = \frac{N(|y| < 0.5; p_i < p_T < p_{i+1})}{\pi(p_{i+1}^2 - p_i^2)} \quad (4.2)$$

There are two global observables, mid-rapidity multiplicity and mean p_T , commonly measured in experiments. They are defined as

$$\begin{aligned} \int_{-0.5}^{0.5} dy \frac{dN}{dy} &= \int dp_T \frac{dN}{dp_T dy} \Big|_{|y| < 0.5} \\ &= N(|y| < 0.5) \end{aligned} \quad (4.3)$$

$$\begin{aligned} \langle p_T \rangle &= \left(\int_{-0.5}^{0.5} dy \frac{dN}{dy} \right)^{-1} \int_{-0.5}^{0.5} dy \int dp_T p_T \frac{dN}{dp_T dy} \\ &= \frac{1}{N(|y| < 0.5)} \sum_{j=1}^{N(|y| < 0.5)} p_{T,j} \end{aligned} \quad (4.4)$$

where $p_{T,j}$ is the magnitude of the transverse momentum of the j -th particle. It can be seen that the mean p_T quantifies how fast the particles are moving outward. While the p_T spectra and associated global observables involve information on the radial expansion, dependence on the azimuthal direction is encoded in Fourier coefficients v_n of the momentum-space distribution. From equation (4.1), one gets for particles satisfying $|y| < 0.5$ and $p_T \in [p_{\min}, p_{\max}]$

$$N \cos(n\Phi_n) = \int_{p_{\min}}^{p_{\max}} dp_T \int d\phi_p \frac{dN}{dp_T d\phi_p} \Big|_{|y| < 0.5} \cos(n\phi_p) \quad (4.5)$$

$$N v_n = \int_{p_{\min}}^{p_{\max}} dp_T \int d\phi_p \frac{dN}{dp_T d\phi_p} \Big|_{|y| < 0.5} \cos[n(\phi_p - \Phi_n)] \quad (4.6)$$

Measurement or calculation of v_n is more complicated compared to the p_T spectra since there is fluctuation of the multiplicity N , reference angle Φ_n and flow coefficient v_n . One conventional method is called event plane method which estimates Φ_n from the event plane angle Ψ_n . The *reference flow particles* (RFP) are defined as a set of particles used to determine the event plane angle. In many heavy ion experiments, the reference flow particles are set to be charged hadrons within a specific kinematic range which incorporates a large number of particles. The event plane angle can be written in terms of flow vectors Q_n

$$Q_n = \sum_{j=1}^N e^{in\phi_j} \quad (4.7)$$

$$= |Q_n| e^{in\Psi_n} \quad (4.8)$$

where ϕ_j is azimuthal angle of the j -th particle and the summation is over the reference flow particles. The flow vector has the following limiting cases

$$Q_n \rightarrow \begin{cases} N v_n e^{in\Phi_n} & \text{if } N \rightarrow \infty \\ e^{in\Psi_n} & \text{if } N \rightarrow 1 \end{cases} \quad (4.9)$$

It must be also noted that, in general, Ψ_n deviates from Φ_n due to statistical fluctuation. For a set of events with the same v_n , one has

$$\left\langle \frac{1}{N_A} Q_{n,A} \frac{Q_{n,B}^*}{|Q_{n,B}|} \right\rangle_{|v_n} = \left\langle \frac{1}{N_A} Q_{n,A} e^{-in\Phi_n} \right\rangle_{|v_n} \left\langle \frac{Q_{n,B}^*}{|Q_{n,B}|} e^{in\Phi_n} \right\rangle_{|v_n} \quad (4.10)$$

$$\rightarrow \begin{cases} v_n & \text{if } N \rightarrow \infty \\ v_n^2 & \text{if } N \rightarrow 1 \end{cases} \quad (4.11)$$

where A and B stand for rapidity (or pseudo-rapidity) windows separated by a finite gap. This separation allows one to assume that the statistical fluctuations of $Q_{n,A}$ and $Q_{n,B}$ are independent. The limiting cases in equation (4.11) can be obtained using $\langle e^{in\Psi_n} \rangle_{|v_n} = v_n e^{in\Phi_n}$. The flow coefficient $v_n^{\{\text{EP}\}}$ of the *particles of interest* (POI) from the event-plane method is defined as

$$v_n^{\{\text{EP}\}} = \frac{1}{R_{\text{EP}}} \left\langle \frac{1}{N'_A} Q'_{n,A} \frac{Q_{n,B}^*}{|Q_{n,B}|} \right\rangle \quad (4.12)$$

$$R_{\text{EP}}^2 = \left\langle \frac{Q_{n,A}}{|Q_{n,A}|} \cdot \frac{Q_{n,B}^*}{|Q_{n,B}|} \right\rangle \quad (4.13)$$

where N' and Q'_n are multiplicity and flow vector of the particles of interest. One can set the POI to be identified hadrons in a specific p_T bin to have the p_T -differential v_n of that species. One has the *integrated flow coefficients* if the particles of interest coincide with the reference flow particles. The event average $\langle \dots \rangle$ is taken over a large number of events with different v_n inside a certain centrality bin

$$\langle \dots \rangle = \int dv_n \frac{dP}{dv_n} \langle \dots \rangle_{|v_n} \quad (4.14)$$

It was shown in [108] that this event-plane method introduces an ambiguity since $v_n^{\{\text{EP}\}}$ yields a value between $\langle v_n \rangle$ and $(\langle v_n^2 \rangle)^{1/2}$ depending on the resolution

$$v_n^{\{\text{EP}\}} \rightarrow \begin{cases} \langle v_n \rangle & \text{if } v_n \sqrt{N} \gg 1 \\ (\langle v_n^2 \rangle)^{1/2} & \text{if } v_n \sqrt{N} < 1 \end{cases} \quad (4.15)$$

which can be obtained by considering the limiting cases of the resolution factor R_{EP}

$$R_{\text{EP}}^2 = \int dv_n \frac{dP}{dv_n} \left\langle \frac{Q_{n,A}}{|Q_{n,A}|} e^{-in\Phi_n} \right\rangle_{|v_n} \left\langle \frac{Q_{n,B}^*}{|Q_{n,B}|} e^{in\Phi_n} \right\rangle_{|v_n} \quad (4.16)$$

$$\rightarrow \begin{cases} 1 & \text{if } N \rightarrow \infty \\ \langle v_n^2 \rangle & \text{if } N \rightarrow 1 \end{cases} \quad (4.17)$$

Therefore, the event-plane method is inadequate for measurements independent of detector acceptance.

One way around this ambiguity is to connect 2-particle correlations and v_n^2 and obtain the event average of v_n^2 weighted by $N(N-1)$ [109, 110]. The 2-particle azimuthal correlation $\langle 2 \rangle$ among the reference flow particles is defined as

$$\begin{aligned} \langle 2 \rangle &\equiv \frac{1}{W_2} \sum_{i,j}^{\wedge} e^{in(\phi_i - \phi_j)} \\ &= \frac{1}{W_2} (|Q_n|^2 - N) \\ W_2 &= N(N-1) \end{aligned} \quad (4.18)$$

where \sum^{\wedge} is summation over $i \neq j$. The reference flow particles are commonly chosen to be charged hadrons within certain pseudorapidity and transverse momentum windows. These correlations of many events are averaged with weight W_2 as

$$\langle \langle 2 \rangle \rangle = \frac{\sum_{i=1}^{N_{\text{ev}}} W_{2,i} \langle 2 \rangle_i}{\sum_{i=1}^{N_{\text{ev}}} W_{2,i}} \quad (4.19)$$

where the subscript i denotes “evaluated for the i -th event”. Then, the second order cumulant $c_n\{2\}$ and 2-particle cumulant $v_n\{2\}$ are given as

$$c_n\{2\} = \langle \langle 2 \rangle \rangle \quad (4.20)$$

$$v_n\{2\} = (c_n\{2\})^{1/2} \quad (4.21)$$

The 2-particle cumulant differential flows $v_n'\{2\}$ can be computed based on correlations between particles of interest and reference flow particles

$$\langle 2' \rangle = \frac{1}{w_2} \sum_{i \in \text{POI}, j \in \text{RFP}}^{\wedge} e^{in(\phi_i - \phi_j)} \quad (4.22)$$

$$= \frac{1}{w_2} (p_n Q_n^* - q_n) \quad (4.23)$$

$$w_2 = n_p N - n_q$$

where n_p and p_n are the number and flow vector of particles of interest, respectively. and n_q and q_n are the number and flow vector of particles of interest which are also reference flow particles. The particles of interest are identified hadrons within specific p_T bin in the case of p_T differential v_n of identified hadrons. The event average $\langle\langle 2' \rangle\rangle$ can be obtained as

$$\langle\langle 2' \rangle\rangle = \frac{\sum_{i=1}^{N_{\text{ev}}} w_{2,i} \langle 2' \rangle_i}{\sum_{i=1}^{N_{\text{ev}}} w_{2,i}} \quad (4.24)$$

and 2-particle cumulant and differential flow become

$$d_n\{2\} = \langle\langle 2' \rangle\rangle \quad (4.25)$$

$$v'_n\{2\} = \frac{d_n\{2\}}{(c_n\{2\})^{1/2}} \quad (4.26)$$

It is also possible to obtain anisotropic flow coefficients from 4-particle correlations. This 4-particle cumulant method begins with computation of azimuthal correlations $\langle 4 \rangle$ of reference flow particles

$$\begin{aligned} \langle 4 \rangle &\equiv \frac{1}{W_4} \sum_{i,j,k,l}^{\hat{}} e^{in(\phi_i + \phi_j - \phi_k - \phi_l)} \\ &= \frac{1}{W_4} [|Q_n|^4 + |Q_{2n}|^2 - 2 \text{Re}(Q_{2n} Q_n^* Q_n^*) - 4(N-2)|Q_n|^2 + 2N(N-3)] \quad (4.27) \\ W_4 &= N(N-1)(N-2)(N-3) \end{aligned}$$

The event average $\langle\langle 4 \rangle\rangle$ is given as

$$\langle\langle 4 \rangle\rangle = \frac{\sum_{i=1}^{N_{\text{ev}}} W_{4,i} \langle 4 \rangle_i}{\sum_{i=1}^{N_{\text{ev}}} W_{4,i}} \quad (4.28)$$

and the 4-particle cumulant $c_n\{4\}$ and integrated flow coefficient $v_n\{4\}$ are

$$c_n\{4\} = \langle\langle 4 \rangle\rangle - 2\langle\langle 2 \rangle\rangle^2 \quad (4.29)$$

$$v_n\{4\} = (-c_n\{4\})^{1/4} \quad (4.30)$$

The differential 4-particle cumulant $v'_n\{4\}$ for an arbitrary set of particles is obtained from the correlations among one particle of interest and three reference flow particles

$$\langle 4' \rangle = \frac{1}{W_4} \sum_{i \in \text{POI}, j,k,l \in \text{RFP}}^{\hat{}} e^{in(\phi_i + \phi_j - \phi_k - \phi_l)} \quad (4.31)$$

$$\begin{aligned}
&= \frac{1}{w_4} (p_n Q_n^* |Q_n|^2 - q_{2n} Q_n^* Q_n^* - p_n Q_n Q_{2n}^* - 2N p_n Q_n^* - 2n_q |Q_n|^2) \\
&\quad + \frac{1}{w_4} (7q_n Q_n^* - Q_n q_n^* + q_{2n} Q_{2n}^* + 2p_n Q_n^* + 2n_q N - 6n_q)
\end{aligned} \tag{4.32}$$

$$\begin{aligned}
w_4 &= (n_p N - 3n_q)(N - 1)(N - 2) \\
\langle\langle 4' \rangle\rangle &= \frac{\sum_{i=1}^{N_{\text{ev}}} w_{4,i} \langle 4' \rangle_i}{\sum_{i=1}^{N_{\text{ev}}} w_{4,i}}
\end{aligned} \tag{4.33}$$

The differential 4-particle cumulant $d_n\{4\}$ and flow coefficient $v'_n\{4\}$ are

$$d_n\{4\} = \langle\langle 4' \rangle\rangle - 2\langle\langle 2' \rangle\rangle\langle\langle 2 \rangle\rangle \tag{4.34}$$

$$v'_n\{4\} = -\frac{d_n\{4\}}{(-c_n\{4\})^{3/4}} \tag{4.35}$$

In this work, $v_n\{2\}$ and $v_n\{4\}$ of charged or identified hadrons were computed and compared with the experimental data. The event-by-event fluctuation of v_n in the model is crucial for the comprehensive descriptions of $v_n\{2\}$ and $v_n\{4\}$. Note that, in the limit of infinite number of particles, one gets

$$v_n\{2\} \rightarrow \langle v_n^2 \rangle^{1/2} = [\langle v_n \rangle^2 + (\langle v_n^2 \rangle - \langle v_n \rangle^2)]^{1/2} \tag{4.36}$$

$$v_n\{4\} \rightarrow [2\langle v_n^2 \rangle^2 - \langle v_n^4 \rangle]^{1/4} = [\langle v_n^2 \rangle^2 - (\langle v_n^4 \rangle - \langle v_n^2 \rangle^2)]^{1/4} \tag{4.37}$$

if the multiplicity fluctuation is neglected. Therefore, it can be seen that $v_n\{2\}$ and $v_n\{4\}$ depend on the fluctuations of v_n and v_n^2 differently.

4.2 Global Observables

The integrated $v_n\{2\}$ and $v_2\{4\}$ of charged hadrons were used for determination of the shear viscosity to entropy density ratio η/s . Figure 4.2 shows $v_2\{2\}$, $v_2\{4\}$, $v_3\{2\}$ and $v_4\{2\}$ as functions of centrality in the case of vanishing bulk viscosity. η/s is chosen to be 0.16 to fit the ALICE data [1]. It is also shown that dependence of integrated flows on the switching temperature is small. The 0 – 5%, 10 – 20%, 20 – 30%, and

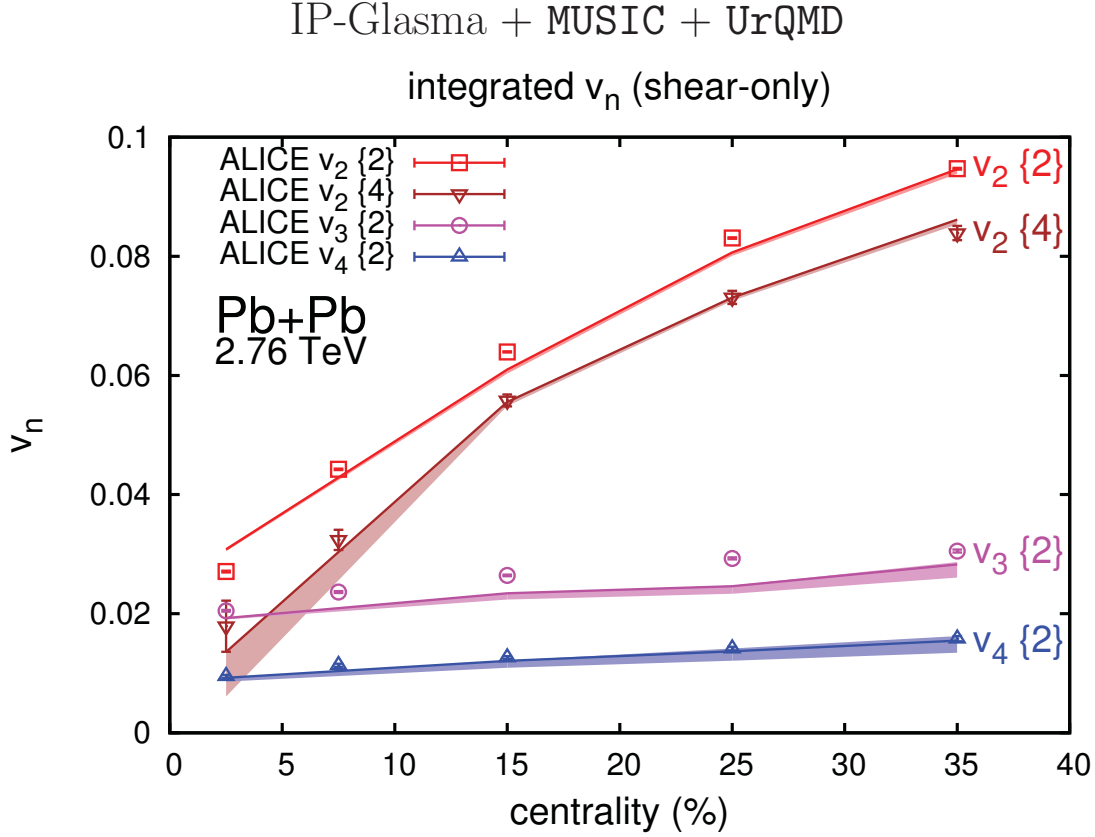


Figure 4.2: Integrated $v_2\{2\}$, $v_2\{4\}$, $v_3\{2\}$ and $v_4\{2\}$ as functions of centrality. The shear viscosity is set to $\eta/s = 0.16$ with vanishing bulk viscosity to fit the ALICE data [1]. The bands show the range of v_n with varying switching temperature between 135 MeV and 165 MeV. The upper and lower limits of bands correspond to 135 MeV and 165 MeV, respectively. The statistical error of the model calculation is approximately 5%.

30 – 40% centrality classes are considered in this work and the number of hydro events in each centrality bin is 100. To enhance the statistics, 200 UrQMD events were run after each hydro event in the 0 – 5% and 10 – 20% centrality classes. A hydro event in the 20 – 30%, and 30 – 40% centrality classes was followed by 500 UrQMD

events. A single hydro event with particlization takes several core-hours. A typical **UrQMD** event takes 5-20 core-minutes depending on the centrality class and switching temperature. Figure 4.3 shows results with non-zero bulk viscosity shown in Figure 2.5. The experimental data favors $\eta/s = 0.095$ and implies that the bulk viscosity changes determination of the shear viscosity. This can be interpreted that both of shear and bulk viscosity act to reduce the anisotropic flows. While the shear viscosity makes expansion isotropic, the bulk viscosity slows down expansion. Therefore, the effect of bulk viscosity on v_n must be compensated by the lower estimate of shear viscosity. The results with **UrQMD** collisions turned off, in the presence of resonance decays, are also shown in 4.3 as dashed lines. The resonance decays without scattering is denoted by *feeddown* from now on. The hadronic re-scattering affects little on the integrated v_n of charged hadrons.

The importance of bulk viscosity can be seen in the mid-rapidity multiplicity and mean p_T of identified hadrons. Figure 4.4 shows the mid-rapidity dN/dy of pions, kaons, and protons as functions of the switching temperature T_{sw} in the case of zero bulk viscosity with $\eta/s = 0.16$. Figure 4.5 shows the switching temperature scan of the mean p_T of identified hadrons. Those figures show that one significantly overestimates the mean p_T given that multiplicity and anisotropic flows are fitted to the data without the bulk viscosity. This discrepancy for vanishing bulk implies that expansion of the fireball develops more radial velocity than the observation and some other transport coefficients must be present to reduce the expansion. It can be seen from equation (2.71) and (2.109) that the bulk viscosity ζ gives a negative contribution to the pressure if the system is expanding since $\Pi \sim -\zeta(\partial_\mu u^\mu)$. It was previously shown in [112] that the bulk viscosity results in reduction of the radial flow. Figures 4.6 and 4.7 show that the bulk viscosity indeed slows down the expansion. One can reproduce all of anisotropic flows, multiplicity, and mean p_T of identified hadrons only if non-zero bulk viscosity is included.

It is also shown in those figures that protons are particularly sensitive to the switching temperature and significantly affected by hadronic re-scattering. The large

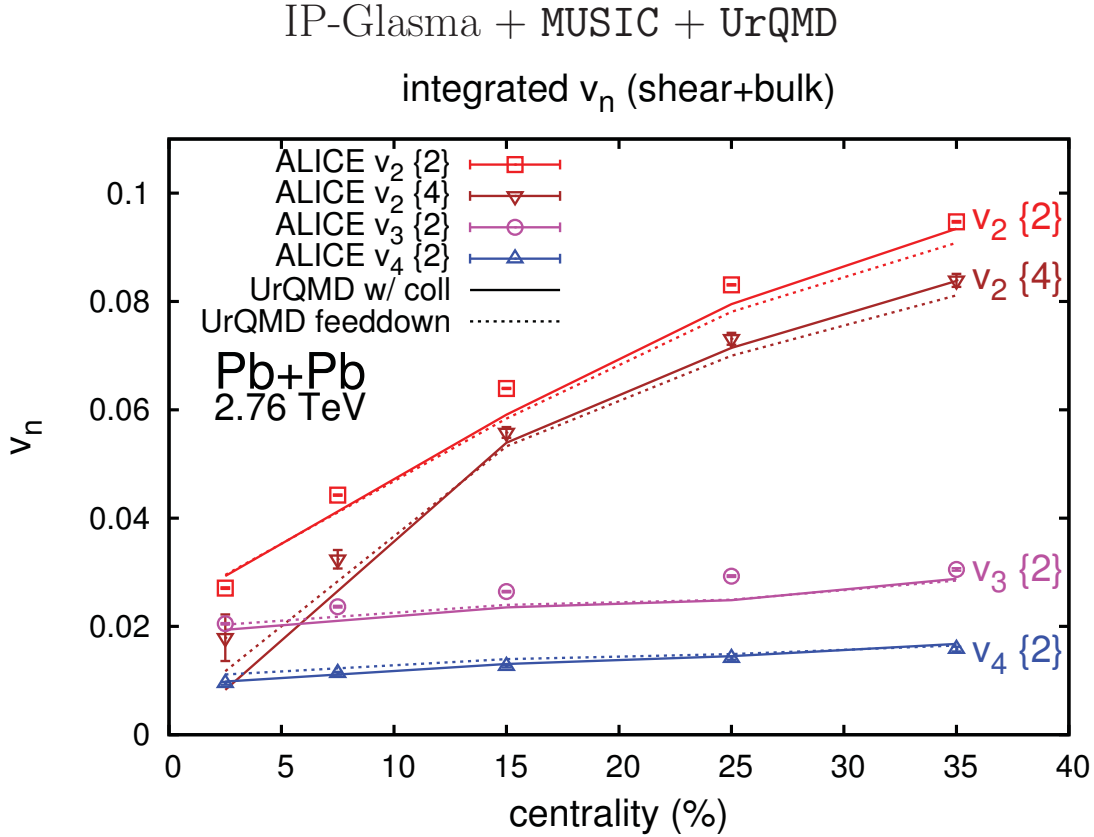


Figure 4.3: Integrated $v_2\{2\}$, $v_2\{4\}$, $v_3\{2\}$ and $v_4\{2\}$ as functions of centrality. The shear viscosity is set to be $\eta/s = 0.095$ with the finite bulk viscosity and the switching temperature is set to be $T_{\text{sw}} = 145 \text{ MeV}$ which is favoured by the proton multiplicity and mean p_T . The solid line and the dashed line correspond to the full UrQMD and the UrQMD without collisions, respectively. The statistical error of the model calculation is approximately 5%.

sensitivity to T_{sw} is due to the fact that proton mass is much larger than T_{sw} and the system is assumed to maintain the chemical equilibrium until particlization. Therefore, the proton multiplicity is a relevant observable which strongly depends on the point where the system gets out of chemical equilibrium. The results without hadronic re-scattering are shown as the dashed lines. A process responsible for the difference in proton multiplicity is baryon-antibaryon ($B\bar{B}$) annihilation in which baryon and antibaryon annihilate to excite two mesonic strings and fragment into other hadrons. It must be noted that reverse process of $B\bar{B}$ annihilation is not implemented in UrQMD and this corresponds to the assumption that the $B\bar{B}$ annihilation dominates baryonic chemistry. It is shown in Section 6.5 that the linearized Boltzmann transport equa-

tion, in conjunction with the viscous correction δf_{bulk} in equation (3.37), leads to a decrease of the baryon yield. It implies that the $B\bar{B}$ annihilation is more likely to occur than $B\bar{B}$ creation in expanding system. Therefore, it is reasonable to suppress the $B\bar{B}$ creation process.

From the fact that the higher switching temperature is favored with the hadronic re-scattering, the $B\bar{B}$ annihilation changes the determination of when the system is chemically frozen out. In addition, the difference between presence and absence of the re-scattering becomes larger if one switches to the afterburner at the higher temperature. Since the number density of proton and antiproton becomes larger as one switches at the higher temperature, the mean-free-path becomes smaller and there are more frequent $B\bar{B}$ annihilations.

The switching temperature scan of mean p_T shows that protons experience significant acceleration in the re-scattering. This phenomenon was described as *pion wind* in the earlier works [13, 113, 114]. This acceleration of protons is a consequence of different radial velocities at the point of particlization. Figure 4.8 shows distribution of radial velocity u^r of pions, Kaons, and protons of a single hydro event for 10 – 20% centrality of Pb + Pb collisions at the LHC. Pions move outward faster than protons since they are lighter. Figure 4.9 shows the acceleration and isotropization by pion-proton resonance scattering. Since the resonance decay is isotropic in the center-of-mass frame, protons tend to be accelerated while the radial velocity of pions becomes slower. In addition, anisotropic flow of proton decreases. Those effects can be seen in p_T -differential observables of protons. The pion wind has the similar effects on kaons due to the resonance scattering of $\pi + K$ via K^* resonance.

Figure 4.10 shows the mid-rapidity multiplicity and mean p_T of pions, kaons and protons as functions of centrality. One can find that the mean p_T of protons increases as a result of re-scattering. The hadronic re-scattering affects on the proton multiplicity mainly through $B\bar{B}$ annihilations. Although the effect is small, $B\bar{B}$ annihilations also increase the mean p_T of protons and this is interpreted as a consequence of more annihilations of low- p_T protons. One can also see that the kaon yield decreases as a

consequence of hadronic re-scattering. One possible explanation is that the resonance scattering $K + \bar{K} \rightarrow \pi + \pi$ and its reverse occur at different rates. Even if the cross section of the reverse process follows equation (3.83), deviation of the distribution function from local thermal equilibrium can result in $\pi + \pi$ preferred to $K + \bar{K}$ before the detailed balance is established.

The switching temperature scan of mid-rapidity multiplicity and mean p_T of multi-strange baryons were also obtained and shown in Figures 4.11 and 4.12, respectively. They show similar dependences on the switching temperature as the $dN/dy|_{|y|<0.5}$ and $\langle p_T \rangle$ of protons. The multiplicity increases with T_{sw} since it is assumed that the system is in local thermal equilibrium until particlization. It can be also seen that re-scattering decreases multiplicity of baryons. The mean p_T of multi-strange baryons are raised by hadronic re-scattering. This can be interpreted as a consequence of acceleration by lighter mesons and annihilation of low- p_T baryons.

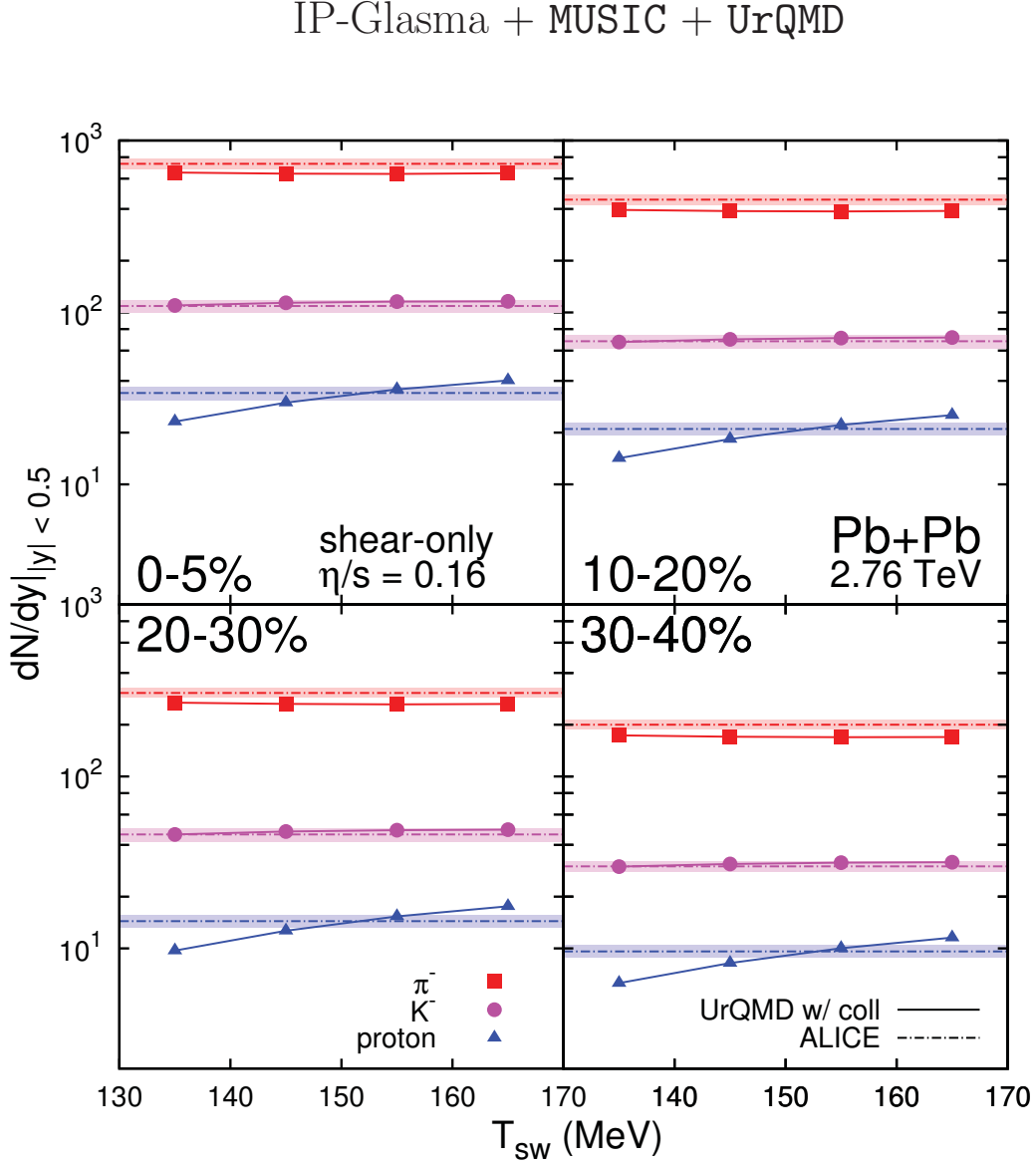


Figure 4.4: Switching temperature scan of mid-rapidity multiplicity of identified particles for centrality classes 0 – 5%, 10 – 20%, 20 – 30% and 30 – 40%. The shear viscosity is set to be $\eta/s = 0.16$ with vanishing bulk viscosity. The dashed lines and bands are the ALICE data [111] and statistical errors. The statistical error of the model calculation is approximately 1%.

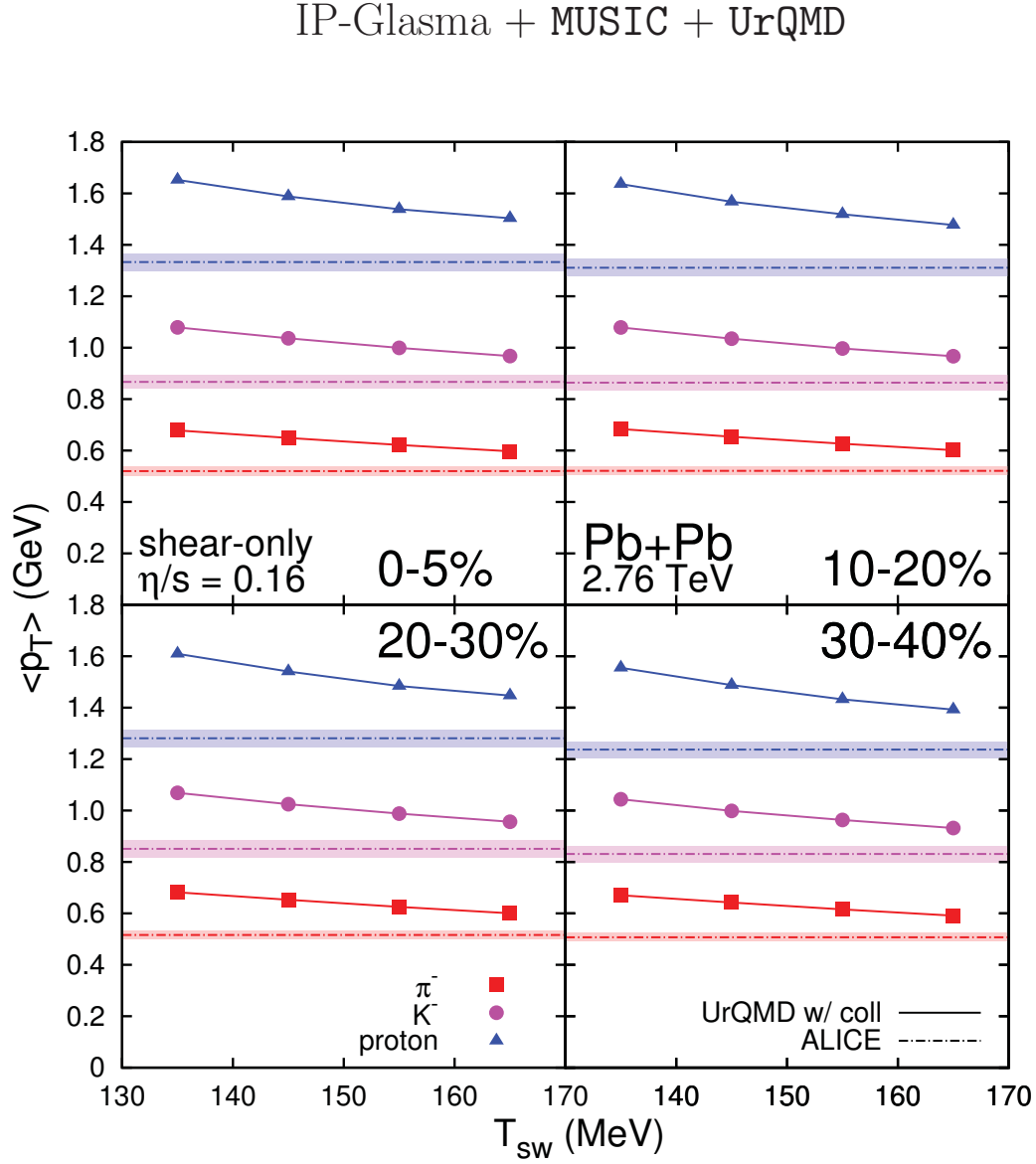


Figure 4.5: Switching temperature scan of mean p_T of identified particles for centrality classes 0–5%, 10–20%, 20–30% and 30–40%. The shear viscosity is set to be $\eta/s = 0.16$ with vanishing bulk viscosity. The dashed lines and bands are the ALICE data [111] and statistical errors. The statistical error of the model calculation is less than 1%.

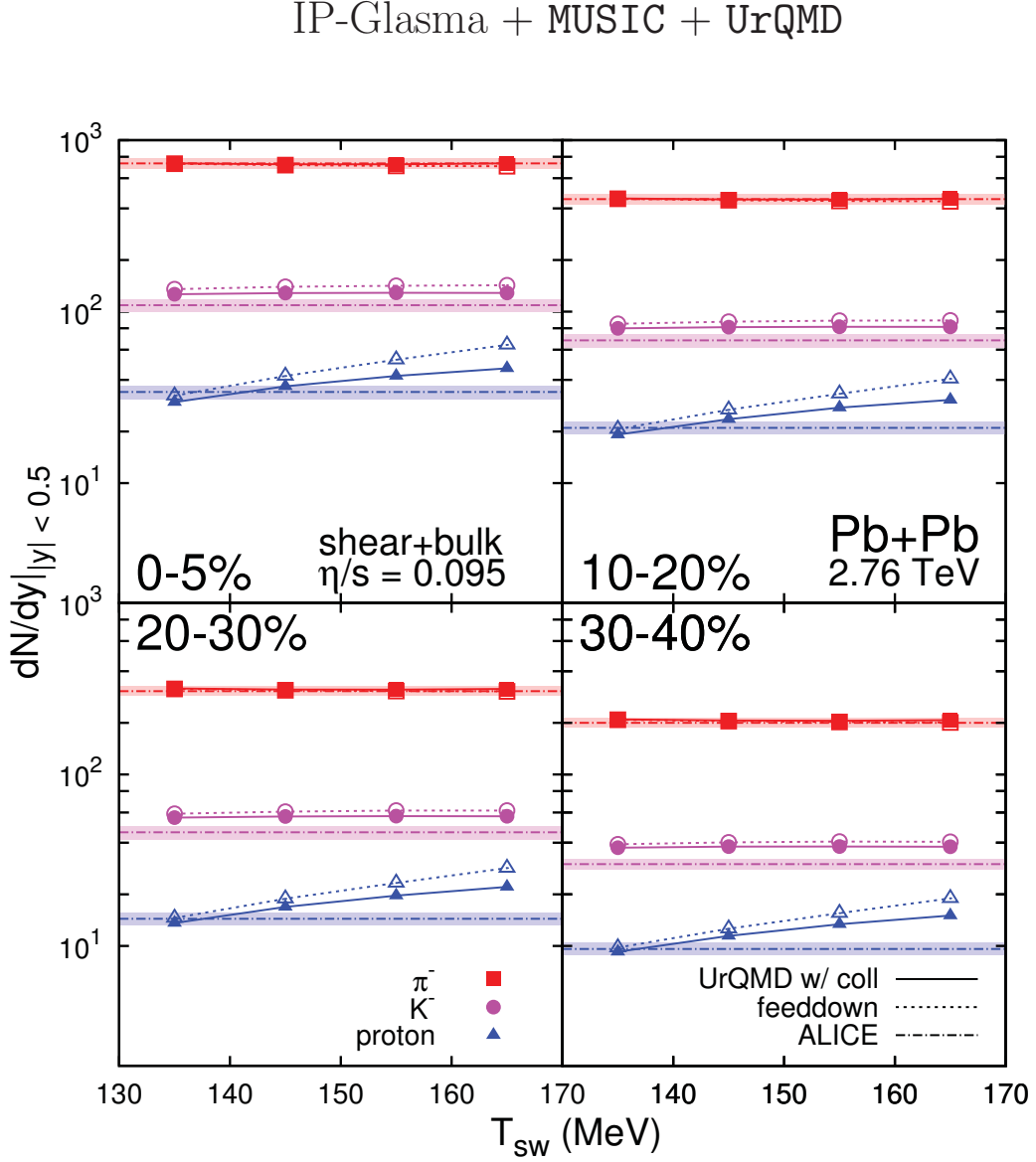


Figure 4.6: Switching temperature scan of mid-rapidity multiplicity of identified particles for centrality classes 0 – 5%, 10 – 20%, 20 – 30% and 30 – 40%. The shear viscosity is set to be $\eta/s = 0.095$ with finite bulk viscosity. The dashed lines and bands are the ALICE data [111] and statistical errors. The statistical error of the model calculation is approximately 1%.

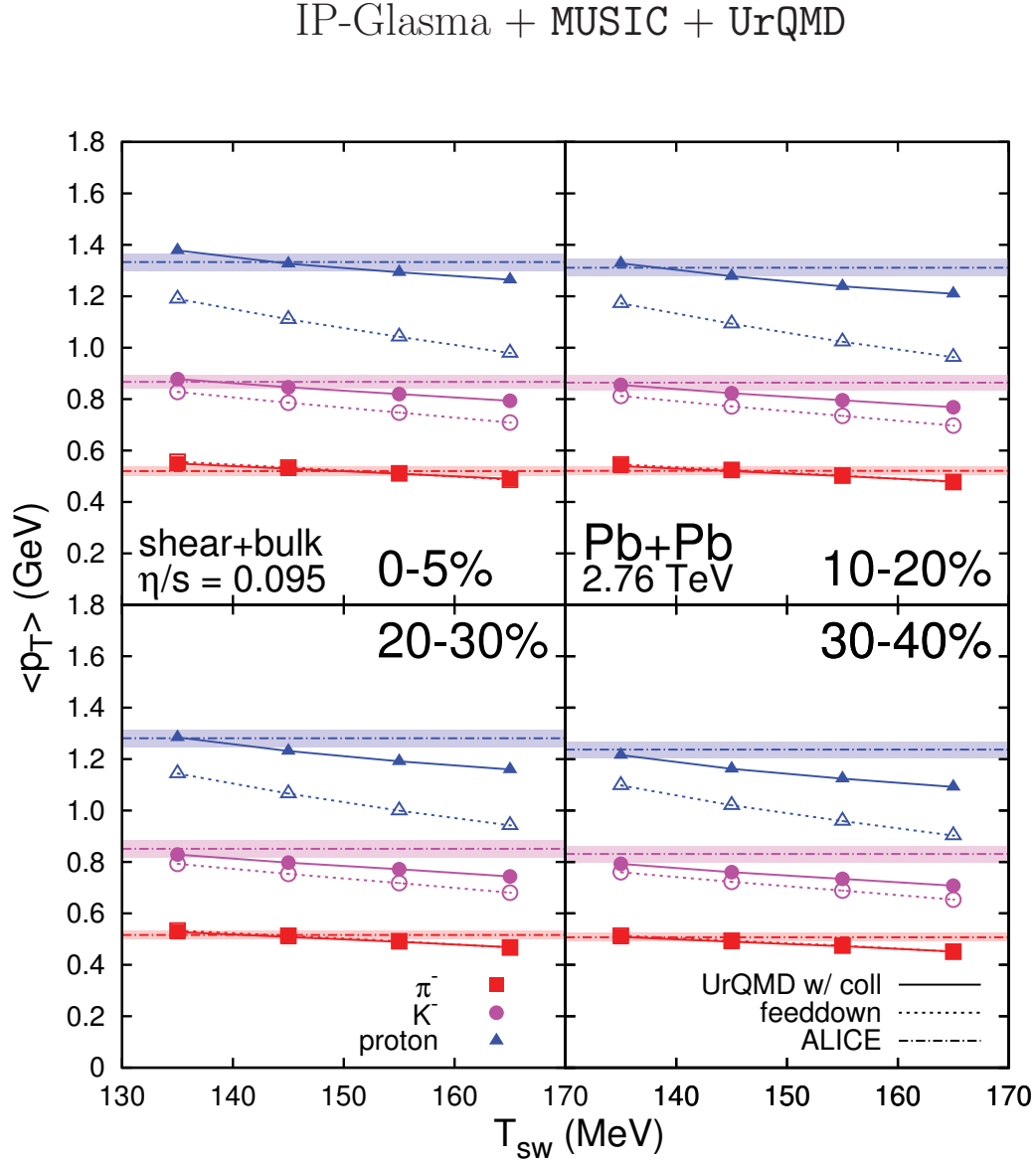


Figure 4.7: Switching temperature scan of mean p_T of identified particles for centrality classes 0–5%, 10–20%, 20–30% and 30–40%. The shear viscosity is set to be $\eta/s = 0.095$ with finite bulk viscosity. The dashed lines and bands are the ALICE data [111] and statistical errors. The statistical error of the model calculation is less than 1%.

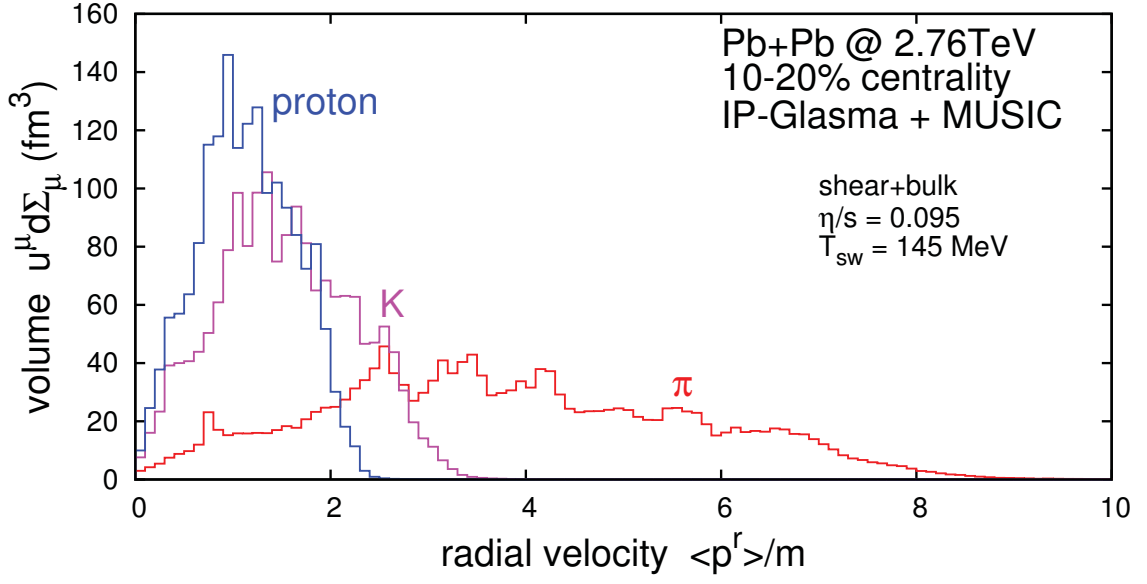


Figure 4.8: Total volume (sum of $u^\mu \Delta \Sigma_\mu$) of surface elements which yield specific transverse speed. Pions move outward faster than heavier particles due to their lower mass. The radial velocity is dimensionless given that the natural unit $c = 1$ is chosen.

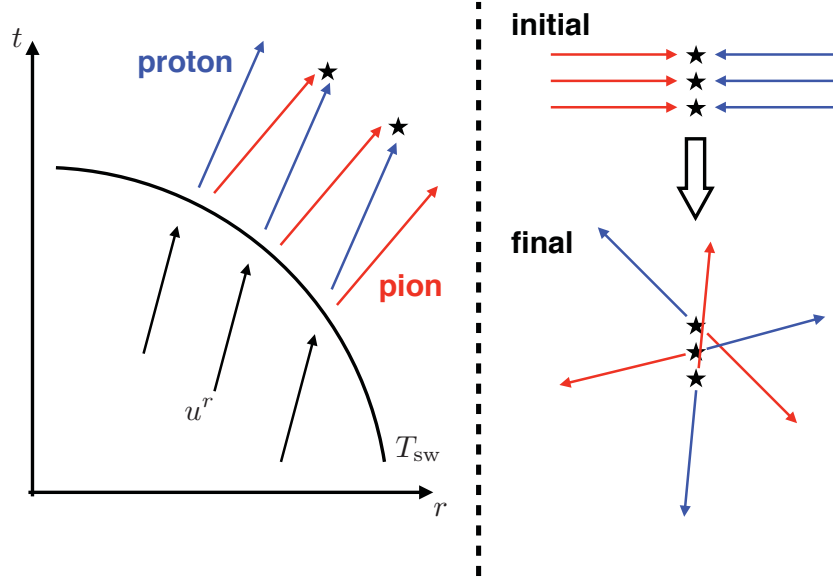


Figure 4.9: Pions have more radial speed than kaons and protons although they originate with the same flow velocity (left). Resonance scattering push protons outward while pions are decelerated. It also makes the spectra isotropic (right).

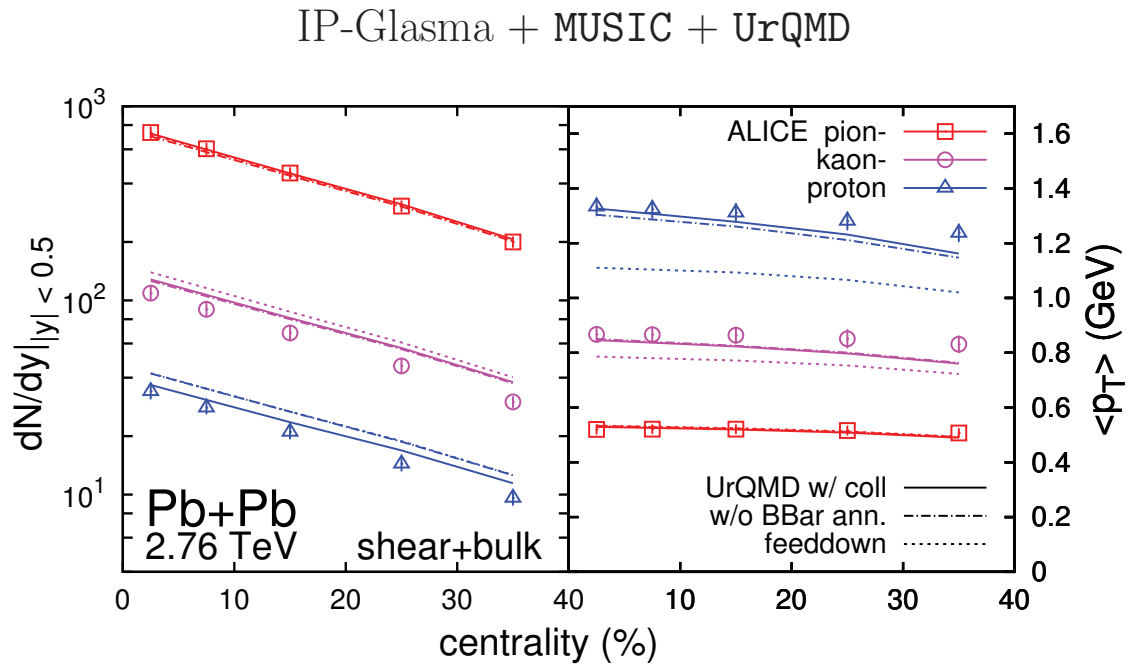


Figure 4.10: Mid-rapidity multiplicity (left panels) and mean p_T (right panels) of identified particles as functions of centrality.

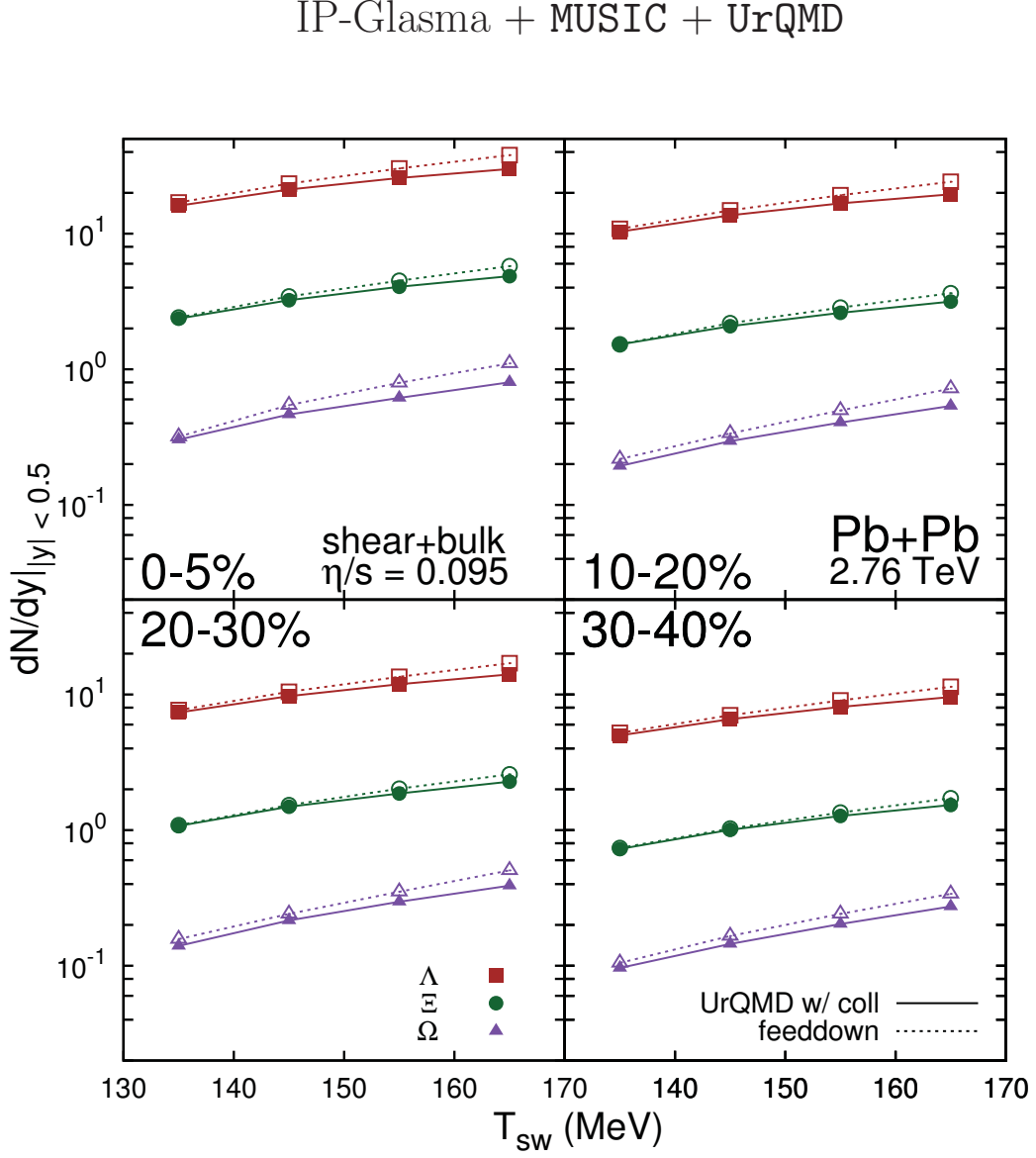


Figure 4.11: Switching temperature scan of mid-rapidity multiplicity of multi-strange baryons for centrality classes 0–5%, 10–20%, 20–30% and 30–40%. The shear viscosity is set to be $\eta/s = 0.095$ with finite bulk viscosity. The statistical error of the model calculation is approximately 2%.

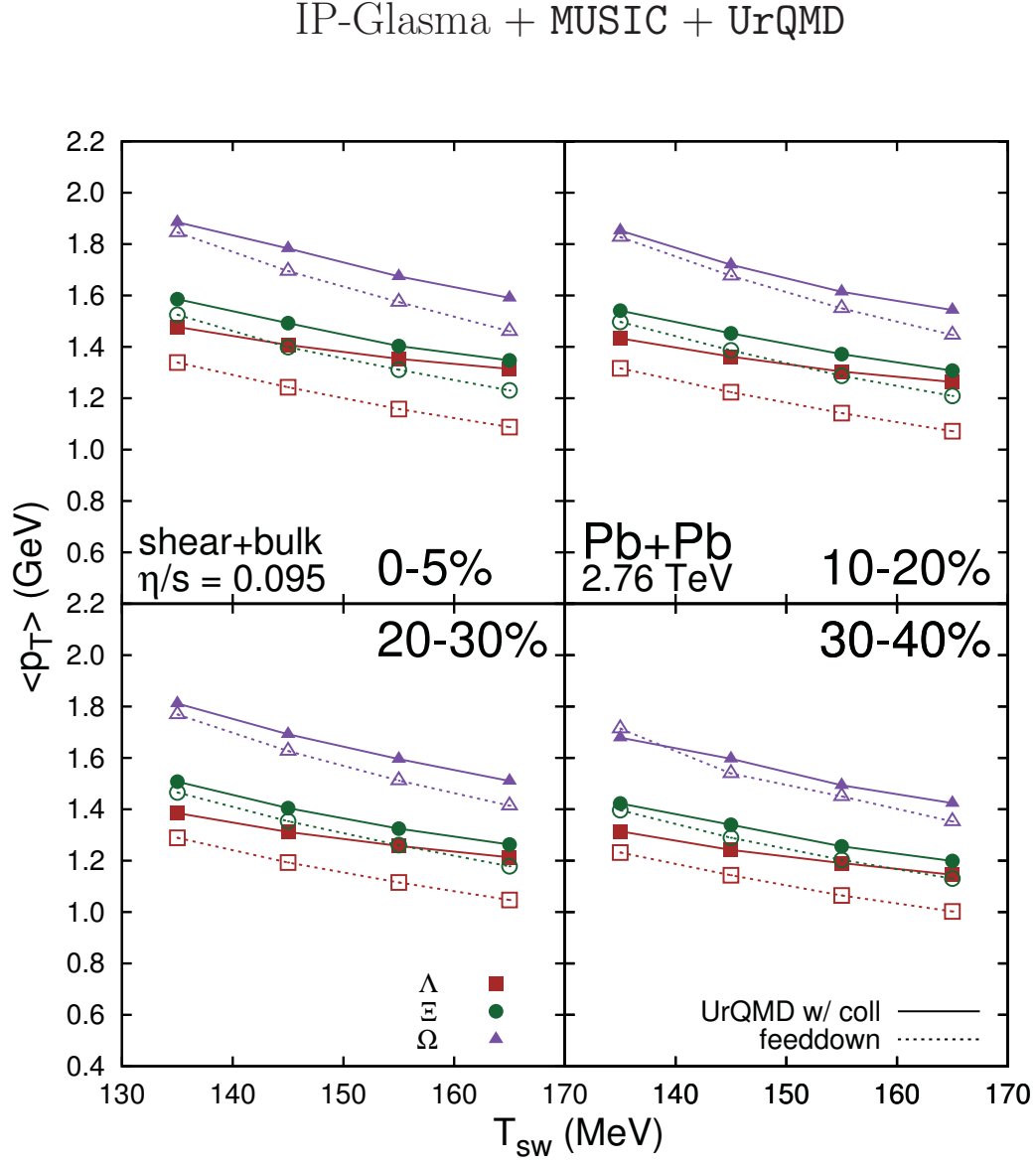


Figure 4.12: Switching temperature scan of mean p_T of multi-strange baryons for centrality classes 0 – 5%, 10 – 20%, 20 – 30% and 30 – 40%. The shear viscosity is set to be $\eta/s = 0.095$ with finite bulk viscosity. The statistical error of the model calculation is approximately 1%.

4.3 p_T -differential Observables

The momentum space distributions of identified hadrons in mid-rapidity can be represented by the p_T spectra and p_T -differential anisotropic flow coefficients. Figure 4.13 shows the p_T spectra of pions, Kaons, and protons of different centrality classes of Pb + Pb collisions with $\sqrt{s_{NN}} = 2.76$ TeV. As seen in the mid-rapidity multiplicity and mean p_T , one can describe the measured proton spectrum [111] by adding hadronic cascade. It also can be found that the pion spectrum deviates from the data for $p_T > 2$ GeV. While the low- p_T bulk dynamics of heavy ion collisions can be described with hydrodynamics, contributions from jets are necessary for the higher p_T .

Since the anisotropic flow coefficients depend on the geometry and fluctuation in different ways, the initial state fluctuation must be properly taken into account for comprehensive discription of v_n . For instance, the triangular flow v_3 is dominated by the fluctuation, while the collision geometry more significantly contributes to the elliptic flow v_2 . Figure 4.14 shows the p_T -differential $v_2\{2\}$, $v_3\{2\}$ and $v_4\{2\}$ of charged hadrons. The way to determine the initial energy density profile, together with the sub-nucleonic fluctuation, is important to reproduce the higher harmonics.

Figures 4.15, 4.16, and 4.17 show the p_T -differential $v_2\{2\}$, $v_3\{2\}$ and $v_4\{2\}$ of identified hadrons, respectively. Comparison with the experimental data [4] implies that the hadronic re-scattering is important in description of the proton v_2 . As seen in v_2 of identified hadrons, the hadronic re-scattering has significant effect on the higher harmonics of protons. This also can be interpreted as a consequence of acceleration and isotropization due to the pion wind as shown in Figure 4.9. The slope of the p_T -differential $v_2\{2\}$ depends on the centrality class since it is dominated by the collision geometry. The p_T -differential $v_3\{2\}$ and $v_4\{2\}$ have the similar behavior throughout all centrality classes because, as shown in [115], ϵ_3 and ϵ_4 from the IP-Glasma initial condition are similar in all centrality classes considered here.

Strange and multi-strange baryons and their distributions must be considered to understand dynamics of heavy ion collisions. The p_T spectra and p_T -differential $v_2\{2\}$

of Λ , Ξ , and Ω are shown in Figure 4.18. The p_T spectra clearly shows that the model underestimates the yields of those baryons. The switching temperature scan of the multiplicity (Figure 4.11) implies that the higher switching temperature is favored by the strange baryons and their chemical freeze-out occur earlier than the model estimate. The baryon number and strangeness are chemically frozen out at different instances since the cross sections are different. The earlier freeze-out of strange particles was argued in the previous studies [118, 119, 120].

This hybrid model can be applied for Au + Au collisions with $\sqrt{s_{NN}} = 200$ GeV at RHIC. p_T spectra and p_T -differential v_2 of identified hadrons are shown in Figure 4.19 and 4.20, respectively. One remarkable point is that the favored values of η/s and T_{sw} are different from Pb + Pb collisions with $\sqrt{s_{NN}} = 2.76$ TeV at the LHC. The momentum dependence of strong coupling α_S implies that the partonic cross section becomes smaller at higher temperature. Provided that the highest temperature reached by the system depends on the collision energy, this result is also consistent with the calculation of η/s for high-temperature QCD [87]

$$\eta \sim \frac{T^3}{\alpha_S^2 \ln(\alpha_S^{-1})} \quad (4.38)$$

The similar effects of hadronic re-scattering on the proton distribution can be seen. The p_T spectrum of proton becomes harder with larger $\langle p_T \rangle$ due to the pion wind. The p_T -differential v_2 of protons is altered in the same way as in the case of Pb + Pb collisions. As presented in Figure 4.21, the model calculations show reasonable agreement with the experimental data of the higher harmonics $v_3(p_T)$ and $v_4(p_T)$, as well as the elliptic flow $v_2(p_T)$.

In contrast to the case of Pb + Pb collisions, hadronic re-scattering has relevant effects on the pion spectrum and v_2 . Pions are accelerated outward and their v_2 is increased as well. It implies that the hadronic re-scattering phase also develops additional anisotropic flows and this can be supported by the eccentricity evaluated at the hypersurface. The eccentricity ϵ_2 on hypersurface Σ can be defined as

$$\epsilon_2(\Sigma) = \frac{\langle x^2 - y^2 \rangle_\Sigma}{\langle x^2 + y^2 \rangle_\Sigma}. \quad (4.39)$$

where $\langle \dots \rangle_\Sigma$ is defined in equation (3.55). Figure 4.22 shows $\epsilon_2(\Sigma)$ evaluated on the hypersurface for different cases. A negative value of eccentricity indicates that spatial distribution of particles emerging from Σ has almond shape. The middle panel of Figure 4.22 is the difference between v_2 in the presence and absence of the hadronic re-scattering. It can be seen that the additional elliptic flow, developed by the re-scattering, is correlated with the eccentricity $-\epsilon_2(\Sigma)$. Therefore, interparticle distance along x -axis is different from that along y -axis and the system is likely to develop additional flows. Dependence of $\epsilon_2(\Sigma)$ on the collision energy is in line with what is shown in [123] from the MC-Glauber and MC-KLN initial conditions. For the higher collision energy, the strongly-coupled QGP can last until the system becomes spatially isotropic.

IP-Glasma + MUSIC + UrQMD

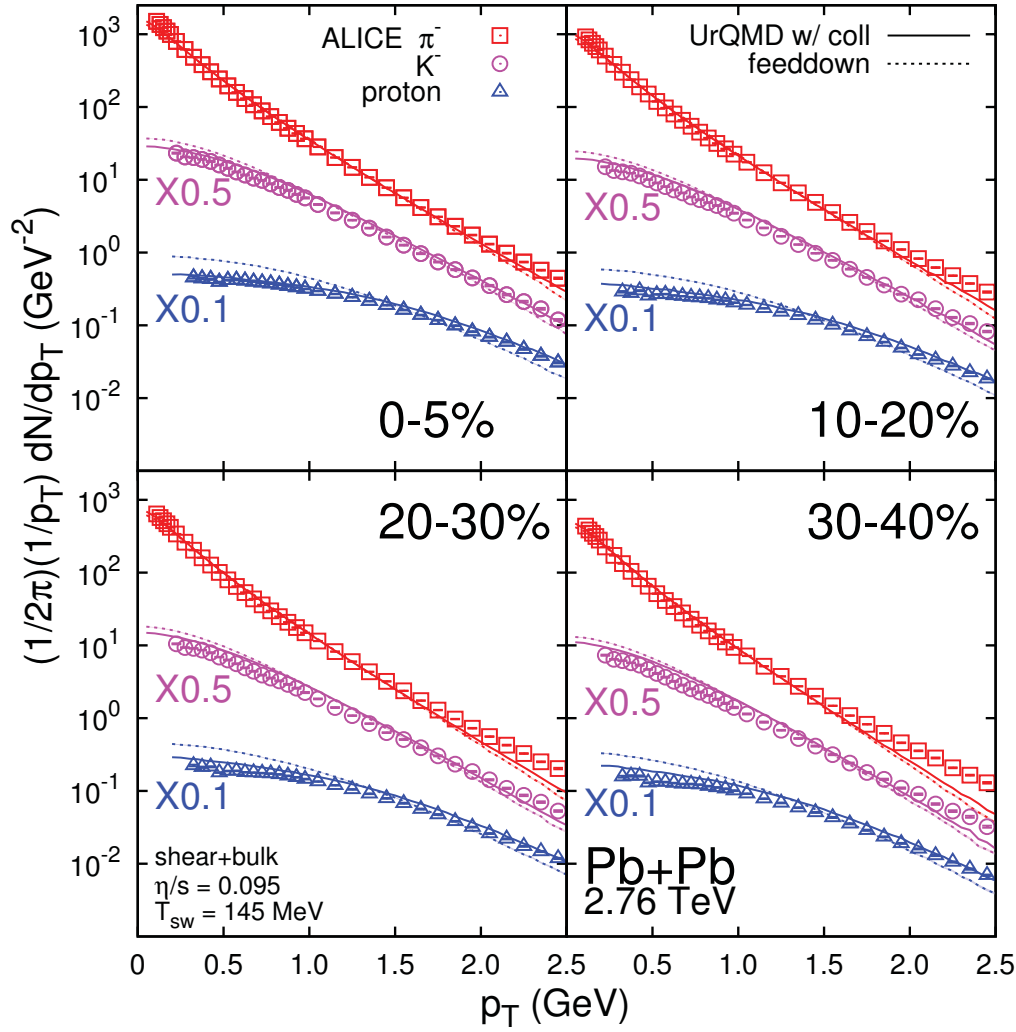


Figure 4.13: p_T spectra of identified hadrons for centrality classes 0 – 5%, 10 – 20%, 20 – 30%, and 30 – 40% of Pb + Pb collisions with $\sqrt{s_{NN}} = 2.76$ TeV. The solid curves and the dashed curves correspond to the full UrQMD and the UrQMD without collisions, respectively. The ALICE data are from [111]. The statistical errors in the calculation are shown as the bands around the curves.

IP-Glasma + MUSIC + UrQMD

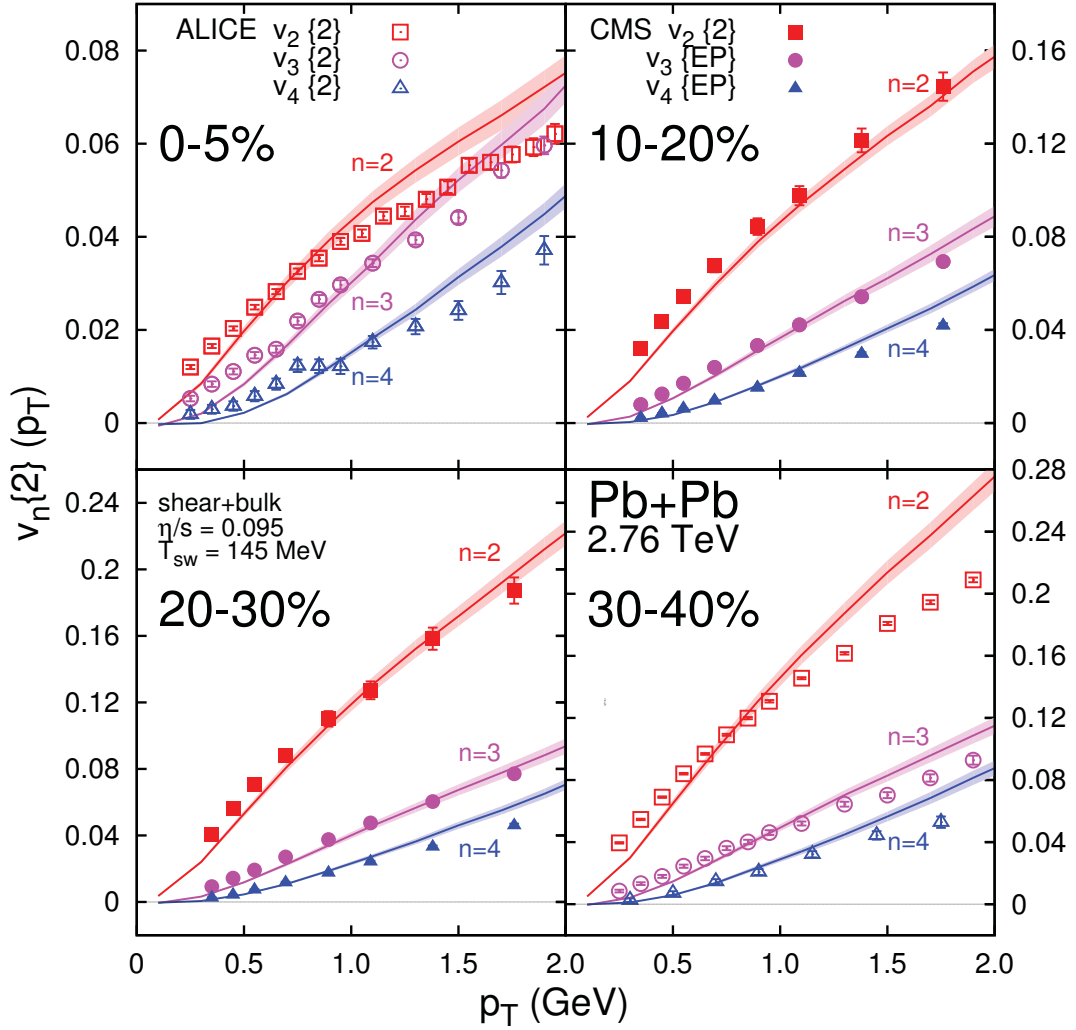


Figure 4.14: p_T differential $v_n\{2\}$ ($n = 2, 3$ and 4) of charged hadrons for centrality classes 0 – 5%, 10 – 20%, 20 – 30% and 30 – 40% of Pb+Pb collisions with $\sqrt{s_{NN}} = 2.76$ TeV. The statistical errors in the calculation are shown as the bands around the curves. The ALICE data [1] and CMS [2, 3] data were also shown for comparison.

IP-Glasma + MUSIC + UrQMD

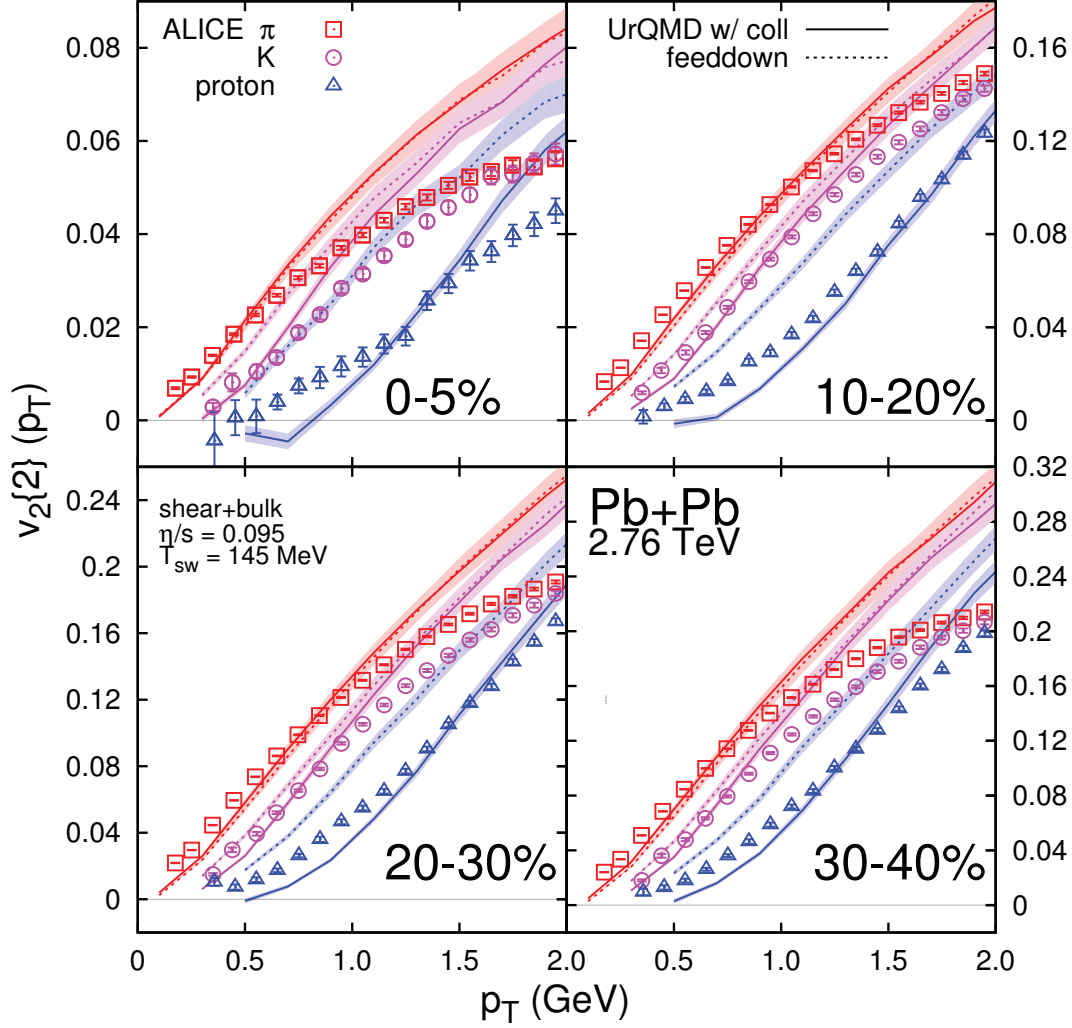


Figure 4.15: p_T -differential $v_2\{2\}$ of identified hadrons for centrality classes 0 – 5%, 10 – 20%, 20 – 30%, and 30 – 40% of Pb + Pb collisions with $\sqrt{s_{NN}} = 2.76$ TeV. The solid curves and the dashed curves correspond to the full UrQMD and the UrQMD without collisions, respectively. The ALICE data are from [4]. The statistical errors in the calculation are shown as the bands around the curves.

IP-Glasma + MUSIC + UrQMD

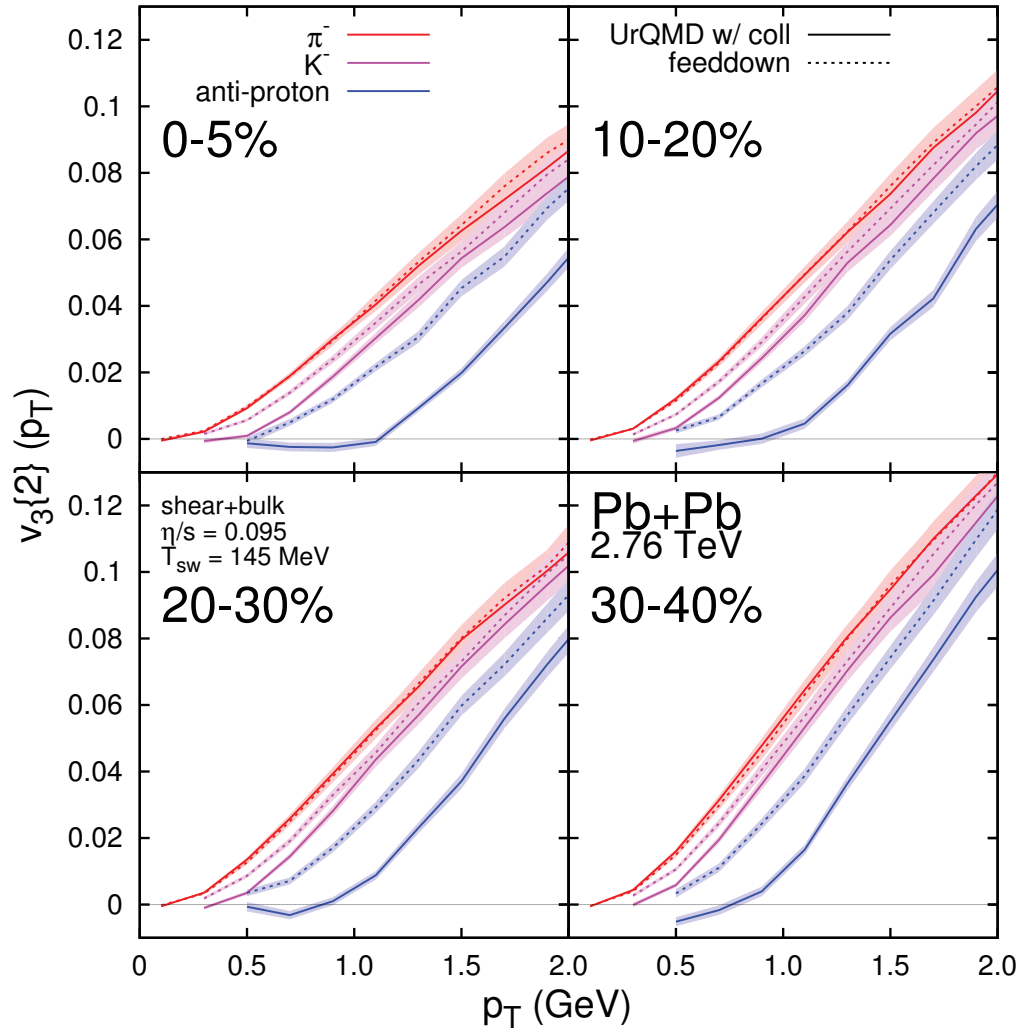


Figure 4.16: $v_3\{2\}$ of identified hadrons for centrality classes 0 – 5%, 10 – 20%, 20 – 30%, and 30 – 40% of Pb + Pb collisions with $\sqrt{s_{NN}} = 2.76$ TeV. The solid curves and the dashed curves correspond to the full UrQMD and the UrQMD without collisions, respectively. The statistical errors in the calculation are shown as the bands around the curves.

IP-Glasma + MUSIC + UrQMD

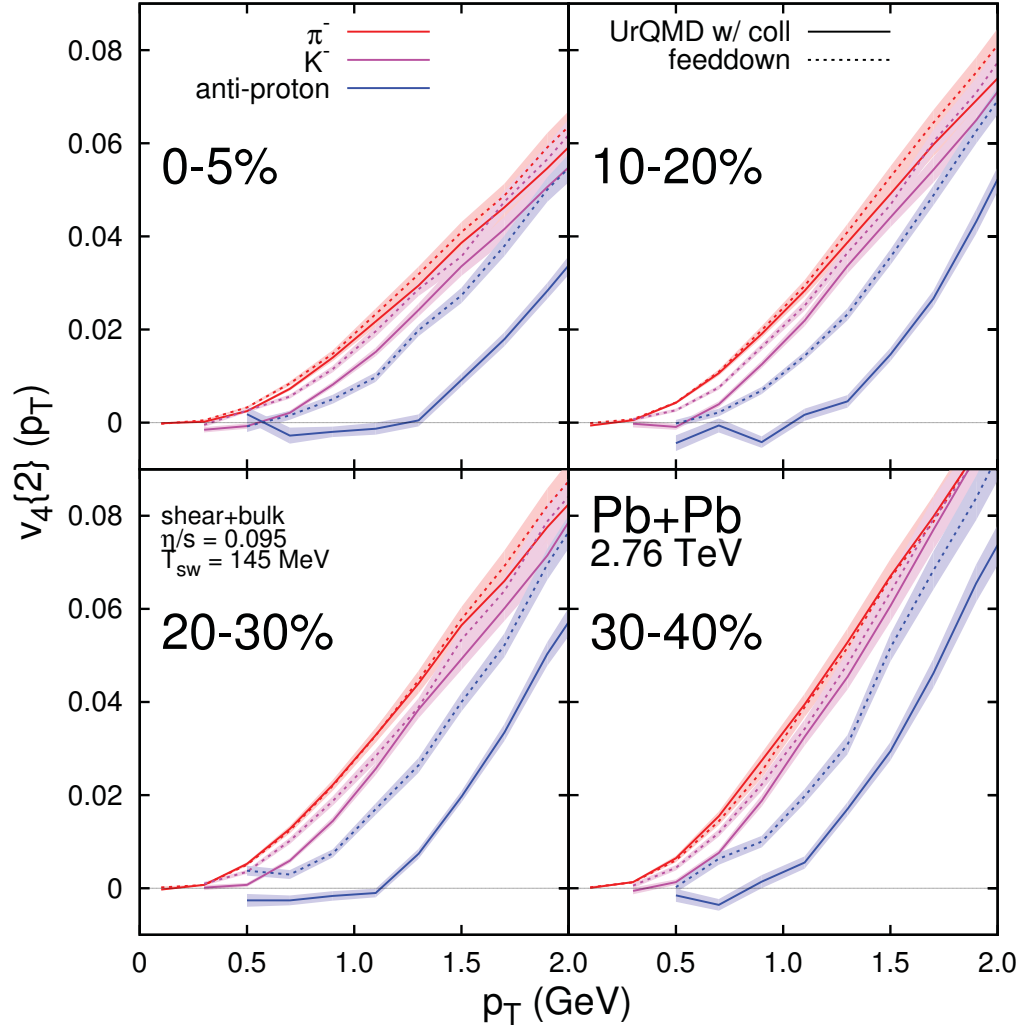


Figure 4.17: $v_4\{2\}$ of identified hadrons for centrality classes 0 – 5%, 10 – 20%, 20 – 30%, and 30 – 40% of Pb + Pb collisions with $\sqrt{s_{NN}} = 2.76$ TeV. The solid curves and the dashed curves correspond to the full UrQMD and the UrQMD without collisions, respectively. The statistical errors in the calculation are shown as the bands around the curves.

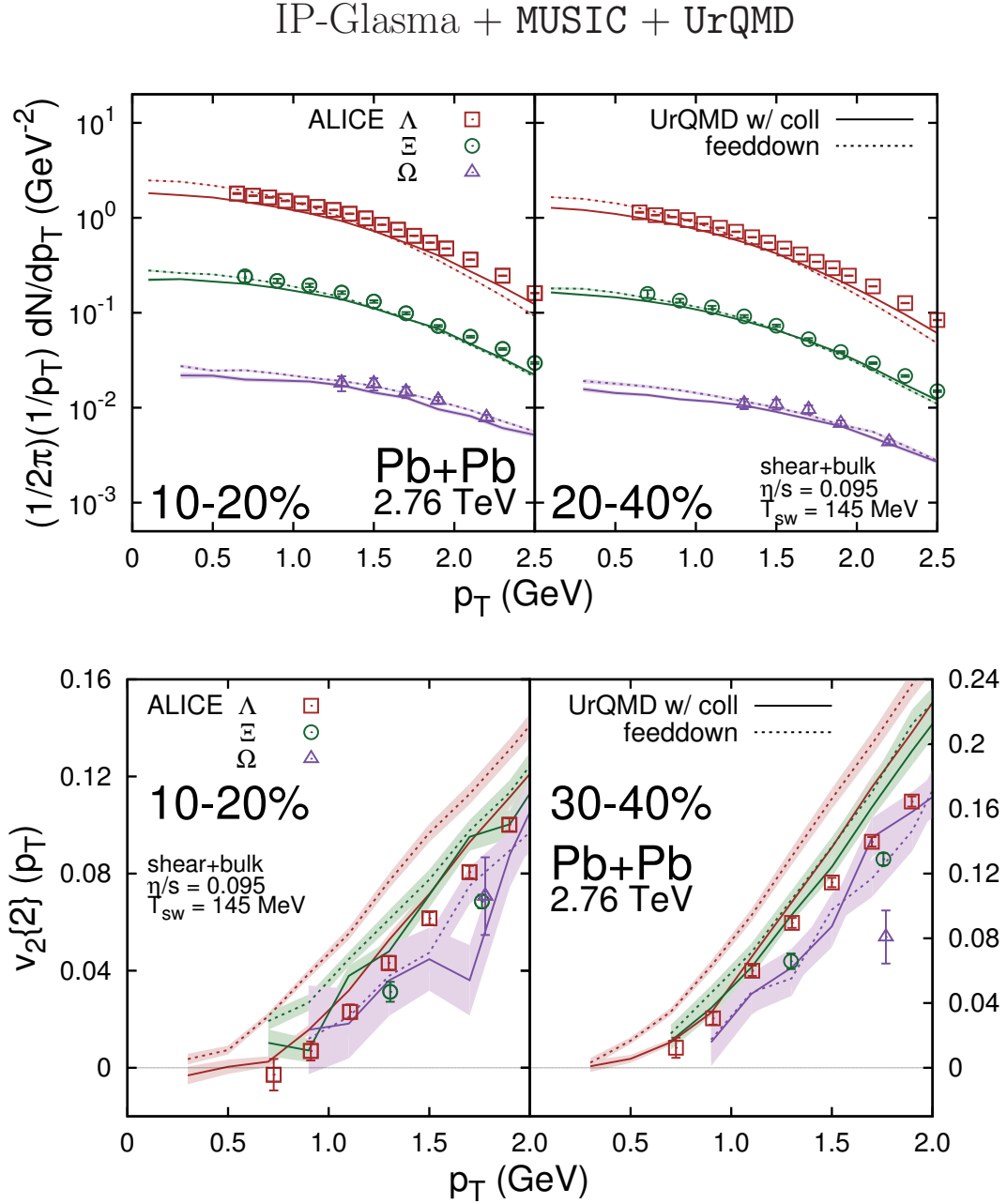


Figure 4.18: p_T spectra (upper) and differential $v_2\{2\}$ (lower) of strange baryons of Pb + Pb collisions with $\sqrt{s_{NN}} = 2.76$ TeV. The solid curves and the dashed curves correspond to the full UrQMD and the UrQMD without collisions, respectively. The ALICE data [116, 117] are also shown. The statistical errors in the calculation are shown as the bands around the curves.

IP-Glasma + MUSIC + UrQMD

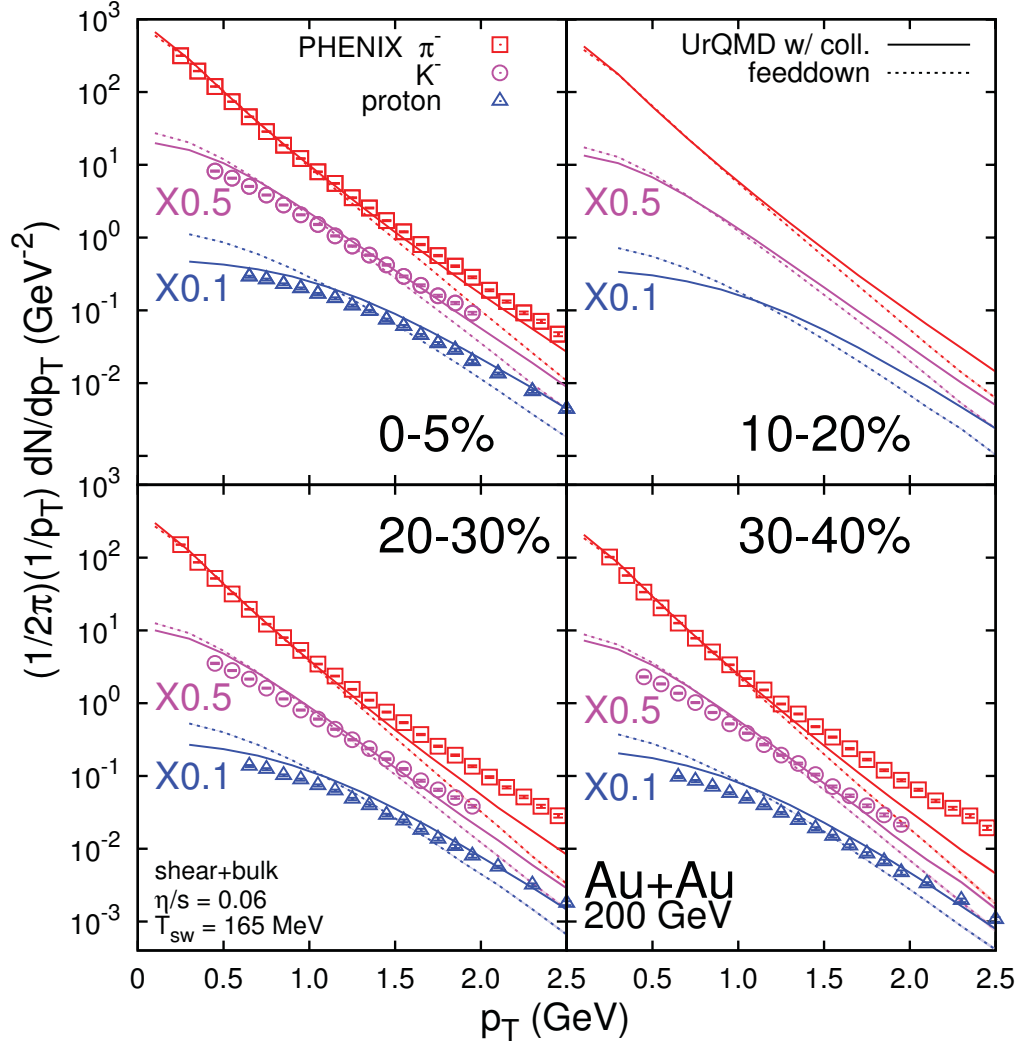


Figure 4.19: p_T spectra of identified hadrons for centrality classes 0 – 5%, 10 – 20%, 20 – 30%, and 30 – 40% of Au + Au collisions with $\sqrt{s_{NN}} = 200$ GeV. The solid curves and the dashed curves correspond to the full UrQMD and the UrQMD without collisions, respectively. The PHENIX data are from [121]. The statistical errors in the calculation are shown as the bands around the curves.

IP-Glasma + MUSIC + UrQMD

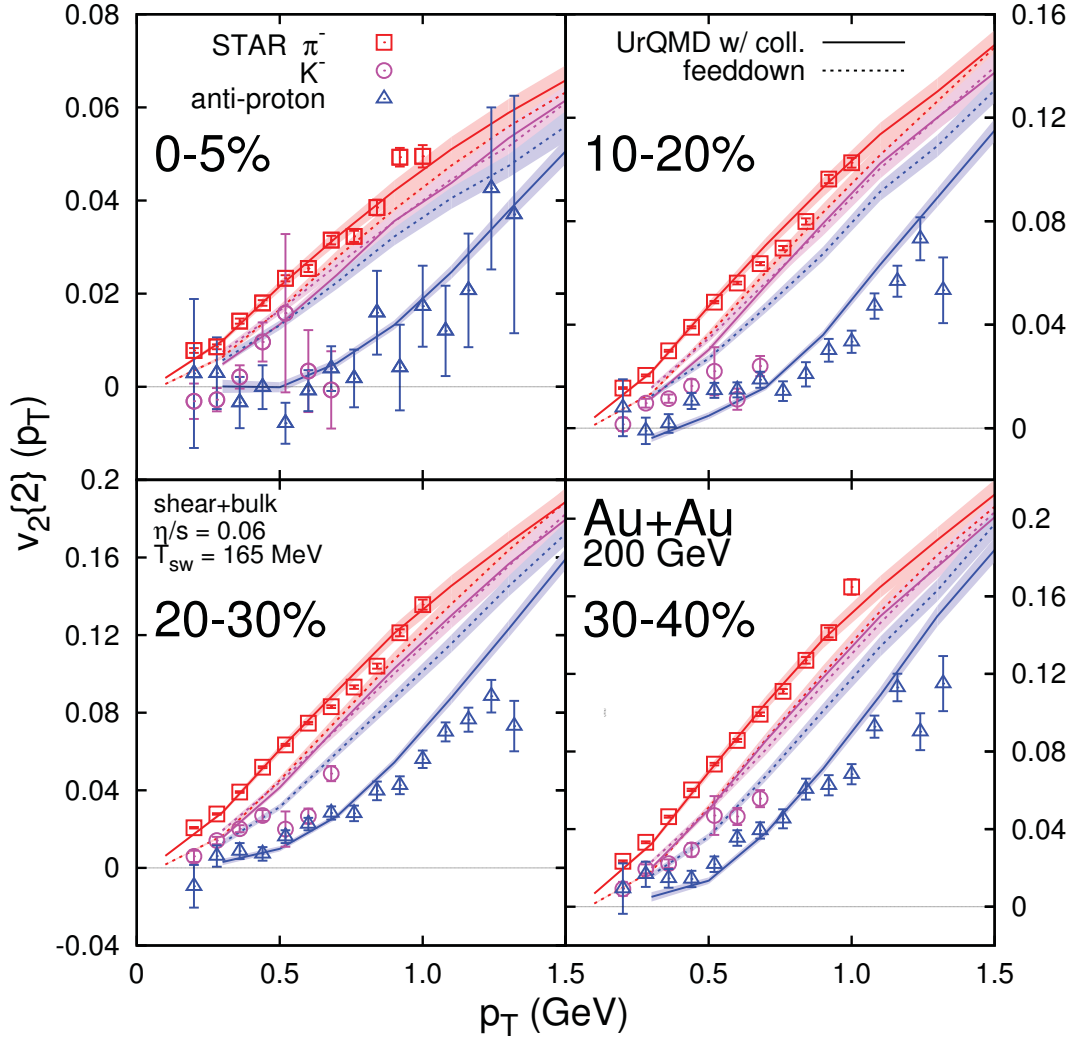


Figure 4.20: p_T -differential $v_2\{2\}$ of identified hadrons for centrality classes 0 – 5%, 10 – 20%, 20 – 30%, and 30 – 40% of Au + Au collisions with $\sqrt{s_{NN}} = 200$ GeV. The solid curves and the dashed curves correspond to the full UrQMD and the UrQMD without collisions, respectively. The STAR data are from [122]. The statistical errors in the calculation are shown as the bands around the curves.

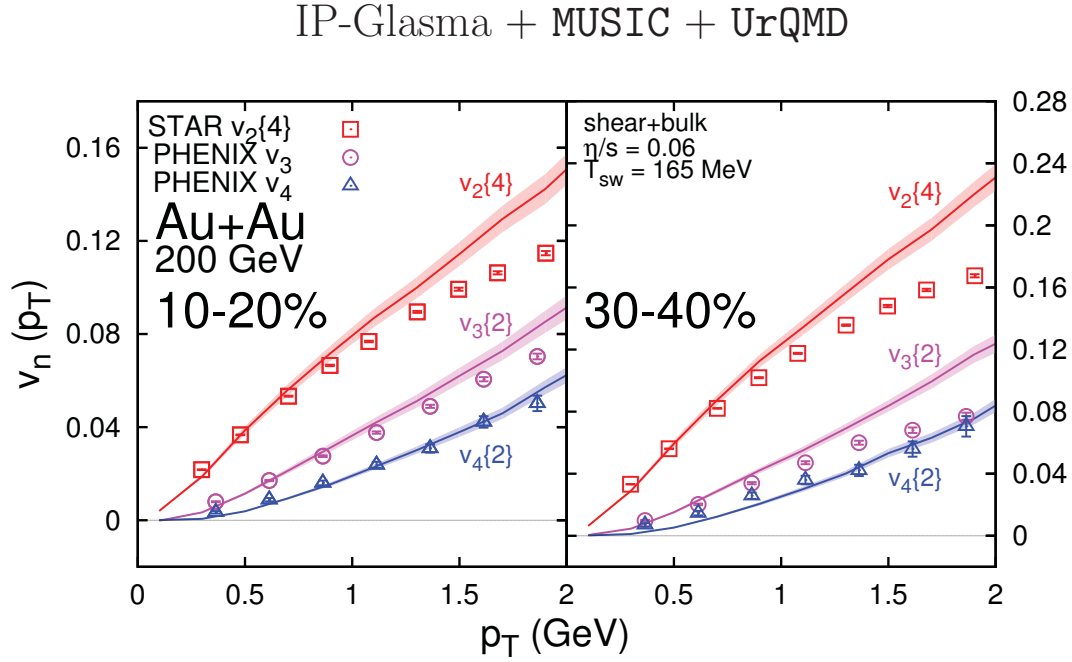


Figure 4.21: p_T -differential $v_2\{4\}$, $v_3\{2\}$, and $v_4\{2\}$ of charged hadrons for centrality classes 0–5%, 10–20%, 20–30%, and 30–40% of Au + Au collisions with $\sqrt{s_{NN}} = 200$ GeV. The PHENIX [5] and STAR [122] data are also shown. The statistical errors in the calculation are shown as the bands around the curves.

IP-Glasma + MUSIC + UrQMD

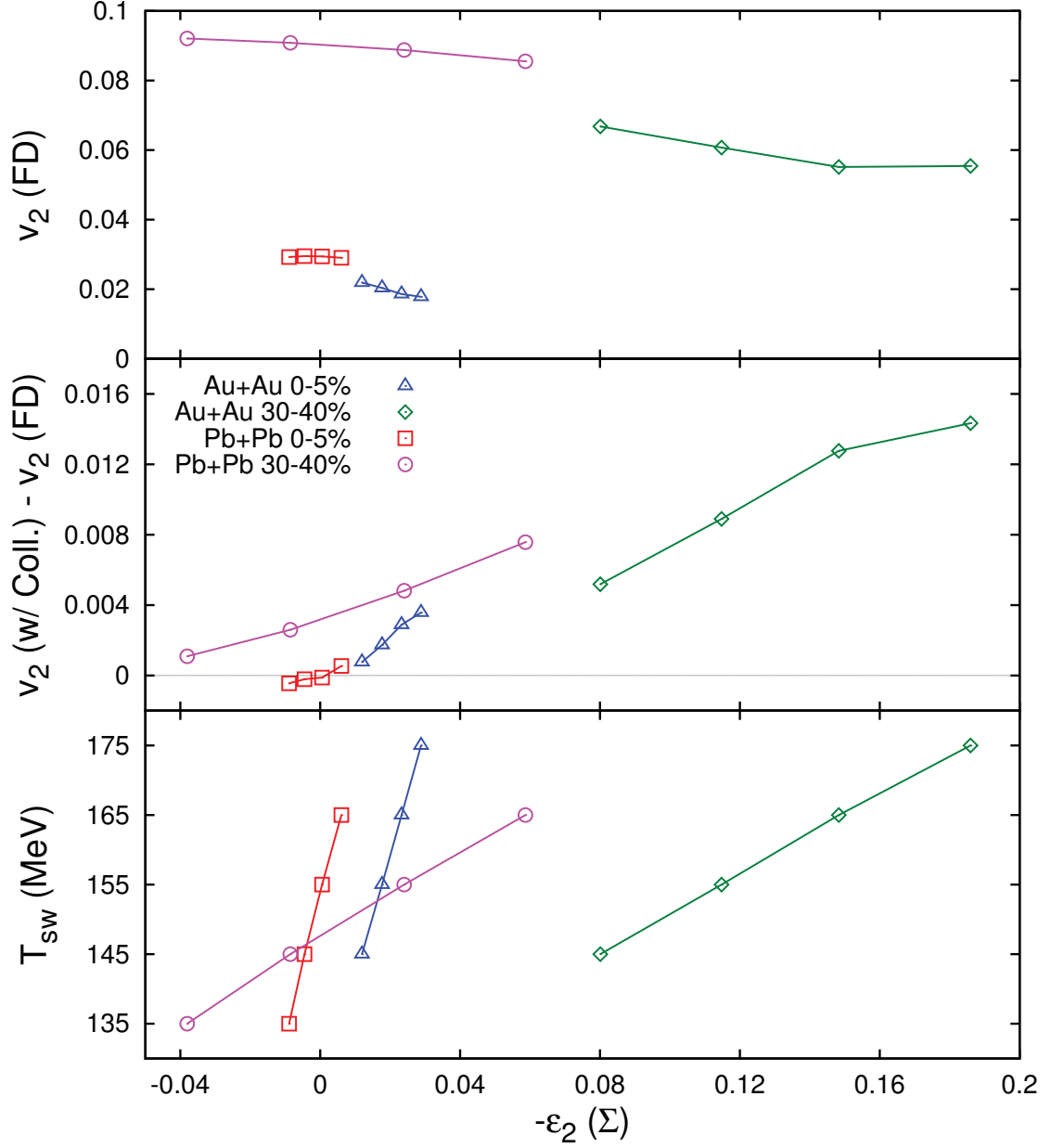


Figure 4.22: Eccentricity $\epsilon_2(\Sigma)$ of isothermal hypersurface with switching temperature T_{sw} of Pb+Pb collisions at the LHC and Au + Au collisions at RHIC. “FD” indicates *feeddown* where one has the resonance decays only while “w/ Coll.” stands for the full UrQMD calculations with scatterings.

4.4 Extension to Higher p_T with Jets

The jet-medium interaction in heavy ion collisions can be studied with hybrid model in this work by extension to the higher- p_T regime. The energy loss in hadronic medium can be taken into account by having the hadronic re-scattering in UrQMD. Since it is necessary to have a reasonable hydrodynamic background, which reproduces hadronic spectra of $p_T < 2$ GeV, the non-zero bulk viscosity (Figure 2.5) with $\eta/s = 0.095$ and $T_{\text{sw}} = 145$ MeV was adopted for the results shown in this section. First of all, it can be seen from Figure 4.23 that the high- p_T jets are essential to reproduce the particle yields at the intermediate and higher- p_T . The p_T spectra without MARTINI decrease exponentially since they stem from the thermal distribution.

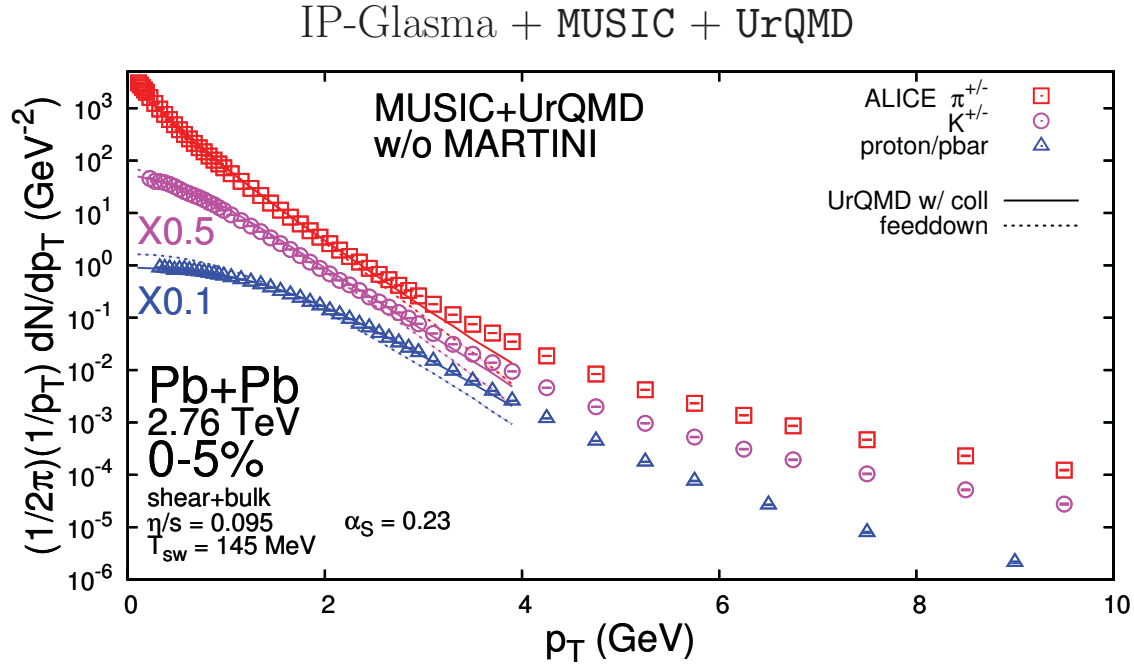


Figure 4.23: p_T spectra of identified hadrons and R_{AA} of charged hadrons of Pb + Pb collisions with $\sqrt{s_{\text{NN}}} = 2.76$ TeV. The calculations do not include the MARTINI jets. The ALICE data of p_T spectra and R_{AA} are from [124] and [7], respectively.

Figure 4.24 shows the p_T spectra of identified hadrons and nuclear modification factor R_{AA} of charged hadrons. One can see that the interaction between jets and hadronic medium has a relevant contribution to the energy loss. The momentum scale $\hat{p}_{T,\text{min}}$ of jets is set to be 10 GeV and the strong coupling of the jet-medium interactions

is set to be $\alpha_S = 0.23$ for the results shown in this section. The fragmentation into hadrons occurs at $T \simeq 190$ MeV by making strings from the jet partons and thermal ones.

Figure 4.25 shows the p_T -differential v_2 of pions, Kaons, and protons. The effects of hadronic re-scattering can be seen in the anisotropic flow coefficients as well. The hadronic re-scattering develops additional v_2 and it implies that the energy loss in hadronic medium is not isotropic. Figure 4.26 demonstrates that the hadronic re-scattering has the similar effects on the higher harmonics. Therefore, the hadronic processes must be properly involved to study the hot QCD matter.

It was previously mentioned in Section 3.3 that the radiative and collisional processes were considered to describe the energy loss of partons in this work. Time evolution of the probability distribution \mathcal{P} of the parton energy was computed in [125] according to the rate equation of Fokker-Planck type

$$\frac{d\mathcal{P}}{dt}(E) = \int_{-\infty}^{\infty} d\omega \left[\mathcal{P}(E + \omega) \frac{d\Gamma}{d\omega}(E + \omega, \omega) - \mathcal{P}(E) \frac{d\Gamma}{d\omega}(E, \omega) \right] \quad (4.40)$$

$$\langle E \rangle(t) \equiv \int_0^{\infty} dE E \mathcal{P}(E) \quad (4.41)$$

where the rates of radiative and collisional energy loss are given by equations (3.88) and (3.93), respectively. It was also shown in [125] that the radiative processes dominate the energy loss as the energy of incident jet parton increases. The amount of radiative energy loss ω is order of energy E_{init} of the initial jet parton, while one has $\omega \sim T$ for collisional processes since the typical momentum scale of thermal partons is T . Even if one considers the running coupling, the average amount of energy loss $\langle \omega \rangle$ would decrease but the dependence of $\langle \omega \rangle$ on E_{init} would be similar to the case of the constant α_S .

By coupling the MARTINI jets with the hadronic cascade, one can simulate the collisional energy loss in the hadronic sector. One has to note that it is also possible that a hadron loses energy by emitting a photon. One can estimate the relative importance of the radiative and collisional energy losses of hadrons based on the argument same as the partonic ones. The energy loss due to the elastic collisions

between jet hadrons and medium ones is on the order of the temperature of the medium. Provided that hadrons with higher energy can emit more energetic photons, it is expected that the radiative processes become more important as one considers the higher p_T range. Formulation and implementation of the radiative processes in the hadronic sector will be the subject of future study.

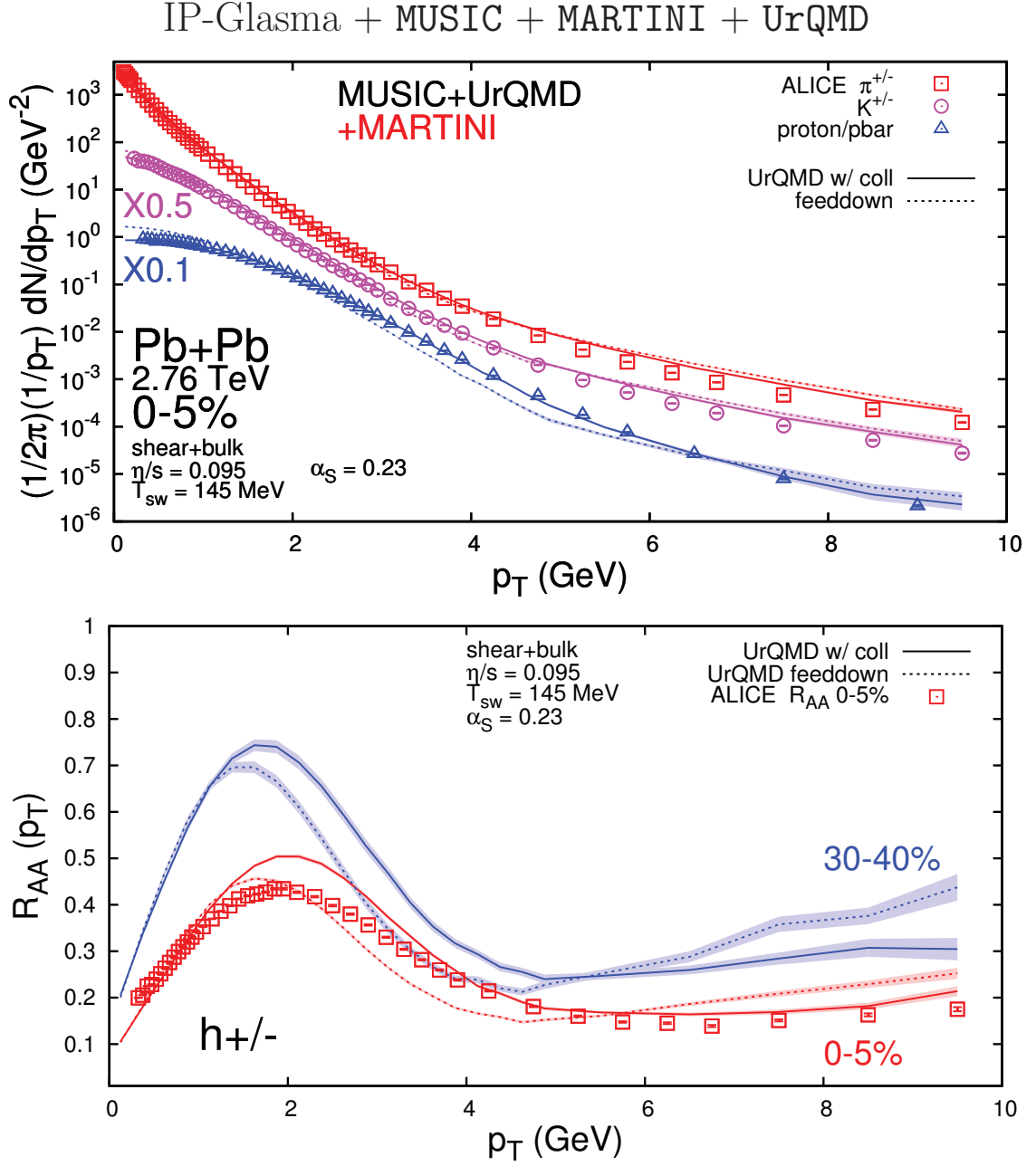


Figure 4.24: p_T spectra of identified hadrons and R_{AA} of charged hadrons of Pb + Pb collisions with $\sqrt{s_{NN}} = 2.76 \text{ TeV}$. The calculations include the MARTINI jets. The ALICE data of p_T spectra and R_{AA} are from [124] and [7], respectively. Figures shown in [23].

IP-Glasma + MUSIC + MARTINI + UrQMD

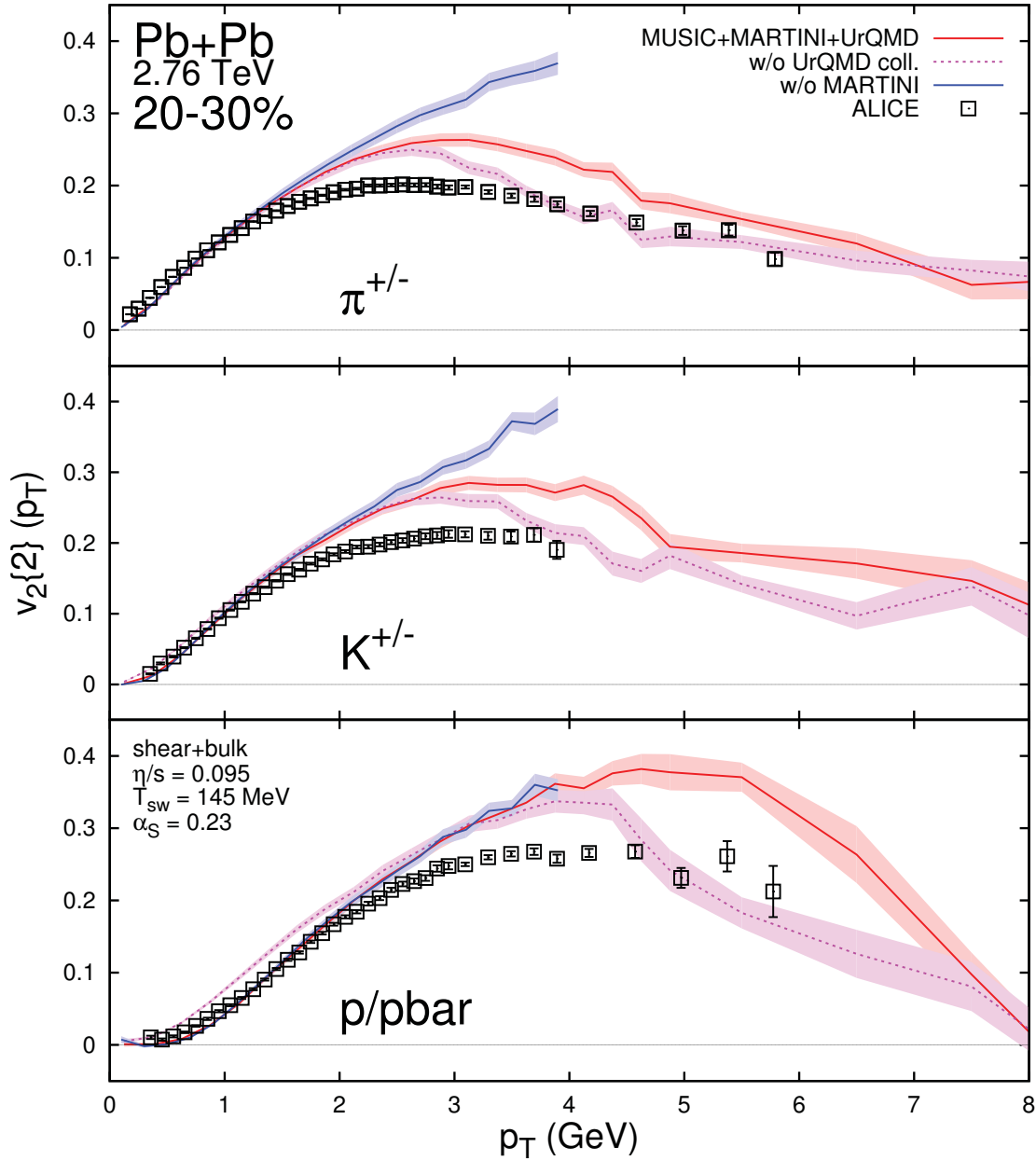


Figure 4.25: p_T -differential $v_2\{2\}$ of identified hadrons for centrality class 20 – 30% of Pb + Pb collisions with $\sqrt{s_{NN}} = 2.76$ TeV. The ALICE data are from [4]. Figures shown in [23].

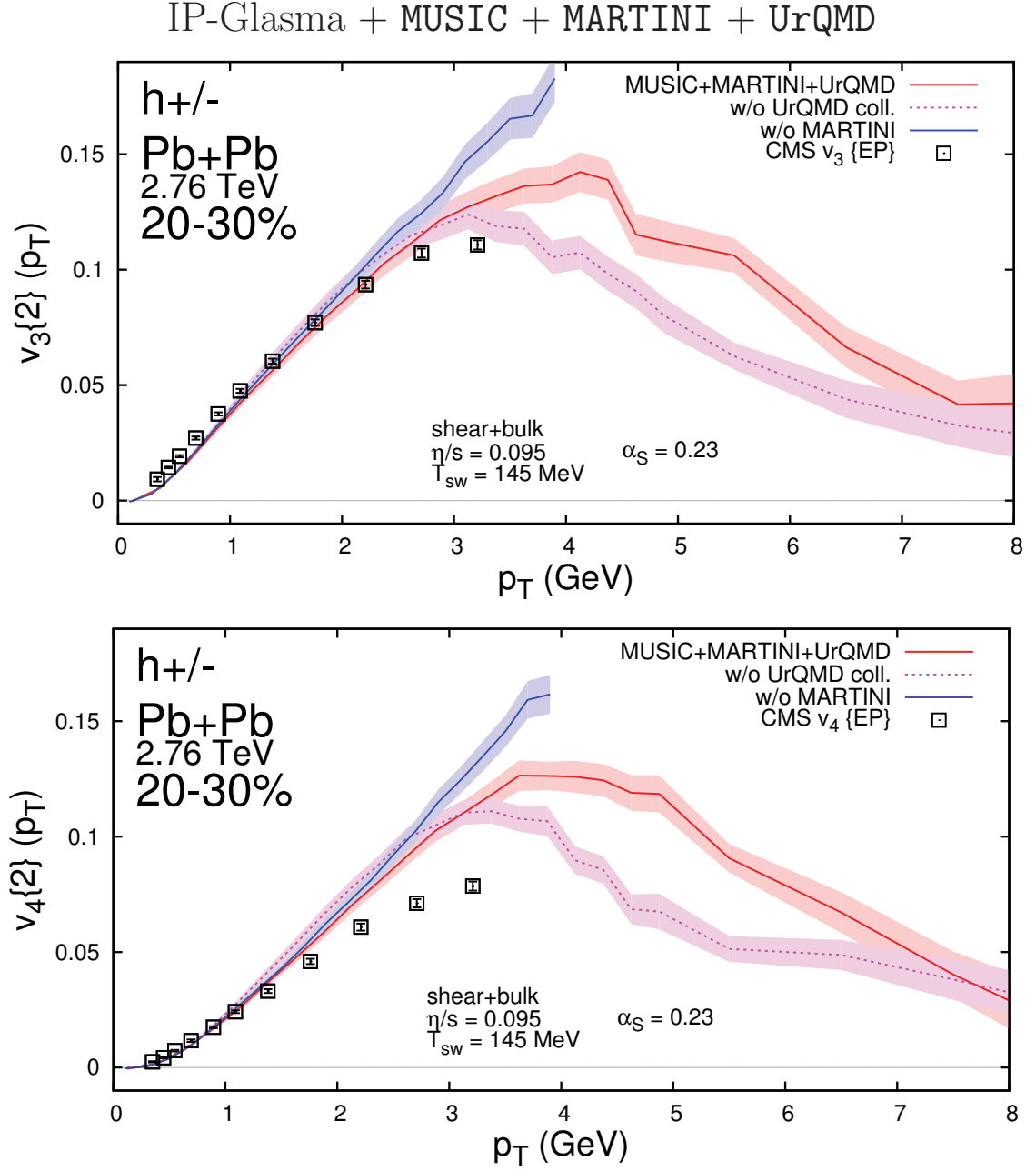


Figure 4.26: Higher harmonics $v_3(p_T)$ (upper) and $v_4(p_T)$ (lower) of charged hadrons for centrality class 20 – 30% of Pb + Pb collisions with $\sqrt{s_{NN}} = 2.76$ TeV. The CMS data are from [3]. Figures shown in [23].

Conclusion

Determination of properties of hot QCD matter is one of the goals of modern nuclear physics. In this work, as part of this effort, a hybrid model for integrated description of heavy ion collisions was constructed and applied for Pb + Pb collisions at the LHC and Au + Au collisions at RHIC. The model combines IP-Glasma [21] as the pre-thermalization dynamics, second-order viscous hydrodynamics MUSIC [33] with both of shear and bulk viscosity, energy loss of high- p_T jets simulated with MARTINI [98], and microscopic transport UrQMD [38, 39] for the hadronic re-scattering after particlization. In Chapter 2 and Chapter 3, the ingredients and how they are consistently connected to make a hybrid model are described. Comparisons with the data for Pb + Pb collisions at the LHC and Au + Au collisions at RHIC are shown in Chapter 4. The observables measured in heavy ion collisions are also defined in more detail. This study leads to some notable conclusions on the properties of hot QCD matters and description of heavy ion collisions.

- The bulk viscosity reduces the effective pressure and its gradient and it is essential to simultaneously describe the mean p_T and anisotropic flow coefficients. In addition, the estimate of shear viscosity is altered by the bulk viscosity given that the shear viscosity is determined by v_n .
- The pion wind, which is a result of non-equilibrium dynamics, leads to the acceleration and isotropization of protons. Due to the fact that the nucleon mass m_N is much larger than the switching temperature T_{sw} , the proton yield is particularly sensitive to when the system gets out of the chemical equilibrium.

The baryon-antibaryon ($B\bar{B}$) annihilation involved in UrQMD significantly affects the estimate of T_{sw} . Therefore, it is critical that both π and p are simultaneously described in any realistic model.

- Contributions from the jet becomes dominant for $p_T > 2 \text{ GeV}$. Inclusion of the high- p_T jets through MARTINI leads to reasonable descriptions of the p_T spectra and differential v_2 of identified hadrons. It was also found that the hadronic interactions, as well as partonic processes, have relevant effects on the jet quenching. Therefore, the energy loss in hadronic medium must be properly considered to study the jet-medium interaction.

In addition to the conclusions shown above, there are also open questions to explore. First of all, it is necessary to take a closer look at the discrepancy between calculations and experimental measurements of hadrons with strangeness. It was shown in the previous chapter that the model overestimates the kaon yield while it underestimates the Λ , Ξ and Ω yields. Secondly, the p_T -differential flow coefficients deviate from experimental data especially for the higher p_T , even though the integrated flow coefficients are well reproduced. The species-dependent viscous corrections δf_n to the distribution function at particlization would be an important step to address those issues. Determination of δf_n can be done based on the kinetic theory in conjunction with the matrix elements of hadronic interactions and this is under investigation [126]. One can also note that δf_n alters the hadronic chemistry since the particle distribution deviates from the thermal equilibrium.

It was also shown in [127] that the non-flow contributions in the re-scattering, as well as hydrodynamic evolution, significantly enhance the pseudo-rapidity correlation. Hence, the microscopic transport for the hadronic re-scattering must be taken into account in a phenomenological study based on the pseudo-rapidity correlations. As shown in Chapter 4, different collision energies favor different values of the shear viscosity. Correlations among the event plane angles are shown to be sensitive to how η/s depends on the temperature [128]. Systematic study of the temperature-dependent η/s is desirable.

While the hadronic re-scattering does not affect the pion v_n for Pb + Pb collisions at the LHC, relevant effects were seen for Au + Au collisions at RHIC. Hence, one can expect more effects for the smaller system or lower collision energy. This is consistent with the idea that non-equilibrium dynamics becomes more important as the Knudsen number is larger for small systems. Therefore, it would be worth applying this hybrid approach for proton-nucleus collisions or nucleus-nucleus collisions with lower energy.

6

Appendices

6.1 *Coordinate Systems and Kinematic Variables*

In this work, the z -axis is set to be the beam axis of colliding nuclei. The x^1 - x^2 plane is called *transverse plane* and the two-dimensional vector $\mathbf{x}_T = (x^1, x^2)$ denotes position on the transverse plane. Since the speed of nuclei is very close to the speed of light, it is convenient to use the Milne Coordinates $(\tau, \mathbf{x}_T, \eta_s)$ in description of heavy ion collisions. The cartesian coordinates (t, \mathbf{x}_T, z) are expressed as in terms of the Milne Coordinates as

$$t = \tau \cosh \eta_s \tag{6.1}$$

$$z = \tau \sinh \eta_s \tag{6.2}$$

where τ and η_s are called *proper time* and *space-time rapidity*, respectively. Inversely, τ and η_s can be written as

$$\tau = (t^2 - z^2)^{1/2} \tag{6.3}$$

$$\eta_s = \frac{1}{2} \ln \left(\frac{t+z}{t-z} \right). \tag{6.4}$$

Non-vanishing components of the metric in the Milne coordinates are $g_{\tau\tau} = 1$, $g_{11} = g_{22} = -1$, and $g_{\eta\eta} = -\tau^2$.

In the momentum space, the *transverse momentum* p_T , *transverse mass* m_T , and *momentum rapidity* y are defined as

$$p_T = ((p^1)^2 + (p^2)^2)^{1/2} \tag{6.5}$$

$$m_T = (m^2 + p_T^2)^{1/2} \tag{6.6}$$

$$\begin{aligned}
E_{\mathbf{p}} &= (m^2 + |\mathbf{p}|^2)^{1/2} = (m^2 + p_T^2 + (p^z)^2)^{1/2} \\
&= m_T \cosh y
\end{aligned} \tag{6.7}$$

$$p^z = m_T \sinh y \tag{6.8}$$

$$y = \frac{1}{2} \ln \left(\frac{E_{\mathbf{p}} + p^z}{E_{\mathbf{p}} - p^z} \right) \tag{6.9}$$

where m is the mass of the particle. The momentum of the particle is also measured in terms of the *pseudo-rapidity* which does not depend on the mass. The pseudo-rapidity η_p is specified once $|\mathbf{p}|$ and p^z are determined

$$|\mathbf{p}| = p_T \cosh \eta_p \tag{6.10}$$

$$p^z = p_T \sinh \eta_p \tag{6.11}$$

$$\eta_p = \frac{1}{2} \ln \left(\frac{|\mathbf{p}| + p^z}{|\mathbf{p}| - p^z} \right) \tag{6.12}$$

One has the following relations regarding the momentum space distribution

$$\frac{1}{p_T} \frac{dN}{dp_T d\phi dy} = E_{\mathbf{p}} \frac{dN}{d^3\mathbf{p}} \tag{6.13}$$

$$\frac{1}{p_T} \frac{dN}{dp_T d\phi d\eta_p} = |\mathbf{p}| \frac{dN}{d^3\mathbf{p}} \tag{6.14}$$

where ϕ is the *azimuthal angle* in the transverse plane.

6.2 Derivation of CYM for the IP-Glasma

The field strength $F^{\mu\nu}$, given by the gauge field as in equations (2.48) and (2.49), becomes

$$F^{-+} = \partial^- A^+ - \partial^+ A^- - ig[A^-, A^+] \quad (6.15)$$

$$\begin{aligned} &= \partial_+ A^+ - \partial_- A^- \\ &= \partial_+ [x^+ \alpha \theta(x^+) \theta(x^-)] + \partial_- [x^- \alpha \theta(x^+) \theta(x^-)] \\ &= [\partial_+ (x^+ \alpha) + \partial_- (x^- \alpha)] \theta(x^+) \theta(x^-) + x^+ \alpha \delta(x^+) \theta(x^-) + x^- \alpha \theta(x^+) \delta(x^-) \\ &= 2 \left(\alpha + \frac{x^+ x^-}{\tau} \partial_\tau \alpha \right) \theta(x^+) \theta(x^-) \\ &= (\tau \partial_\tau \alpha + 2\alpha) \theta(x^+) \theta(x^-) \end{aligned} \quad (6.16)$$

$$F^{i+} = \partial^i A^+ - \partial^+ A^i - ig[A^i, A^+] \quad (6.17)$$

$$\begin{aligned} &= \partial^i A^+ - \partial_- A^i - ig[A^i, A^+] \\ &= x^+ \partial^i \alpha \theta(x^+) \theta(x^-) - \frac{x^+}{\tau} \partial_\tau \alpha_3^i \theta(x^+) \theta(x^-) - \partial_- \alpha_2^i \theta(-x^+) \theta(x^-) \\ &\quad - \alpha_3^i \theta(x^+) \delta(x^-) + \alpha_1^i \theta(x^+) \delta(x^-) - \alpha_2^i \theta(-x^+) \delta(x^-) \\ &\quad - igx^+ [\alpha_3^i, \alpha] \theta(x^+) \theta(x^-) \end{aligned} \quad (6.18)$$

$$F^{-i} = \partial^- A^i - \partial^i A^- - ig[A^-, A^i] \quad (6.19)$$

$$\begin{aligned} &= \partial_+ A^i - \partial^i A^- - ig[A^-, A^i] \\ &= x^- \partial^i \alpha \theta(x^+) \theta(x^-) + \frac{x^-}{\tau} \partial_\tau \alpha_3^i \theta(x^+) \theta(x^-) + \partial_+ \alpha_1^i \theta(x^+) \theta(-x^-) \\ &\quad + \alpha_3^i \delta(x^+) \theta(x^-) + \alpha_1^i \delta(x^+) \theta(-x^-) - \alpha_2^i \delta(x^+) \theta(x^-) \\ &\quad - igx^- [\alpha_3^i, \alpha] \theta(x^+) \theta(x^-) \end{aligned} \quad (6.20)$$

$$F^{ij} = \partial^i A^j - \partial^j A^i - ig[A^i, A^j] \quad (6.21)$$

$$\begin{aligned} &= (\partial^i \alpha_3^j - \partial^j \alpha_3^i - ig[\alpha_3^i, \alpha_3^j]) \theta(x^+) \theta(x^-) \\ &\quad + (\partial^i \alpha_1^j - \partial^j \alpha_1^i - ig[\alpha_1^i, \alpha_1^j]) \theta(x^+) \theta(-x^-) \\ &\quad + (\partial^i \alpha_2^j - \partial^j \alpha_2^i - ig[\alpha_2^i, \alpha_2^j]) \theta(-x^+) \theta(x^-) \end{aligned} \quad (6.22)$$

Provided that $\Sigma_{(1,2)}$ is defined as equation (2.53), one can integrate the \pm component of the CYM equation over x^\pm

$$-\Sigma_{(2)} = \int_{-\epsilon}^{+\epsilon} dx^- \partial_- F^{-+} + \partial_i \int_{-\epsilon}^{+\epsilon} dx^- F^{i+}$$

$$-ig \int_{-\epsilon}^{+\epsilon} dx^- [A_-, F^{-+}] - ig \int_{-\epsilon}^{+\epsilon} dx^- [A_i, F^{i+}] \quad (6.23)$$

$$= F^{-+}(x^- = +\epsilon) - F^{-+}(x^- = -\epsilon) - \partial_i(\alpha_3^i - \alpha_1^i) \theta(x^+) - \partial_i \alpha_2^i \theta(-x^+) \\ - \frac{ig}{2} \int_{-\epsilon}^{+\epsilon} dx^- ([\alpha_{3i}, \alpha_1^i - \alpha_3^i] + [\alpha_{1i}, \alpha_1^i - \alpha_3^i]) \theta(x^+) \delta(x^-) \quad (6.24)$$

$$= \left\{ \tau \partial_\tau \alpha + 2\alpha + ig[\alpha_{1i}, \alpha_3^i] - \partial_i(\alpha_3^i - \alpha_1^i - \alpha_2^i) \right\}_{x^-=0} \theta(x^+) \\ - \partial_i \alpha_2^i |_{x^-=0} \quad (6.25)$$

$$-\Sigma_{(1)} = \int_{-\epsilon}^{+\epsilon} dx^+ \partial_+ F^{+-} + \partial_i \int_{-\epsilon}^{+\epsilon} dx^+ F^{i-} \\ - ig \int_{-\epsilon}^{+\epsilon} dx^+ [A_+, F^{+-}] - ig \int_{-\epsilon}^{+\epsilon} dx^+ [A_i, F^{i-}] \quad (6.26)$$

$$= F^{+-}(x^+ = +\epsilon) - F^{+-}(x^+ = -\epsilon) - \partial_i(\alpha_3^i - \alpha_2^i) \theta(x^-) - \partial_i \alpha_1^i \theta(-x^-) \\ - \frac{ig}{2} \int_{-\epsilon}^{+\epsilon} dx^+ ([\alpha_{3i}, \alpha_2^i - \alpha_3^i] + [\alpha_{2i}, \alpha_2^i - \alpha_3^i]) \theta(x^-) \delta(x^+) \quad (6.27)$$

$$= - \left\{ \tau \partial_\tau \alpha + 2\alpha - ig[\alpha_{2i}, \alpha_3^i] + \partial_i(\alpha_3^i - \alpha_1^i - \alpha_2^i) \right\}_{x^+=0} \theta(x^-) \\ - \partial_i \alpha_1^i |_{x^+=0} \quad (6.28)$$

Also, by integrating the i component over x^+ and x^- , one obtains

$$0 = \int_{-\epsilon}^{+\epsilon} dx^+ \int_{-\epsilon}^{+\epsilon} dx^- (\partial_- F^{-i} + \partial_+ F^{+i} + \partial_j F^{ji} \\ - ig[A_-, F^{-i}] - ig[A_+, F^{+i}] - ig[A_j, F^{ji}]) \quad (6.29)$$

$$= \int_{-\epsilon}^{+\epsilon} dx^+ [F^{-i}(x^- = +\epsilon) - F^{-i}(x^- = -\epsilon)] \\ + \int_{-\epsilon}^{+\epsilon} dx^- [F^{+i}(x^+ = +\epsilon) - F^{+i}(x^+ = -\epsilon)] \quad (6.30)$$

$$= -2 (\alpha_3^i - \alpha_1^i - \alpha_2^i) |_{x^+=x^-=0} \quad (6.31)$$

and deduces

$$\alpha_3^i(\tau = +0) = \alpha_1^i(x^+ = 0) + \alpha_2^i(x^- = 0). \quad (6.32)$$

Since the LHS of equations (6.25) and (6.28) do not depend on x^\pm , while one has the step function $\theta(x^\pm)$ in the RHS, it can be seen

$$\Sigma_{(1,2)}(\mathbf{x}_T) = \partial_i \alpha_{1,2}^i(x^\pm = 0) \quad (6.33)$$

$$\tau \partial_\tau \alpha + 2\alpha = -ig[\alpha_{1i}, \alpha_3^i] + \partial_i(\alpha_3^i - \alpha_1^i - \alpha_2^i) \quad \text{for } \tau \rightarrow +0. \quad (6.34)$$

By multiplying equation (6.34) by τ and integrating over τ , one gets the initial condition for α as follows

$$\epsilon^2 \alpha(\tau = +0) = \int_0^\epsilon d\tau (\tau^2 \partial_\tau \alpha + 2\tau \alpha) \quad (6.35)$$

$$= -ig \int_0^\epsilon d\tau \tau [\alpha_{1i}, \alpha_3^i] + \int_0^\epsilon d\tau \tau \partial_i (\alpha_3^i - \alpha_1^i - \alpha_2^i) \quad (6.36)$$

$$= -\frac{ig}{2} \epsilon^2 [\alpha_{1i}(x^+ = 0), \alpha_3^i(\tau = +0)] \\ + \frac{\epsilon^2}{2} \partial_i [\alpha_3^i(\tau = +0) - \alpha_1^i(x^+ = 0) - \alpha_2^i(x^- = 0)] + o(\epsilon^3) \quad (6.37)$$

$$= -\frac{ig}{2} \epsilon^2 [\alpha_{1i}(x^+ = 0), \alpha_2^i(x^- = +0)] + o(\epsilon^3) \quad (6.38)$$

Therefore, one finds

$$\alpha(\tau = +0) = -\frac{ig}{2} [\alpha_{1i}(x^+ = 0), \alpha_2^i(x^- = 0)] . \quad (6.39)$$

6.3 Necessity of Second-Order Viscous Hydrodynamics

This section is dedicated to demonstrate that the first-order Navier-Stokes hydrodynamics violates the causality. This can be done by showing that it allows a perturbation to propagate with the group velocity larger than the speed of light. The Navier-Stokes relations for the shear viscous tensor $\pi^{\mu\nu}$ and the bulk pressure Π read

$$\pi^{\mu\nu} = 2\eta \sigma^{\mu\nu} \quad (6.40)$$

$$\Pi = -\zeta \theta \quad (6.41)$$

where ζ and η are the bulk and shear viscosities, respectively. $\sigma^{\mu\nu}$ is defined in equation (2.86) and $\theta = \nabla_\alpha u^\alpha$. One can intuitively expect that the Navier-Stokes viscous hydrodynamics is not causal. While the spatial gradients are determined from the flow velocities in the neighborhood of given position, it is assumed that the system responds immediately to alter the energy-momentum tensor $T^{\mu\nu}$.

It is also possible to consider a perturbation propagating with the wavevector $k^\mu = (\omega, \mathbf{k})$ to obtain the dispersion relation and group velocity. In the presence of the perturbation, the thermodynamic quantities are given as

$$\epsilon(t, \mathbf{x}) = \epsilon_0 + \delta\epsilon e^{-i(\omega t + \mathbf{k} \cdot \mathbf{x})} \quad (6.42)$$

$$P(t, \mathbf{x}) = P_0 + \delta P e^{-i(\omega t + \mathbf{k} \cdot \mathbf{x})} \quad (6.43)$$

$$u^\mu(t, \mathbf{x}) = (1, \delta \mathbf{u} e^{-i(\omega t + \mathbf{k} \cdot \mathbf{x})}) \quad (6.44)$$

where the second and higher-order terms in $\delta \mathbf{u}$ are neglected. Given that dependence on the spacetime position has the form of the plane wave, one can make the following replacements

$$D_u = u^\mu \partial_\mu \rightarrow -i\omega \quad (6.45)$$

$$\nabla^\mu = \Delta^{\mu\alpha} \partial_\alpha \rightarrow (0, -i\mathbf{k}) \quad (6.46)$$

Substitution into equations (2.85) and (2.87) respectively yield

$$\omega \delta\epsilon = (\epsilon_0 + P_0) \mathbf{k} \cdot \delta \mathbf{u} \quad (6.47)$$

$$\mathbf{k} \delta P = (\epsilon_0 + P_0) \omega \delta \mathbf{u} + i \left(\zeta + \frac{1}{3} \eta \right) (\mathbf{k} \cdot \delta \mathbf{u}) \mathbf{k} + i\eta |\mathbf{k}|^2 \delta \mathbf{u}. \quad (6.48)$$

If the perturbation is propagating in a direction perpendicular to the flow velocity i.e., $\mathbf{k} \cdot \delta \mathbf{u} = 0$, the dispersion relation becomes

$$\omega = -i \left(\frac{\eta}{\epsilon_0 + P_0} \right) k_{\perp}^2 \quad (6.49)$$

$$\mathbf{k}_{\perp} = \mathbf{k} - \frac{\mathbf{k} \cdot \delta \mathbf{u}}{|\delta \mathbf{u}|^2} \delta \mathbf{u}. \quad (6.50)$$

Then one can consider time evolution of a Gaussian wave packet $\phi(t, \mathbf{x})$ to see how this leads to the causality violation. The thermodynamic quantities are now as follow

$$\epsilon(t, \mathbf{x}) = \epsilon_0 + \delta \epsilon \phi(t, \mathbf{x}) \quad (6.51)$$

$$P(t, \mathbf{x}) = P_0 + \delta P \phi(t, \mathbf{x}) \quad (6.52)$$

$$u^{\mu}(t, \mathbf{x}) = (1, \delta \mathbf{u} \phi(t, \mathbf{x})) \quad (6.53)$$

where the initial condition of $\phi(t, \mathbf{x})$ is

$$\phi(t=0, \mathbf{x}) = \exp \left(-\frac{x_{\perp}^2}{2R_0^2} \right) \quad (6.54)$$

$$= \frac{R_0^2}{2\pi} \int d^2 \mathbf{k}_{\perp} \exp \left(-\frac{R_0^2 k_{\perp}^2}{2} \right) e^{i \mathbf{k}_{\perp} \cdot \mathbf{x}} \quad (6.55)$$

$$\mathbf{x}_{\perp} = \mathbf{x} - \frac{\mathbf{x} \cdot \delta \mathbf{u}}{|\delta \mathbf{u}|^2} \delta \mathbf{u}. \quad (6.56)$$

From the dispersion relation in equation (6.49), one can evaluate $\phi(t, \mathbf{x})$ as a function of time

$$\phi(t, \mathbf{x}) = \frac{R_0^2}{2\pi} \int d^2 \mathbf{k}_{\perp} \exp \left(-\frac{R_0^2 k_{\perp}^2}{2} \right) e^{-i\omega t} e^{i \mathbf{k}_{\perp} \cdot \mathbf{x}} \quad (6.57)$$

$$= \frac{R_0^2}{2\pi} \int d^2 \mathbf{k}_{\perp} \exp \left[-\frac{1}{2} \left(R_0^2 + \frac{\eta t}{\epsilon_0 + P_0} \right) k_{\perp}^2 \right] e^{i \mathbf{k}_{\perp} \cdot \mathbf{x}} \quad (6.58)$$

$$= \frac{R_0^2}{R^2(t)} \exp \left(-\frac{x_{\perp}^2}{2R^2(t)} \right) \quad (6.59)$$

$$R^2(t) = R_0^2 + \frac{\eta t}{\epsilon_0 + P_0} \quad (6.60)$$

One can define a radius $r_{1/2}$ at which magnitude of the perturbation is half of that at the origin $x_{\perp} = 0$

$$\phi(t, x_{\perp} = r_{1/2}(t)) = \frac{1}{2} \phi(t, x_{\perp} = 0) \quad (6.61)$$

The time derivative of $r_{1/2}$ quantifies how fast the perturbation spreads out. If $v_{1/2} \equiv dr_{1/2}/dt$ is larger than the speed of light, it can be interpreted that the causality is violated. From equation (6.59), $r_{1/2}$ and its time derivative at $t = +0$ can be deduced as

$$r_{1/2}(t) = \sqrt{2 \ln 2} \left(R_0^2 + \frac{\eta t}{\epsilon_0 + P_0} \right)^{1/2} \quad (6.62)$$

$$v_{1/2}|_{t=+0} = \sqrt{\frac{\ln 2}{2}} \frac{\eta}{(\epsilon_0 + P_0) R_0} \quad (6.63)$$

It can be seen that $v_{1/2}$ can be larger than 1 for small R_0 . Therefore, the speed of diffusion can exceed the speed of light given that the perturbation is localized. One can read [129] for more detailed discussion.

6.4 Derivation of Viscous Hydrodynamics

This section is devoted to derivation of the equations of motion of viscous hydrodynamics in Ref. [34]. It is required to get the equations of motion for the viscous corrections Π and $\pi^{\mu\nu}$ to have viscous hydrodynamics in a closed form. Although the equation (2.73) involves time derivatives of viscous corrections, one has to specify the last three terms of the equation (2.75). Let us consider the integration of $p^\mu p^\nu p^\alpha f_n$. Based on its tensor structure, it is possible to write

$$\begin{aligned} \sum_n d_n \int_{\mathbf{p}} \frac{p^\mu p^\nu}{p \cdot u} p^\alpha f_n &= W_{3,3} u^\mu u^\nu u^\alpha + (W_{3,2})^\mu u^\nu u^\alpha + (W_{3,2})^\nu u^\alpha u^\mu + (W_{3,2})^\alpha u^\mu u^\nu \\ &+ (W_{3,1})^{\mu\nu} u^\alpha + (W_{3,1})^{\nu\alpha} u^\mu + (W_{3,1})^{\alpha\mu} u^\nu + (W_{3,0})^{\mu\nu\alpha} \end{aligned} \quad (6.64)$$

where $(W_{3,2})^\mu u_\mu = 0$, $(W_{3,1})^{\mu\nu} u_\nu = 0$ and $(W_{3,0})^{\mu\nu\alpha} u_\alpha = 0$. Contraction of the previous equation with $u_\mu u_\nu u_\alpha$ yields $W_{3,3} = \epsilon_0$ and contraction with u_α yields $(W_{3,2})^\mu = 0$ and $(W_{3,1})^{\mu\nu} = -(P_0 + \Pi)\Delta^{\mu\nu} + \pi^{\mu\nu}$. Lastly, $(W_{3,0})^{\mu\nu\alpha}$ becomes

$$(W_{3,0})^{\mu\nu\alpha} = \sum_n d_n \int_{\mathbf{p}} \frac{1}{p \cdot u} (p_\perp)^\mu (p_\perp)^\nu (p_\perp)^\alpha \delta f_n \quad (6.65)$$

where $(p_\perp)^\mu \equiv p^\mu - u^\mu (p \cdot u)$. It is possible to have nonzero $W_{3,0}$ if there is particle diffusions. Due to the assumption of a non-diffusive system, $(W_{3,0})^{\mu\nu\alpha} = 0$. Therefore, one has

$$\begin{aligned} \sum_n d_n \int_{\mathbf{p}} \frac{p^\mu p^\nu}{p \cdot u} p^\alpha f_n &= \epsilon_0 u^\mu u^\nu u^\alpha - (P_0 + \Pi)(\Delta^{\mu\nu} u^\alpha + \Delta^{\nu\alpha} u^\mu + \Delta^{\alpha\mu} u^\nu) \\ &+ \pi^{\mu\nu} u^\alpha + \pi^{\nu\alpha} u^\mu + \pi^{\alpha\mu} u^\nu. \end{aligned} \quad (6.66)$$

and the spatial divergence becomes

$$\begin{aligned} (H_3)^{\mu\nu} &= \nabla_\alpha \left[\sum_n d_n \int_{\mathbf{p}} \frac{p^\mu p^\nu}{p \cdot u} p^\alpha f_n \right] \\ &= \nabla_\alpha [\epsilon_0 u^\mu u^\nu u^\alpha - (P_0 + \Pi)(\Delta^{\mu\nu} u^\alpha + \Delta^{\nu\alpha} u^\mu + \Delta^{\alpha\mu} u^\nu)] \\ &\quad + \nabla_\alpha (\pi^{\mu\nu} u^\alpha + \pi^{\nu\alpha} u^\mu + \pi^{\alpha\mu} u^\nu) \\ &= \epsilon_0 \theta u^\mu u^\nu - [u^\mu \nabla^\nu (P_0 + \Pi) + u^\nu \nabla^\mu (P_0 + \Pi)] \\ &\quad - (P_0 + \Pi) [\theta \Delta^{\mu\nu} + \nabla^\mu u^\nu + \nabla^\nu u^\mu - 2 \theta u^\mu u^\nu] \end{aligned} \quad (6.67)$$

$$+\theta \pi^{\mu\nu} + \pi^{\mu\alpha} \nabla_\alpha u^\nu + \pi^{\nu\alpha} \nabla_\alpha u^\mu + u^\mu \nabla_\alpha \pi^{\nu\alpha} + u^\nu \nabla_\alpha \pi^{\mu\alpha} \quad (6.68)$$

$$\begin{aligned} &= T^{\mu\nu} \theta - [u^\mu \nabla^\nu (P_0 + \Pi) + u^\nu \nabla^\mu (P_0 + \Pi)] \\ &\quad - 2(P_0 + \Pi) \left(\sigma^{\mu\nu} + \frac{1}{3} \theta \Delta^{\mu\nu} - \theta u^\mu u^\nu \right) \\ &\quad + \pi^{\mu\alpha} \nabla_\alpha u^\nu + \pi^{\nu\alpha} \nabla_\alpha u^\mu + u^\mu \nabla_\alpha \pi^{\nu\alpha} + u^\nu \nabla_\alpha \pi^{\mu\alpha} \end{aligned} \quad (6.69)$$

$$\begin{aligned} &= T^{\mu\nu} \theta - u^\mu [\nabla^\nu (P_0 + \Pi) - \nabla_\alpha \pi^{\nu\alpha}] - u^\nu [\nabla^\mu (P_0 + \Pi) - \nabla_\alpha \pi^{\mu\alpha}] \\ &\quad - 2(P_0 + \Pi) \left(\sigma^{\mu\nu} + \frac{1}{3} \theta \Delta^{\mu\nu} - \theta u^\mu u^\nu \right) \\ &\quad + \pi^{\mu\alpha} \left(\sigma_\alpha^\nu + \omega_\alpha^\nu + \frac{1}{3} \theta \Delta_\alpha^\nu \right) + \pi^{\nu\alpha} \left(\sigma_\alpha^\mu + \omega_\alpha^\mu + \frac{1}{3} \theta \Delta_\alpha^\mu \right) \end{aligned} \quad (6.70)$$

$$\begin{aligned} &= T^{\mu\nu} \theta - u^\mu [\nabla^\nu (P_0 + \Pi) - \nabla_\alpha \pi^{\nu\alpha}] - u^\nu [\nabla^\mu (P_0 + \Pi) - \nabla_\alpha \pi^{\mu\alpha}] \\ &\quad - 2(P_0 + \Pi) \left(\sigma^{\mu\nu} + \frac{1}{3} \theta \Delta^{\mu\nu} - \theta u^\mu u^\nu \right) \\ &\quad + \frac{2}{3} \theta \pi^{\mu\nu} + \frac{2}{3} (\pi^{\alpha\beta} \sigma_{\alpha\beta}) \Delta^{\mu\nu} + 2\pi^{\alpha(\mu} \sigma_{\alpha}^{\nu)} - 2\pi^{\alpha(\mu} \omega_{\alpha}^{\nu)} \end{aligned} \quad (6.71)$$

The integration of $p^\mu p^\nu p^\alpha p^\beta f_n$ can be performed in the similar way

$$\begin{aligned} \sum_n d_n \int_{\mathbf{p}} \frac{p^\mu p^\nu p^\alpha p^\beta}{(p \cdot u)^2} f_n &= W_{4,4} u^\mu u^\nu u^\alpha u^\beta \\ &\quad + (W_{4,3})^\mu u^\nu u^\alpha u^\beta + (W_{4,3})^\nu u^\alpha u^\beta u^\mu \\ &\quad + (W_{4,3})^\alpha u^\beta u^\mu u^\nu + (W_{4,3})^\beta u^\mu u^\nu u^\alpha \\ &\quad + (W_{4,2})^{\mu\nu} u^\alpha u^\beta + (W_{4,2})^{\mu\alpha} u^\beta u^\nu + (W_{4,2})^{\mu\beta} u^\nu u^\alpha \\ &\quad + (W_{4,2})^{\nu\alpha} u^\beta u^\mu + (W_{4,2})^{\nu\beta} u^\mu u^\alpha + (W_{4,2})^{\alpha\beta} u^\mu u^\nu \\ &\quad + (W_{4,1})^{\mu\nu\alpha} u^\beta + (W_{4,1})^{\nu\alpha\beta} u^\mu + (W_{4,1})^{\alpha\beta\mu} u^\nu + (W_{4,1})^{\beta\mu\nu} u^\alpha \\ &\quad + X_{4,4} (\Delta^{\mu\nu} \Delta^{\alpha\beta} + \Delta^{\mu\alpha} \Delta^{\beta\nu} + \Delta^{\mu\beta} \Delta^{\nu\alpha}) \\ &\quad + (X_{4,2})^{\mu\nu} \Delta^{\alpha\beta} + (X_{4,2})^{\mu\alpha} \Delta^{\beta\nu} + (X_{4,2})^{\mu\beta} \Delta^{\nu\alpha} \\ &\quad + (X_{4,2})^{\nu\alpha} \Delta^{\beta\mu} + (X_{4,2})^{\nu\beta} \Delta^{\mu\alpha} + (X_{4,2})^{\alpha\beta} \Delta^{\mu\nu} \\ &\quad + (X_{4,0})^{\mu\nu\alpha\beta} \end{aligned} \quad (6.72)$$

where $(W_{4,3})^\mu u_\mu = 0$, $(W_{4,2})^{\mu\nu} u_\nu = 0$, $(W_{4,1})^{\mu\nu\alpha} u_\alpha = 0$ and X tensors are transverse to u^μ and also traceless i.e., contraction of any two indices with $\Delta^{\mu\nu}$ gives zero. Contraction of the previous equation with u_β provides

$$W_{4,4} = W_{3,3} = \epsilon_0 \quad (6.73)$$

$$(W_{4,3})^\mu = (W_{3,2})^\mu = 0 \quad (6.74)$$

$$(W_{4,2})^{\mu\nu} = (W_{3,1})^{\mu\nu} = -(P_0 + \Pi)\Delta^{\mu\nu} + \pi^{\mu\nu} \quad (6.75)$$

$$(W_{4,1})^{\mu\nu\alpha} = (W_{3,0})^{\mu\nu\alpha} = 0 \quad (\text{non-diffusive case}) \quad (6.76)$$

Contraction with $\Delta_{\alpha\beta}$ yields

$$\sum_n d_n \int_{\mathbf{p}} \frac{p^\mu p^\nu}{(p \cdot u)^2} (\Delta_{\alpha\beta} p^\alpha p^\beta) f_n = (W_{4,2})^{\alpha\beta} \Delta_{\alpha\beta} u^\mu u^\nu + 5X_{4,4} \Delta^{\mu\nu} + 7(X_{4,2})^{\mu\nu} \quad (6.77)$$

and therefore one has

$$\begin{aligned} X_{4,4} &= \frac{1}{15} \sum_n d_n \int_{\mathbf{p}} \frac{(-\Delta_{\mu\nu} p^\mu p^\nu)^2}{(p \cdot u)^2} f_n \\ &= \frac{1}{15} \sum_n d_n \int_{\mathbf{p}} \left[(p \cdot u)^2 - 2m_n^2 + \frac{m_n^4}{(p \cdot u)^2} \right] f_n \\ &= \frac{1}{15} \left[T^{\mu\nu} u_\mu u_\nu - 2T^\mu_\mu + \sum_n d_n m_n^4 \int_{\mathbf{p}} \frac{1}{(p \cdot u)^2} f_n \right] \\ &= \frac{1}{15} \left[\epsilon_0 - 2(\epsilon_0 - 3P_0 - 3\Pi) + \sum_n d_n m_n^4 (I_{n|-2,0} + \rho_{n|-2}) \right] \quad (6.78) \\ (X_{4,2})^{\mu\nu} &= -\frac{1}{7} \sum_n d_n \int_{\mathbf{p}} \frac{p^{(\mu} p^{\nu)}}{(p \cdot u)^2} (-\Delta_{\alpha\beta} p^\alpha p^\beta) f_n \\ &= -\frac{1}{7} \sum_n d_n \int_{\mathbf{p}} p^{(\mu} p^{\nu)} \left[1 - \frac{m_n^2}{(p \cdot u)^2} \right] f_n \\ &= -\frac{1}{7} \left(\pi^{\mu\nu} - \sum_n d_n m_n^2 (\rho_{n|-2})^{\mu\nu} \right) \quad (6.79) \end{aligned}$$

and $(H_4)^{\mu\nu}$ can be written as

$$\begin{aligned} (H_4)^{\mu\nu} &= \left(\sigma_{\alpha\beta} + \frac{1}{3} \theta \Delta_{\alpha\beta} \right) \left[\sum_n d_n \int_{\mathbf{p}} \frac{p^\mu p^\nu}{(p \cdot u)^2} p^\alpha p^\beta f_n \right] \\ &= (W_{4,2})^{\alpha\beta} \left(\sigma_{\alpha\beta} + \frac{1}{3} \theta \Delta_{\alpha\beta} \right) u^\mu u^\nu + X_{4,4} \left(2\sigma^{\mu\nu} + \frac{5}{3} \theta \Delta^{\mu\nu} \right) \\ &\quad + 2(X_{4,2})^{\mu\alpha} \sigma_\alpha{}^\nu + 2(X_{4,2})^{\nu\alpha} \sigma_\alpha{}^\mu + (X_{4,2})^{\alpha\beta} \sigma_{\alpha\beta} \Delta^{\mu\nu} + \frac{7}{3} \theta (X_{4,2})^{\mu\nu} \\ &\quad + (X_{4,0})^{\mu\nu\alpha\beta} \sigma_{\alpha\beta} \quad (6.80) \\ &= \left[-(P_0 + \Pi) \theta + \pi^{\alpha\beta} \sigma_{\alpha\beta} \right] u^\mu u^\nu \\ &\quad + \frac{1}{15} \left[-\epsilon_0 + 6(P_0 + \Pi) + \sum_n d_n m_n^4 (I_{n|-2,0} + \rho_{n|-2}) \right] \left(2\sigma^{\mu\nu} + \frac{5}{3} \theta \Delta^{\mu\nu} \right) \end{aligned}$$

$$\begin{aligned}
& -\frac{1}{7} \left(\pi^{\alpha\beta} - \sum_n d_n m_n^2 (\rho_{n|-2})^{\alpha\beta} \right) \sigma_{\alpha\beta} \Delta^{\mu\nu} - \frac{1}{3} \theta \left(\pi^{\mu\nu} - \sum_n d_n m_n^2 (\rho_{n|-2})^{\mu\nu} \right) \\
& - \frac{2}{7} (\pi^{\mu\alpha} \sigma_{\alpha}{}^{\nu} + \pi^{\nu\alpha} \sigma_{\alpha}{}^{\mu}) + \frac{2}{7} \sum_n d_n m_n^2 [(\rho_{n|-2})^{\mu\alpha} \sigma_{\alpha}{}^{\nu} + (\rho_{n|-2})^{\nu\alpha} \sigma_{\alpha}{}^{\mu}] \\
& + (X_{4,0})^{\mu\nu\alpha\beta} \sigma_{\alpha\beta} \tag{6.81}
\end{aligned}$$

$$\begin{aligned}
& = [-(P_0 + \Pi) \theta + \pi^{\alpha\beta} \sigma_{\alpha\beta}] u^{\mu} u^{\nu} \\
& + \frac{1}{15} \left[-\epsilon_0 + 6(P_0 + \Pi) + \sum_n d_n m_n^4 (I_{n|-2,0} + \rho_{n|-2}) \right] \left(2\sigma^{\mu\nu} + \frac{5}{3} \theta \Delta^{\mu\nu} \right) \\
& - \frac{1}{7} \left(\pi^{\alpha\beta} - \sum_n d_n m_n^2 (\rho_{n|-2})^{\alpha\beta} \right) \sigma_{\alpha\beta} \Delta^{\mu\nu} \\
& - \frac{1}{3} \theta \left(\pi^{\mu\nu} - \sum_n d_n m_n^2 (\rho_{n|-2})^{\mu\nu} \right) - \frac{4}{7} \pi^{\alpha\langle\mu} \sigma^{\nu\rangle}_{\alpha} - \frac{4}{21} (\pi^{\alpha\beta} \sigma_{\alpha\beta}) \Delta^{\mu\nu} \\
& + \frac{4}{7} \sum_n d_n m_n^2 \left[(\rho_{n|-2})^{\alpha\langle\mu} \sigma^{\nu\rangle}_{\alpha} + \frac{1}{3} (\rho_{n|-2})^{\alpha\beta} \sigma_{\alpha\beta} \Delta^{\mu\nu} \right] + (X_{4,0})^{\mu\nu\alpha\beta} \sigma_{\alpha\beta} \tag{6.82}
\end{aligned}$$

$$\begin{aligned}
& = [-(P_0 + \Pi) \theta + \pi^{\alpha\beta} \sigma_{\alpha\beta}] u^{\mu} u^{\nu} \\
& + \frac{1}{15} \left[-\epsilon_0 + 6(P_0 + \Pi) + \sum_n d_n m_n^4 (I_{n|-2,0} + \rho_{n|-2}) \right] \left(2\sigma^{\mu\nu} + \frac{5}{3} \theta \Delta^{\mu\nu} \right) \\
& - \frac{1}{3} \left(\pi^{\alpha\beta} - \sum_n d_n m_n^2 (\rho_{n|-2})^{\alpha\beta} \right) \sigma_{\alpha\beta} \Delta^{\mu\nu} - \frac{1}{3} \theta \left(\pi^{\mu\nu} - \sum_n d_n m_n^2 (\rho_{n|-2})^{\mu\nu} \right) \\
& - \frac{4}{7} \pi^{\alpha\langle\mu} \sigma^{\nu\rangle}_{\alpha} + \frac{4}{7} \sum_n d_n m_n^2 (\rho_{n|-2})^{\alpha\langle\mu} \sigma^{\nu\rangle}_{\alpha} + (X_{4,0})^{\mu\nu\alpha\beta} \sigma_{\alpha\beta} . \tag{6.83}
\end{aligned}$$

The equation of motion (2.76) for the viscous corrections becomes

$$\begin{aligned}
& D_u \pi^{\mu\nu} - (D_u \Pi) \Delta^{\mu\nu} \\
& = -(D_u \epsilon_0) (u^{\mu} u^{\nu} - c_s^2 \Delta^{\mu\nu}) - (\epsilon_0 + P_0 + \Pi) (u^{\nu} D_u u^{\mu} + u^{\mu} D_u u^{\nu}) \\
& - T^{\mu\nu} \theta + u^{\mu} [\nabla^{\nu} (P_0 + \Pi) - \nabla_{\alpha} \pi^{\nu\alpha}] + u^{\nu} [\nabla^{\mu} (P_0 + \Pi) - \nabla_{\alpha} \pi^{\mu\alpha}] \\
& + 2(P_0 + \Pi) \left(\sigma^{\mu\nu} + \frac{1}{3} \theta \Delta^{\mu\nu} - \theta u^{\mu} u^{\nu} \right) \\
& - \frac{2}{3} \theta \pi^{\mu\nu} - \frac{2}{3} (\pi^{\alpha\beta} \sigma_{\alpha\beta}) \Delta^{\mu\nu} - 2\pi^{\alpha\langle\mu} \sigma^{\nu\rangle}_{\alpha} + 2\pi^{\alpha\langle\mu} \omega^{\nu\rangle}_{\alpha} \\
& + [(P_0 + \Pi) \theta - \pi^{\alpha\beta} \sigma_{\alpha\beta}] u^{\mu} u^{\nu} \\
& + \frac{1}{15} \left[\epsilon_0 - 6(P_0 + \Pi) - \sum_n d_n m_n^4 (I_{n|-2,0} + \rho_{n|-2}) \right] \left(2\sigma^{\mu\nu} + \frac{5}{3} \theta \Delta^{\mu\nu} \right)
\end{aligned}$$

$$\begin{aligned}
& + \frac{1}{3} \left(\pi^{\alpha\beta} - \sum_n d_n m_n^2 (\rho_{n|-2})^{\alpha\beta} \right) \sigma_{\alpha\beta} \Delta^{\mu\nu} + \frac{1}{3} \theta \left(\pi^{\mu\nu} - \sum_n d_n m_n^2 (\rho_{n|-2})^{\mu\nu} \right) \\
& + \frac{4}{7} \pi^{\alpha\langle\mu} \sigma^{\nu\rangle}_{\alpha} - \frac{4}{7} \sum_n d_n m_n^2 (\rho_{n|-2})^{\alpha\langle\mu} \sigma^{\nu\rangle}_{\alpha} - (X_{4,0})^{\mu\nu\alpha\beta} \sigma_{\alpha\beta} \\
& + \sum_n d_n \int_{\mathbf{p}} \frac{p^\mu p^\nu}{p \cdot u} \mathcal{C}_n[f] \tag{6.84} \\
= & - [D_u \epsilon_0 + (P_0 + \Pi) \theta + \pi^{\alpha\beta} \sigma_{\alpha\beta}] u^\mu u^\nu - T^{\mu\nu} \theta \\
& + u^\mu [\nabla^\nu (P_0 + \Pi) - (\epsilon_0 + P_0 + \Pi) D_u u^\nu - \nabla_\alpha \pi^{\nu\alpha}] \\
& + u^\nu [\nabla^\mu (P_0 + \Pi) - (\epsilon_0 + P_0 + \Pi) D_u u^\mu - \nabla_\alpha \pi^{\mu\alpha}] \\
& + c_s^2 (D_u \epsilon_0) \Delta^{\mu\nu} + 2 (P_0 + \Pi) \left(\sigma^{\mu\nu} + \frac{1}{3} \theta \Delta^{\mu\nu} \right) \\
& + \frac{1}{15} \left[\epsilon_0 - 6 (P_0 + \Pi) - \sum_n d_n m_n^4 (I_{n|-2,0} + \rho_{n|-2}) \right] \left(2\sigma^{\mu\nu} + \frac{5}{3} \theta \Delta^{\mu\nu} \right) \\
& - \frac{1}{3} \left(\pi^{\alpha\beta} + \sum_n d_n m_n^2 (\rho_{n|-2})^{\alpha\beta} \right) \sigma_{\alpha\beta} \Delta^{\mu\nu} - \frac{1}{3} \theta \left(\pi^{\mu\nu} + \sum_n d_n m_n^2 (\rho_{n|-2})^{\mu\nu} \right) \\
& - \frac{10}{7} \pi^{\alpha\langle\mu} \sigma^{\nu\rangle}_{\alpha} - \frac{4}{7} \sum_n d_n m_n^2 (\rho_{n|-2})^{\alpha\langle\mu} \sigma^{\nu\rangle}_{\alpha} + 2\pi^{\alpha\langle\mu} \omega^{\nu\rangle}_{\alpha} \\
& - (X_{4,0})^{\mu\nu\alpha\beta} \sigma_{\alpha\beta} + \sum_n d_n \int_{\mathbf{p}} \frac{p^\mu p^\nu}{p \cdot u} \mathcal{C}_n[f] \tag{6.85}
\end{aligned}$$

By applying the energy-momentum conservation equations, one can rewrite it as

$$\begin{aligned}
& D_u \pi^{\langle\mu\nu\rangle} - (D_u \Pi) \Delta^{\mu\nu} = \Delta_\alpha^\mu \Delta_\beta^\nu D_u \pi^{\alpha\beta} - (D_u \Pi) \Delta^{\mu\nu} \tag{6.86} \\
= & (P_0 + \Pi) \theta \Delta^{\mu\nu} - \theta \pi^{\mu\nu} + c_s^2 (D_u \epsilon_0) \Delta^{\mu\nu} + 2 (P_0 + \Pi) \left(\sigma^{\mu\nu} + \frac{1}{3} \theta \Delta^{\mu\nu} \right) \\
& + \frac{1}{15} \left[\epsilon_0 - 6 (P_0 + \Pi) - \sum_n d_n m_n^4 (I_{n|-2,0} + \rho_{n|-2}) \right] \left(2\sigma^{\mu\nu} + \frac{5}{3} \theta \Delta^{\mu\nu} \right) \\
& - \frac{1}{3} \left(\pi^{\alpha\beta} + \sum_n d_n m_n^2 (\rho_{n|-2})^{\alpha\beta} \right) \sigma_{\alpha\beta} \Delta^{\mu\nu} - \frac{1}{3} \theta \left(\pi^{\mu\nu} + \sum_n d_n m_n^2 (\rho_{n|-2})^{\mu\nu} \right) \\
& - \frac{10}{7} \pi^{\alpha\langle\mu} \sigma^{\nu\rangle}_{\alpha} - \frac{4}{7} \sum_n d_n m_n^2 (\rho_{n|-2})^{\alpha\langle\mu} \sigma^{\nu\rangle}_{\alpha} + 2\pi^{\alpha\langle\mu} \omega^{\nu\rangle}_{\alpha} \\
& - (X_{4,0})^{\mu\nu\alpha\beta} \sigma_{\alpha\beta} + \sum_n d_n \int_{\mathbf{p}} \frac{p^\mu p^\nu}{p \cdot u} \mathcal{C}_n[f] \tag{6.87}
\end{aligned}$$

The equations of motions for $\pi^{\mu\nu}$ and Π are [34]

$$D_u \Pi + C = - \left[\left(\frac{1}{3} - c_s^2 \right) (\epsilon_0 + P_0) - \frac{2}{9} (\epsilon_0 - 3P_0) - \frac{1}{9} \sum_n d_n m_n^4 I_{n|-2,0} \right] \theta$$

$$\begin{aligned}
& -(1 - c_s^2)\Pi\theta + \frac{1}{9}\left(\sum_n d_n m_n^4 \rho_{n|-2}\right)\theta \\
& + \left(\frac{1}{3} - c_s^2\right)\pi^{\alpha\beta}\sigma_{\alpha\beta} + \frac{1}{3}\sum_n d_n m_n^2 (\rho_{n|-2})^{\alpha\beta}\sigma_{\alpha\beta}
\end{aligned} \tag{6.88}$$

$$\begin{aligned}
D_u \pi^{\langle\mu\nu\rangle} + C^{\mu\nu} = & 2\left[\frac{4}{5}P_0 + \frac{1}{15}(\epsilon_0 - 3P_0) - \frac{1}{15}\sum_n d_n m_n^4 I_{n|-2,0}\right]\sigma^{\mu\nu} \\
& - \left(\frac{4}{3}\pi^{\mu\nu} + \frac{1}{3}\sum_n d_n m_n^2 (\rho_{n|-2})^{\mu\nu}\right)\theta \\
& + \left(\frac{6}{5}\Pi - \frac{2}{15}\sum_n d_n m_n^4 \rho_{n|-2}\right)\sigma^{\mu\nu} \\
& - \frac{10}{7}\pi^{\alpha\langle\mu}\sigma^{\nu\rangle}_{\alpha} - \frac{4}{7}\sum_n d_n m_n^2 (\rho_{n|-2})^{\alpha\langle\mu}\sigma^{\nu\rangle}_{\alpha} + 2\pi^{\alpha\langle\mu}\omega^{\nu\rangle}_{\alpha} \\
& - (X_{4,0})^{\mu\nu\alpha\beta}\sigma_{\alpha\beta}
\end{aligned} \tag{6.89}$$

where C and $C^{\mu\nu}$ are defined as

$$C = \frac{1}{3}\sum_n d_n \int_{\mathbf{p}} \frac{m_n^2}{p \cdot u} \mathcal{C}_n[f] \tag{6.90}$$

$$C^{\mu\nu} = -\sum_n d_n \int_{\mathbf{p}} \frac{p^{\langle\mu} p^{\nu\rangle}}{p \cdot u} \mathcal{C}_n[f]. \tag{6.91}$$

6.5 Linearized Boltzmann Transport Equation

6.5.1 General Formulation

Although the collision term (2.67) of the Boltzmann equation is a complicated functional of the distribution function, one can simplify the problem if the deviation of the distribution function f_n from the thermal equilibrium $f_{n,0}$ is small. In this case, f_n can be written as

$$f_n = f_{n,0}(\mathbf{p}) + f_{n,0}\tilde{f}_{n,0}\chi_n(\mathbf{p}) \quad (6.92)$$

where $\chi_n(\mathbf{p})$ can also depend on the thermodynamic quantities and intrinsic properties of particle species n . \tilde{f}_n are defined in equation (2.68). By substituting equation (6.92) into equation (2.67) and keeping terms first-order in χ , one has the linearized Boltzmann equation. Given that energy, momentum and charges are conserved, it can be shown that the zeroth-order contribution vanishes. For the Bose-Einstein or Fermi-Dirac distributions, one finds

$$\tilde{f}_{n,0}(\mathbf{p}) = f_{n,0}(\mathbf{p}) \exp\left(\frac{\mathbf{p} \cdot \mathbf{u} - \mu_n}{T}\right) \quad (6.93)$$

$$\mu_n = \sum_C \mu_C C_n \quad (6.94)$$

where the summation is over all conserved charges and C_n is the charge C carried by the particle species n . For the $(l, l') \rightarrow (n, n')$ process with momenta k, k', p and p' , respectively, one has

$$\begin{aligned} & f_{l,0}(\mathbf{k}) f_{l',0}(\mathbf{k}') \tilde{f}_{n,0}(\mathbf{p}) \tilde{f}_{n',0}(\mathbf{p}') \\ &= f_{l,0}(\mathbf{k}) f_{l',0}(\mathbf{k}') f_{n,0}(\mathbf{p}) f_{n',0}(\mathbf{p}') \exp\left[\frac{(\mathbf{p} + \mathbf{p}') \cdot \mathbf{u} - (\mu_n + \mu_{n'})}{T}\right] \end{aligned} \quad (6.95)$$

$$= f_{l,0}(\mathbf{k}) f_{l',0}(\mathbf{k}') f_{n,0}(\mathbf{p}) f_{n',0}(\mathbf{p}') \exp\left[\frac{(\mathbf{p} + \mathbf{p}') \cdot \mathbf{u}}{T}\right] \prod_C \exp\left[-\frac{\mu_C}{T}(C_n + C_{n'})\right] \quad (6.96)$$

$$= f_{l,0}(\mathbf{k}) f_{l',0}(\mathbf{k}') f_{n,0}(\mathbf{p}) f_{n',0}(\mathbf{p}') \exp\left[\frac{(\mathbf{k} + \mathbf{k}') \cdot \mathbf{u}}{T}\right] \prod_C \exp\left[-\frac{\mu_C}{T}(C_l + C_{l'})\right] \quad (6.97)$$

$$= f_{n,0}(\mathbf{p}) f_{n',0}(\mathbf{p}') \tilde{f}_{l,0}(\mathbf{k}) \tilde{f}_{l',0}(\mathbf{k}') \quad (6.98)$$

where the energy-momentum conservation and charge conservation lead to the third equality. Similarly, it can be shown that $f_{l,0}(\mathbf{k}) f_{l',0}(\mathbf{k}') = f_{n,0}(\mathbf{p}) f_{n',0}(\mathbf{p}')$ for the

Boltzmann statistics. Then, the collision term can be written as

$$\mathcal{C}_n[f] = \sum_i \mathcal{C}_n^{(i)}[f] \quad (6.99)$$

$$\begin{aligned} \mathcal{C}_n^{(i)}[f] = & \frac{1}{2} \sum_{n', l, l'} d_{n'} d_l d_{l'} \frac{1}{16} \int_{\mathbf{p}'} \int_{\mathbf{k}} \int_{\mathbf{k}'} (2\pi)^4 \delta^{(4)}(p + p' - k - k') \\ & \times |\mathcal{M}((l, \mathbf{k}), (l', \mathbf{k}') \rightarrow (n, \mathbf{p}), (n', \mathbf{p}'))|^2 \mathcal{K}_{l, l'|n, n'}^{(i)}(\mathbf{k}, \mathbf{k}' | \mathbf{p}, \mathbf{p}') \\ & \times f_{l,0}(\mathbf{k}) f_{l',0}(\mathbf{k}') \tilde{f}_{n,0}(\mathbf{p}) \tilde{f}_{n',0}(\mathbf{p}') \end{aligned} \quad (6.100)$$

where $\mathcal{C}_n^{(i)}[f]$ is the contribution which involves the i -th order terms in χ . The previous argument leading to equation (6.98) implies $\mathcal{K}_{l, l'|n, n'}^{(0)} = 0$. The first and second order contributions are given by

$$\mathcal{K}_{l, l'|n, n'}^{(1)}(\mathbf{k}, \mathbf{k}' | \mathbf{p}, \mathbf{p}') = \chi_l(\mathbf{k}) + \chi_{l'}(\mathbf{k}') - \chi_n(\mathbf{p}) - \chi_{n'}(\mathbf{p}') \quad (6.101)$$

$$\begin{aligned} \mathcal{K}_{l, l'|n, n'}^{(2)}(\mathbf{k}, \mathbf{k}' | \mathbf{p}, \mathbf{p}') = & (1 + a_l f_{l,0}(\mathbf{k}) + a_{l'} f_{l',0}(\mathbf{k}')) \chi_l(\mathbf{k}) \chi_{l'}(\mathbf{k}') \\ & + (a_n f_{n,0}(\mathbf{p}) - a_l f_{l,0}(\mathbf{k})) \chi_l(\mathbf{k}) \chi_n(\mathbf{p}) \\ & + (a_n f_{n,0}(\mathbf{p}) - a_{l'} f_{l',0}(\mathbf{k}')) \chi_{l'}(\mathbf{k}') \chi_n(\mathbf{p}) \\ & + (a_{n'} f_{n',0}(\mathbf{p}') - a_l f_{l,0}(\mathbf{k})) \chi_l(\mathbf{k}) \chi_{n'}(\mathbf{p}') \\ & + (a_{n'} f_{n',0}(\mathbf{p}') - a_{l'} f_{l',0}(\mathbf{k}')) \chi_{l'}(\mathbf{k}') \chi_{n'}(\mathbf{p}') \\ & - (1 + a_n f_{n,0}(\mathbf{p}) + a_{n'} f_{n',0}(\mathbf{p}')) \chi_n(\mathbf{p}) \chi_{n'}(\mathbf{p}') \end{aligned} \quad (6.102)$$

where a_n is defined in equation (2.68).

6.5.2 Two-component System of Meson and Baryon

It can be demonstrated that, for a two-component system of meson and baryon, the bulk viscous correction employed in this work is consistent with the consequences of hadronic re-scattering. Equation (3.37) for the viscous correction due to the bulk viscosity implies that

$$\chi_n(\mathbf{p}) = -\frac{C_{\text{bulk}} \Pi}{3T} \left[\frac{m_n^2}{(p \cdot u)} - 3 \left(\frac{1}{3} - c_s^2 \right) (p \cdot u) \right]. \quad (6.103)$$

Substitution into equation (6.101) yields

$$\begin{aligned}
\mathcal{C}_n^{(1)}[f] = & -\frac{C_{\text{bulk}}\Pi}{3T} \cdot \frac{1}{32} \sum_{n',l,l'} d_{n'} d_l d_{l'} \int_{\mathbf{p}'} \int_{\mathbf{k}} \int_{\mathbf{k}'} (2\pi)^4 \delta^{(4)}(p + p' - k - k') \\
& \times |\mathcal{M}((l, \mathbf{k}), (l', \mathbf{k}') \rightarrow (n, \mathbf{p}), (n', \mathbf{p}'))|^2 f_{l,0}(\mathbf{k}) f_{l',0}(\mathbf{k}') \tilde{f}_{n,0}(\mathbf{p}) \tilde{f}_{n',0}(\mathbf{p}') \\
& \times \left[\frac{m_l^2}{(k \cdot u)} + \frac{m_{l'}^2}{(k' \cdot u)} - \frac{m_n^2}{(p \cdot u)} - \frac{m_{n'}^2}{(p' \cdot u)} \right]
\end{aligned} \tag{6.104}$$

It is shown in Chapter 4 that the hadronic re-scattering reduces baryon yields by $B\bar{B}$ annihilations. In addition, baryons are also accelerated outward as a result of pion wind. One can consider a two-component system of meson and baryon with $B\bar{B}$ annihilation ($B, \bar{B} \rightarrow M, M$), creation ($M, M \rightarrow B, \bar{B}$), and $M, B \rightarrow M, B$ scattering processes. Since meson and baryon are considered to have spins 0 and 1/2, respectively, the degeneracy factors are set as $d_M = 1$ and $d_B = 2$. The Boltzmann transport equation for the baryon B reads

$$p^\mu \partial_\mu f_B \simeq \mathcal{C}_B^{(1)}[f] \tag{6.105}$$

$$\begin{aligned}
= & -\frac{C_{\text{bulk}}\Pi}{3T} \cdot \frac{1}{16} \int_{\mathbf{p}'} \int_{\mathbf{k}} \int_{\mathbf{k}'} (2\pi)^4 \delta^{(4)}(p + p' - k - k') \\
& \times |\mathcal{M}(M, M \rightarrow B, \bar{B})|^2 f_{M,0}(\mathbf{k}) f_{M,0}(\mathbf{k}') \tilde{f}_{B,0}(\mathbf{p}) \tilde{f}_{\bar{B},0}(\mathbf{p}') \\
& \times \left[\frac{m_M^2}{(k \cdot u)} + \frac{m_M^2}{(k' \cdot u)} - \frac{m_B^2}{(p \cdot u)} - \frac{m_{\bar{B}}^2}{(p' \cdot u)} \right] \\
& - \frac{C_{\text{bulk}}\Pi}{3T} \cdot \frac{1}{8} \int_{\mathbf{p}'} \int_{\mathbf{k}} \int_{\mathbf{k}'} (2\pi)^4 \delta^{(4)}(p + k - p' - k') \\
& \times |\mathcal{M}(M, B \rightarrow M, B)|^2 f_{B,0}(\mathbf{p}') f_{M,0}(\mathbf{k}') \tilde{f}_{B,0}(\mathbf{p}) \tilde{f}_{M,0}(\mathbf{k}) \\
& \times \left[\frac{m_B^2}{(p' \cdot u)} + \frac{m_M^2}{(k' \cdot u)} - \frac{m_B^2}{(p \cdot u)} - \frac{m_M^2}{(k \cdot u)} \right]
\end{aligned} \tag{6.106}$$

where $|\mathcal{M}(M, M \rightarrow B, \bar{B})|^2 = |\mathcal{M}(B, \bar{B} \rightarrow M, M)|^2$ is assumed due to the detailed balance. The time evolution of particle yield can be expressed in terms of the divergence of the number flux

$$n_B^\mu \equiv d_B \int_{\mathbf{p}} p^\mu f_B(x, \mathbf{p}) \tag{6.107}$$

$$\partial_\mu n_B^\mu = d_B \int_{\mathbf{p}} \mathcal{C}_B[f] \quad (6.108)$$

$$\begin{aligned} &\simeq -\frac{C_{\text{bulk}}\Pi}{3T} \cdot \frac{1}{8} \int_{\mathbf{p}} \int_{\mathbf{p}'} \int_{\mathbf{k}} \int_{\mathbf{k}'} (2\pi)^4 \delta^{(4)}(p + p' - k - k') \\ &\quad \times |\mathcal{M}(M, M \rightarrow B, \overline{B})|^2 f_{M,0}(\mathbf{k}) f_{M,0}(\mathbf{k}') \tilde{f}_{B,0}(\mathbf{p}) \tilde{f}_{\overline{B},0}(\mathbf{p}') \\ &\quad \times \left[\frac{m_M^2}{(k \cdot u)} + \frac{m_M^2}{(k' \cdot u)} - \frac{m_B^2}{(p \cdot u)} - \frac{m_B^2}{(p' \cdot u)} \right] \end{aligned} \quad (6.109)$$

where the contribution from $M, B \rightarrow M, B$ scattering vanishes since it does not change the baryon yield. It can be easily seen that, if $m_M < m_B$, quantity in the bracket $[\dots]$ is negative in the center-of-mass frame of the collision. Since $[\dots]$ is Lorentz-invariant, it is negative in any frame and one has $\partial_\mu n_B^\mu < 0$ in the case of expansion ($\Pi < 0$). The third term in the brackets $[\dots]$ of equation (6.106) implies that $f_B(x, \mathbf{p})$ increases faster (or decreases slower) for the larger p and the p_T spectrum of baryon becomes harder.

6.6 String Excitation and Fragmentation in UrQMD

The string excitation and fragmentation are dominant processes in the high-energy hadronic collisions. This section is based on Refs. [38, 130]. If a collision happens to result in the string excitation, two colliding hadrons exchange momentum \mathbf{p}_\perp which is perpendicular to the collision axis in the center-of-mass frame. The probability distribution of \mathbf{p}_\perp is assumed to be Gaussian

$$\frac{dP}{d^2\mathbf{p}_\perp} = \frac{1}{\sqrt{\pi}\sigma^2} \exp\left(-\frac{p_\perp^2}{\sigma^2}\right) \quad (6.110)$$

with $\sigma = 1.6 \text{ GeV}$. Then, mass M_i , energy E_i and longitudinal momentum p_\parallel of the i -th string are determined such that

$$\sqrt{s} = E_1 + E_2 \quad (6.111)$$

$$E_i^2 = p_\parallel^2 + p_\perp^2 + M_i^2 \quad (6.112)$$

in conjunction with the probability distribution of string mass $dP/dM \propto 1/M^2$. The longitudinal momenta of two outcoming strings have opposite direction with same magnitude p_\parallel . One can rewrite the equation (6.112) in terms of the transverse mass M_T and light-cone momenta P^\pm of the string

$$P^\pm = \frac{1}{\sqrt{2}}(E \pm p_\parallel) \quad (6.113)$$

$$M_T^2 = 2(p_q^+ + p_{\bar{q}/qq}^+)(p_q^- + p_{\bar{q}/qq}^-) \quad (6.114)$$

$$= \begin{cases} 2p_q^+ p_{\bar{q}/qq}^- & \text{if } q \text{ is moving forward} \\ 2p_{\bar{q}/qq}^+ p_q^- & \text{if } \bar{q}/qq \text{ is moving forward} \end{cases} \quad (6.115)$$

where the parton momenta are lightlike i.e., $p_q^+ p_q^- = p_{\bar{q}/qq}^+ p_{\bar{q}/qq}^- = 0$. The momentum fraction $x = p_q^\pm / P^\pm$ of the quark is determined according to the parton distribution function defined in equation (1.26). The light-cone momentum of antiquark/diquark, in the case of forward-moving quark, becomes

$$p_{\bar{q}/qq}^- = \frac{M_T^2}{2xP^+}. \quad (6.116)$$

Once the string is excited with specific mass and momentum, it is followed by fragmentation into hadrons where a $q\bar{q}$ pair creation results in production of a hadron and new string. This is implemented according to the following procedure.

1. Creation of $q\bar{q}$ Pair and Identification of Hadronic Species

In *UrQMD*, $u\bar{u}$, $d\bar{d}$, and $s\bar{s}$ pairs can be created and put between two ends of the string. The probability to create $q\bar{q}$ with certain flavor is given as

$$P_{u\bar{u}} : P_{d\bar{d}} : P_{s\bar{s}} = 1 : 1 : 0.35. \quad (6.117)$$

If the string is baryonic, the $q\bar{q}$ is placed between the quark and diquark constituents and the consequence of fragmentation can be either a baryon with mesonic string or a meson with baryonic string. The $q\bar{q}$ creation is followed by the determination of hadron species from the flavors of the constituents and created quark/antiquark. The probability of having a specific spin and isospin state is given as

$$P(J^{PC}) \propto \frac{2S+1}{\langle m \rangle_{J^{PC}}}. \quad (6.118)$$

where $\langle m \rangle_{J^{PC}}$ is the average mass of J^{PC} state.

2. Determination of The Momentum of Produced Hadron

After identifying the hadron species, the momentum must be assigned to the produced hadron. This is done by determining the light-cone momentum fraction and transverse momentum of the hadron. If q and \bar{q}/qq in a string are moving forward and backward, respectively, the meson produced at the forward end is assumed to carry a lightcone momentum $p_h^+ = x_h^+ p_q^+$. The remaining quark of the $q\bar{q}$ pair carries $(1 - x_h^+) p_q^+$

$$\begin{array}{ccccc} p_q^+ & = & (1 - x_h^+) p_q^+ & + & x_h^+ p_q^+ \\ \text{string} & & \text{new string} & & \text{meson} \\ (\bar{q}/qq \cdots q\bar{q}q) & & (\bar{q}/qq \cdots q) & & (\bar{q}q) \end{array} \quad (6.119)$$

The same procedure for $p_h^- = x_h^- p_{\bar{q}/qq}^-$ is implemented at the backward end of the string

$$\begin{array}{ccccc} p_{\bar{q}/qq}^- & = & x_h^- p_{\bar{q}/qq}^- & + & (1 - x_h^-) p_{\bar{q}/qq}^- \\ \text{string} & & \text{meson/baryon} & & \text{new string} \\ (\bar{q}/qq q\bar{q} \cdots q) & & (q\bar{q}/qqq) & & (\bar{q} \cdots q) \end{array} \quad (6.120)$$

Fragmentation function $D(x_h)$ is defined as the probability distribution of x_h carried by the produced hadron. In UrQMD, two fragmentation functions are used depending on which hadron is produced

$$D_{\text{nucl}}(x_h) = \exp \left[-\frac{(x_h - B)^2}{2A^2} \right] \quad \text{for leading nucleons} \quad (6.121)$$

$$D_{\text{prod}}(x_h) = (1 - x_h)^2 \quad \text{for other produced hadrons} \quad (6.122)$$

where $A = 0.275$ and $B = 0.42$. The Field-Feynman fragmentation function [131, 132] is used for produced hadrons other than the leading nucleons. Given that p_h^+ (p_h^-) is determined, the transverse mass $m_{T,h}$ and p_h^- (p_h^+) are obtained according to

$$m_{T,h} = (m_h^2 + p_{T,h}^2)^{1/2} \quad (6.123)$$

$$p_h^\mp = \frac{m_{T,h}^2}{2p_h^\pm} \quad (6.124)$$

where the transverse momentum $p_{T,h}$ is determined according to the Gaussian distribution function (6.110). This fragmentation process is iterated until the energy of string is depleted and the remaining energy is not sufficient to produce a hadron.

3. Determination of The Formation Time

To obtain the formation time of the hadron, “yo-yo” formation time is used in UrQMD. It is described by the Hamiltonian of massless two-body system [130]

$$H = |p_{\parallel,1}| + |p_{\parallel,2}| + \kappa |x_{\parallel,1} - x_{\parallel,2}| \quad (6.125)$$

where $\kappa \simeq 1 \text{ GeV/fm}$ is the string constant which is energy contained in unit length of the tube. Provided that $q_n \bar{q}_n$ and $q_{n-1} \bar{q}_{n-1}$ pairs are created at the vertices V_n and V_{n-1} (Figure 6.1), respectively, the $q_{n-1} \bar{q}_n$ pair forms a new hadron whose energy and momentum are

$$E_n = \kappa (x_{\parallel,n-1} - x_{\parallel,n}) \quad (6.126)$$

$$p_{\parallel,n} = \kappa (t_{n-1} - t_n) . \quad (6.127)$$

In terms of light-cone coordinates, one has $p_n^\pm = \pm\kappa (x_{n-1}^\pm - x_n^\pm)$. The formation time $t_{f,n}$ becomes

$$t_{f,n} = \frac{1}{2}(t_{n-1} + t_n) + \frac{1}{2}(x_{\parallel,n-1} - x_{\parallel,n}) \quad (6.128)$$

$$= \frac{1}{\sqrt{2}}(x_{n-1}^+ + x_n^-). \quad (6.129)$$

The possibility that the produced hadron interacts during the formation time is also taken into account. If the hadron contains leading quark constituents q or \bar{q}/qq at the end of the string, its cross section is suppressed according to the number of leading constituents

$$\sigma_{(q,h)} = \frac{1}{3}\sigma_{(B,h)} \quad \text{for baryons} \quad (6.130)$$

$$\sigma_{(qq,h)} = \frac{2}{3}\sigma_{(B,h)} \quad \text{for baryons} \quad (6.131)$$

$$\sigma_{(q/\bar{q},h)} = \frac{1}{2}\sigma_{(M,h)} \quad \text{for mesons} \quad (6.132)$$

The cross section vanishes during the formation time if a newly produced hadron does not contain any leading constituent.

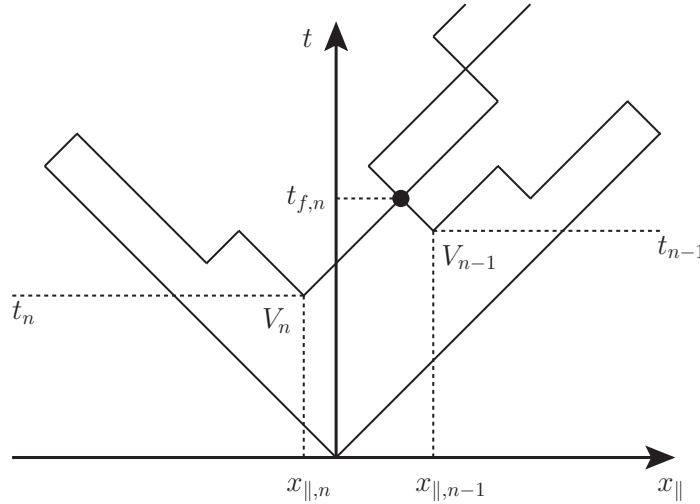


Figure 6.1: Production of hadrons in string fragmentation of *UrQMD* shown in configuration space. The “yo-yo” formation time [130] is used.

BIBLIOGRAPHY

- [1] K. Aamodt, *et al.* [ALICE Collaboration], Phys. Rev. Lett. **107**, 032301 (2011).
- [2] S. Chatrchyan, *et al.* [CMS collaboration], Phys. Rev. C **87**, 014902 (2013).
- [3] S. Chatrchyan, *et al.* [CMS collaboration], Phys. Rev. C **89**, 044906 (2014).
- [4] B. Abelev, *et al.* [ALICE collaboration], JHEP **06**, 190 (2015).
- [5] A. Adare, *et al.* [PHENIX collaboration], Phys. Rev. Lett. **107**, 252301 (2011).
- [6] B. Abelev, *et al.* [STAR Collaboration], Phys. Rev. C **77**, 054901 (2008).
- [7] K. Aamodt, *et al.* [ALICE collaboration], Phys. Lett. B **696**, 30 (2011).
- [8] J. Adams *et al.* [STAR Collaboration], Phys. Rev. Lett. **91**, 172302 (2003).
- [9] A. Adare *et al.* [PHENIX Collaboration], Phys. Rev. Lett. **101**, 232301 (2008).
- [10] [CMS Collaboration], Eur. Phys. J. C **72**, 1945 (2012).
- [11] G. Aad *et al.* [ATLAS Collaboration], Phys. Rev. Lett. **114**, 072302 (2015).
- [12] S. A. Bass and A. Dumitru, Phys. Rev. C **61**, 064909 (2000).
- [13] D. Teaney, J. Lauret, and E. Shuryak, Phys. Rev. Lett. **86**, 4783 (2001).
- [14] T. Hirano, U. Heinz, D. Kharzeev, R. Lacey, and Y. Nara, Phys. Lett. B **636**, 299 (2006).
- [15] C. Nonaka and S. A. Bass, Phys. Rev. C **75**, 014902 (2007).
- [16] H. Petersen, J. Steinheimer, G. Burau, M. Bleicher, and H. Stöcker Phys. Rev. C **78**, 044901 (2008).

- [17] C. Nonaka, AIP Conf. Proc. **1235** 165-171 (2010).
- [18] H. Petersen, G.-Y. Qin, S. A. Bass, and B. Müller, Phys. Rev. C **82**, 041901 (2010).
- [19] H. Song, S. A. Bass, and U. Heinz, Phys. Rev. C **83**, 054912 (2011).
- [20] H. Song, S. A. Bass, U. Heinz, T. Hirano, and C. Shen, Phys. Rev. Lett. **106**, 192301 (2012).
- [21] B. Schenke, P. Tribedy and R. Venugopalan, Phys. Rev. Lett. **108**, 252301 (2012).
- [22] F. Cooper and G. Frye, Phys. Rev. D **10**, 186 (1974).
- [23] S. Ryu, *et al.*, Talk given at *Second Conference on Heavy Ion Collisions in the LHC Era and Beyond*, Jul 26 - 31, 2015, Quy Nhon, Vietnam.
- [24] S. Ryu, J.-F. Paquet, C. Shen, G. S. Denicol, B. Schenke, S. Jeon and C. Gale, Phys. Rev. Lett. **115**, 132301 (2015).
- [25] M. L. Miller, K. Reygers, S. J. Sanders, and P. Steinberg, Ann. Rev. Nucl. Part. Sci. **57**, 205 (2007).
- [26] D. Kharzeev, E. Levin, and M. Nardi, Phys. Rev. C **71**, 054903 (2005).
- [27] L. V. Gribov, E. M. Levin, and M. G. Ryskin, Phys. Rep. **100**, 1 (1983).
- [28] T. Hirano and Y. Nara, Nucl. Phys. A **743**, 305 (2004).
- [29] C. Gale, S. Jeon, B. Schenke, P. Tribedy, and R. Venugopalan, Phys. Rev. Lett. **110**, 012302 (2013).
- [30] P. F. Kolb, J. Sollfrank, and U. Heinz Phys. Rev. C **62**, 054909 (2000).
- [31] K. J. Eskola, H. Honkanen, H. Niemi, P. V. Ruuskanen, and S. S. Räsänen, Phys. Rev. C **72**, 044904 (2005).

- [32] H. Song and U. Heinz Phys. Rev. C **77**, 064901 (2008).
- [33] B. Schenke, S. Jeon and C. Gale, Phys. Rev. C **82**, 014903 (2010); Phys. Rev. Lett. **106**, 042301 (2011); Phys. Rev. C **85**, 024901 (2012).
- [34] G. S. Denicol, S. Jeon and C. Gale, Phys. Rev. C **90**, no. 2, 024912 (2014).
- [35] P. Arnold, G. D. Moore, and L. G. Yaffe, JHEP **06**, 030 (2002).
- [36] P. Arnold, G. D. Moore, and L. G. Yaffe, JHEP **11**, 057 (2001).
- [37] B. Schenke, C. Gale, and G.-Y. Qin, Phys. Rev. C **79**, 054908 (2009).
- [38] S. A. Bass, *et al.*, Prog. Part. Nucl. Phys. **41**, 255 (1998).
- [39] M. Bleicher, *et al.*, J. Phys. G: Nucl. Part. Phys. **25**, 1859 (1999).
- [40] O. W. Greenberg, Phys. Rev. Lett. **13**, 598 (1964).
- [41] M. Y. Han and Y. Nambu, Phys. Rev. **139**, B1006 (1965).
- [42] M. E. Peskin and D. V. Schroeder, *An Introduction to Quantum Field Theory* (1995).
- [43] G. Altarelli and G. Parisi, Nucl. Phys. B **126**, 298 (1997).
- [44] H. Jung, Lecture Notes on *QCD and Collider Physics* (2005),
http://www.desy.de/~jung/qcd_collider_physics_2005/lecture5.pdf
- [45] C. Marquet, Nucl. Phys. A **904**, 294 (2013).
- [46] K. Golec-Biernat and M. Wüsthoff, Phys. Rev. D **59**, 014017 (1998).
- [47] H1 Collaboration, Nucl. Phys. B **497**, 3 (1997).
- [48] ZEUS Collaboration, Phys. Lett. B **407**, 432 (1997).
- [49] H. Kowalski and D. Teaney, Phys. Rev. D **68**, 114005 (2003).
- [50] J. L. Albacete and C. Marquet, Prog. Part. Nucl. Phys. **76**, 1 (2014).

- [51] J. I. Kapusta and C. Gale, *Finite-Temperature Field Theory : Principles and Applications* (2006).
- [52] J. Bartels, K. Golec-Biernat and H. Kowalski, Phys. Rev. D **66**, 014001 (2002).
- [53] L. Frankfurt, A. Radyushkin, and M. Strikman, Phys. Rev. D **55**, 98 (1997).
- [54] J. Breitweg, *et al.* [ZEUS Collaboration], Phys. Lett. B **487**, 53 (2000).
- [55] S. Chekanov, *et al.* [ZEUS Collaboration], Eur. Phys. J. C **21**, 443 (2001).
- [56] A. D. Martin, R. G. Roberts, W. J. Stirling, and R. S. Thorne, Eur. Phys. J. C **23**, 73 (2002).
- [57] H. Kowalski, L. Motyka and G. Watt, Phys. Rev. D **74**, 074016 (2006).
- [58] A. H. Rezaeian, M. Siddikov, M. Van de Klundert, and R. Venugopalan, Phys. Rev. D **87**, 034002 (2013).
- [59] L. D. McLerran and R. Venugopalan, Phys. Rev. D **49**, 2233 (1994).
- [60] L. D. McLerran and R. Venugopalan, Phys. Rev. D **49**, 3352 (1994).
- [61] L. D. McLerran and R. Venugopalan, Phys. Rev. D **50**, 2225 (1995).
- [62] A. Krasnitz and R. Venugopalan, Nucl. Phys. A **698**, 209 (2002).
- [63] A. Krasnitz, Y. Nara and R. Venugopalan, Nucl. Phys. A **717**, 268 (2003).
- [64] R. Venugopalan, J. Phys. G: Nucl. Part. Phys. **35**, 104003 (2008).
- [65] W. Israel and J. M. Stewart, Ann. Phys. (NY) **118**, 341 (1979).
- [66] G. S. Denicol, H. Niemi, E. Molnár and D. H. Rischke, Phys. Rev. D **85**, 114047 (2012).
- [67] E. Molnár, H. Niemi, G. S. Denicol, and D. H. Rischke, Phys. Rev. D **89**, 074010 (2014).

- [68] P. J. Ellis, J. I. Kapusta, and H.-B. Tang, Phys. Lett. B **443**, 63 (1998).
- [69] D. Kharzeev and K. Tuchin, JHEP. **09**, 093 (2008).
- [70] G. Boyd, *et al.*, Nucl. Phys. B **469**, 419 (1996).
- [71] F. Karsch, D. Kharzeev and K. Tuchin, Phys. Lett. B **663**, 217 (2008).
- [72] P. Arnold, C. Dogan, and G. D. Moore, Phys. Rev. D **74**, 085021 (2006).
- [73] J. Noronha-Hostler, J. Noronha and C. Greiner, Phys. Rev. Lett. **103**, 172302 (2009).
- [74] C. Amsler, *et al.*, Phys. Lett. B **667** 1 (2008).
- [75] P. Blanchard, S. Fortunato and H. Satz, Eur. Phys. J. C **34**, 361 (2004).
- [76] P. Huovinen and P. Petreczky, Nucl. Phys. A **837**, 26 (2010).
- [77] P. Petreczky, Nucl. Phys. A **830**, 11C (2009).
- [78] A. Bazavov, *et al.*, Phys. Rev. D **80**, 014504 (2009).
- [79] R. Venugopalan and M. Prakash, Nucl. Phys. A **546**, 718 (1992).
- [80] S. Eidelman, *et al.*, Particle Data Group, Phys. Lett. B **592**, 1 (2004).
- [81] P. Huovinen and S. Jeon, private communication.
- [82] H. Bebie, P. Gerber, J. L. Goity, and H. Leutwyler, Nucl. Phys. B **378**, 95 (1992).
- [83] P. Huovinen, Eur. Phys. J. A **37**, 121 (2008).
- [84] M. Bluhm, P. Alba, W. Alberico, A. Beraudo, and C. Ratti, Nucl. Phys. A **929**, 157 (2014).
- [85] A. Monnai and T. Hirano, Phys. Rev. C **80**, 054906 (2009).
- [86] P. Bozek, Phys. Rev. C **81**, 034909 (2010).

- [87] P. Arnold, G. D. Moore and L. G. Yaffe, JHEP **11**, 001 (2000).
- [88] D. Teaney, Phys. Rev. C **68**, 034913 (2003).
- [89] R. Baier, P. Romatschke, and U. A. Wiedemann, Phys. Rev. C **73**, 064903 (2006).
- [90] P. Huovinen and H. Petersen, Eur. Phys. J. A **48**, 171 (2012).
- [91] <http://pdg.lbl.gov/2015/reviews/rpp2015-rev-naming-scheme-hadrons.pdf>
- [92] Particle Data Group, Phys. Rev. D **54**, 1 (1996).
- [93] P. Koch and C. B. Dover, Phys. Rev. C **40**, 145 (1989).
- [94] T. Elioff, L. Agnew, O. Chamberlain, H. M. Steiner, C. Wiegand, and T. Ypsilantis, Phys. Rev. **128**, 869 (1962).
- [95] K. Goulianos, Phys. Rep. **101**, 169 (1983).
- [96] V. Flaminio, W. G. Moorhead, D. R. O. Morrison, and N. Rivoire, CERN, Geneva Report No. CERN-HERA-84-01 (1984).
- [97] G. Mao, Z. Li, and Y. Zhuo, Phys. Rev. C **53**, 2933 (1996).
- [98] B. Schenke, C. Gale, and S. Jeon, Phys. Rev. C **80**, 054913 (2009).
- [99] A. B. Migdal, Phys. Rev. **103**, 1811 (1956).
- [100] S. Turbide, C. Gale, S. Jeon, and G. D. Moore, Phys. Rev. C **72**, 014906 (2005).
- [101] S. Jeon and G. D. Moore, Phys. Rev. C **71**, 034901 (2005).
- [102] M. Djordjevic, Phys. Rev. C **74**, 064907 (2006).
- [103] T. Sjöstrand, S. Mrenna, and P. Skands, Comput. Phys. Commun. **178**, 852 (2008).

- [104] T. Sjöstrand, S. Mrenna, and P. Skands, *JHEP* **05**, 026 (2006).
- [105] M. R. Whalley, D. Bourilkov, and R. C. Group (2005), hep-ph/0508110.
- [106] H. L. Lai, *et al.* (CTEQ), *Eur. Phys. J. C* **12**, 375 (2000).
- [107] K. J. Eskola, V. J. Kolhinen, and C. A. Salgado, *Eur. Phys. J. C* **9**, 61 (1999).
- [108] M. Luzum and J. Y. Ollitrault, *Phys. Rev. C* **87**, 044907 (2013).
- [109] N. Borghini, P. M. Dinh, and J. Y. Ollitrault, *Phys. Rev. C* **64**, 054901 (2001).
- [110] A. Bilandzic, R. Snellings and S. Voloshin, *Phys. Rev. C* **83**, 044913 (2011).
- [111] B. Abelev, *et al.* [ALICE Collaboration], *Phys. Rev. C* **88**, no. 4, 044910 (2013).
- [112] J.-B. Rose, J.-F. Paquet, G. S. Denicol, , M. Luzum, B. Schenke, S. Jeon, and C. Gale, *Nucl. Phys. A* **931**, 926 (2014).
- [113] M. J. Bleicher, S. A. Bass, L. V. Bravina, W. Greiner, S. Soff, H. Stoecker, N. Xu and E. E. Zabrodin, *Phys. Rev. C* **62**, 024904 (2000) [hep-ph/9911420].
- [114] E. L. Bratkovskaya, W. Cassing, C. Greiner, M. Effenberger, U. Mosel and A. Sibirtsev, *Nucl. Phys. A* **675**, 661 (2000) [nucl-th/0001008].
- [115] B. Schenke, P. Tribedy and R. Venugopalan, *Phys. Rev. C* **86**, 034908 (2012).
- [116] [ALICE collaboration], *Phys. Lett. B* **728** 216 (2014).
- [117] B. Abelev, *et al.* [ALICE Collaboration], *Phys. Rev. Lett.* **111**, 222301 (2013).
- [118] H. van Hecke, H. Sorge and N. Xu, *Nucl. Phys. A* **661**, 493 (1999).
- [119] N. Arbex, F. Grassi, Y. Hama and O. Socolowski, *Phys. Rev. C* **64**, 064906 (2001).
- [120] S. Chatterjee, R. M. Godbole and S. Gupta, *Phys. Lett. B* **727**, 554 (2013) [arXiv:1306.2006 [nucl-th]].

- [121] S. S. Adler, *et al.* [PHENIX collaboration], Phys. Rev. C **69**, 034909 (2004).
- [122] J. Adams, *et al.* [STAR Collaboration], Phys. Rev. C **72**, 014904 (2005).
- [123] C. Shen and U. Heinz, Nucl. Phys. A **904-905** (2013) 361c-364c.
arXiv:1210.2074 [nucl-th]
- [124] B. Abelev, *et al.* [ALICE collaboration], Phys. Lett. B **736**, 196 (2014).
- [125] Q.-Y. Qin, J. Ruppert, C. Gale, S. Jeon, G. D. Moore, and M. G. Mustafa, Phys. Rev. Lett. **100**, 072301 (2008).
- [126] Z. Wolff and D. Molnar, arXiv:1407.6413
- [127] G. S. Denicol, A. Monnai, S. Ryu, and B. Schenke, arXiv:1512.08231, Proceedings of *the Quark Matter 2015 conference*, Sep 27 - Oct 3, 2015, Kobe, Japan.
- [128] H. Niemi, K. J. Eskola, and R. Paatelainen, Phys. Rev. C **93**, 024907 (2016).
- [129] P. Romatschke, Int. J. Mod. Phys. E **19**, 1 (2010).
- [130] B. Andersson, G. Gustafson, G. Ingelman, and T. Sjöstrand Phys. Rep. **97**, 31 (1983).
- [131] R. D. Field and R. P. Feynman, Phys. Rev. D **15**, 2590 (1977).
- [132] R. D. Field and R. P. Feynman, Nucl. Phys. B **136**, 1 (1978).